Neuronavigation-Guided Transcranial Ultrasound: Development towards a Clinical System & Protocol for Blood-Brain Barrier Opening

Shih-Ying Wu

Submitted in partial fulfillment of the
requirements for the degree of
Doctor of Philosophy
in the Graduate School of Arts and Sciences

COLUMBIA UNIVERSITY

2017

Abstract

Neuronavigation-Guided Transcranial Ultrasound: Development towards a Clinical System & Protocol for Blood-Brain Barrier Opening

Shih-Ying Wu

Brain diseases including neurological disorders and tumors remain undertreated due to the challenge in accessing the brain, and blood-brain barrier (BBB) restricting drug delivery, which also profoundly limits the development of pharmacological treatment. Focused ultrasound (FUS) with acoustic agents including microbubbles and nanodroplets remains as the only method to open the BBB noninvasively, locally, and transiently to assist drug delivery. For an ideal medical system to serve a broad patient population, it requires precise and flexible targeting with simulation to personalize treatment, real-time monitoring to ensure safety and effectiveness, and rapid application, as repetitive pharmacological treatment is often required. Since none of current systems fulfills all the requirements, here we designed a neuronavigation-guided FUS system with protocol assessed in in vivo mice, in vivo non-human primates, and human skulls from in silico preplanning, online FUS treatment and real-time acoustic monitoring and mapping, to post-treatment assessment using MRI. Both sedate and awake non-human primates were evaluated with total treatment time averaging 30 min and 3-mm targeting accuracy in cerebral cortex and subcortical structures. The FUS system developed would enable transcranial FUS in patients with high accuracy and independent of MRI guidance.

TABLE OF CONTENTS

Chapter 2 Simulation of transcranial FUS with in vivo BBB opening validation

Chapter 4 Acoustic monitoring to characterize BBB opening through the primate skulls

Chapter 5 Real-time acoustic mapping to localize cavitation through the primate skulls

Chapter 6 Neuronavigation-guided FUS and acoustic mapping for BBB opening in NHP

Chapter 7 Conclusion & future works

List of tables

List of figures

occurred when bubbles oscillated stably and periodically (stable cavitation). Ultraharmonic frequency (n*f+f/2) refers to as bubble shell oscillation or asymmetric oscillation during stable cavitation. Broadband respond occurs when bubbles undergoing inertial cavitation and release shock waves.

Figure 1.10. Schematic of microbubble structure. Modified from Wu et al. [77] and Chen et al [100].

Figure 1.11. Schematic of phase-shift nanodroplets vaporized to microbubbles. Modified from Chen et al [78].

Figure 2.1. Design of acoustic source for simulation. (A) 3D image of the ring-shaped, spherically focused ultrasound transducer for simulation, and the central space was reserved of passive cavitation detector (PCD). This design is to mimic the FUS transducer used in experiments (B). The generated acoustic pressure field in silico (C) showed an ellipsoidal focus in water.

Figure 2.2. Calibration of simulation with the FUS pressure field in water (used for primate experiments). (A) The in silico acoustic profile in the focal region was calibrated to be the same as the profile from the FUS transducer measured in water using a hydrophone, including the focal width and the side-lobes in lateral (B) and axial (C) direction.

Figure 2.3. In vivo mice experimental setup. The animals were positioned in a stereotaxic frame during the sonication. Microbubbles were injected through the tail immediately prior to the sonication. Water containers coupled the animal's head to the ultrasonic transducers using coupling gel. A therapeutic transducer was driven by an arbitrary waveform generator (AWG). A 10 MHz transducer was used for targeting and passive cavitation detection (PCD).

Figure 2.4. Customized chirp and random signal used for sonication. The varied magnitude in the temporal domain was due to the adjustment of FUS transducer sensitivity in order to reach the same pressure. Both the chirp and the random signals composed of a frequency range from 1.4-1.9 MHz as shown in the frequency spectra.

Figure 2.5. In vivo NHP experimental setup. (A) A focused ultrasound (FUS) transducer was used for sonication and a hydrophone coaxially and confocally aligned with the FUS transducer served for passive cavitation detection (PCD). (B) Targeting was performed using stereotaxis with pre-planning for focusing at the caudate nucleus (left) or putamen (right) based on the preoperative MRI scan with a stereotax.

Figure 2.6. Simulation of acoustic pressure field through the mice skull using customized pulses. (A) The mice skull was imaged in microCT. The peak negative pressure fields for different coded pulses using (B) regular sonication (1.5 MHz); (C) Chirp: 1.5-1.9 MHz, 10 kHz, 3 cycles; (D) Chirp: 1.5-1.9 MHz, 10 kHz, 2 cycles; (E) Chirp: 1.23-2.29 MHz, 10 kHz, 3 cycles; (F) Random: 1.5-1.9 MHz, 10 kHz, 3 cycles; (G) Random: 1.5-1.9 MHz, 1 kHz, 2 cycles; and (H) Random:1.23-2.29 MHz,1kHz,3 cycles. The lateral (H) and axial (I) beam profiles were plotted comparing the regular pulses to the coded pulses with best focusing quality and less standing wave in (E) and (H).

Figure 2.7. BBB opening in mice using customized pulses. (A) The spectrograms of the cavitation signals demonstrated varied harmonic frequencies using chirp or random coded pulses compared to consistent frequencies in the regular pulses. (B) Contrast enhanced T1- weighted MRI images showed the BBB opening for chirp, random and regular sonication methods, respectively. (C) Using coded pulses resulted in a more localized BBB opening. (D) The quantified stable cavitation dose showed a lower cavitation activity with coded excitation.

Figure 2.8. Simulation of acoustic pressure field through the NHP skull using customized pulses. (A) The peak negative pressure fields for different coded pulses using regular sonication (frequency: 0.5 MHz, pulse length: 10 ms), short logarithmic chirp (sweeping frequency: 0.5-2.0 MHz, pulse length: 0.5 ms), and long logarithmic chirp (sweeping frequency: 0.5-2.0 MHz, pulse length: 0.05 ms). Pressure profiles for the corresponding pulses in the (B) axial and (C) lateral direction.

Figure 2.9. Simulation of the acoustic pressure field to estimate the BBB opening in NHP. (A) The CT scan of a monkey used to calculate the acoustic properties of the skull including density and the speed of sound. (B) The simulated transcranial peak-negative pressure (PNP) field (unit normalized to the pressure without the skull) corresponded to the BBB opening in the caudate and putamen (arbitrary unit, A.U.).

Figure 2.10. Estimated skull attenuation and focal shift in silico. (A) The in situ PNP was negatively correlated with the thickness and density of the skull in the acoustic beam path as shown in the plane-fitting result with a R^2 of 0.6. (B) The in silico focal shift due to the skull in the lateral and axial direction of the acoustic wave propagation was estimated to be 0.8 mm laterally and 1 mm axially.

Figure 2.11. BBB opening in two NHPs showing inter-animal variation. (A-B) Two representative cases of BBB opening at the putamen were visualized by overlaying the contrast enhancement onto the post-Gd T_{1w} image (A: NHP 1 at 300 kPa; B: NHP 2 at 600 kPa). (C) The

opening volume was quantified at various pressures, and the error bar represents standard deviation. It was found that NHP 1 had larger opening volume than NHP 2 using the same pressure.

Figure 2.12. Targeted BBB opening in NHP in both the caudate and the putamen. (A) Visualization of targeting in the caudate nucleus (dashed contour in the left column) and the putamen (dashed contour in the right column) and the BBB opening by overlaying the contrast enhancement onto the post-Gd T1w image, where * denotes the centroid of BBB opening. (B) Targeting trajectory and the opening trajectory showed in the stacked horizontal slices. (C) 3D images with the trajectory of acoustic beam (light blue) and BBB opening (dark blue) relative to the skull.

Figure 2.13. Targeting accuracy for in vivo BBB opening in NHP. (A) Schematic of the angle definition to the skull. Target shift in BBB opening was quantified in distance (B) and in angle (C), where lPut represents left putamen, rPut for right putamen, lCd for left caudate, and rCd for right caudate. The error bar represents standard deviation.

Figure 2.14. The transducer was targeted the human brain at various orientation through the skull.

Figure 2.15. Simulation of acoustic pressure field through the human skull at various angle of incidence. The pressure distribution for placing the FUS transducer toward the brain through the occipital area of the human skull at (A) 0° and (B) 20° angle of incidence. The focal properties were quantified for the parietal (blue), occipital (red), and temporal (black) bone. (C) The FWHM focal size. (Solid line: axial direction. Dotted line: lateral direction.) (D) The focal shift or deviation. (Solid line: axial direction. Dotted line: lateral direction.) (E) The skull attenuation.

Figure 2.16. Simulation of acoustic pressure field through the human skull at various separation distance between the transducer and the skull. The pressure distribution for placing the FUS transducer toward the brain through the occipital area of the human skull at (A) 20 mm and (B) 60 mm separation distance. The focal properties through the occipital bone were quantified. (C) The FWHM focal size. (Blue line: axial direction. Red line: lateral direction.) (D) The focal shift or deviation. (Blue line: axial direction. Red line: lateral direction.) (E) The skull attenuation.

Figure 3.1. Experimental setup (A) and timeline (B) for FUS-induced BBB opening in mice *in vivo*. A focused ultrasound (FUS) transducer was used for sonication, while a pulse-echo transducer at the center of the FUS transducer was used for both targeting and passive cavitation detection (PCD) purposes. After the targeting procedure, a 30 s of sonication before microbubble injection was performed as a baseline control for PCD. The freshly diluted microbubble solution

was then co-administered with dextran intravenously, and the sonication (1 min for microbubbles and 5 min for nanodroplets) for BBB opening started 5 s after injection. 1 hr after the end of sonication the mice was sacrificed using transcardial perfusion, and its brain was extracted and preserved for future processing.

Figure 3.2. Schematic of the lipid-shelled microbubble used in this study (A) and their representative size distribution in number (B) and volume (C). Three different lipid acyl chain lengths (C16, C18, C24) were used to generate microbubbles of different physicochemical properties, while the emulsifier (DSPE-PEG2000), the molar ratio between the main lipid and the emulsifier (9:1), the gas core (PFB), and the size of the microbubbles (4-5 μm) were kept the same in order to focus on the effects of lipid hydrophobic chain length. The size of the different-shelled microbubbles was statistically the same. All microbubble suspensions were diluted to the same concentration (8×10^8 particle/mL) immediately prior to injection.

Figure 3.3. Fluorescently-tagged microbubble structure. (A) Molecular structure of 5-dodecanoylaminofluorescein (C-12). (B) Cartoon showing how the C-12 alkyl tail protrudes into the microbubble lipid shell converting the microbubble into a fluorescent drug carrier. (C) Epi-fluorescence image of a fluorescent microbubble sample. C-12 did not enter the core of the microbubbles; all the fluorescence is located at the lipid shell. The scale bar corresponds to 10 μm.

Figure 3.4. Nanodroplet characteristics. (A) Schematics of phase-shift nanodroplets through condensation process using microbubbles. The average size distribution of (B) the nanodroplets and (C) their precursor microbubbles. The average concentration and the median size for DFP droplets were 2.8×10^{11} particles/mL and 171 nm, respectively; those for DFP droplets were 1.3×10^{11} particles/mL and 183 nm, respectively.

Figure 3.5. Effects of lipid hydrophobic chain length on delivery efficiency for 3-kDa dextran after FUS-induced BBB opening using 100-cycle (67 μs) pulses. (A-L) Representative fluorescence images comparing the targeted and the control (insets) hippocampi when C16, C18 or C24 microbubbles were used to mediate BBB opening at various pressures. The scale bar in A depicts 1 mm. (M) The quantified fluorescence enhancement between the sonicated and the control ROIs showed no significant shell effect on the 3-kDa dextran delivery across the BBB.

Figure 3.6. Effects of lipid hydrophobic chain length on delivery efficiency of 40-kDa dextran after FUS-induced BBB opening using 100-cycle (67 μs) pulses. (A-L) Representative fluorescence images compare the targeted and the control (insets) hippocampi when C16, C18 or C24 microbubbles were used to mediate BBB opening at various pressures. The scale bar in A depicts 1 mm. (M) The quantified fluorescence enhancement between the sonicated and the control

ROIs showed significant shell effects on the 40-kDa dextran delivery across the BBB at higher pressures.

Figure 3.7. Effects of lipid hydrophobic chain length on delivery efficiency of 40-kDa dextran after FUS-induced BBB opening using 1000-cycle (670 μs) pulses. (A-L) Representative fluorescence images compare the targeted and the control (insets) hippocampi when C16, C18 or C24 microbubbles were used to mediate BBB opening at various pressures. The scale bar in A depicts 1 mm. (M) The quantified fluorescence enhancement between the sonicated and the control ROIs showed significant shell effects with C24 microbubbles on the 40-kDa dextran delivery across the BBB at higher pressures.

Figure 3.8. Quantified acoustic emission detected during BBB opening at various pressures and pulse lengths. For 100-cycle pulses, stable cavitation dose with harmonics (SCD_h) (A), inertial cavitation dose (B), and stable cavitation dose with ultraharmonics (SCD_u) (C) was calculated. The three types of cavitation dose for 1000-cycle pulses were also quantified (D-F).

Figure 3.9. Representative histological images of the targeted (left) and control (right) hippocampi using 100-cycle (A-F) and 1000-cycle pulses (G-L) at 600 kPa. No erythrocyte extravasation, dark neurons, gross hemorrhage or microvacuolations were observed when C16 microbubbles were used to mediate BBB opening using either 100-cycle (A-B) or 1000-cycle (G-H) pulses. Small clusters of dark neurons (indicated with stars) were identified when C18 microbubbles were used with 100-cycle pulses (C-D), while a few petechial hemorrhages (indicated with triangles) were observed with 1000-cycle pulses (I-J). Larger degree of perivascular hemorrhages was seen with C24 microbubbles regardless of the pulse length (E-F, K-L). The scale bar in A depicts 1 mm.

Figure 3.10. Using stable cavitation dose ($SCD_{h+u} = SCD_h + SCD_u$) to evaluate the opening outcomes qualitatively for classification (A) and quantitatively for delivery efficiency assessment (B). In the qualitative analysis (A), the SCD_{h+u} was separated into groups of no opening and opening (fluorescence enhancement was higher than the mean plus 2 times of standard deviation of the sham cohort), while based on the histological results it was separated into groups of no damage and damage (erythrocyte extravasation or dark neurons appeared). In the quantitative analysis (B), the fluorescence enhancement was positively correlated with the SCD_{h+u}, with a R^2 of 0.63 and 0.61 using linear fitting for 100-cycle pulses and 1000-cyle pulses, respectively.

Figure 3.11. Fluorescence enhancement in the sonicated region showed successful drug delivery at (A) 600 kPa and (B) 750 kPa.

Figure 3.12. PCD monitoring of the cavitation doses in the cases of (A) significant and (B) insignificant fluorescence delivery.

Figure 3.13. Still-frame images showing nanodroplet activation within the first two cycles of the pulse as a function of sonication pressure. Frames A-D and G-J were taken in the first rarefactional half-cycle, while E-F and K-L were taken in the following compressional cycle. No nanodroplet vaporization was detected at 0.35 MPa (left) while micron-scale acoustically-responsive bubbles were seen expanding in the rarefactional cycle at 0.45 MPa (G-J). When transitioned to the next positive pressure cycle (K, L), the newly formed bubbles were observed to respond to the acoustic pressure by compressing until no longer visible in the field of view. Times shown are relative to the start of the pulse, and the scale bars indicate 5 μm.

Figure 3.14. Normalized fluorescence enhancement between the targeted and the control hippocampi using either nanodroplets (A) or microbubbles (B) to mediate BBB opening at distinct sonication pressures. The normalized fluorescence enhancement with pressure followed a linear relationship with correlation coefficient R^2 being 0.76 and 0.94 for nanodroplets and microbubbles, respectively. Significant dextran delivery was observed at pressures higher than 0.45 MPa using nanodroplets while the BBB opening threshold was decreased down to 0.30 MPa when microbubbles were administered. All numbers are reported as mean ± standard deviation. (ns: not significant; *: $P<0.05$; **: $P<0.01$; ***: $P<0.001$)

Figure 3.15. Representative fluorescence images comparing the targeted and the control (insets) hippocampi when nanodroplets (top) or microbubbles (bottom) were used to mediate BBB opening at various sonication pressures. The left hippocampus was sonicated in the presence of either nanodroplets or microbubbles and fluorescently-labeled 3-kDa dextran. Sonications were achieved at distinct peak-rarefactional pressures: 0.15 MPa (A&F), 0.225 MPa (B&G), 0.30 MPa (C&H), 0.45 MPa (D&I) and 0.60 MPa (E&J). The scale bar in A depicts 1 mm.

Figure 3.16. Quantified acoustic emission detected during BBB opening at various sonication pressures. Stable cavitation implied that vaporized nanodroplets or microbubbles underwent stable nonlinear oscillation during sonication, while inertial cavitation signified particle fragmentation. Significant SCD increase was detected after nanodroplet injection at the highest pressure level (A), but no significant ICD increase was measured (B). On the other hand, significant increase of SCD was detected for all pressures after microbubble administration (C), and ICD increase was detected at the highest acoustic exposure level (D). All numbers are reported as mean ± standard deviation. (ns: not significant; *: $P<0.05$; ***: $P<0.001$)

Figure 3.17. Correlation between differential stable cavitation dose (SCD) and fluorescence enhancement. The SCD was normalized based on the background emission signal measured prior to contrast agent injection. Linear correlations were obtained for both (A) nanodroplets (R^2=0.74) and (B) microbubbles (R^2=0.67).

Figure 3.18. Stable cavitation dose (SCD)-indicated BBB opening threshold. The SCD was grouped based on whether significant dextran delivery was detected. Each individual brain was concluded to have significant BBB opening when the difference in fluorescence intensity between the sonicated and the control hippocampi was two standard deviations greater than the average value obtained for the corresponding sham group. Sonication using microbubbles as the contrast agents produced a much wider range of SCD values comparing to when nanodroplets were used. The SCD threshold for predicting BBB opening appeared to be contrast agent dependent. 7 out of 10 mice showed significant dextran delivery with SCD values greater than 74 V·s using nanodroplets while 92.3% of the animals showed significant dextran delivery at SCD above 1.4 kV·s using microbubbles. The slightly weaker threshold for the nanodroplet group indicated secondary mechanism other than cavitation could induce the BBB opening. (*: $P<0.05$; ***: $P<0.001$)

Figure 3.19. Representative histological images of the targeted and control hippocampi. The animals were sacrificed 1 h after sonication. (Left) No erythrocyte extravasations, dark neurons, gross hemorrhage or microvacuolations were observed when nanodroplets were used to mediate BBB opening at either 0.45 MPa or 0.60 MPa. (Right) When microbubbles were used, erythrocyte extravasations or dark neurons were not seen at 0.45 MPa. However, small clusters of erythrocyte extravasations and a few dark neurons were observed (arrow heads in O), indicating minor damage, after sonication at 0.60 MPa. The boxed regions in all 4x images are further zoomed into 10x. The scale bars in A and C depict 1 mm and 100 μm, respectively.

Figure 3.20. Detection of acoustic droplet vaporization using high-speed optical microscopy. (A) OFP-filled droplets were found to vaporize at pressures at and above 300 kPa, but not at 150 kPa. (B) DFB droplets were found to vaporize inconsistently at 600 kPa (vaporization did not occur with every activation pulse). Vaporization was consistently observed at 750 kPa and 900 kPa for DFB droplets. On average, more bubbles were generated from OFP droplets at low pressures (300-450 kPa) compared to those generated from DFB droplets at higher pressures (750-900 kPa). Scale bar represents 10 μm. (C) The vaporization efficiency defined as the number of bubbles formed in the field of view after normalized by the nanodroplets concentration was calculated. The vaporization efficiency of OFP droplets was higher than that of DFB droplets.

Figure 3.21. Delivery efficiency (40 kDa dextran) using fluorescence microscopy after BBB opening. Fluorescence images of sonicated vs. non-sonicated hippocampi (insets) using (A) OFP droplets at 300 kPa, (B) OFP droplets at 450 kPa, (C) microbubbles at 450 kPa, and (D) DFB droplets at 900 kPa. The stacked slices showed localized delivery across the entire sonicated hippocampi for (E) OFP droplets at 450 kPa, (F) microbubbles at 450 kPa, and (G) DFB droplets at 900 kPa. (H) The mean BBB opening area (normalized to the entire hippocampus) and (I) mean fluorescence intensity increase for all cohorts, with a dash line representing the threshold of successful delivery defined by the sham group (mean plus 2 time of the standard deviation). Successful delivery was found to be at and above 300 kPa for OFP droplets, and 900 kPa for DFB droplets.

Figure 3.22. Passive cavitation detection during the sonication for BBB opening, with the cavitation evolution within a pulse (spectrograms) and within the whole sonication duration (cavitation level for stable cavitation dose SCD_h, SCD_u, and inertial cavitation dose ICD) shown on the left panel and the right panel, respectively. (A) OFB droplets at 150 kPa without delivery. (B) OFP droplets at 300 kPa with delivery. (C) OFP droplets at 450 kPa with delivery. (D) Microbubbles at 450 kPa with delivery. (E) DFB droplets at 750 kPa without delivery. (F) DFB droplets at 900 kPa with successful delivery. Strong and abundant cavitation events including both stable and inertial cavitation were observed in cases with successful delivery (B, C, D, F).

Figure 3.23. Cavitation dose of the entire sonication. (A) SCD_h or stable cavitation dose with harmonic emissions. (B) SCD_u or stable cavitation dose with ultraharmonic emissions. (C) ICD or inertial cavitation dose with broadband emissions. (D) The area of BBB opening and (E) the fluorescence intensity increase using OFP droplets was linearly correlated with the total stable cavitation dose ($SCD_{u+h} = SCD_h + SCD_u$) for the cases with successful delivery. The dash line represents the threshold of successful delivery defined by the sham group (mean plus 2 times of the standard deviation).

Figure 3.24. Safety assessment using histological staining (H&E). Sonicated (A, C, E) and nonsonicated (B, D, F) hippocampi using OFB at 300 kPa (A, B), 450 kPa (C, D), and DFB at 900 kPa (E, F). The results showed no damage (erythrocyte extravasations or dark neurons) using OFP droplets. For DFB droplets at 900 kPa, only 1 out of 3 animals showed an increased amount of dark neurons on the hippocampi. The scalebar in (A) represents 1 mm.

Figure 3.25. Extravascular delivery using fluorescently tagged nanodroplets. OFP droplets were used at 450 kPa. (A) Fluorescent microscopy showed low or no delivery on the sonicated side compared to the control. (B) The quantified fluorescence intensity showed no statistical significance. Therefore, higher pressures would be required to delivery nanodroplets to the brain.

Figure 4.1. In vitro experimental setup. A focused ultrasound (FUS) transducer was used for sonication, while a flat-band hydrophone at the center of the FUS transducer was used for passive cavitation detection (PCD). The cranial part of the macaque skull (including frontal bone, parietal bones, and occipital bone) was 3.09-mm thick in average of the beam-path region, and the human skull (including the frontal and the parietal bones) was 4.65-mm thick.

Figure 4.2. In vivo NHP experimental setup. (A) A focused ultrasound (FUS) transducer was used for sonication and a hydrophone coaxially and confocally aligned with the FUS transducer served for passive cavitation detection (PCD). (B) Targeting was performed using stereotaxis with pre-planning for focusing at the caudate nucleus (left) or putamen (right) based on the preoperative MRI scan with a stereotax.

Figure 4.3. Pipeline for BBB opening volume quantification and drug delivery analysis based on MRI processing. (A) To quantify BBB opening volume, the contrast enhancement map (upper: horizontal slice, lower: coronal slice) were used after dividing the post-Gd T_1 images by the pre-Gd images. Then, after applying the brain mask and the vessel mask in order to filter out the contrast enhancement outside of the BBB opening area (B), the opening volume was calculated by subtracting the VOI in the contralateral area (dashed rectangle) from the targeted area (solid rectangle) (C). On the other hand, the pre- Gd $T_{1,0}$ (D) and post-Gd T_1 maps (E) were used to quantify the amount of Gd delivered and its delivery efficiency since the Gd shorted the T1 time after diffused the BBB opening region (arrowhead). The Gd concentration map (F)(upper: horizontal slice, lower: coronal slice) was acquired by calculating the change of T_1 time between pre- and post-Gd T_1 maps. After applying the brain mask and excluding the Gd retention in the vessels by thresholding (G), the amount of Gd delivered was calculated by subtracting the VOI in the contralateral area (dashed rectangle) from the targeting area (solid rectangle) (H).

Fig. 4.4. In vitro cavitation monitoring: spectrograms. (A) Sonicating water without the skull in place. (B) Sonicating microbubbles without the skull in place. (C) Sonicating microbubbles with the macaque skull in place. (D) Sonicating microbubbles with the human skull in place. (i), (ii), (iii), and (iv) represents 50 kPa, 150 kPa, 200 kPa, and 450 kPa, respectively. The colorbar shows the intensity of the spectra, with a dynamic range of 25 dB and 15 dB for the macaque and human skull experiments, respectively, based on the preamplification (macaque: 20 dB, human: 10 dB).

Figure 4.5. In vitro cavitation monitoring: B-mode images in transverse plane after the sonication. (A) Without the skull in place using 100 cycles. (B) With the macaque skull in place using 100 cycles. (C) With the human skull in place using 100 cycles. (D) Without the skull in place using 5000 cycles. (i), (ii), (iii), and (iv) represents 50 kPa, 150 kPa, 200 kPa, and 450 kPa, respectively. The arrows indicate the spot losing echogenicity at the pressure threshold (200 kPa).

The images showed good focal alignment to the channel and the bubbles lost the property of contrast enhancement at or above 200 kPa. The shape to the hypoechogenitic area was roughly a circle with an averaged diameter of 1.3 mm at 200 kPa and 4 mm at 450 kPa.

Figure 4.6. In vitro cavitation doses. (A) SCD_h, (B) SCD_u, and (C) ICD for the macaque skull experiments using 100-cycle pulses. (D) SCD_h, (E) SCD_u, and (F) ICD for the human skull experiments using 100-cycle pulses. (G) SCD_h, (H) SCD_u, and (I) ICD without the skull in place using 100- and 5000-cycle pulses. The error bar shows the standard deviation. *: $p<0.05$. Green *: comparison made in the cases without the skull in place. Red *: comparison made in the cases with the skull in place. All of the comparisons in (G)-(I) showed statistical significance. All of the cavitation doses became detectable at 50 kPa, while this detectable pressure threshold may change after placing the skull. The nonlinear effect of the skull was seen after placing the human skull at high pressures as the SCD_h increased significantly. Applying long pulses (5000 cycles) was effective in generating high cavitation doses at low pressures when compared with applying short pulses (100 cycles).

Figure 4.7. In vitro cavitation SNR (a) without the skull in place using 100-cycle pulses, (b) without the skull in place using 5000-cycle pulses, (c) with the macaque skull in place using 100 cycles, and (d) with the human skull in place using 100 cycles. The error bar shows the standard deviation. The dash lines in (a) represent the SNR threshold for surpassing the skull attenuation (macaque: 15.2 dB, human: 34.1 dB). For SNR higher than 1 dB, the detected cavitation doses were significantly higher than that of control. This 1 dB was deemed as the detection threshold with and without the skull.

Figure 4.8. In vivo cavitation doses using 100- and 5000-cycle pulses. (A) SCD_h. (B) SCD_u. (C) ICD. *: $p<0.05$. The error bar shows the standard deviation. When using 5000-cycle pulses, the SCD_h became detectable transcranially at 100 kPa; for the ICD, 250 kPa; while the SCD_u was unrealiable and could be detected at high pressures. When using 100-cycle pulses, the pressure threshold in detecion increased.

Figure 4.9. In vivo cavitation SNR using (A) 100-cycle and (B) 5000-cycle pulses. The error bar shows the standard deviation. The cavitation SNR using 100-cycle pulses increased with pressure. When using 5000-cycle pulses, the SNR of the SCD_u and ICD increased with pressure, while it for the SCD_h reached plateau due to the nonlinear effect of the skull at high pressures.

Figure 4.10. Real-time cavitation monitoring during in vivo BBB opening at (a) 275 kPa, (b) 350 kPa, (c) 450 kPa, and (d) 600 kPa in the thalamus (orange arrow) or the putamen (green arrow).

The upper and middle rows show the post-contrast T1 weighted images with calculated enhancement (with colorbar) in axial and coronal view, respectively. The opening volume of (a) to (d) was 494.7, 230.9, 112.9, and 299.2 mm^3, respectively. The bottom row shows the real-time monitoring of the SCD_h, SCD_u, and ICD for sonicating the thalamus. Note that in (d) the microbubbles were injected before the sonication was started. Case (b)-(d) were performed in the same macaque.

Figure 4.11. Safety assessment using MRI at (a) 275 kPa, (b) 350 kPa, (c) 450 kPa, and (d) 600 kPa. The upper row shows the T2-weighted images (coronal view) for detecting the edema, which is lighter if occurred. The lower row shows the SWI (coronal view) for detecting the hemorrhage, which is darker if occurred. In all cases, no hemorrhage and edema was detected.

Figure 4.12. BBB opening with real-time acoustic cavitation monitoring in two NHPs. FUS-induced BBB opening in NHPs was visualized in T_{1w} images after overlaying the contrast enhancement onto the post-Gd T_{1w} image (A-B) (A: NHP 2 at 300 kPa; B: NHP 3 at 600 kPa). The corresponded Gd concentration map ($[Gd]_c$) (C-D) showed the variation of Gd delivered in gray and white matter according to the tissue segmentation map based on the pre-Gd T_1 map (E-F)(dark gray: gray matter, light gray: white matter, black: blood, white: CSF). The acoustic cavitation emission were recorded and calculated in real time. (G-H). The BBB opening of NHP 2 and 3 showed an inter-animal variation and may be due to the skull.

Figure 4.13. Cavitation monitoring in assessing the BBB opening and drug delivery. (A) In order to study the intra-animal variation, NHP 1 was sonicated with the same targeting (putamen) and acoustic parameters (275 kPa) in a bi-weekly basis five times. FUS-induced BBB opening was performed in three NHPs with the opening volume (B), and the drug delivery analysis was performed in two NHPs for the amount of Gd delivered and the delivery efficiency (C). NHP 1 to NHP 3 were sonicated 7, 12, and 24 times, respectively, and the error bar represents standard deviation. Both (B) and (C) showed an inter-animal variation as the BBB opening threshold for NHP 1 and 2 were lower than that for NHP 3. Quantified cavitation doses (SCD_h: stable cavitation dose with harmonics, SCD_u: stable cavitation dose with ultraharmonics, ICD: inertial cavitation dose) were correlated with the BBB opening outcomes. The SCD_h can be used to detect the effectiveness of BBB opening (D). For a quantitative assessment, the opening volume (E), the amount of delivered Gd and delivery efficiency (F) was positively correlated with the total cavitation dose (SCD_h + SCD_u + ICD). (The R^2 of the linear fitting in (E) for NHP 1 to 3 and all experiments across animals was 0.81, 0.63, 0.50, and 0.47, respectively; that in (F) for NHP 2, 3, and all experiments across animals was 0.52, 0.71, and 0.61, respectively.)

Figure 4.14. Effect of gray and white matter. FUS was applied in the caudate and putamen in three animals causing a BBB opening volume close to 400 mm^3 (300 kPa for NHP 2, 450 kPa for

NHP 3 and 4). The opening volume was shown in (A), and the total cavitation dose in (B). Based on the tissue segmentation, the gray-and-white matter composition in the sonicated area (C) and in the BBB opening area (D) were calculated. The correlation of total cavitation dose to the BBB opening volume was calculated in (E), in which it was better correlated with the total opening volume than with the volume in gray matter.

Figure 4.15. Vasculature effect. MR angiography (MRA) in NHP in (A) coronal, (B) sagittal, and (C) horizontal view, and the middle cerebral artery (MCA) was indicated by an arrowhead. (D) Four BBB opening cases targeting regions proximal to the MCA (arrowhead) at 450 kPa in NHP 4, where the upper row showed the opening volume overlaying onto the post-Gd T_{1w} images and the lower row was the cavitation response along the sonication time. PCD calibration (E-G) after BBB opening in cases i-iii was performed in order to assess the cavitation level at different pressures (10 pulses per pressure) with targeted regions near or include the MCA (E: SCD_h, F: SCD_u, G: ICD), and the errorbar represented the standard deviation of the 10 sonications. Note that the opening volume for case i to iv was 309, 469, 443, and 758 mm^3 and angle of incidence to the skull: 24°, 18°, 35°, 41°, respectively. The cavitation level varied as the targeted region approached the MCA that was correlated with the opening volume but was found to be independent of the incidence angle.

Figure 4.16. Safety assessments in the MRI. (A) NHP 1 targeting putamen at 275 kPa. (B) NHP 2 targeting caudate nucleus and putamen at 400 kPa. (C) NHP 3 targeting putamen at 450 kPa. (D) NHP 4 targeting caudate nucleus and putamen at 600 kPa. No edema or hemorrhage was detected in any of the cases. 1st row: contrast enhancement of the BBB opening overlaying onto the post-Gd T_{1w} imaging; 2nd row: T_{2w} imaging for edema; 3rd row: susceptibility-weighted imaging (SWI) for hemorrhage.

Figure 5.1 Schematic of passive cavitation mapping algorithm based on time exposure acoustics. The passive cavitation signal was acquired in a PCD array, stored as channel data for each sonicated pulse. Several passive frames were reconstructed in one single FUS pulse with different time windows representing the cavitation map in each time segment. They were summed together as integration over the exposure time (T_e) to enhance the cavitation signals in a spatial domain.

Figure 5.2. Matrix calculation for reconstructing a cavitation map. (A) Delay-and-sum (DAS) beamforming to reconstruct a series of radiofrequency (RF) frames using sparse matrix calculation. (B) The cavitation map of a single pulse is the sum of squared RF frames at each time window, i.e., the time integration of TEA. (C) The channel dataset in (A) is extracted from a series of time window in the channel data received from a single pulse during sonication.

Figure 5.3. Experimental setups for (A) the in vitro skull and phantom and (B) the in vivo BBB opening in NHP. In the in vitro experiment, the FUS transducer was place on top of the channel phantom orthogonal to the PCD array, and the skull was placed in between the phantom and the PCD array for assessing the skull effects on the cavitation mapping. In the in vivo experiment, the FUS transducer was targeted to the region of interest based on the stereotaxis while the PCD array was placed against the temporal bone toward the FUS focus.

Figure 5.4. The impact of exposure time on computational time and mapping characteristics. (A) The exposure time (T_e) was linearly correlated with the computational time (T_c) since it determined the number of RF frames required to be reconstructed for one single cavitation map. (B) This exposure time also affected the mapping quality in terms of denoising and homogeneity of cavitation distribution. The maximal intensity of the map increased until reached to a plateau as more RF frames were added. This cavitation distribution also formed in a localized region at a very short exposure time (1.44 μs) as shown in the cavitation region (-6 dB area) until reaching a steady state at 62.5 μs. This representative case was performed at 450 kPa, while all other cases at various pressure showed the same trend.

Figure 5.5. Detection threshold of cavitation mapping through the primate skulls. Cavitation maps at various pressures (A) without the skull in place, (B) with the NHP skull, (C) with the human skull in place were acquired. The cavitation distribution was successfully reconstructed at all pressures from 150 kPa to 600 kPa. It can be detected at and above 300 kPa and 450 kPa through the monkey skull and human skull, respectively.

Figure 5.6. Cavitation mapping during BBB opening in NHP 1. (A) BBB opening (colored) revealed after post processing in the horizontal slice of the contrast-enhanced T1w MRI. BBB opening was induced at 450 kPa while the PCD array (placed against the temporal bone toward the FUS focus) acquired cavitation signals for reconstruction of cavitation maps. (B) Both the single-element PCD and the PCD array acquired cavitation signal for real-time monitoring. The calculated cavitation doses from the single-element PCD is shown on the left, and the total intensity of cavitation signals (sum of the squared channel data) from the PCD array on the right. (C) The reconstructed cavitation maps at each time point revealed the location cavitation events in the brain (using the -6 dB scale relative to the maxima).

Figure 5.7. Stable cavitation mapping during BBB opening in NHP 2. (A) BBB opening (colored) revealed after post processing in the horizontal slice of the contrast-enhanced T1w MRI. BBB opening was induced at 450 kPa while the PCD array (placed against the temporal bone toward the FUS focus) acquired cavitation signals for reconstruction of cavitation maps. (B) Both the single-element PCD and the PCD array acquired cavitation signal for real-time monitoring. The calculated cavitation doses from the single-element PCD is shown on the left, and the total

intensity of cavitation signals from the PCD array on the right. (C) The reconstructed cavitation maps at each time point revealed the location and intensity increase of cavitation events in the brain (using the intensity as the color scale).

Figure 6.1. Acquiring preoperative anatomical images with fiducials for registration. (A) A NHP skull with a bite bar connecting unique teeth impression to the fiducial plates. (C) NHP brain images with donut-shape fiducials (D) in T1w MRI. The fiducial landmarks (center of the fiducials) were identified in the neuronavigation system for registration.

Figure 6.2. Experimental setup with neuronavigation for (A) the sedate and (B) the awake animal. Infrared (IR) camera was the position tracking device connected to the computer to process image registration in real time in the neuronavigation system. The trackers bared three reflective spheres for the IR camera to detect transducers (tool trackers) relative to the animal subject in the physical space (subject tracker). At the beginning of the treatment session, the fiducials were attached to the invariant traits (bite bars or head post) of the animal for registering the animal subject to the neuronavigation system. After the registration, the fiducials were removed and the FUS transducer was aligned to the preplanned targeting and secured with the free-guide arm or stereotactic arm for sonication.

Figure 6.3. Preplanning procedure for FUS targeting. (A) Flowchart for preplanning and FUS treatment procedure of neuronavigation-guided ultrasound. (B) Screenshots of the preplanning on the neuronavigation system. Preplanning for the FUS target and trajectory through the 3D segmented and reconstructed skull (1), basal ganglia (2), and the scalp with the donut-shaped fiducials (3), and the focus was at the crosshair of the MRI slices (4-6) acquired preoperatively.

Figure 6.4. Neuronavigation-guided FUS treatment procedure. (A) Flowchart for implementing FUS targeting to the preplanning. (B) Screenshots of the online session showing the FUS trajectory in the reconstructed 3D brain (1) targeted the putamen in two orthogonal MRI slices, in which the vertical arrows represent the FUS trajectory pointing at the focus (2-3). (4) The implementation accuracy of the FUS transducer to the preplanning was displayed as a feedback for the distance (visualized as the distance between the red dot and the center of the larger circle) and the angle deviation (visualized as the distance between the red dot and the center of the smaller circle) during the guiding process. (5) The PCD array for cavitation mapping was aligned to the FUS focus before the sonication with neuronavigation guidance.

Figure 6.5. Neuronavigation-guided FUS for BBB opening in the sedate animal. Accurate BBB disruption were achieved with neuronavigation in the caudate nucleus (NHP 2 at 450 kPa) and in the putamen (NHP 3 at 600 kPa). The coronal slices in (A) and (E), the sagittal slices in (B)

and (F), the horizontal slices in (C) and (G), and the stacked horizontal slices with the BBB opening trajectory (red line) and the planned trajectory (blue line) in (D) and (H). The cross represents the centroid of BBB opening and the circle the FUS focus in the neuronavigation system.

Figure 6.6. Neuronavigation-guided FUS for BBB opening in the awake animal trained to sit in the customized chair. Accurate BBB disruption were achieved with neuronavigation in the central sulcus and in caudate nucleus (NHP 4 at 300 kPa). The coronal slices in (A) and (E), the sagittal slices in (B) and (F), the horizontal slices in (C) and (G), and the stacked horizontal slices with the BBB opening trajectory (red line) and the planned trajectory (blue line) in (D) and (H). The cross represents the centroid of BBB opening and the circle the FUS focus in the neuronavigation system.

Figure 6.7. Accuracy for the neuronavigation-guided ultrasound system compared with frame-based method. (A) The total focal shift with the neuronavigation was slightly smaller than with the stereotaxis although it showed no statistical significance. (B) After breaking into the lateral (lat), the axial (ax) direction and the angle, the neuronavigation showed a significant improvement on the lateral direction.

Figure 6.8. Neuronavigation-guided cavitation mapping during sonication for BBB opening. (A) The averaged frequency spectra in the channel data of the PCD array. (B) The total intensity of the channel data during the 2-min sonication showed significant cavitation response after microbubbles perfused the brain. The reconstructed cavitation maps showed the exact location of the BBB opening in the caudate at 450 kPa (C) and the putamen at 450 kPa (D). (E) The cavitation mapping showed an accurate monitoring at the location of BBB opening.

Figure 7.1. Flowcharts for the (A) in silico preplanning and (B) online FUS treatment procedure.

Abbreviations

Aβ	Amyloid plaques made up of beta-amyloid peptides
AD	Alzheimer's disease
AFM	Atomic force microscopy
BBB	Blood-brain barrier
Cau	Caudate nucleus
CNS	Central nervous system
CSF	Cerebral spinal fluid
CT	Computerized tomography
DBS	Deep brain stimulation
DFB	Decafluorobutane
DLiPC (C24)	1,2-dilignoceroyl-sn-glycero-3-phosphocholine
DPPC (C16)	1,2-dipalmitoyl-sn-glycero-3-phosphocholine
DSPC (C18)	1,2-distearoyl-sn-glycero-3-phosphocholine
DSPE-PEG2000	1,2-distearoyl-sn-glycero-3phosphoethanolamine-N-[methoxy(polyethylene glycol)2000]
H&E	Hematoxylin and eosin staining
IACUC	Institutional Animal Care and Use Committee
ICD	Inertial cavitation dose
IV	Intravenous
IP	Intraperitoneal
IR	Infrared
IRB	Institutional Review Boards
FDA	U.S. Food and Drug Administration
FUS	Focused ultrasound
FWHM	Full-width at half maximum
GBM	Glioblastoma multiform
Gd	Gadolinium
GDNF	Glia-derived neurotrophic factor

GPU	Graphic processing unit
HIFU	High-intensity focused ultrasound
MRgFUS	Magnetic resonance imaging guided focused ultrasound
MRI	Magnetic resonance imaging
NIH	National institutes of health
NINDS	National institute of neurological disorders and stroke
NHP	Non-human primates
ns	Not statistically significant
OFP	Octafluoropropane
PBS	Phosphate-buffered saline
PCD	Passive cavitation detection
PD	Parkinson's disease
PFC	Perfluorocarbon
PL	Pulse length
PNP	Peak-negative pressure
PRF	Pulse repetition frequency
Put	Putamen
RF	Radiofrequency
RMS	Root mean square
SCD_h	Stable cavitation dose with harmonics
SCD_u	Stable cavitation dose with ultraharmonics
SWI	Susceptibility-weighted imaging
T1w	T1 weighted MRI
T2w	T2 weighted MRI
TEA	Time exposure acoustics
WHO	World health organization

Acknowledgements

I am thankful to my advisor, Dr. Elisa Konofagou, for giving me this wonderful chance to study at Columbia University in New York, and being so supportive of my study and life being a new mom in the last year of PhD. My dissertation committee, Dr. Andrew Laine, Dr. Paul Sajda, Dr. Vincent Ferrera, Dr. Sheng-Han Kuo, who spend time giving suggestions to my thesis research. Thanks to my colleagues and friends, who helped me through the entire PhD. Dr. Cherry Chen, Dr. Yao-Sheng Tung, Dr. Fabrice Marquet, Dr. Tobias Teichert, Dr. Carlos Sierra Sanchez, Dr. Hong Chen, Dr. Hermes Kamimura, Dr. Julien Grondin, Dr. Gesthimani Samiotaki, Dr. Matthew Downs, Dr. Shutao Wang, Dr. Mark Burgess, Dr. Mathew McGarry, who as senior students or post-docs, have taught me and brought insightful thoughts to my study. PhD students, Christian Aurup, Marilena Karakatsani, Robin Ji, who are learning and helping me. The interns I mentored, Wenlan Zheng and Marc Heidmann, who were great helper to my experiments and projects. The veterinarians and technologist for the monkey projects, Amanda Buch, Chad Samaroo, Amy Cassano, Girma Asfaw, who dramatically ease the experiments. The lab assistants, Oluyemi Olumolade, Tara Kugelman, Nancy Kwon, Pablo Abreu, who helped with the experiments or administrative work. My collaborators outside of Columbia University, Dr. Paul Dayton, Dr. Samantha Fix, Dr. Christopher Arena, Dr. Francisco Femenia, for giving insightful discussions in the joint projects. Lastly, my constant appreciation from my heart that words can never express to my dear husband Chi-Chao Chen and most adorable baby boy Danli Wuchen, my family in Taiwan, and friends spread almost all over the world, for always being on my side to cheer me up. Without you, I could not have achieved all the work. It is the end of a journey, yet another journey to start.

Chapter 1

Background & Thesis Overview

1.1 THE BRAIN & DISEASES

1.1.1 The brain in the central nervous system

The brain (encephalon) is the information processing center of central nervous system (CNS) that interprets sensation and controls movement through the sensory and motor nerves in spinal cord and the functional circuits [1, 2]. It is protected by the skull (Fig. 1.1A). Under the skull, it is covered by meninges that enclose a cavity filled with cerebral spinal fluid (CSF) to provide cushioning effect (Fig. 1.1B). Inside the brain, it consists of ventricular system for CSF circulation, cerebrum, cerebellum, brain stem, with cerebral vascular system supports the nutrition and metabolism (Fig. 1.2A). The highest nervous organ lies in cerebral cortex and its subcortical structures (e.g. caudate nucleus, putamen, thalamus, hippocampus) (Fig. 1.2B) in the cerebrum that process consciousness, memory, thoughts, and voluntary activities. It is dark and light color of the tissue known as gray and white matter is due to different composition of the nerve cells. The gray matter represents concentrated neuronal cell bodies, and the white matter for fiber tracks or axons and dendrites with rich lipoproteins on the myelin sheath.

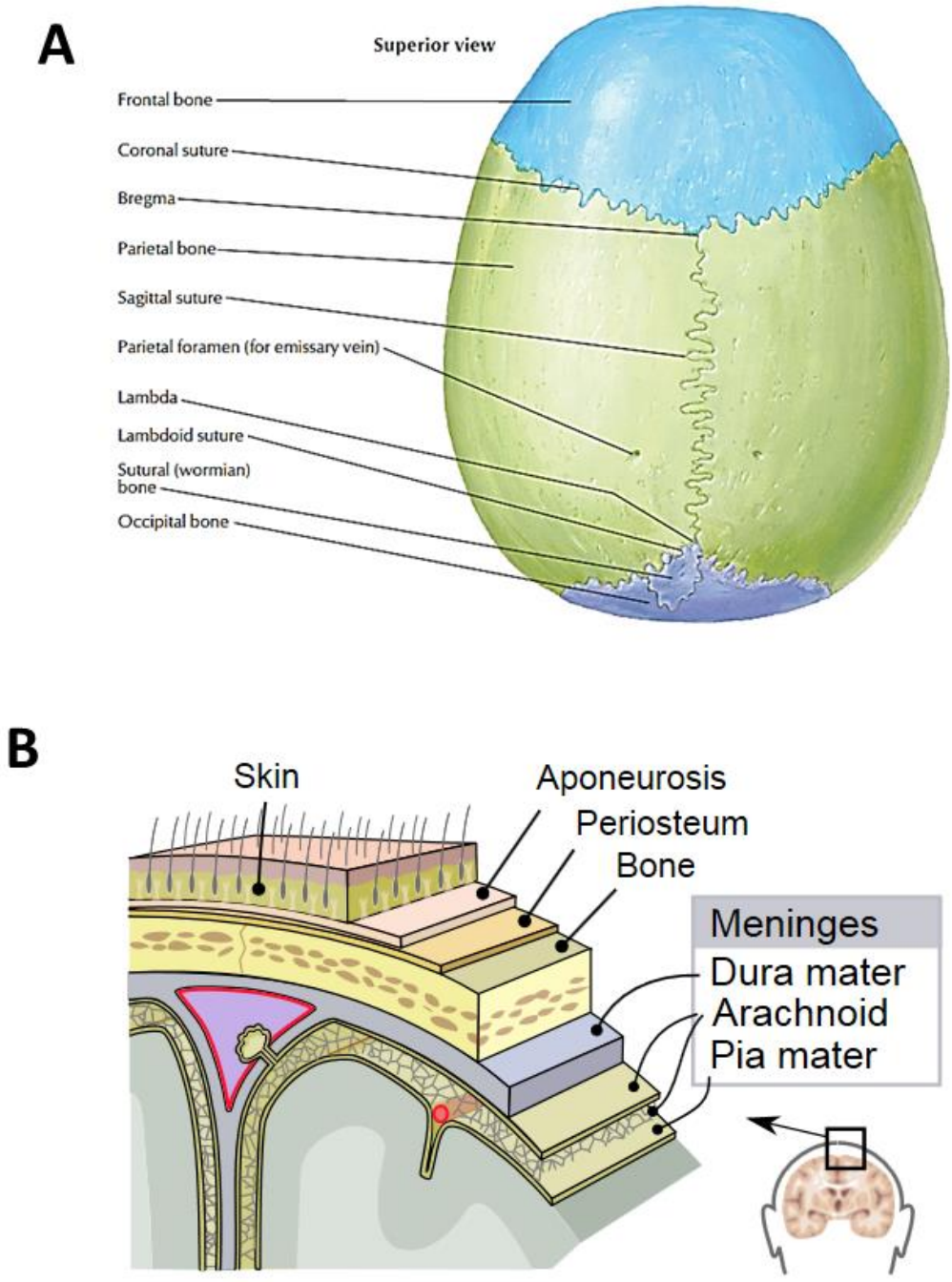

Figure 1.1. Anatomy of human skull and meninges structures. (A) Superior view of the human skull bone. (B) Schematic cross section of the meninges and the scalp. Modified from Netter [2], and NIH training materials [3].

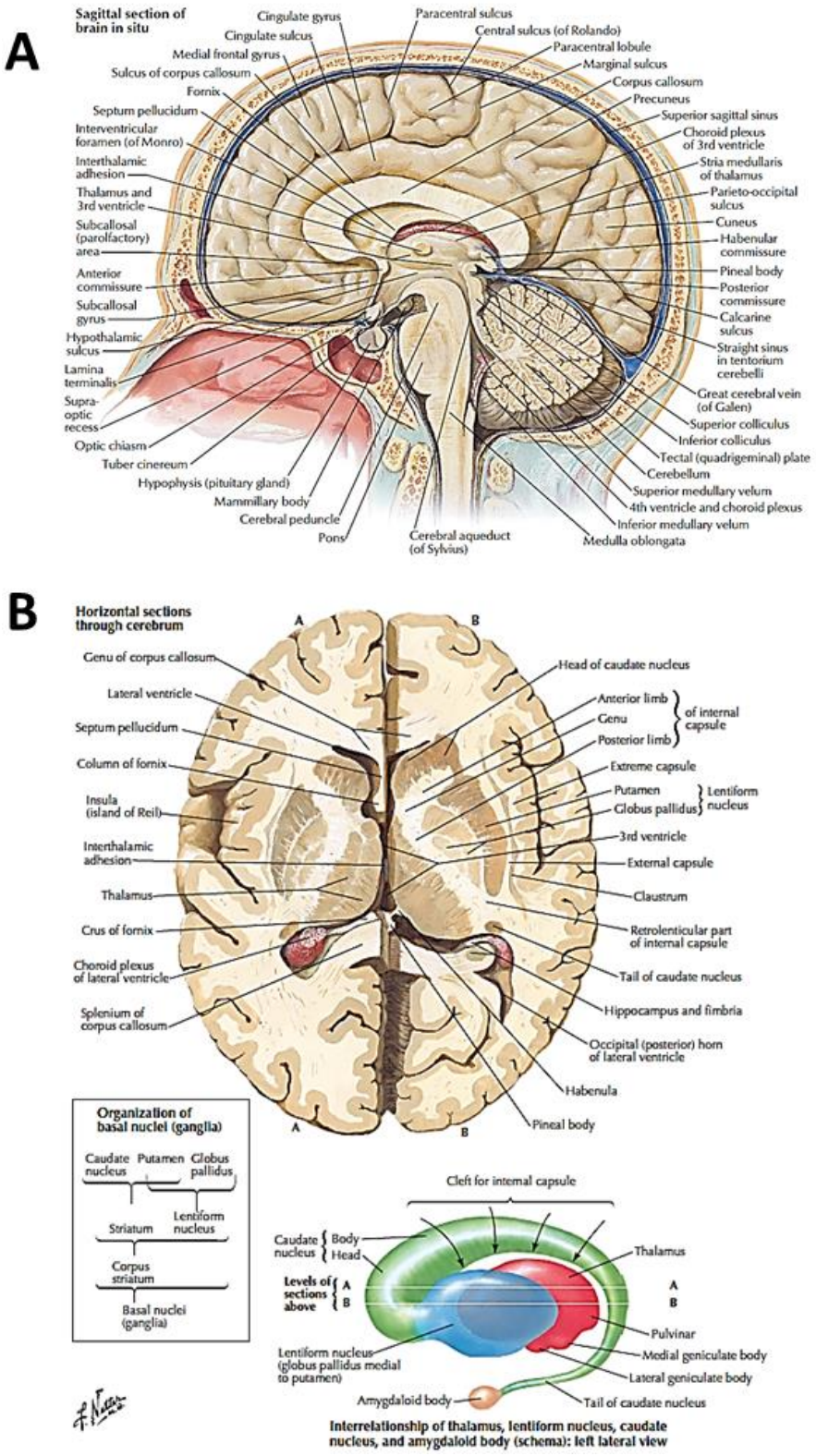

Figure 1.2. Human brain structure. Source: (A) Sagittal view of the head cutting from mid-sagittal plane. (B) Horizontal view of the human brain showed subcortical structures including basal ganglia and thalamus. Modified from Netter [2].

1.1.2 The blood-brain barrier (BBB)

Besides the outer protection of the skull and meninges, the brain tissue is sealed from the rest of the body by the blood-brain barrier (BBB), a highly selective barrier preventing most molecules entering the brain parenchyma from the bloodstream [4]. The BBB is formed by the endothelial cells lining the cerebral microvessels and interconnected with the tight junctions (Fig. 1.3A) forming a physical barrier to block paracellular passage. The specific transport systems on the luminal and abluminal membranes also strictly regulate the transcellular traffic, permitting the entry of few small hydrophilic molecules (Fig. 1.3B). Moreover, a combination of intracellular and extracellular enzymes in the BBB form another metabolic barrier by selectively metabolizing or inactivating many neuroactive and toxic compounds. These factors result in a much lower degree of cellular trafficking activity than other peripheral endothelium and shape the properties of the BBB.

1.1.3 Neurological diseases and treatments

Since the brain controls consciousness, memory, thoughts, and voluntary activities as described previously, its malfunction or alteration of any single component could result in a drastic disease ranging from epilepsy to Alzheimer's disease. In fact, neurological diseases have affected up to one million people worldwide according to the report from World Health Organization [5]. They affect people in all countries irrespective of age, sex, education or income, which result in death of 6.8 billion people every year. What's worse, the impact to the worldwide society is still increasing due to the aging of global population. Even so, the treatments are still limited due to the challenge in accessing the brain through the skull or the BBB and the risk of infection, damage of

health tissue, etc. The following described a few common neurological disorders [6] currently targeted by FUS treatment.

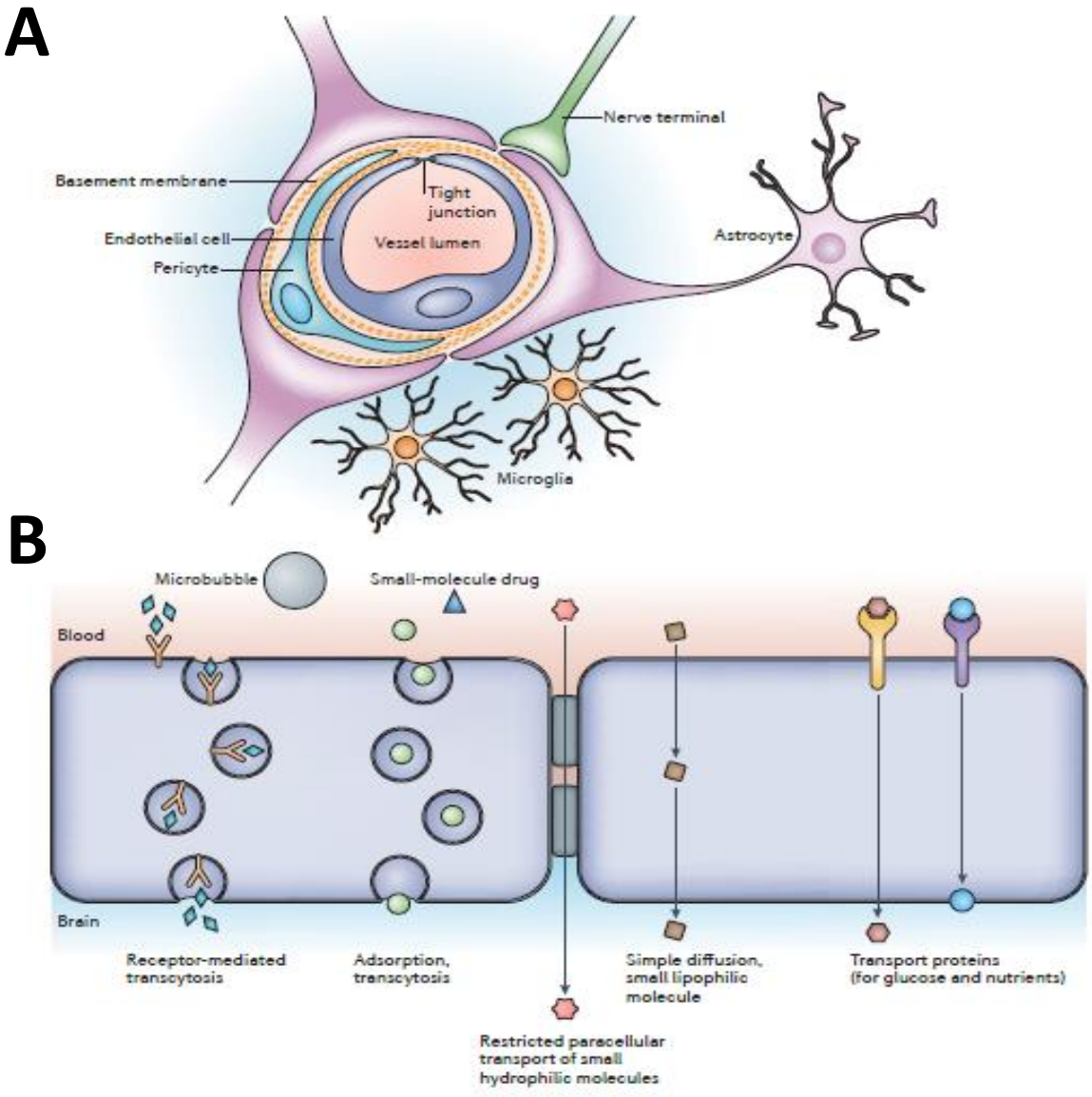

Figure. 1.3. The blood-brain barrier. (A) The neurovascular unit interacting with the BBB. It consists of endothelium with tight junctions lining the cerebral vessels, pericytes, and astrocyte end-feets. Nerve terminals and microglia surround and interaction with the neurovascular unit and BBB. (B) Various mechanisms across the BBB, including both transcellular and paracellular passages. Modified from Abbot et al [7] and Leinenga et al [8].

Essential tremor is the most common movement disorder that causes unintentional muscle movement most often in hands, while sometimes in head, arms, voice, tongue, legs, and trunk [6]. It may be mild or progressive, starting on one side of the body to both sides in the end. There is no cure for essential tremor, but medication, deep brain stimulation (DBS), or thalamotomy (destroying a small volume of tissue in the thalamus that is known to cause the tremor) could relief symptoms in a short term. Thalamotomy could be performed with stereotactic radiosurgery or radiofrequency ablation. FUS is also FDA approved for noninvasive ablation in thalamotomy since 2016 [9, 10].

Alzheimer's disease (AD) is a type of neurodegenerative diseases. It is also the most common cause of dementia, often age-related and developed over a period of time [6]. Patients initially experience memory loss and confusion, and gradually show behavior and personality changes, with declining cognitive abilities such as decision making and language skills, and inability to recognize family and friends. Major characteristics in the brain associated with AD include amyloid plaques made up of beta-amyloid peptides (Aβ) mixed with neuronal cells, and neurofibrillary tangles inside the neurons as abnormal aggregation of tau protein. As a result, neurons die and loss of connection in the functional circuits, leading to memory loss. It causes widespread damage of the brain tissue and significant shrinkage in the final stage of AD. There are no successful disease-modifying therapies, but only symptomatic treatment to improve personality and behavioral changes.

Parkinson's disease (PD) is a group of motor system disorders including tremor, rigidity (muscle stiffness), bradykinesia (slowness of movement), and postural instability (loss of coordination) resulted from the loss of dopamine-producing cells in the brain [6]. PD is a chronic

and progressive disease that will interfere with the patients' daily activities. Other symptoms include depression; difficulty in swallowing, chewing, and speaking; urinary problems or constipation; skin problems; and sleep disruption. Currently, there is no treatment to cure PD, but only a few medication including levodopa combined with carbidopa and DBS to relief symptoms.

Primary brain tumors have more than 688,000 patients in the U.S., with 68% of benign cases and 37% of malignant cases [11]. Besides, approximately 20-40% of all other cancers develop a brain metastases. Among them all, glioblastoma multiform (GBM) is the most common and aggressive malignant brain tumor in adults, representing 17% of all brain tumors and 52% of primary brain tumors [12] and causing approximately 15,000 deaths per year in the U.S. [13]. Standard treatment includes surgical removal, followed by radiation therapy and may accompany by chemotherapy [12]. Chemotherapy is less common to treat brain tumors because of BBB blocking the entry to cancerous cells.

Most of the diseases remain undertreated due to complicated or unknown pathogenesis, difficulties in accurate diagnosis on the early stage, and inaccessibility of the brain through the skull or BBB. Available treatments, though limited, include medication, surgery, radiotherapy, or DBS that may introduce risks such as infection, damage of healthy tissue, exposure of radiation, etc. Developing noninvasive techniques for surgery and BBB opening is thus of vital importance.

1.2 THERAPEUTIC ULTRASOUND

1.2.1 Medical ultrasound and its biological effects

Ultrasound are material waves that propagates through compressional particle movement in the medium, with frequencies higher than 20 kHz outside of the audible limit in humans. In medicine, it was first used for diagnostic imaging by sending short pulses (1 to 5 cycles in 2 to 12 MHz range at pressures of 2 MPa or lower) to see the internal tissue structure and elasticity. While with different settings of the acoustic parameters, ultrasound can induce certain biological effects to achieve therapeutic purposes, including heating, cavitation or gas body activation, compressional or shear stresses [14]. For example, increasing the frequency, nonlinear acoustic distortion, or pulse length can generate heating and enhance non-thermal mechanical effects such as radiation force. While decreasing the frequency with extended pulse lengths increases the likelihood of cavitation. In general, increasing the power and intensity of acoustic waves tends to increase the likelihood and magnitude of all biological effects.

Heating can be induced by high-intensity ultrasound due to tissue absorption of the ultrasonic energy. It can be achieved with unfocused heating as used in physical therapy to enhance bone or tendon healing without injury [14]. Alternatively, the heat can be concentrated by focused ultrasound (FUS) to achieve thermal ablation (57-60 °C causing coagulation necrosis) comparable to surgery, as show in Fig. 1.4 [15, 16]. Besides, elevating and maintaining tissue temperature to 42 °C can increase blood flow and drug absorption without causing permanent damage, a technique known as hyperthermia [17].

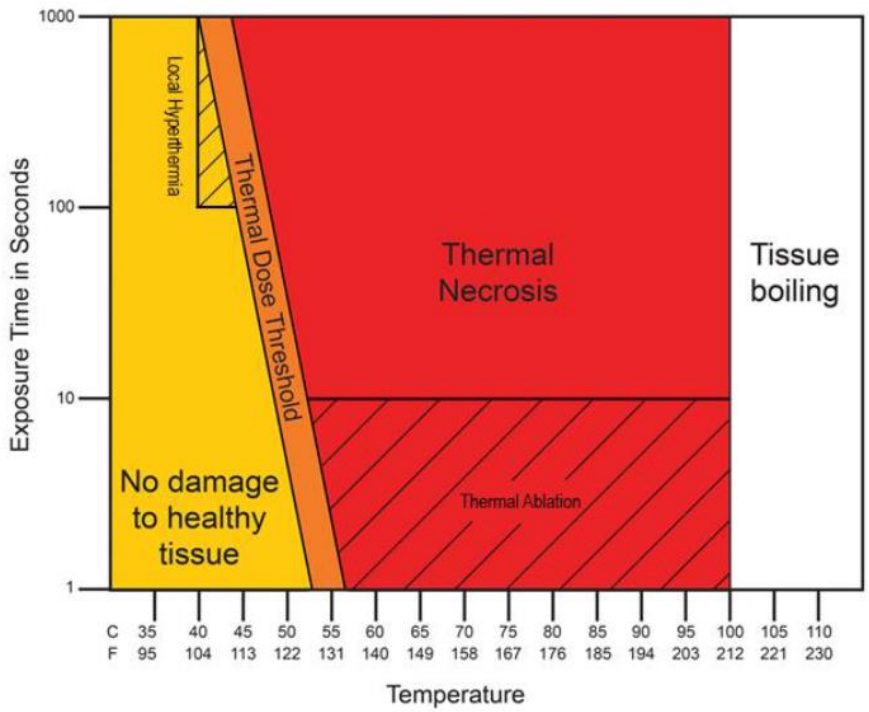

Figure. 1.4. The heating threshold for desired thermal effects in the tissue. Heat treatment is dependent on both the temperature and the exposure time. Modified from FUS foundation [16].

Ultrasound can also induce mechanical effects such as cavitation and radiation force. Cavitation, the most prominent one, refers to as the bubble inception and dynamics including the formation of bubbles and bubble oscillation (Fig. 1.5), and is associated with the rarefactional pressure amplitude of ultrasonic waves [18, 19]. After bubble formation, it can oscillate stably with pressure changes at relatively low amplitude (stable cavitation), causing microstreaming and shear forces. While it can collapse at higher pressure (usually rarefactional pressure) known as inertial cavitation, generating shock waves, shear forces, heat, or free radicals. Therefore, cavitation is used in a variety of applications for tissue destruction and drug delivery, which will be described as follows. Other mechanical effects include radiation force or compressional, tensile, and shear stressed from the applied ultrasound waves, which causes displacement of the tissue and may activate mechanosensitive biological response.

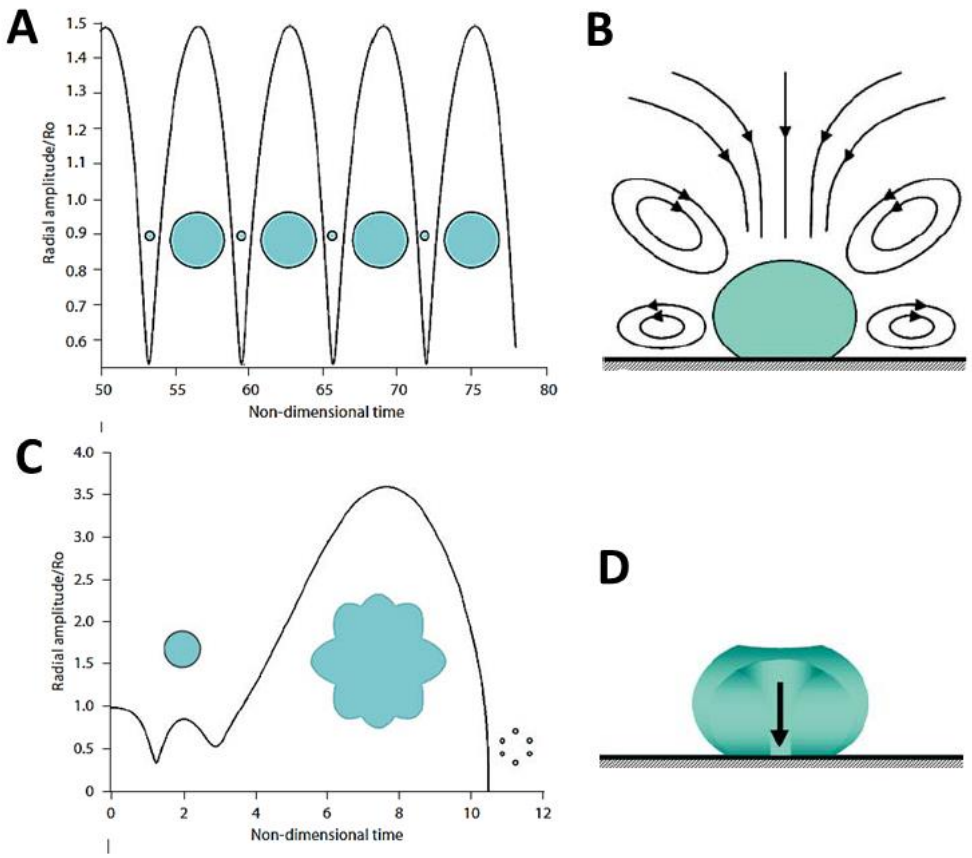

Figure. 1.5. The acoustic cavitation. (A) Stable cavitation occurs at low pressures, and bubbles oscillates periodically in the volume and shape. (B) Stable cavitation by the wall generates microstreaming and induced shear stress. (C) Inertial cavitation at higher pressures lead to bubble collapse that generates shock waves and sometimes along with smaller bubbles. (D) Inertial cavitation may form microjets generating high force against the wall. Modified from Stride [19].

The following lists a few therapeutic applications in the brain and other organs:

1.2.2 Tissue destruction

FUS serves as a surgical tool to noninvasively and locally destroy tissues such as tumors via thermal or mechanical ablation (histotripsy). High intensity focused ultrasound (HIFU) provides

highly focused acoustic energy deposition to induce protein denaturation, and the temperature is often monitored with thermocouple or MR thermometry [15] to ensure efficacy. It has been used to treat uterine fibroids [20], prostate cancer [21], and neurological disorders such as essential tremor [9]. Besides, mechanical ablation (histotripsy) can also be achieved via sending a short and extremely high intensity pulse to induce inertial cavitation that releases strong shock waves to destroy or liquefy cells [22]. Histotripsy is promising with a shorter treatment duration and more precise targeting compared with thermal ablation.

1.2.3 Targeted drug delivery

Using FUS in conjunction with microbubbles, targeted drug delivery can be achieved with FUS to enhance cell uptake of the pharmaceuticals and increase vascular permeability for delivery to tumors via sonoporation [23], or to the brain via BBB opening [24]. The mechanisms behind are mainly cavitation and radiation force, and the microbubbles can be engineered for loading drugs or ligands for cell specificity [25, 26]. Enhanced drug delivery enables treatments such as chemotherapy with less systemic toxicity as less circulating drugs are required than with traditional chemotherapy. It also increase the specificity to the targeted location in the FUS focus. The delivery efficacy and safety is associated with cavitation and should be closely monitored.

1.2.4 Neuromodulation

FUS, with specific acoustic parameters, can stimulate or suppress neuronal activity. While the mechanism is still under investigation, the majority tend to believe that mechanical effects dominate this mechanism [16]. It has been reported that low-intensity and low-frequency

ultrasound stimulated electrical activity in neurons in vitro and ex vivo through activating voltage-gated sodium and calcium channels [27]. FUS also disrupted electrographic seizure activity in mice [28], and suppressed somatosensory response in human [29]. FUS induced neuromodulation therefore holds the potential to treat epilepsy, study brain function, and assist surgical ablation for functional area testing.

1.3 TRANSCRANIAL ULTRASOUND THERAPY & CURRENT CLINICAL TRIALS

While facing an increasing need of efficacious brain treatments due to the continuous growth of world population and average age increase [5], brain diseases including neurological disorders and tumors remain poorly treated due to the challenge of access through the skull and the blood-brain barrier (BBB) for drug delivery. Focused ultrasound (FUS) resides as the only way to treat the brain noninvasively and locally for ablation (thermal effects) and BBB opening for drug delivery (mechanical effects through cavitation)[8]. It is also a valuable tool to study brain functions through neuromodulation [29]. With the exciting announcement of FDA approval to treat essential tremor with surgical ablation using FUS [9], several clinical trials are underway worldwide including surgical ablation to treat Parkinson's disease and BBB opening for chemotherapy of glioblastoma [8, 30].

1.3.1 Essential tremor

Essential tremor is the first and foremost milestone of transcranial ultrasound therapy been successful in clinical trials and approved by FDA [10]. Since for patients do not respond to

medication (about 30%), surgical treatment such as thalamotomy may be carried out. FUS remains the only noninvasive and non-ionizing way to heat and destroy target cells locally among all other surgical procedures including stereotactic radio surgery or radiofrequency ablation. It requires no anesthesia, no incisions in the scalp, and no burr holes through the skull. The targeting and ablation procedure can be closely monitored using MRI. There are currently two locations been targeted such as the ventralis intermedius, a small cluster of cells in the thalamus [9] and the cerebellothalamic tract below the thalamus [31].

1.3.2 Alzheimer's diseases

FUS with microbubbles could opening the BBB and facilitate drug delivery. BBB opening alone has been shown to treat AD in two different AD models via clearance of Aβ and improvement of memory loss [32, 33]. Its application with disease-modifying therapeutic drugs under development (anti-Aβ and anti-Tau antibodies, stem cells, gene therapy, etc.) may have potential to treat AD in different aspects [34]. An overview of pilot clinical trial for BBB opening to treat AD has been proposed in 2015 [34]. It will evaluate safety, reproducibility, and efficacy in patients with mild AD in Phase 1, targeting the cortex (gray matter with the presence of Aβ) in the right frontal lobe and/or the hippocampus (memory related structure).

1.3.3 Parkinson's disease

Both ablation and BBB opening for drug delivery could help treat PD. Only symptomatic treatments are available currently. When patients face refractory period in levodopa therapy in the late stage, often surgical option is considered to improve their quality of life through lesioning

targeted cells interfering motor functions. FUS is undergoing clinical trials to treat Parkinsonian tremor (lesioning target in the thalamus) [35] and Parkinsonian dyskinesia (lesioning target in the globus pallidus or subthalamic nucleus)[36] via ablation. On the other hand, disease-modifying treatments are being investigated through BBB opening to delivery neurotrophic factors. FUS-induced BBB opening to delivery therapeutic gene of glia-derived neurotrophic factor (GDNF) showed neuroprotective effects in a PD model [37]. Neurturin neurotrophic factor delivery after BBB opening also showed bioactivity that triggered nigrostriatal pathway [38]. Therefore, BBB opening with antibody delivery such as neurotrophic factors may have potential to restore neurodegeneration in PD.

1.3.4 Brain tumors

Current treatment options for brain tumors involve in surgical removal or radiofrequency ablation for partial or complete tumors with chemotherapy. FUS can improve the treatment via ablation and BBB opening to assist chemotherapy, which outlines the ongoing clinical trials as well. In the reported patient results, the tumor was successfully heated and monitored suing MR thermometry [39] and the tumor has been successfully ablated [40]. Successful BBB opening was reported with no adverse events [41].

1.4 FUS-INDUCED BBB OPENING & DRUG DELIVERY

1.4.1 Cavitation disrupts tight junctions and permeates endothelium

As described in Section 1.1, the BBB inhibits most molecules including toxic substances from entering the brain parenchyma, while it also blocks therapeutic agents ≥ 400 Da for therapeutic delivery [42]. Many strategies have been used to overcome this limitation, such as intracranial injection [43], disruption by mannitol [44], and endogenous transport mechanisms [45]. However, there are either invasive or nonspecific, risking the brain in infection and systemic toxicity.

Focused ultrasound (FUS) alone has been found to occasionally disrupt the BBB without neuronal damage [46]. With the intravenous circulation of microbubbles (1-10 μm), BBB opening could be achieved consistently and reversibly with low-intensity ultrasound. Cavitation has been regarded as the major reason increasing BBB permeability by bubble deformation to physically stretch the cerebral microvessels and induce vessel distention and invagination as seen under a high speed camera [47], and it was found to correlate with BBB opening [48]. Once the BBB is disrupted, molecules in the blood stream could pass via transcytosis, endothelial cell cytoplasmic openings, tight junction disintegration, or free passage through the injured cells if higher acoustic power is used [49, 50].

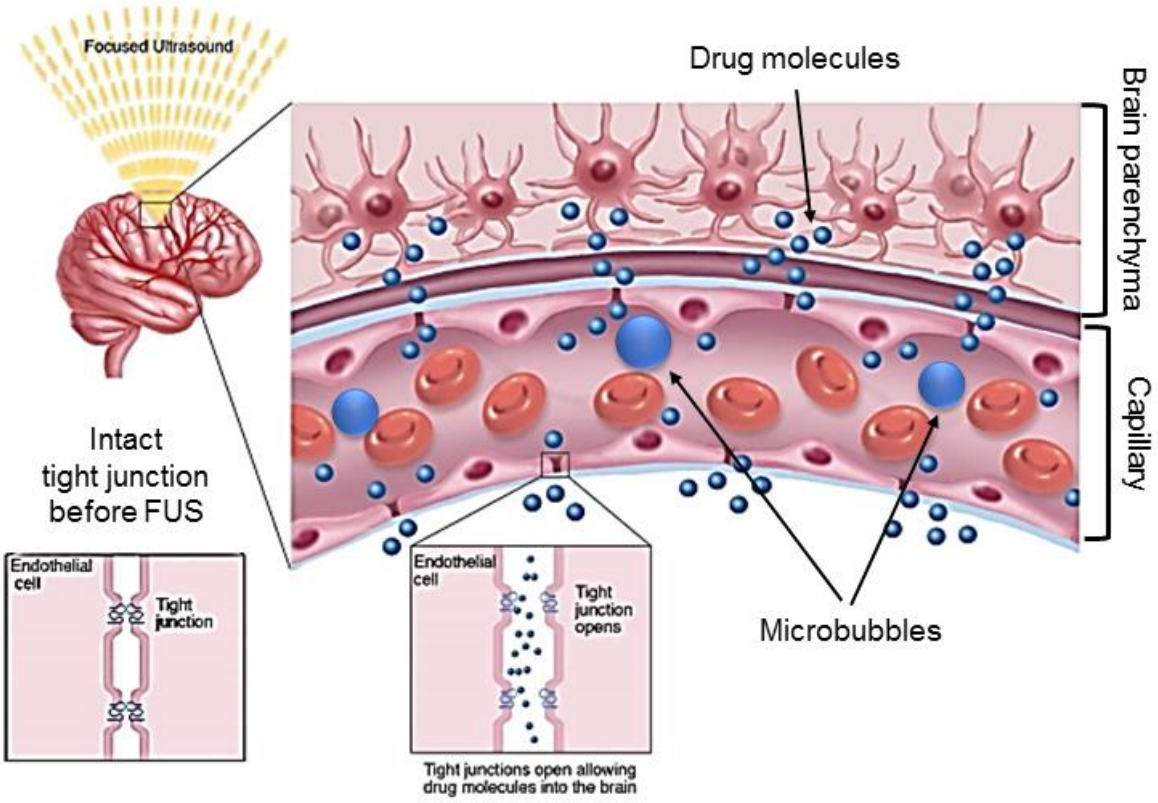

Figure 1.6. FUS-induced BBB opening disrupt the tight junction and increase the BBB permeability to allow drug molecules delivered to the brain. Modified from FUS foundation [16].

1.4.2 Molecules delivered and treatment applications

Focused ultrasound (FUS) in conjunction with microbubbles (1-10 μm) is currently the only way to open the BBB noninvasively, locally, and transiently for drug delivery and treatment for central-nervous-system (CNS) diseases. Various therapeutic agents have been successfully delivered with with FUS-induced BBB opening [51], including chemotherapeutic molecules [52], antibodies and neurotrophic factors [53] [54], siRNA [55], viral vectors [56], , nanoparticles [57, 58], neural stem cells [59], etc. The delivery efficiency can vary depending on the size of molecules been delivered,

the acoustic energy applied, and microbubbles used. In general, small molecules (< 70 kDa or 10.2 nm) require less acoustic energy compared with large molecules (> 500 kDa or 30.6 nm) [60].

It has been shown to treat brain tumors [61, 62] and Alzheimer's disease [32, 33], Parkinson's disease [37], Huntington's disease [63], and cerebral ischemia/reperfusion induced neuronal injury [64]. More applications are to be explored. This technique has been translated to large animals such as non-human primates (NHP) [65, 66], with short-term (hours to 9 weeks) and long-term (4 to 20 months) safety confirmed with MRI, histology, and behavioral assessment [67, 68]. The recent findings in the ongoing clinical trial also proved safe for the repetitive BBB opening [41].

1.5 TRANSCRANIAL ULTRASOUND SYSTEMS & ACOUSTIC AGENTS

The key to FUS treatment success in clinics is a robust system with 1) precise and flexible targeting to personalize treatment planning, 2) in silico simulation, and 3) real-time monitoring to ensure safety and effectiveness. Besides the system, streamlining the procedure is crucial to allow minimal cost and repetitive treatment. For BBB opening, the properties of acoustic agents are crucial as the treatment effectiveness relies on cavitation.

1.5.1 Targeting: MRgFUS vs. stereotaxis and neuronavigation

Magnetic resonance-guided FUS (MRgFUS) system (Fig. 1.7) is been used in several clinical trials, especially for surgical ablation [8]. Its integration of MRI and FUS allows to target and monitor

the thermal ablation process through MR thermometry [15, 39]. At the beginning of the targeting procedure, FUS focus is visualized in the MRI by applying relatively low intensity FUS to the patient that increases temperature in the focal area. Then the position of the FUS transducer is adjusted with motorized positioner until the focus reaches the desired location. Since MRgFUS is time-consuming and costly, its utilization in non-thermal and transient treatment (BBB opening and neuromodulation) is suboptimal as they often require repetitive procedure.

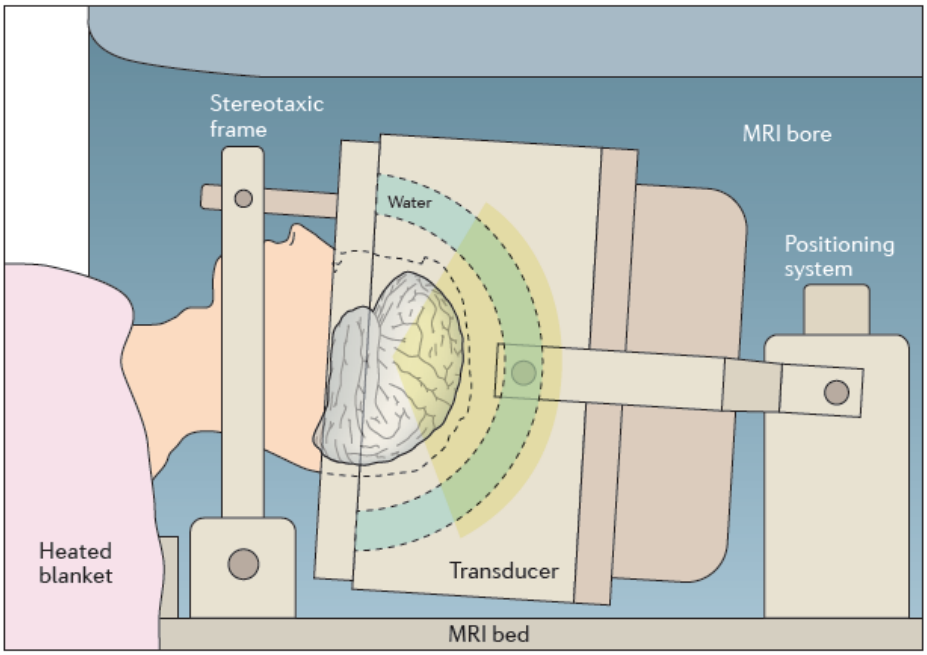

Figure 1.7. Schematic of the transcranial MRgFUS system. Modified from Leinenga et al [8].

The stereotactic FUS system has the advantages of providing precise targeting and fast treatment procedure, and can be coupled with real-time acoustic monitoring for BBB opening as previously shown in non-human primates (discussed in Chapter 2 and Chapter 4) [69, 70]. This targeting method can be achieved by acquiring a pre-operative MRI scan with stereotaxis to serve as a personalized brain atlas [71]. Although it had achieved BBB opening consistently in monkeys

[65, 66], this frame-based method can only be used in the laboratory setting or operating room. Moreover, the preplanning process was tedious in stereotactic calculation to set the stereotactic manipulator, and the orientation of the transducer was restricted by the stereotactic manipulator as well. Its accuracy could also be affected by the way of fixing the subject's head to the stereotactic frame and placing the transducer due to the lack of online feedback of the positioning.

Utilizing image-guided neuronavigation technology could overcome the drawbacks of frame-based stereotaxis while maintaining the translational capability to human applications. Neuronavigation is a frameless, computer-aided, and interactive stereotaxis that localizes the instrument in real-time on the neuro-radiologic images acquired before the procedure, and thus allows real-time feedback for positioning and intraoperative changes [72, 73]. It requires an imaging system to acquire preoperative neuro-radiologic images (MRI, CT, etc.), a position-tracking device to track the positioning of the patient and instruments such as surgical tools, and an image-processing system to reconstruct and store the images with the information of the instrument location relative to patients. During the treatment session, it provides registration between the preoperative images and the physical operating space after calibration based on common features (or fiducials) on the patient and the preoperative images. The registration transforms the images in real time and in different orientations interactively based on the instrument location detected by the position tracking device, and guides the operators to position the instruments. Incorporating neuronavigation with FUS sonication has been shown feasible in swine with BBB opening [74].

Another system undergoing clinical trials is the implantable ultrasound device [41]. Since it requires invasive surgery and does not provide targeting flexibility, it is not listed here.

Figure 1.8. Neuronavigation system (Brainsight). (A) Computer to store and process brain images. (B) Position sensor camera.

1.5.2 Monitoring: MRI vs. passive cavitation detection

Besides targeting, real-time monitoring is essential to provide control feedback in ensuring effectiveness and safety of the FUS treatment. MRI is used as an online monitoring tool for thermal ablation in the MRgFUS system. For BBB opening, however, it serves as a post-treatment assessment tool to evaluate the BBB opening through contrast-enhanced T1 weighted imaging as contrast agent does not cross intact BBB. Since BBB opening is associated with cavitation [48] that cannot be monitored with the MRI, the acoustic monitoring method passive cavitation detection (PCD) is used during the sonication.

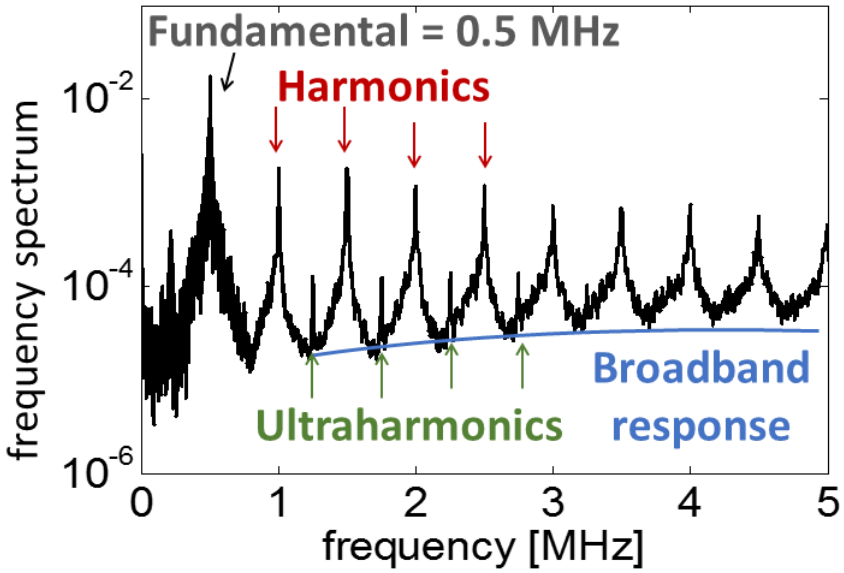

Figure 1.9. Frequency spectrum of PCD signals during sonication with microbubbles. Fundamental frequency corresponded to the excitation frequency (f). Harmonic frequency (n*f) occurred when bubbles oscillated stably and periodically (stable cavitation). Ultraharmonic frequency (n*f+f/2) refers to as bubble shell oscillation or asymmetric oscillation during stable cavitation. Broadband respond occurs when bubbles undergoing inertial cavitation and release shock waves.

This association of cavitation and BBB opening lies on the physical mechanism for BBB opening. Cavitation occurs in the vessels in the focal area during the FUS treatment, and the oscillating bubbles generated an acoustic signature reflecting both the strength and type of bubble activity [18, 19] (Fig. 1.9). If bubbles oscillate periodically without disruption, harmonic (bubble volumetric oscillation; n*f, where n = 1,2,3,… and f = excitation frequency) and/or ultraharmonic signals (bubble shell oscillation; n*f+f/2, where n = 1,2,3,… and f = excitation frequency) will be generated, a phenomenon known as stable cavitation. At higher pressures when bubbles oscillate violently and collapse rapidly, shock waves and microjets are generated with broadband emission known as inertial cavitation. Both stable and inertial cavitation applies mechanical stress onto the

vessel walls [47, 75] which could disrupt the tight junctions and other processes of BBB and increase the permeability of capillary endothelium[50].

PCD can achieve real-time transcranial monitoring during FUS, and could serve as an online treatment evaluation complement to the post-operative MRI-based methods (discussed in Chapter 3-5). Since its initial use during BBB opening in small animals [48], PCD has been expanded to various types of contrast agents such as microbubbles of various sizes [76], various shells [77], and nanodroplets [78] reporting a positive correlation between BBB opening and cavitation dose. A feedback control mechanism for BBB opening based on ultraharmonics and subharmonics was established in small animals [79, 80]. The permeability and reversibility of BBB opening could also be predicted based on cavitation in mice [81].

Furthermore, PCD can be applied transcranially in large animals as well [71, 77], and has been shown feasible through the human skull [70] (discussed in Chapter 4). With the advent of passive acoustic mapping technique [82, 83] guided with neuronavigation (discussed in Chapter 5 and Chapter 6), the acoustic monitoring could then visualize the acoustic events such as cavitation in the brain in order to assess and control the treatment more precisely in various locations, which is unachievable in any other imaging modalities including MRI.

1.5.3 Microbubbles

Microbubbles, gas-filled microspheres (1-10 μm) (Fig. 1.10) initially used merely as contrast agents for ultrasound imaging, have recently been shown critical in ultrasound-mediated therapeutic applications such as sonothrombolysis [84, 85], molecular delivery to the cell via sonoporation [23, 86] and/or endocytosis [87, 88], and to the brain parenchyma via blood-brain

barrier (BBB) opening [24, 89] paracellularly or transcellularly. For molecular delivery purposes, although the biological mechanisms may vary, sonoporation and/or endocytosis and BBB opening share the same physical mechanism that cavitation increases the permeability of the cell membranes. In all the cases, the microbubble properties play important roles in determining the delivery efficiency. For example, larger microbubbles (4-5 μm in diameter) induce larger BBB opening and delivery efficiency than smaller microbubbles (1-2 μm in diameter) [76, 90]; soft-shelled (lipid or protein) microbubbles gave higher cell viability and transfection rate of gene delivery than hard-shelled (polymer) microbubbles [91].

Overall, the main goal of drug delivery is to achieve high efficiency without causing cell damage, and with the use of lipid-coated microbubbles it is achievable. In fact, with lipid-coated microbubbles the overall drug delivery efficiency could be influenced by changing the lipid hydrophobic chain length that modulates the overall physicochemical properties of the monolayer shell. Borden *et al.* have shown that increasing the lipid hydrophobic chain length increased the gas permeation resistance to the environment [92], decreased the acoustic dissolution rate while enhancing the lipid-shedding phenomenon during insonification [93]. Kwan *et al.* have reported that bubbles with longer lipid hydrophobic chains required longer re-stabilization following shell rupture, and longer to dissolve after the onset of collapse due to stronger attractive intermolecular forces [94, 95]. Longer acyl chains can also increase the lipid monolayer thickness [96] and microbubble mechanical properties such as in-plane rigidity [97], thereby modulating cavitation response and the shear stress applied on the cell membrane [98, 99]. Those results suggest that the physicochemical properties of the lipid-shelled microbubbles may play a role in affecting the drug delivery efficiency, but the exact effects remain to be discovered (discussed in Chapter 3).

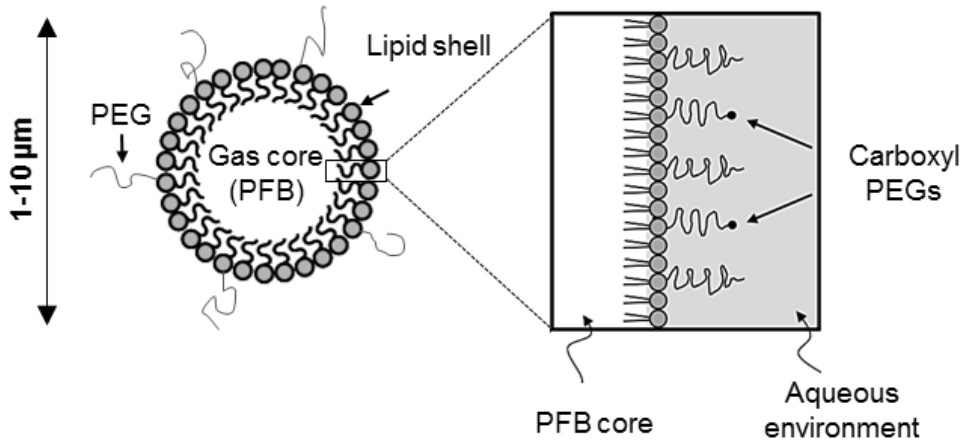

Figure 1.10. Schematic of microbubble structure. Modified from Wu et al. [77] and Chen et al [100].

1.5.4 Nanodroplets

Shell-stabilized liquid perfluorocarbon (PFC) droplets (Fig. 1.11) [101-103] are new generation of acoustic contrast agents for imaging [104, 105] and therapeutic mediators to assist tumor occlusion, thermal ablation or drug delivery [106]. They retain the acoustic characteristics after vaporization while possessing several advantages over conventional gaseous microbubbles. First, refraining from the gas dissolution in the blood stream has granted better in vivo stability for droplets [107]. Second, the small size distribution of nanodroplets after microbubble condensation enables extravascular interrogation once entering the interstitial space before phase transition, including imaging in the extravascular space, cell-specific targeting, drug delivery, and tumor ablation [105, 108]. Third, their capability of carrying high payloads demonstrates significant improvement on targeted treatment and imaging [109-111].

These characteristics of nanodroplets are promising to revolutionize the brain treatment with ultrasound as challenges are faced in human trials with prolonged procedure and requirement

of enhanced treatment in the sonicated region. For surgical ablation, prolonged sonication is often required to achieve the desired temperature at multiple locations with scalp and skull cooling taken exchangeably [39]. The use of droplets in the brain could shorten the treatment time since ablation with droplets has been achieved in a shorter time (decreased by a factor of 2.5 in tissue-mimicking phantoms) or with a larger lesion volume at equal exposure time (increased by a factor of 7 in tissue-mimicking phantoms or 15 in canine liver) [106, 112, 113]. On the other hand, drug delivery to the brain through blood-brain barrier opening with focused ultrasound (FUS) was found more difficult for large molecules [60, 114], and bubble shielding effects (clusters of bubbles in the pre-focal area scattering acoustic waves) caused failure of BBB opening [65] or BBB opening in the undesired pre-focal area in large animals [71]. These problems can be solved by droplets vaporized only in the focal area generating highly concentrated mechanical stress during sonication. Moreover, both thermal ablation and drug delivery in the brain can be further improved with extravascular cavitation once nanodroplets enter into the brain parenchyma.

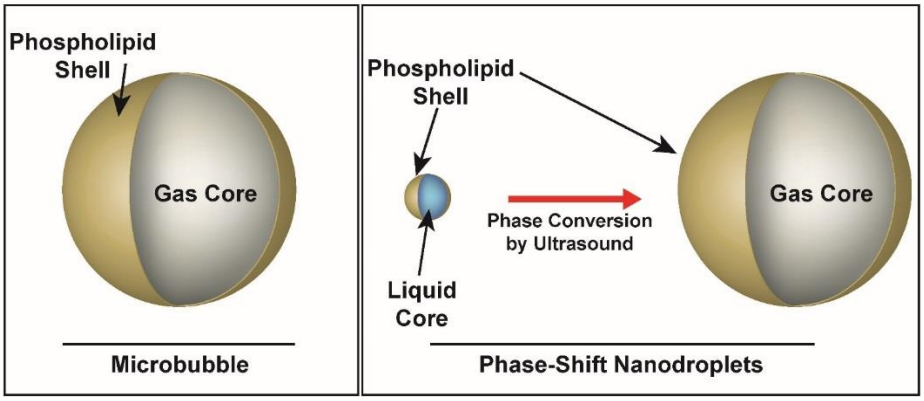

Figure 1.11. Schematic of phase-shift nanodroplets vaporized to microbubbles. Modified from Chen et al.[78]

1.5.5 Clinical use of acoustic agents

Microbubbles after been developed for more than 50 years since 1968 [115] have been approved for imaging in Europe and for echocardiography in the U.S. [116]. They are often injected as a bolus through the peripheral vein in the arm with a dosage of 0.2-2 mL, a number similar to the number of red blood cells in 1 mL of blood. The contrast is increased in the blood and last for 5 min, then it diminished gradually since the microbubbles are filtered out through the lung or metabolized in the body over time. With infusion through saline drip or an infusion pump, the contrast could then last up to 20 min. They are well-tolerated after injecting in the human body. The most severe adverse event is caused by anaphylactoid reaction with a probability of 0.014% (one in 7000)[117-119], while its usage is considered safe as the rate of the adverse event is comparable to other analgesics and antibiotics (0.005%-0.015%)[120, 121]. For therapeutic use, however, they are still under investigation as the bubble behavior or cavitation can be difficult to predict or control and thus may cause tissue damage. Currently the clinical trials including BBB opening for drug delivery are undergoing in France [41] and Canada [122], and sonothrombolysis to treat ischemic stroke has been recently completed in Spain with the results unpublished yet [123].

On the other hand, droplets are new generations of acoustic agents that have been developed for less than 20 years. They have not yet been used in humans.

1.6 MOTIVATION & AIMS

Brain diseases including neurological disorders and tumors remain undertreated due to the challenge in accessing the brain, and blood-brain barrier (BBB) restricting drug delivery, which also profoundly limits the development of pharmacological treatment. Focused ultrasound (FUS) with microbubbles remains as the only method to open the BBB noninvasively, locally, and transiently to assist drug delivery. For an ideal medical system to serve a broad patient population, it requires precise and flexible targeting with simulation to personalize treatment, real-time monitoring to ensure safety and effectiveness, and rapid application, as repetitive pharmacological treatment is often required. Since none of current systems fulfills all the requirements, here we designed a neuronavigation-guided FUS system with protocol assessed in non-human primates from in silico preplanning, online FUS treatment and real-time acoustic mapping for monitoring, to post-treatment assessment.

The objective of this thesis was to develop a seamless neuronavigation-guided transcranial ultrasound system with targeted sonication and acoustic monitoring for clinical use, and the protocol demonstrated from in silico preplanning, online treatment and monitoring, to post-treatment assessment. The system and protocol were tested in both sedate and awake non-human primates (NHP) with BBB opening to evaluate the performance of simulation, targeting accuracy, and monitoring. In achieving the goal, three sub-aims were listed as follows.

1) To develop a treatment preplanning tool (Chapter 2), numerical simulation of the transcranial pressure distribution was established and validated with the in vivo BBB opening.

2) To develop an online treatment monitoring tool (Chapter 3-5), real-time cavitation detection and mapping were built and evaluated in NHP with BBB opening.
3) To facilitate efficient and precise FUS treatment procedure (Chapter 6), the neuronavigation system was customized with FUS system including targeting and cavitation mapping. The established system and protocol was evaluated in NHPs in both a sedate setting, where the animal was lying prone on the operating table under anesthesia, and an awake setting, while the animal was trained to sit in a customized chair. The accuracy of targeting as well as the cavitation mapping was evaluated comparing to the BBB opening based on contrast enhanced MRI.

1.7 THESIS OVERVIEW & SIGNIFICANCE

The world is facing the increasing need of efficacious brain treatments due to the continuous growth of world population and average age increase [5]. According to the report from World Health Organization (WHO), neurological disorders have affected more than 1 million people [5]. The burden not only lies in the health care, but also the caregiver in the whole society. Given the challenge in accessing the brain either through the skull or the BBB for drug delivery, focused ultrasound (FUS) remains the sole technique for treating the brain noninvasively and locally for surgical ablation (thermal effects) and BBB opening for drug delivery (mechanical effects through cavitation)[8]. With an efficient transcranial FUS system to assist pharmaceutical treatment, it can prevent the situation from going worse.

The key to FUS treatment's success is a robust clinical system with 1) precise and flexible targeting to personalize treatment planning, 2) in silico simulation, and 3) real-time monitoring to ensure safety and effectiveness. Besides the system, fast application is crucial to allow minimal cost and re-application. Magnetic resonance-guided FUS (MRgFUS) system reliably ablates the brain tissue with temperature monitored by the MRI[15, 39]. Non-thermal treatment such as BBB opening and neuromodulation that are transient and may require re-application, a more suitable system is still yet to be established, as the MRgFUS system is time-consuming and costly, while implantable ultrasound devices require invasive surgery without targeting flexibility[41].

Our developed neuronavigation-guided FUS system could provide a streamlined procedure with both efficacy and efficiency of the treatment. Since its evaluation in sedate and awake non-human primates (NHP) with BBB opening, it is ready for approval for clinical use. This dissertation will thus be beneficial to both research and clinical applications for BBB opening and neuromodulation.

This dissertation is structured to fulfill three sub-aims described in Section 1.6. Followed by the background of brain and diseases, and the state of art in FUS in this chapter (**Chapter 1**), numerical simulation will be described in **Chapter 2**. It includes three studies: the first one utilized pulse design in simulation to improve the focal quality, and validated with in vivo BBB opening in mice; the second one using 3D simulation to evaluate intra- and inter- animal variation in NHP, and validated with in vivo BBB opening in NHP; the last one exploring focal properties through the human skull with various targeting parameters. Real-time cavitation monitoring will be covered in Chapter 3 to Chapter 5. Starting from mice (**Chapter 3**) to investigate physical mechanisms with various customized acoustic agents, including microbubbles of different shells, microbubbles with model drug loaded on the shell and acoustically-activated nanodroplets with

different vaporization efficiency. This PCD method was then translated to large animals such as monkeys and humans (**Chapter 4**). The transcranial performance was evaluated through both the monkey and the human skull, and it correlation to the in vivo BBB opening findings were investigated in NHP, including BBB opening volume, amount of drug delivered and delivery efficiency, and the heterogeneous brain effects such as gray and white matter and vasculature. This lead to the development of cavitation mapping as the previous single-element PCD does not provide spatial information of cavitation. Therefore in **Chapter 5**, an efficient cavitation mapping algorithm was developed using sparse matrix multiplication in a GPU to achieve real-time monitoring. Again, its performance through both the monkey and the primate skull were investigated. Lastly in **Chapter 6**, the developed FUS system was integrated with the neuronavigation system, with a seamless protocol evaluated in both sedate NHP lying supine under anesthesia and the awake NHP sitting on the customized chair. Both the accuracy of targeted BBB opening and cavitation mapping were analyzed. A clinical protocol for neuronavigation-guided ultrasound was thus proposed in **Chapter 7**, with future work listed for getting approval for clinical studies.

Chapter 2

Simulation of Transcranial FUS with *In Vivo* BBB Opening Validation

2.1 INTRODUCTION

As shown in Chapter 1, focused ultrasound (FUS) is the only non-ionizing, noninvasive, and targeted technique that can treat brain diseases through tissue ablation or blood-brain barrier (BBB) disruption for drug delivery. Tissue ablation utilizes the thermal effects of ultrasound requiring high intensity or pressure, while BBB disruption relies on nonthermal effect at low intensity with microbubbles such as cavitation generating mechanical stress onto the microvessel wall. In both types of brain therapy, it is of vital importance to estimate the transcranial focal quality and the pressure attenuation before FUS treatment, since the skull as hard tissue hinders the transmission of ultrasound waves. In this chapter, a simulation tool has been built and validated with in vivo BBB opening to assist transcranial FUS treatment planning for future clinics. With this aim to facilitate the preplanning process for BBB opening, three sub-objectives were listed as follows.

1) To improve the focal quality of the therapeutic FUS, the excitation pulse design was investigated in simulation in mice and NHP and validated in the in vivo BBB opening in mice. The excitation pulse design was optimized in the simulation of the acoustic pressure distribution through the skull, including regular pulses (pulsed single-frequency sinusoidal

waves with a fixed pulse length), chirp-coded pulses (continuous sinusoidal waves with linearly-increased frequency in a small frequency range), and random-coded pulses (continuous sinusoidal waves with randomized frequency variation in a small frequency range). Chirp- and random-coded pulses were chosen as they have been reported to effectively reducing standing waves in the skull cavity [124, 125]. The evaluation of the focusing capability was quantified by the volume of BBB opening and the cavitation dose was evaluated for each technique.

2) To investigate the inter- and intra-animal variation with various targeting in large animals, the acoustic pressure field through the skull has been simulated and compared with the BBB opening in non-human primates (NHP). Both the pressure loss and focal shift due to the skull were estimated in silico, and compared with the in vivo findings using the standard stereotactic targeting method. This study thus demonstrated the validity of using simulation to compensate the treatment variation in large animals.

3) To investigate the targeting effects on focal properties in human, simulation with human skull through different bone regions (parietal, occipital, temporal) and with various targeting parameters including the angle of incidence and the transducer-skull distance were explored. The focal properties were evaluated in each targeting design, including the focal size, focal shift, and the skull attenuation. This study could provide crucial information for targeting design in future clinics.

2.2 METHODS

2.2.1 Preoperative acquisition of skull CT

CT of the animal was acquired to extract skull properties (density and speed of sound) in order to construct the animal model in simulation to estimate the acoustic pressure decrease. For mice, ex vivo mice (C57BL/6) was imaged with a microCT (resolution = 80 ×80 × 80 mm^3; RmCT2, Rigaku, Tokyo, Japan). For monkeys, in vivo rhesus macaques (Macaca mulatta) was imaged under anesthesia with a helical CT (resolution = 0.2 × 0.2 × 0.6 mm^3; Siemens, Biograph 64, Malvern, PA, USA). For humans, the human cadavers were scanned (resolution = 1 × 1 × 1 mm^3) as described in The Visible Human Project® (National Library of Medicine in National Institutes of Health, U.S.) [126] [126] [125] [124] [123] [122] [121] [120] [119] [119] [118] [117] [117] [117].

2.2.2 Numerical simulation of acoustic wave propagation

The numerical simulations were performed using k-Wave Matlab toolbox [127, 128] for the acoustic wave propagation. This toolbox provides the k-space pseudo spectral time domain solution for the coupled first-order acoustic equations in either homogeneous or heterogeneous media:

Conservation of momentum: $$\frac{\partial \boldsymbol{u}}{\partial t} = -\frac{1}{\rho_0}\nabla p,$$

Conservation of mass: $$\frac{\partial \rho}{\partial t} = -\rho_0 \nabla \boldsymbol{u} - \boldsymbol{u}\nabla\rho_0,$$

Pressure-density relation: $$p = c_0^2(\rho + \boldsymbol{d}\nabla\rho_0 - L\rho),$$

where $\boldsymbol{u}$ is the acoustic particle velocity, p the acoustic pressure, ρ the acoustic density, ρ_0 the

equilibrium density, c_0 the isentropic sound speed, $\boldsymbol{d}$ the acoustic particle displacement, and L the linear integro-differential operator that accounts for acoustic absorption (τ) and dispersion (η) that follows a frequency power law: $\mathrm{L} = \tau\frac{\partial}{\partial \mathrm{t}}(-\nabla^2)^{\frac{y}{2}-1} + \eta\,(-\nabla^2)^{\frac{y+1}{2}-1}$, and $\tau = -2\alpha_0 c_0^{y-1}$, $\eta = 2\alpha_0 c_0^{y}\tan\left(\frac{\pi y}{2}\right)$. α_0 is the power law perfactor in Np (rad/s)$^{-y}$/m, and y is the power law exponent.

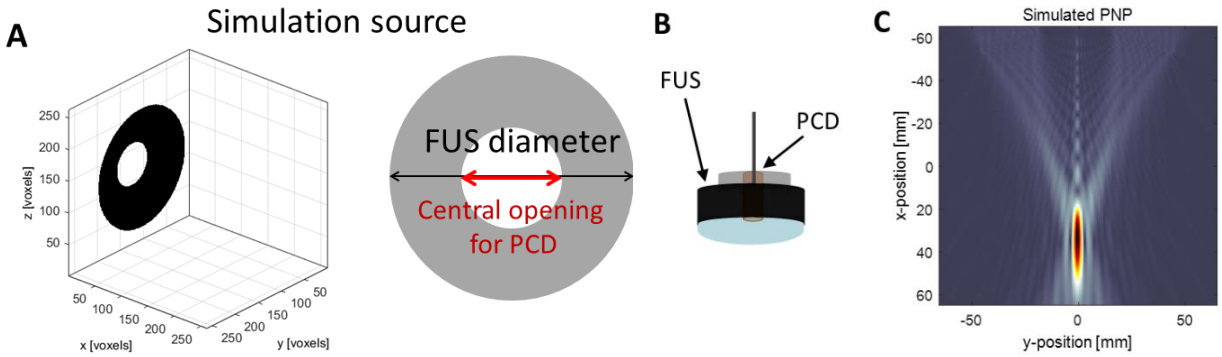

Figure 2.1. Design of acoustic source for simulation. (A) 3D image of the ring-shaped, spherically focused ultrasound transducer for simulation, and the central space was reserved of passive cavitation detector (PCD). This design is to mimic the FUS transducer used in experiments (B). The generated acoustic pressure field in silico (C) showed an ellipsoidal focus in water.

The ring-shape focused transducer (Fig. 2.1) was created in silico with the focal size calibrated based on the FUS transducer calibration in water at room temperature (Fig. 2.2), with the same excitation frequency and pulse length used for the in vivo experiments. The acoustic properties of the skull including the speed of sound and density were converted from the Hounsfield units in CT [129], with an attenuation of 20 dB.cm^{-1} and the power law absorption exponent of 1.1 based on previous measurements in humans [130, 131], and 29 dB.cm^{-1} for mice based on calibration. The medium properties surrounding the skull were the same as water at the

body temperature (37^0C, speed of sound = 1524 m/s, density = 1000 kg/m^3, attenuation = 3.5×10^{-4}).

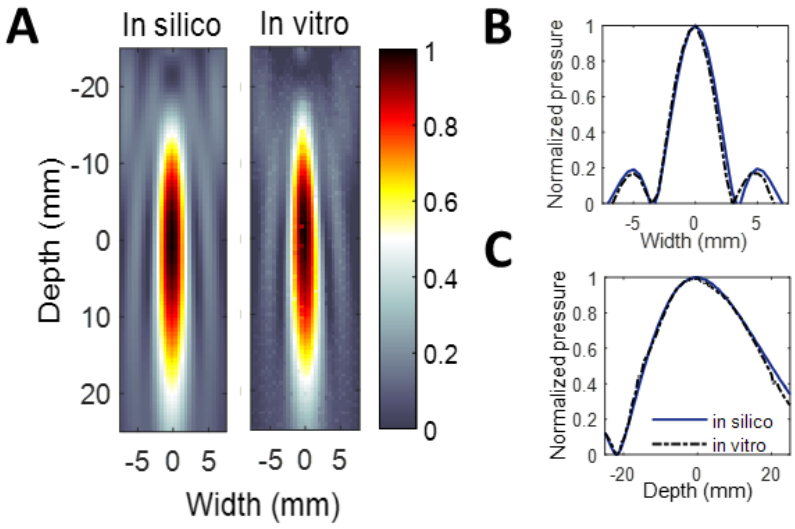

Figure 2.2. Calibration of simulation with the FUS pressure field in water (used for primate experiments). (A) The in silico acoustic profile in the focal region was calibrated to be the same as the profile from the FUS transducer measured in water using a hydrophone, including the focal width and the side-lobes in lateral (B) and axial (C) direction.

2.2.3 Ultrasound System

Mice

As shown in Fig. 2.3, a single-element FUS transducer (1.5 MHz; Imasonic SAS, Voray-sur-lOgnon, France) was used for sonication, and a small pulse-echo transducer (center frequency: 10 MHz, focal depth: 60 mm, radius 11.2 mm; Olympus NDT, Waltham, MA, USA) confocal to the FUS transducer was used for the targeting and passive cavitation detection (PCD) during the sonication. The transducer was attached to a 3-D positioning system (Velmex Inc., Lachine, QC, Canada) and controlled by a computer for targeting procedure developed previously [132]. The coded excitation signals were generated in Matlab, uploaded to the arbitrary waveform generator

(33220A, Agilent Technologies, Palo Alto, CA, USA), and transmitted to the FUS transducer through a 50 dB power amplifier (ENI Inc., Rochester, NY, USA).

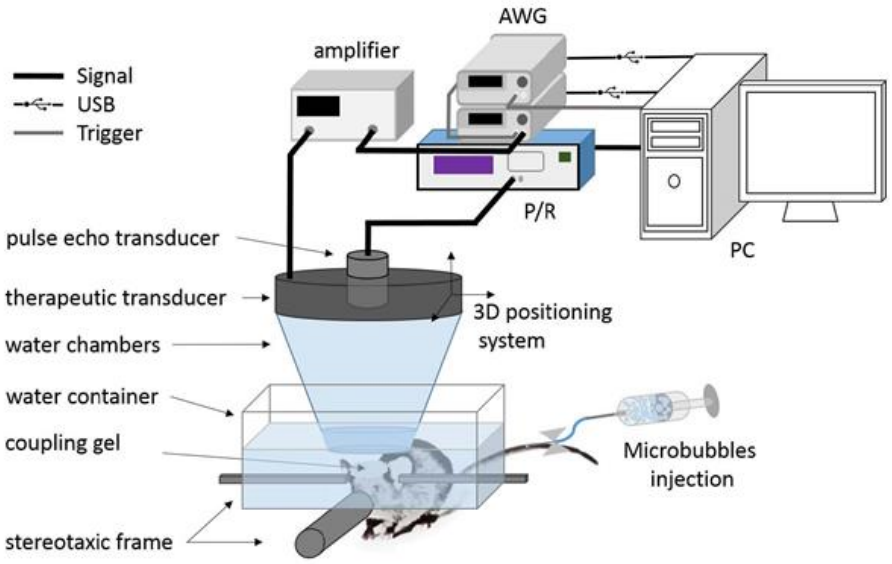

Figure 2.3. In vivo mice experimental setup. The animals were positioned in a stereotaxic frame during the sonication. Microbubbles were injected through the tail immediately prior to the sonication. Water containers coupled the animal's head to the ultrasonic transducers using coupling gel. A therapeutic transducer was driven by an arbitrary waveform generator (AWG). A 10 MHz transducer was used for targeting and passive cavitation detection (PCD).

The regular pulses (1.5 MHz), chirp-coded pulses, and random-coded pulsed were generated separately for sonication in each experimental cohorts. Pulses coded with varying frequency component were designed to enhance the focal quality while minimizing standing waves. The signals were composed of sinusoidal waves with the carrier frequency f_c varying linearly (chirp) or randomly (random) between 1.5-1.9 MHz in $\sin(2\pi f_c + \varphi_0)$ as shown in Fig. 2.4.

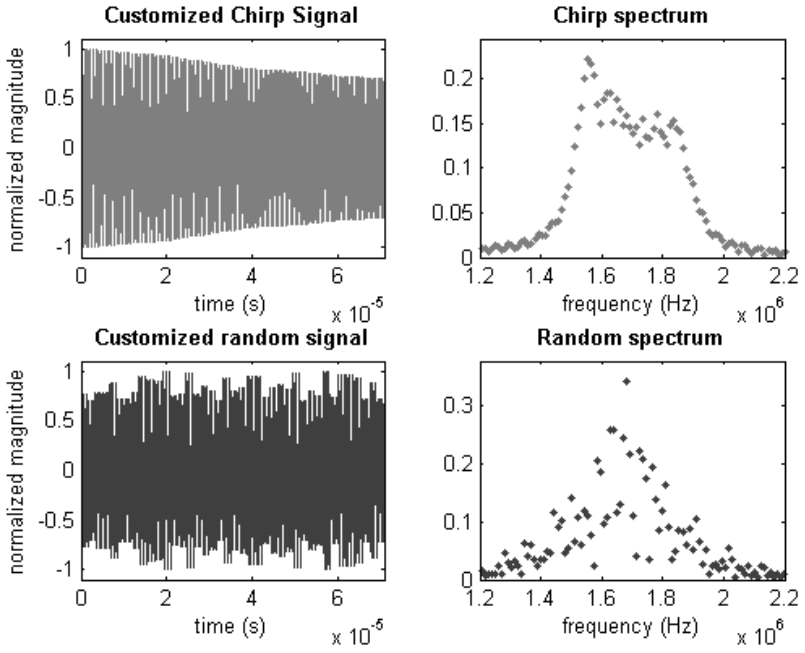

Figure 2.4. Customized chirp and random signal used for sonication. The varied magnitude in the temporal domain was due to the adjustment of FUS transducer sensitivity in order to reach the same pressure. Both the chirp and the random signals composed of a frequency range from 1.4-1.9 MHz as shown in the frequency spectra.

Monkey

The system setup is shown in Fig. 2.5A. For sonication with FUS, a spherically-focused single-element transducer (H-107, Sonic Concepts, WA, USA) operating at 0.5 MHz (full-width-at-half-maximum focal size: 5.85 mm in width and 34 mm in depth, geometric focal depth: 62.6 mm) was used. For real-time monitoring of the acoustic cavitation emission (passive cavitation detection, PCD), a spherically focused, flat-band, polyvinylidene fluoride (PVDF) hydrophone (Y-107, Sonic Concepts, WA, USA), coaxially and confocally aligned with the FUS transducer, served as the passive cavitation detector. A PC workstation (model T7600, Dell) with a customized program in MATLAB® (Mathworks, MA, USA) was developed to automatically control the sonication

through a programmable function generator (model 33220A, Agilent Technologies, CA, USA) and a 50-dB amplifier (A075, ENI, NY, USA). The PCD signal acquisition was performed with a 14-bit analog-to-digital converter (Gage Applied Technologies, QC, Canada) (sampling rate: 50 MHz) after 20-dB amplification.

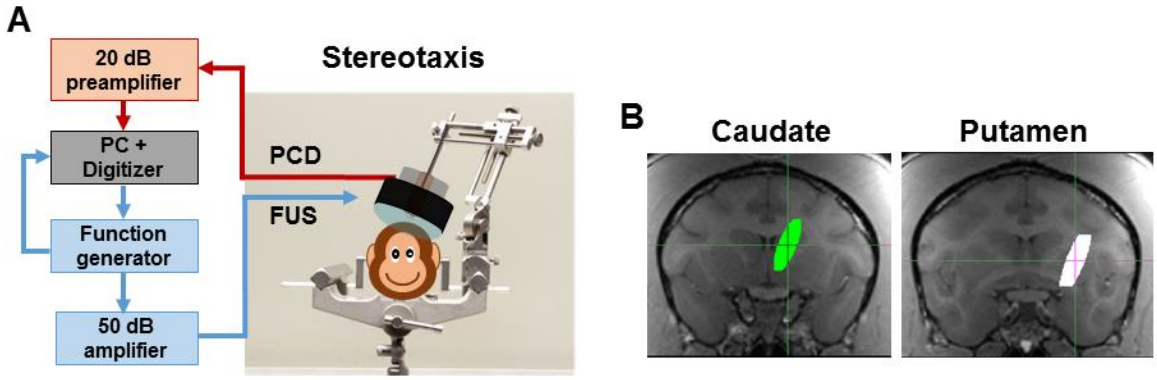

Figure 2.5. In vivo NHP experimental setup. (A) A focused ultrasound (FUS) transducer was used for sonication and a hydrophone coaxially and confocally aligned with the FUS transducer served for passive cavitation detection (PCD). (B) Targeting was performed using stereotaxis with pre-planning for focusing at the caudate nucleus (left) or putamen (right) based on the preoperative MRI scan with a stereotax.

Table 2.1. Acoustic parameters used in the in vivo BBB opening

Animal	*Excitation frequency (MHz)*	*Pressure (kPa)*	*Pulse length*	*PRF (Hz)*	*Duration (s)*
Mice	1.5	520	20 ms	5	5 min
*Mice**	1.5-1.9		70.7 µs		30 s on-time
Monkey	0.5	200-600	10 ms	2	2 min

*: using coded pulses

2.2.4 Experimental Procedures of in vivo BBB opening

Mice

All procedures with animals were approved and conducted in accordance with the Institutional Animal Care and Use Committee at Columbia University. A total of 17 C57BL/6 mice (mass: 20–28 g, sex: male, Harlan, Indianapolis, IN, USA) were used in this study. During the experiment while the animal was under anesthesia with isoflurane (1-2%; SurgiVet, Smiths Medical PM Inc., Waukesha, WI, USA), its head was depilated and immobilized in the stereotaxic frame (David Kopf Instruments, Tujunga, CA, USA), and a small tank filled with degassed water was placed above the mice with the head coupled using coupling gel. After the targeting procedure aligning the FUS focus to the right caudate putamen region, a catheter was inserted to the tail vein for injection of polydisperse microbubbles (average size: 1.39 μm ± 0.99, 30 μL of 8×10^8 bubbles/mL) immediately before the sonication. During the sonication, cavitation signal was monitored through PCD. The mice were divided in 3 randomized groups with 5 animals each. The Chirp group was sonicated for 30 seconds using the chirp method sweeping between 1.5 MHz and 1.9 MHz with an increment of 10 kHz, PNP = 0.52 MPa, and 3 cycles per frequency. The random group was sonicated using the randomly ordered frequency pulses between 1.5 to 1.9 MHz with the same parameters. The regular group was sonicated with a pulsed wave with f = 1.5 MHz, 20 ms, 5 Hz of burst rate, 0.52 MPa for 5 min.

Monkey

In accordance with the National Institutes of Health Guidelines for animal research, all procedures were reviewed and approved by the Institutional Animal Care and Use Committee at Columbia University and the New York State Psychiatric Institute. Four male rhesus macaques (Macaca

mulatta, weight: 7-10 kg, age: 8-20 yo) were used in this study. Each animal was sedated with ketamine (5-15 mg/kg in conjunction with 0.04 mg/kg of atropine through intramuscular injection) for placement of an endotracheal tube and an intravenous catheter in the saphenous vein, and was under anesthesia using 1-2% isoflurane-oxygen mixture with vital signs (electrocardiography, heart rate, blood pressure, SpO_2, breathing rate, end-tidal CO_2) monitored during the entire experiments. No animals were euthanized in this study.

A stereotaxis-based method developed previously [69] was used for targeting the dorsal striatum (caudate and putamen) (Fig. 2.5B), deep subcortical structures associated with neurodegenerative diseases such as Parkinson's disease. For preplanning of the stereotactic sonication, the anatomical scan of the brain was acquired in T1-weighted MRI (3D turbo field echo sequence, TR/TE = 11.1/5.1 ms, FA=8^0, resolution = 0.7 × 0.7 × 0.7 mm; Philips 3T). The pressures at the focus of the FUS transducer were calibrated using a bullet hydrophone through *ex vivo* rhesus macaque skulls, and 50% of pressure loss due to the skull was compensated in the *in vivo* experiments [133]. The in-house made, lipid-shelled, monodisperse microbubbles (4-5 μm in diameter)[134] were freshly diluted to 3 mL with a dosage of 2.5×10^8 bubbles/kg of body weight. Another 3 mL of saline was used to flush after microbubble injection.

At the beginning of the FUS procedure, the control sonication (duration = 5 s) was performed before microbubble injection as a baseline for cavitation monitoring, and then the microbubbles were injected in a bolus intravenously (saphenous vein) followed by saline flush within 30 s while the sonication started at the same time (peak negative pressure = 200-600 kPa, pulse length = 10 ms, pulse-repetition frequency = 2 Hz, duration = 2 min). A second sonication was performed in 11 out of a total of 47 experiments at a second non-overlapping target 20 min after the microbubbles were eliminated from the first experiment.

After the FUS procedure, the animal was transferred to the MRI suite for assessing the BBB opening and safety within 1 h. Two sham cohorts were also performed by applying FUS without injecting microbubbles (FUS+/MB-, N = 4) or without FUS procedure (FUS-/MB-, N = 3) for comparison to determine BBB opening in the experimental groups.

Table 2.2. Number of experiments performed

Animal	*Number of animals*	*Number of sonications*	*Targeting region*
Mice	17	17	Basal ganglia
Monkey	4	70	Basal ganglia

2.2.5 Postoperative MRI Acquisition

Mice

In order to confirm the BBB opening and calculate its volume, contrast enhanced T_1-weighted MRI (spatial resolution of 80×80×400 μm^3) were acquired for all mice using a 2-D FLASH sequence in a 9.4-T system (DRX400, Bruker BioSpin, Boston, MA, USA). MR contrast agent, gadodiamide (molecular weight = 573.66 Da; Omniscan®, GE Healthcare, NJ, USA) was injected intraperitoneally immediately after the sonication, and the animal was scanned after 30 min.

Monkey

A 3.0 T clinical system (Achieva, Philips Medical Systems, USA) with an eight-channel head coil was used for assessing BBB opening. Both pre- and post- contrast agent T_1-weighted images were acquired before and 30 min after injection of gadodiamide (molecular weight = 573.66 Da;

Omniscan®, GE Healthcare, NJ, USA) with the same dosage suggested for patients (0.2 mL/kg or 0.1 mmol/kg of body weight) using 3D spoiled gradient echo (SPGR) sequence (TR/TE = 8.5/4.8 ms, FA = 8º, spatial resolution = 0.97×0.97×1 mm^3).

2.2.6 Quantification for BBB Opening

Mice

The acquired T_1-weighted images were used to quantify the BBB opening volume firstly by thresholding based on the signals on non-sonicated region (mean+2.5 times of standard deviation) to exclude the voxels without opening [135]. Then an ellipsoid region-of-interest (5.5 mm of diameter in long axis, 4.0 mm of diameter in short axis, 0.4 mm of height, throughout 9 slices) was selected in the sonicated region of the horizontal slices.

Monkey

The BBB opening volume was quantified using pre- and post-Gd T_{1w} images in Matlab with custom-built programs [70]. In brief, both pre- and post-Gd images were first registered to the individual stereotactically-aligned images (IST) with FSL's FLIRT toolbox[136], computing the ratio of post- to pre-Gd images as a measurement of contrast enhancement, which was normalized by linear scaling with reference to the unsonicated thalamus and the anterior cerebral artery (ACA). In order to filter out the background contrast enhancement in the cerebral vessels and muscle tissue outside the brain for quantifying the BBB opening volume, the brain mask was applied (generated using pre-Gd T_{1w} images from the no-FUS sham cohort with FSL's Brain Extraction Toolbox

[137]) and the enhancement images of the FUS-/MB- sham cohort for each individual was subtracted from the enhancement images. Finally, the opening volume was calculated by applying a volume of interest (VOI, $10 \times 10 \times 32.5$ mm^3) on the targeted region subtracting the VOI on the contralateral side. The threshold of BBB opening (80 mm^3) was defined by the average opening volume plus 3 times the standard deviation in the FUS+/MB- sham cohort.

2.2.7 Analysis of targeting accuracy in NHP experiments

The targeting accuracy was analyzed by comparing the planned targeting to the quantified BBB opening results using the T_{1w} images as described in the previous section. The planned targeting was composed of a targeting vector with a focus and an approaching direction (trajectory) for an interested brain structure. The BBB opening vector was subsequently defined by the 3-D center of mass in the BBB opening in the VOI described previously and the vector from the 3D linear curve fitting of the 2-D center of mass in each of the horizontal slices, respectively. Finally, the target shift was defined as the distance between the center of focus in the targeting vector and the center of mass in the BBB opening, and the lateral and axial shift was the shift perpendicular and parallel to the targeting vector, respectively.

2.3 RESULTS

2.3.1 Simulation vs. BBB opening using customized pulses

2.3.1.1 Simulated transcranial pressure field using customized pulses in mice

After acquiring the microCT of the mice skull (Fig. 2.6A), the transcranial peak negative pressure (PNP) fields were simulated using regular and frequency-coded pulses (chirp or random frequency) in mice. As shown in Fig. 2.6B, the regular sonication presented standing wave formation clearly in the focal region. In comparison, both the chirp-coded pulses (Fig. 2.6C-E) and the random-coded pulses (Fig. 2.6F-H) generated significantly less standing waves due to a range of frequencies transmitted. The chirp and random methods were then explored to optimize the pulse design by varying the frequency range, incremental frequency bandwidths, and the number of cycles. For the chirp method, the best parameters were found to be with a bandwidth of 1.23 to 2.29 MHz, 10 kHz of incremental frequency and 2 cycles (Fig. 2.6E) because of the lowest standing waves and side lobes with the best focal quality. The other two cases (Fig. 2.6C-D) not only showed higher side lobes and standing waves were observed, but also points of maxima outside of the focus due to the interference pattern caused by the multiple scattering of the waves in the brain. Likewise, the random-based method showed better focusing for a bandwidth of 1.23 to 2.29 MHz, 1 kHz of incremental frequency, and 3 cycles (Fig. 2.6H).

For the three types of pulses (with optimized parameters), the axial and lateral beam profiles are shown in Fig. 2.6I-J. The axial profile shows the standing wave formation by the regular sonication which is not observed in the coded methods, and the lateral beam profiles shows the side lobes generated by the three techniques. The regular sonication presented higher oscillations on the pressure field with higher peak negative pressure, so it is more likely to enhance cavitation and drug diffusion. These parameters were thus used in the in vivo BBB opening experiments for comparison and validation of the simulation.

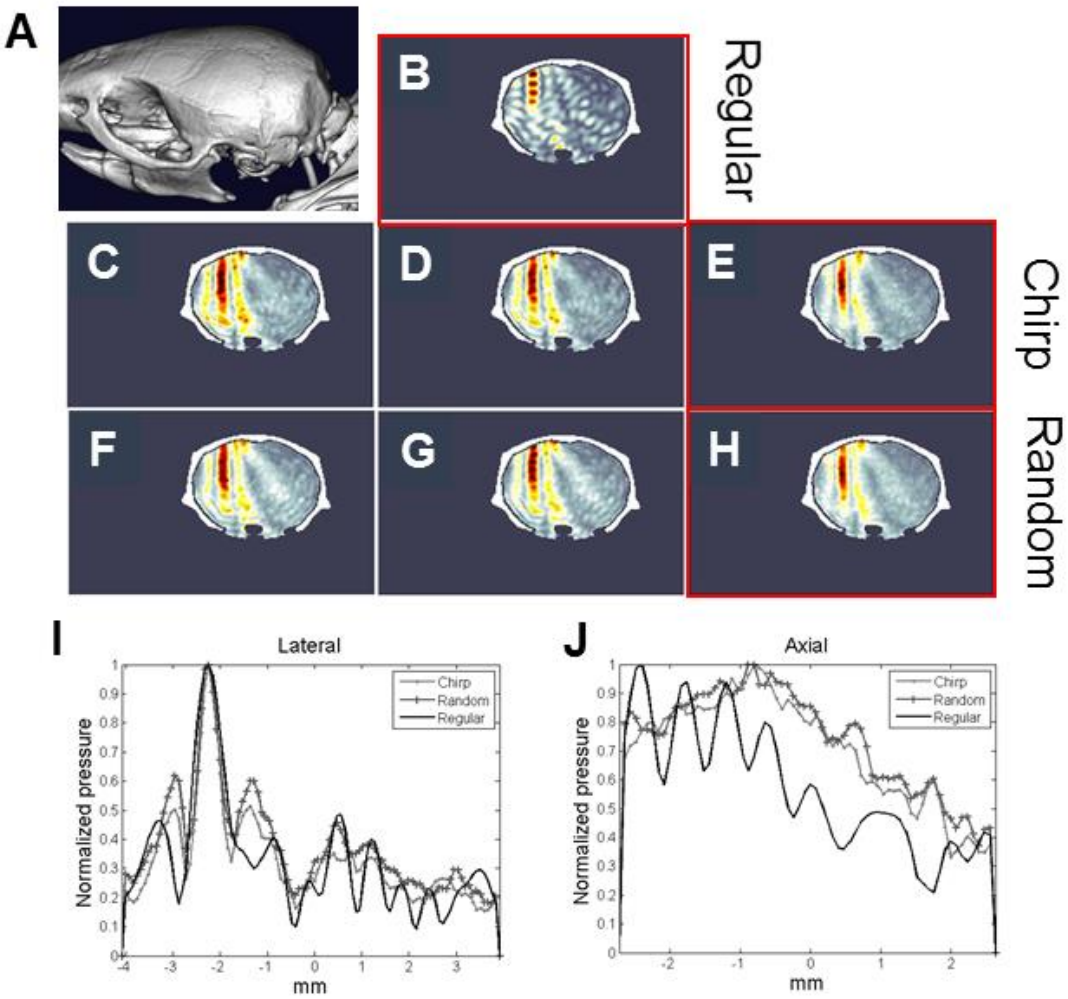

Figure 2.6. Simulation of acoustic pressure field through the mice skull using customized pulses. (A) The mice skull was imaged in microCT. The peak negative pressure fields for different coded pulses using (B) regular sonication (1.5 MHz); (C) Chirp: 1.5-1.9 MHz, 10 kHz, 3 cycles; (D) Chirp: 1.5-1.9 MHz, 10 kHz, 2 cycles; (E) Chirp: 1.23-2.29 MHz, 10 kHz, 3 cycles; (F) Random: 1.5-1.9 MHz, 10 kHz, 3 cycles; (G) Random: 1.5-1.9 MHz, 1 kHz, 2 cycles; and (H) Random:1.23-2.29 MHz,1kHz,3 cycles. The lateral (H) and axial (I) beam profiles were plotted comparing the regular pulses to the coded pulses with best focusing quality and less standing wave in (E) and (H).

2.3.1.2 BBB opening using customized pulses in mice

As shown in Fig. 2.7A, the spectrograms of the received PCD signals demonstrated varying harmonic frequencies in the coded pulses while the regular method remained the same harmonic frequencies. The corresponded BBB opening results with the MRI were shown in Fig. 2.7B. The brighter regions in the brain show the extravasation of the contrast agent from the vascularity to the brain. The extravasation indicate where the ultrasound successfully opened the BBB. The chirp method and the random-based method presented smaller openings in comparison to that with the regular sonication method. The opening volumes showed the same trend for the three groups (Fig. 2.7C), in which the mean opening volumes were 9.38 ± 5.71 mm^3, 8.91 ± 3.91 mm^3 and 35.47 ± 5.10 mm^3 for chirp, random and regular sonication, respectively. As predicted by the enhanced cavitation due to the varying pressure field using the regular pulses, the in vivo results also presented larger BBB opening volumes. While the coded excitation methods showed the about same opening volumes, which corresponded well with the simulation. Fig. 2.7D shows the ANOVA statistical analysis of the cavitation level (figure 5 middle). The cavitation level for the regular sonication was higher than the coded excitation methods. No significance difference was found for the coded excitation methods.

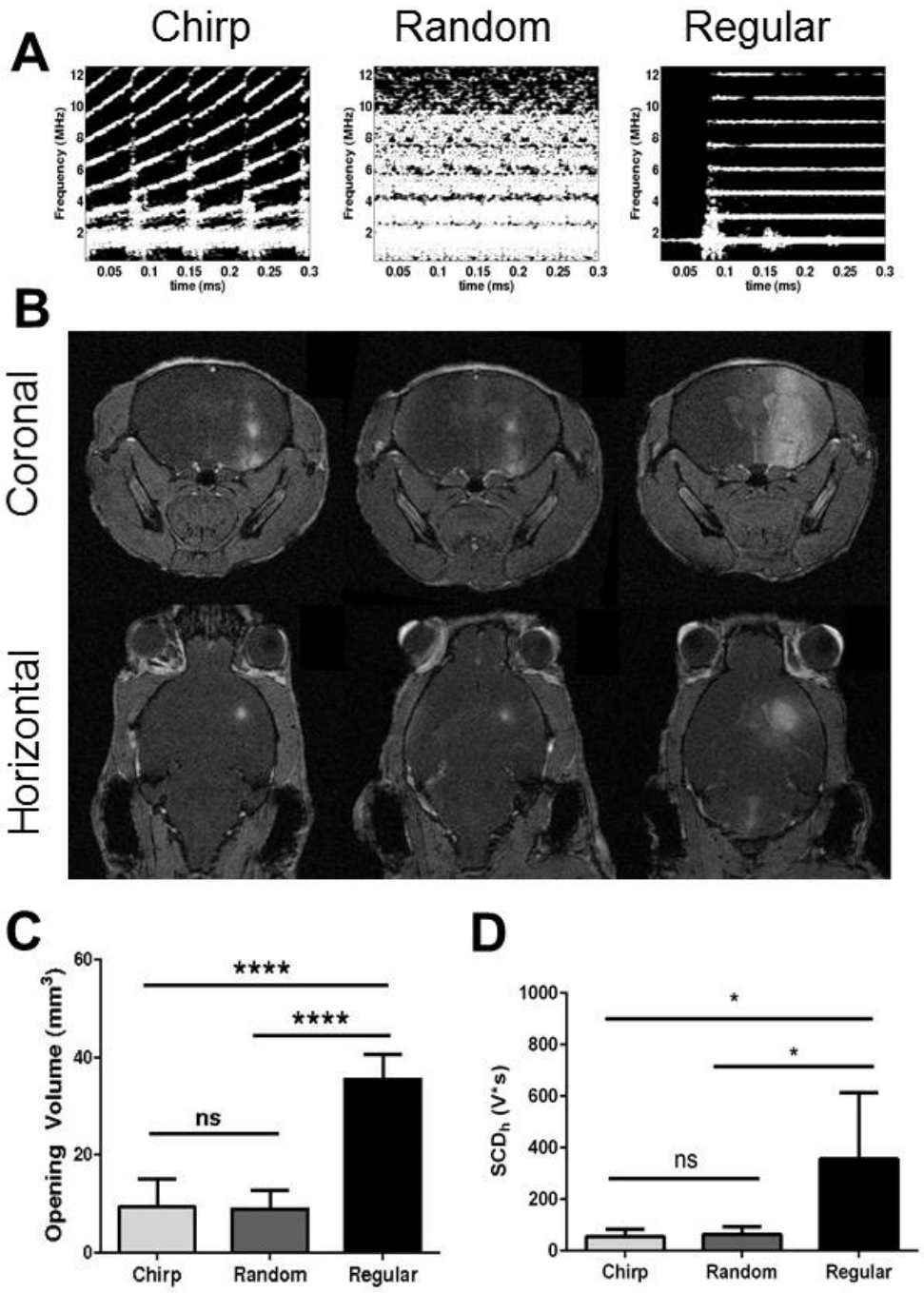

Figure 2.7. BBB opening in mice using customized pulses. (A) The spectrograms of the cavitation signals demonstrated varied harmonic frequencies using chirp or random coded pulses compared to consistent frequencies in the regular pulses. (B) Contrast enhanced T1- weighted MRI images showed the BBB opening for chirp, random and regular sonication methods, respectively. (C) Using coded pulses resulted in a more localized BBB opening. (D) The quantified stable cavitation dose showed a lower cavitation activity with coded excitation.

2.3.1.3 Simulated transcranial pressure field using customized pulses in NHP

The pulse design scheme was further studied in NHP to remove standing waves in the brain and improve the focal quality in large animals. After acquiring the CT of the NHP skull, the transcranial peak negative pressure (PNP) fields were simulated using regular (frequency: 0.5 MHz, pulse length: 10 ms) pulses that have shown to disrupt the BBB in NHP (Section 2.3.2) and chirp-coded pulses (sweeping frequency: 0.5-2 MHz, pulse length: 0.05 -0.5 ms). While the standing waves were clear in using regular pulses as shown in Fig. 2.8, the peak magnitudes relative to the baseline pressure (axial profile in Fig. 2.8B) were less significant compared with those in mice and may be due to the nature of lower-frequency waves in a larger brain. Using long logarithmic chirp pulses ($f_i(t) = f_0 \times \beta^t \; where \; \beta = 1.02^{10^5} and \; f_0 = 0.5 \; MHz$, pulse length: 0.5 ms) eliminated a majority of standing waves, and increasing the sweeping rate of the pulses successfully enhanced the effect as shown with short logarithmic chirp pulses ($f_i(t) = f_0 \times \beta^t \; where \; \beta = 1.02^{10^6} and \; f_0 = 0.5 \; MHz$, pulse length: 0.05 ms). Similar to the long logarithmic chirp pulses, using linear chirp pulses (increasing frequency in a linear rate) was less effective than using the short logarithmic chirp pulses. In all pulses used, the focal size remained the same as the regular pulses since the axial and lateral size was determined by the lowest frequency (0.5 MHz) in the chirp pulses and the aperture size of the transducer, respectively.

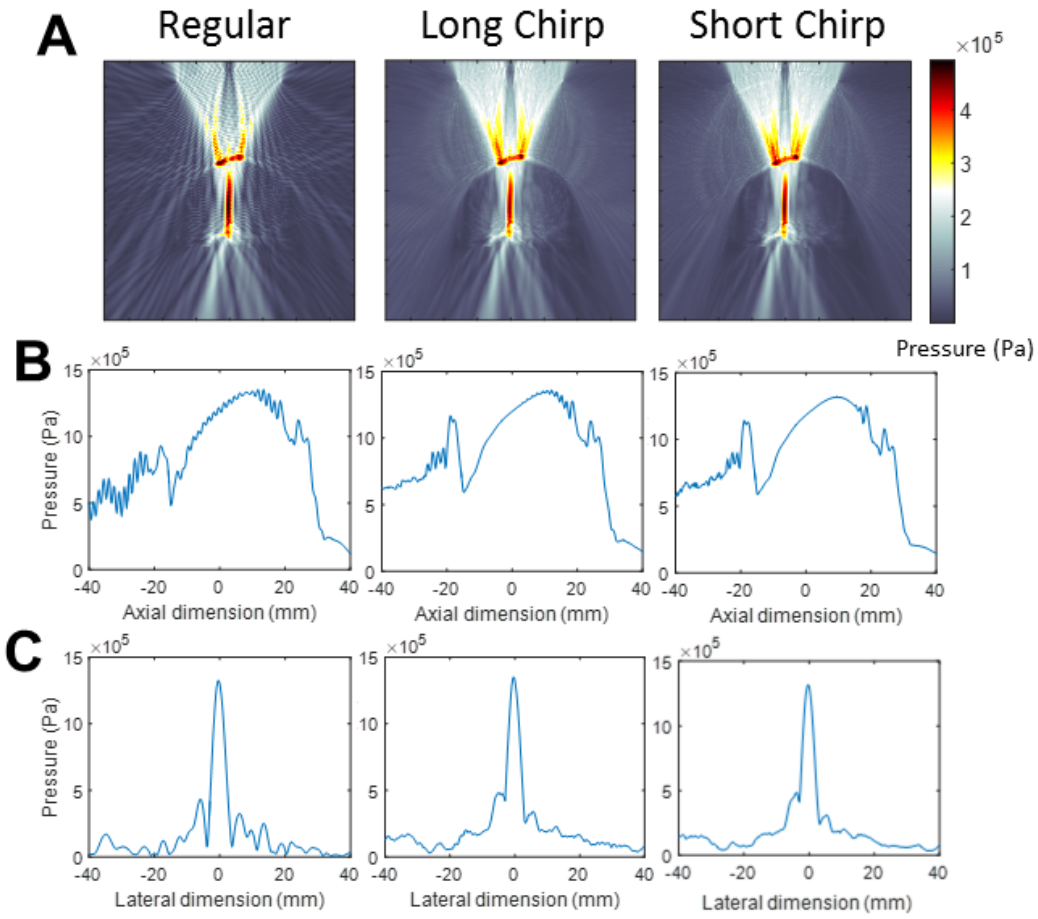

Figure 2.8. Simulation of acoustic pressure field through the NHP skull using customized pulses. (A) The peak negative pressure fields for different coded pulses using regular sonication (frequency: 0.5 MHz, pulse length: 10 ms), short logarithmic chirp (sweeping frequency: 0.5-2.0 MHz, pulse length: 0.5 ms), and long logarithmic chirp (sweeping frequency: 0.5-2.0 MHz, pulse length: 0.05 ms). Pressure profiles for the corresponding pulses in the (B) axial and (C) lateral direction.

2.3.2 Simulation vs. BBB opening in NHP

The skull effect on the acoustic pressure distribution was investigated with respect to the focal shift and the pressure in situ. Also, to validate the established 3D simulation of the transcranial acoustic pressure field through the primate skull, it was compared with the BBB opening in NHPs in vivo. The in silico acoustic focus was calibrated with the transducer focus in water in terms of

the focal length, width, and the side lobes (Fig. 2.2), and the acoustic properties of the skull such as the density and the speed of sound were converted from the CT images (Fig. 2.9A).

2.3.2.1 Simulated transcranial pressure decrease and focal shift

Through the NHP skull, the full-width at half maximum focal size decreased from 4 mm laterally and 35.3 mm axially without the skull to an average of 2.6 mm laterally and 16.7 mm axially Due to the skull lensing effect, which similar to the BBB opening size (Fig. 2.9B).

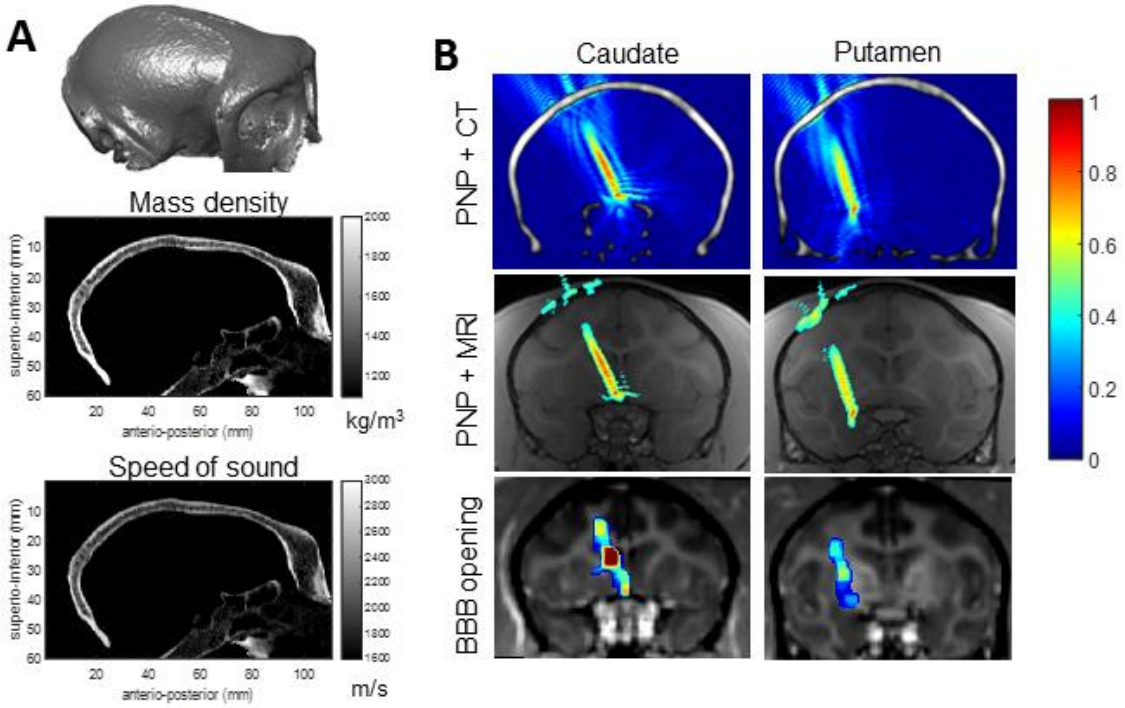

Figure 2.9. Simulation of the acoustic pressure field to estimate the BBB opening in NHP. (A) The CT scan of a monkey used to calculate the acoustic properties of the skull including density and the speed of sound. (B) The simulated transcranial peak-negative pressure (PNP) field (unit normalized to the pressure without the skull) corresponded to the BBB opening in the caudate and putamen (arbitrary unit, A.U.).

In order to investigate the pressure decrease and focal shift due to the skull, three NHP skull CT were acquired in vivo for simulation in the targeted basal ganglia. In the statistics from 12 targeting in 3 NHPs, the average skull thickness was 2.6 mm, with an average density of 1532 kg/m^3 and a speed of sound of 2293 m/s. From the quantification of the peak-negative pressure (PNP) field distribution, an average focal shift of 2.1 mm (0.8 mm laterally, 1.8 mm axially)(Fig. 2.10B) and a pressure decrease of 41% were found due to the skull. Furthermore, the transcranial pressure varied between animals and targeting was found to be highly correlated with the density and thickness of the skull in the beam path (R^2=0.6) (Fig. 2.10A).

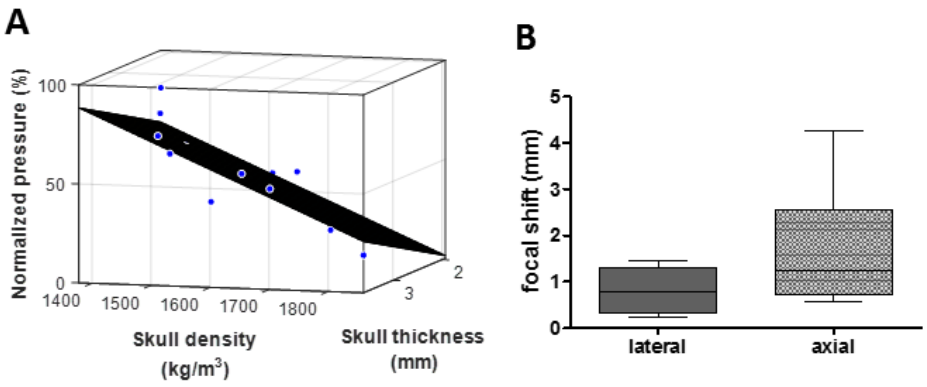

Figure 2.10. Estimated skull attenuation and focal shift in silico. (A) The in situ PNP was negatively correlated with the thickness and density of the skull in the acoustic beam path as shown in the plane-fitting result with a R^2 of 0.6. (B) The in silico focal shift due to the skull in the lateral and axial direction of the acoustic wave propagation was estimated to be 0.8 mm laterally and 1 mm axially.

2.3.2.2 Pressure threshold and target shift for BBB opening in NHP

In the in vivo BBB opening experiments, an inter-animal variation was observed in the pressure threshold for BBB opening after applying an estimate of 50% pressure increase to compensate the skull attenuation. As shown in Fig. 2.11, the pressure threshold for NHP 1 was lower (200 kPa)

than that in NHP 2 (350 kPa). This inter-animal variation was found to be due the difference in skull in simulation. As based on the simulation results, an average of 67% and 46% of remnant pressure was found in NHP 1 and NHP 2, respectively. This then result in a similar BBB opening threshold of 268 kPa and 322 kPa for NHP 1 and 2, respectively after taking the in silico pressure decrease in to account instead of a general 50% decrease. Since the individual difference in the skull properties contributed to variation in skull attenuation and affects the in situ pressure, it is of vital importance to perform simulation for large animals and humans in order to account for pressure loss due to the skull and achieve safe and effective FUS treatment.

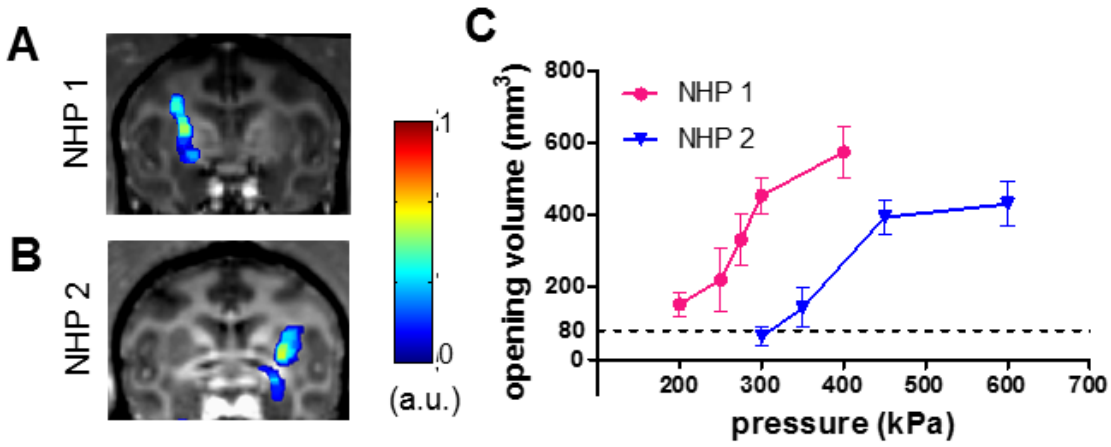

Figure 2.11. BBB opening in two NHPs showing inter-animal variation. (A-B) Two representative cases of BBB opening at the putamen were visualized by overlaying the contrast enhancement onto the post-Gd T_{1w} image (A: NHP 1 at 300 kPa; B: NHP 2 at 600 kPa). (C) The opening volume was quantified at various pressures, and the error bar represents standard deviation. It was found that NHP 1 had larger opening volume than NHP 2 using the same pressure.

The in vivo target shift in BBB opening was also investigated. Following targeting planning in the caudate and putamen, the resulting BBB opening along the FUS beam trajectory was visualized in brain in the 2D coronal plane (Fig. 2.12A), the stacked 2D horizontal planes (Fig. 2.12B), and the trajectory through the 3D skull piece (Fig. 2.12C). The targeting accuracy was

quantified in four animals based on the defined FUS orientation (axial and lateral distance shift relative to the planned FUS trajectory) and the angle relative to the skull (Fig. 2.13). The lateral and axial shift ranged between 0.9 mm to 6.4 mm and 1.0 mm to 7.6 mm. When targeting the caudate, the overall shift ranged between 2.4 mm to 6.5 mm with an average of 3.7 mm. When targeting the putamen, it ranged between 4.4 mm to 10.1 mm with an average of 7.5 mm. A larger shift in axial direction compared with the lateral direction was expected due to the simulation with NHP skulls.

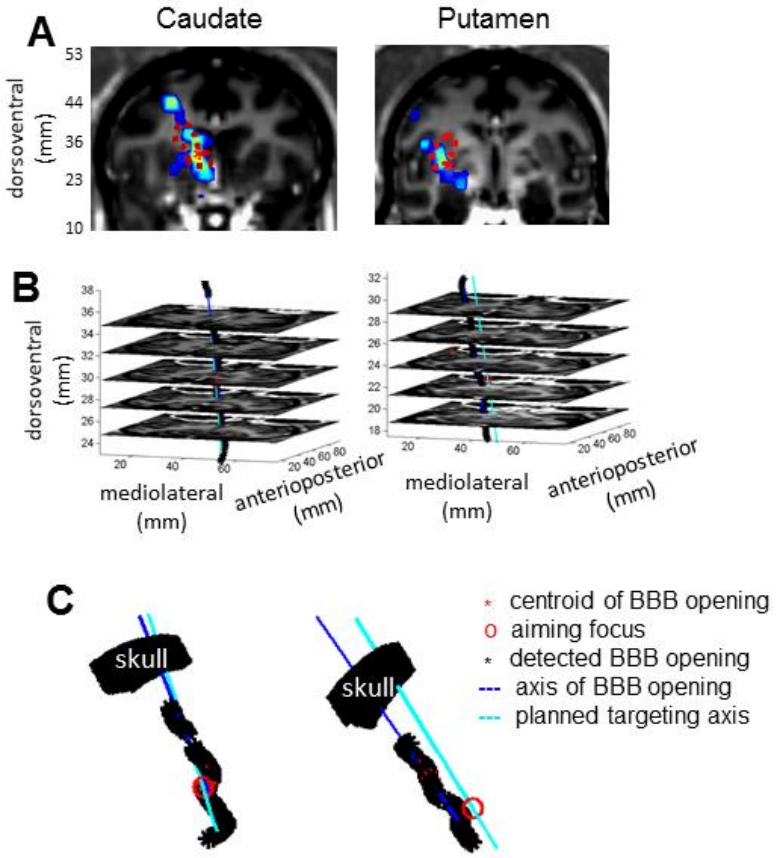

Figure 2.12. Targeted BBB opening in NHP in both the caudate and the putamen. (A) Visualization of targeting in the caudate nucleus (dashed contour in the left column) and the putamen (dashed contour in the right column) and the BBB opening by overlaying the contrast enhancement onto the post-Gd T1w image, where * denotes the centroid of BBB opening. (B) Targeting trajectory and the opening trajectory showed in the stacked horizontal slices. (C) 3D images with the trajectory of acoustic beam (light blue) and BBB opening (dark blue) relative to the skull.

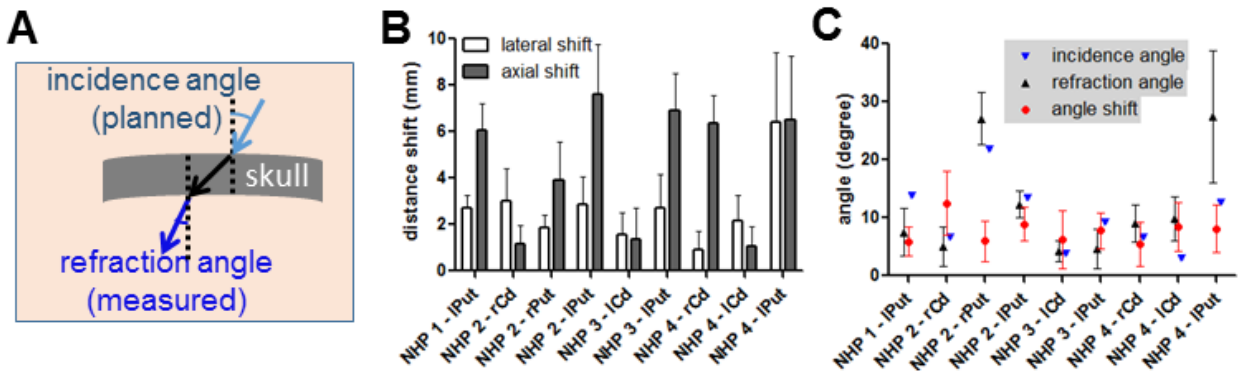

Figure 2.13. Targeting accuracy for in vivo BBB opening in NHP. (A) Schematic of the angle definition to the skull. Target shift in BBB opening was quantified in distance (B) and in angle (C), where lPut represents left putamen, rPut for right putamen, lCd for left caudate, and rCd for right caudate. The error bar represents standard deviation.

2.3.3 Simulation of FUS targeting in human

This 3D simulation has been validated with in vivo experiment using coded excitation in mice and regular pulses in NHP, it was then used with human skulls to investigate the targeting effects in clinically relevant settings. Various incidence angles (0-20°) and transducer-skull distance (separation distances between the transducer and the skull) (20-60 mm) were evaluated from three skull regions (parietal, occipital, and temporal bone). The focal qualities including the focal size in axial and lateral direction (FWHM or -6 dB size), the focal shift in axial and lateral direction (distance between the local maxima in the focal region and the ideal focal spot), and the skull attenuation were measured.

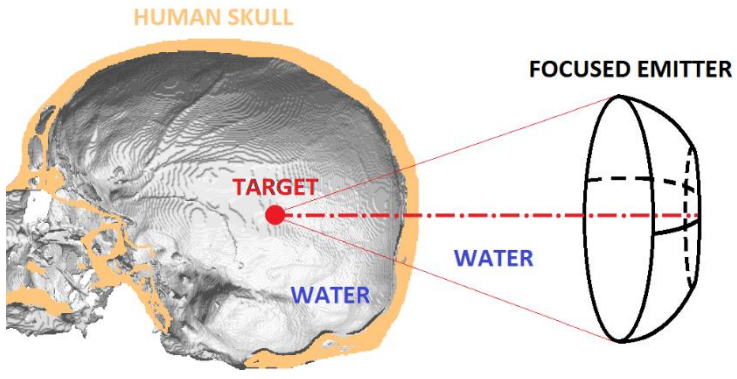

Figure 2.14. The transducer was targeted the human brain at various orientation through the skull.

2.3.3.1 Effect of incidence angle to the skull

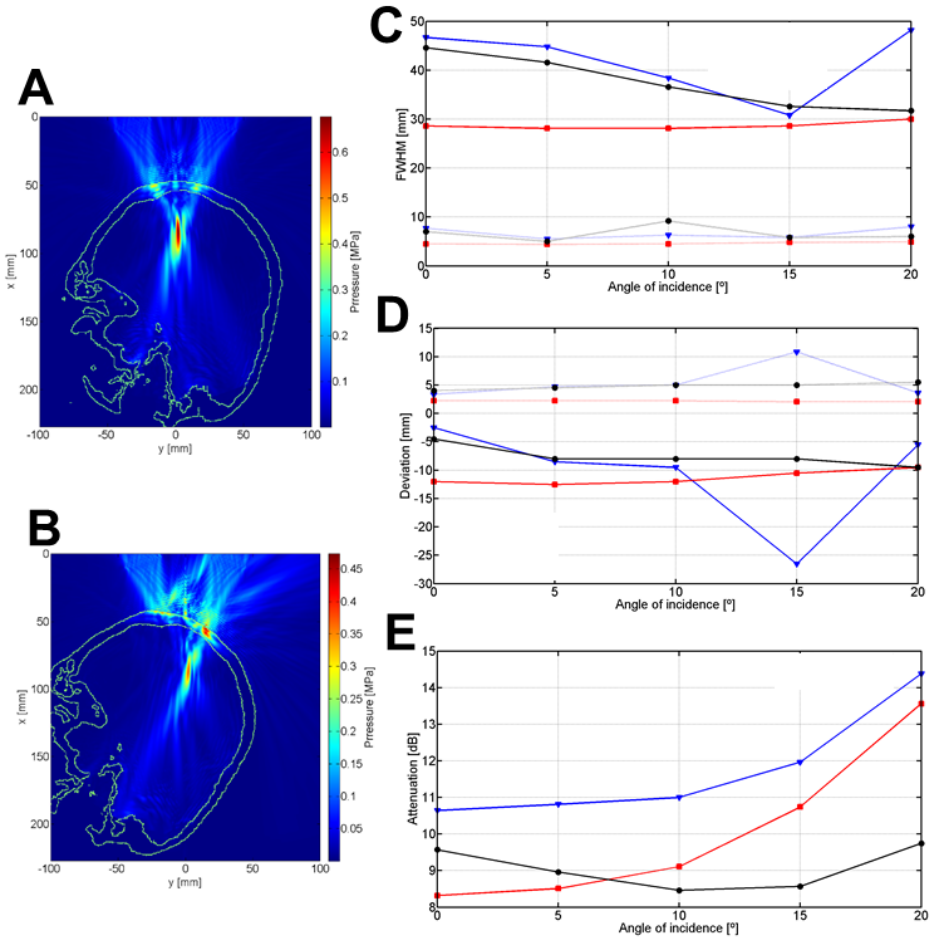

Figure 2.15. Simulation of acoustic pressure field through the human skull at various angle of incidence. The pressure distribution for placing the FUS transducer toward the brain through the occipital area of the human skull at (A) 0° and (B) 20° angle of incidence. The focal properties were quantified for the parietal (blue), occipital (red), and temporal (black) bone. (C) The FWHM focal size. (Solid line: axial direction. Dotted line: lateral direction.) (D) The focal shift or deviation. (Solid line: axial direction. Dotted line: lateral direction.) (E) The skull attenuation.

Both the pressure distribution and the quantified focal properties at various angles of incidence were shown in Fig. 2.15. A minimal change was shown in the lateral focal size and deviation, while the axial size decreased as the angle increased in most cases. Generally, the focal size through the skull fell at 7 mm laterally, and 30-50 mm axially. The deviation fell in 5 mm

laterally and 5-15 mm axially in most cases. On the other hand, the pressure loss increased with the angle, ranging between 8 to 14 dB.

2.3.3.2 Effect of separation distance of the transducer to the skull

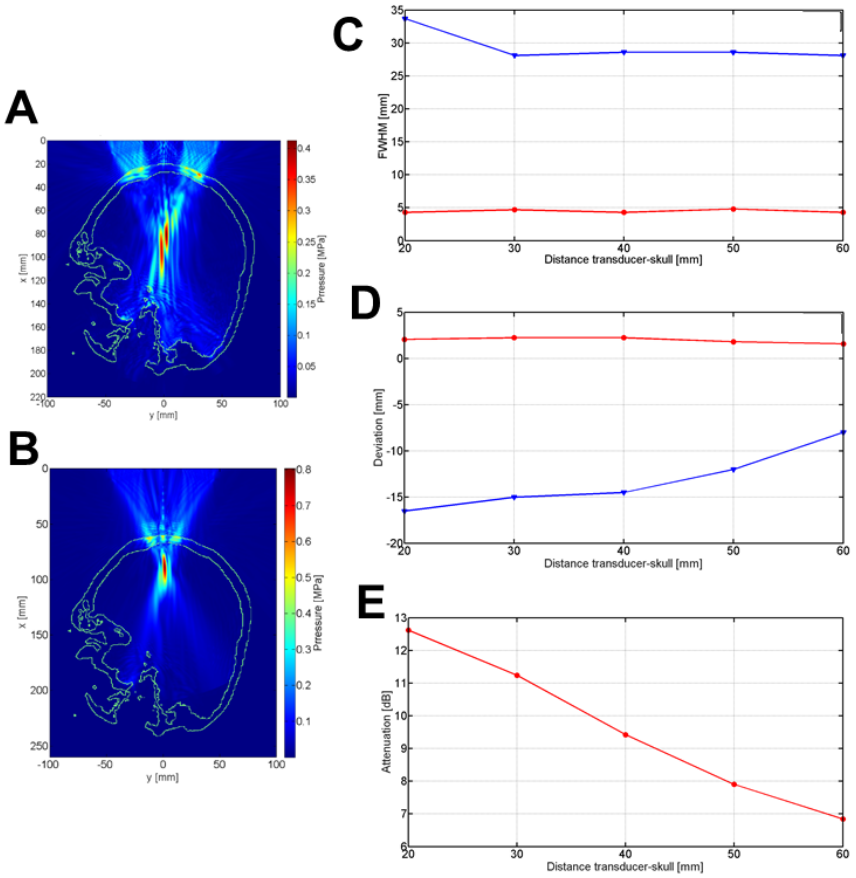

Figure 2.16. Simulation of acoustic pressure field through the human skull at various separation distance between the transducer and the skull. The pressure distribution for placing the FUS transducer toward the brain through the occipital area of the human skull at (A) 20 mm and (B) 60 mm separation distance. The focal properties through the occipital bone were quantified. (C) The FWHM focal size. (Blue line: axial direction. Red line: lateral direction.) (D) The focal shift or deviation. (Blue line: axial direction. Red line: lateral direction.) (E) The skull attenuation.

Both the pressure distribution and the quantified focal properties were shown in Fig. 2.16 for the separation distance of transducer to the skull through the occipital bone. The focal size

remained the same, while the axial deviation decreased with the increase of separation distance. Furthermore, the pressure loss decreased with the increase of separation distance as well. Therefore, the further the transducer is to the skull, the better the focal quality it would be.

2.4 DISCUSSION

In this chapter, simulation of the acoustic pressure distribution was utilized for pulse design in mice and targeting design in monkeys and humans. To improve the focal quality, chirp pulses with a frequency range of 1.5-1.9 MHz were explored to eliminate standing waves and scattering from the skull cavity. To evaluate the validity of 3D simulation with the primate skull model, it was performed with the same targeting used for BBB opening in NHP. Both the focal quality and the skull attenuation in silico corresponded to the in vivo results. This 3D simulation was then performed with the human skull model to investigate the focal property change at various targeting factors including the skull bones, approaching angle of incidence to the skull, the separation distance of the transducer to the skull. These findings provide crucial information to plan for the FUS treatment. The developed simulation tool therefore will be valuable for in silico preplanning in clinics for pressure and targeting estimation.

2.4.1 Pulse design using chirp to improve focal quality

In this study, frequency-coded pulses were used for sonication in mice in silico and in vivo and NHP in silico. The coded excitation methods were driven continuously to facilitate the standing wave formation caused by the multiple scattered of the wave inside the brain. The coded methods were capable of avoiding the standing wave formation predicted by the simulations. The lower cavitation levels detected for the coded excitation methods indicate lower microbubble activity

which was confirmed with the more confined openings detected by the MRI images in mice. Those results corroborated other studies that demonstrated the cavitation reduction using random methods [125, 138]. Hence, the coded methods were capable to enhance the targeting of the BBB opening.

The coded ultrasonic methods were capable of improving the targeting of the BBB opening. The larger bandwidth was concluded to achieve better focusing and lower standing wave formation for coded methods. Though, the choice of the frequency bandwidth needs to take into account the frequency response of the transducer, the skull attenuation and the microbubble optimum frequency range. The higher focusing capability found here improves the precision of the method allowing specific regions of the brain to be treat with drugs and other pharmacological substances. The coded methods can be easily implemented in different setups. The use of these methods together with large phased arrays may improve the focusing and reduce standing wave formation. Therefore, other techniques may benefit by this coded excitation method, for example, reducing hemorrhage found in sonothrombolysis trials. The improvement in targeting is an important advantage especially for HIFU which uses higher pressure levels and needs to be very precise to ablate the prescribed region and avoid damage to the healthy tissue.

2.4.2 Simulation through the NHP skull predicted the BBB opening characteristics

The 3D simulation predicted a varied skull attenuation between individuals and targeting parameters due to the difference in skull density and thickness. The inter-animal variation was also confirmed with the in vivo BBB opening threshold, implying that the variation is mainly associated with the skull attenuation while the pressure to induce BBB opening remained similar between animals (same threshold reported in mice [76] and rats [79]).

The simulation also predicted an average focal shift of 2 mm (0.8 mm laterally and 1 mm axially with higher variation in the axial direction). This also corresponded well to the in vivo findings (Fig. 2.13), while more factors may affect the targeting accuracy in vivo. For example, the targeting shift in the putamen was higher than in the caudate. Both the gyrencephalic brain and the incidence angle could play an important role as more layers of gyrus and sulcus were included in the beam path when targeting the putamen with larger incidence angles. Heterogeneous tissue in the acoustic beam path may affect the targeting accuracy due to the refraction between layers and the heterogeneous BBB opening in the gray and white matter affecting the analysis. Higher incidence angles could cause larger shifts due to the wave distortion in the skull [139] and refraction between the skull layer as well (refraction angle > incidence angle). Besides, the stereotactic arm holding the heavy FUS transducer may cause shift while targeting with a large angle deviating from the mid-sagittal plane.

2.4.3 The focal quality through the human skull depended on the targeting design

The targeting effects on the focal properties such as focal shift, focal size as well as skull attenuation were explored in human, providing crucial information for preplanning in the future. The skull attenuation was found to be related with both the skull thickness and density in monkeys, it was also found to be increased with the incidence angle that determines wave propagation mode and distortion [139]. It also increased when the transducer was placed closer to the skull, as the waves propagated through a higher volume of skull and may be distorted at a higher extent.

The focal shift was affected by the angle of incidence as refraction of the ultrasonic waves in the skull determined the axial deviation. It can go from -2 to -15 mm depending on the area, angle and distance of incidence. However, it was not affected when the angle of incidence was

lower than 10°. Placing the transducer closer to the skull increased the axial shift as the skull volume in the beam path increased. On the other hand, lateral deviation of the focus provided the information about the non-axisymmetry of the skull. It ranged between 2 to 5 mm and remained stable with various angle of incidence and the separation distance. Besides, the focal size (axial and lateral FWHM size) showed different variations depending on the incidence zone. The occipital zone resulted in the shortest axial size of 30 mm, which was smaller than that in water (38.5 mm). This can be due to a focusing effect of the skull called skull lensing effect. On the other hand, lateral size remained stable in values between 5 and 9 mm, slightly higher than in water (4.4 mm).

Although several trends can be found in this study, local heterogeneities in the area where the ultrasound beam crosses the skull have shown to affect drastically the location and the quality of the focus. To validate most of the present conclusions, more simulations should be done in each area, as well as in different CTs. Future work will also incorporate both the skull volume as well as the distribution of skull density and incidence angle in the beam path for a more quantitative way to correlate with the focal characteristics. Once the correlation between the skull and the focal characteristics is established, an efficient estimation of focal quality can then be used for a quick preplanning before running a full simulation. This way, CT only can be used for an estimation of focal qualities by quantifying the skull characteristics such as thickness, density, and curvature in the beam path during preplanning. Lastly, ultrashort echo-time MRI utilizes the cortical bone nature of short T_2* decay time to image the skull which may be able to replace the CT for preplanning and simulation and improve the workflow [140].

2.5 CONCLUSION

In this chapter, a simulation tool was established and validated with in vivo BBB opening in small and large animals. It provided focal properties as well as in situ pressure with respect to various pulse design and targeting planning. To improve focal quality, chirp and random pulses with a small frequency range could eliminate standing waves. The skull-transducer distance and angle of incidence could also be optimized to improve the focal quality. Since the variation in the skull properties could dramatically change the in situ pressure and the focal characteristics, it is of vital importance to perform pre-operative simulation to ensure safety and effectiveness in the transcranial FUS treatment including BBB opening. The proposed in silico preplanning was thus summarized in chapter 7 followed by the neuronavigation-guided treatment procedure.

2.6 SIGNIFICANCE & CONTRIBUTION

The safety and effectiveness of transcranial FUS is directly determined by the applied pressure in the brain, but there exists no method to measure the pressure with unknown skull attenuation. Although several methods of numerical simulation have been developed to estimate the pressure, none of them was implemented and validated for BBB opening. In this chapter, the specific aim to develop a treatment preplanning tool for BBB opening has been achieved by modeling the acoustic wave propagation through the skull (mice, NHP, and human) and extensively validated with in vivo BBB opening (mice and NHP) for the first time. This simulation tool not only can be used to compensate for the animal variation, improve the focal quality, it also sheds lights on the clinical targeting design. In the first step of clinical trial in which safety is the utmost important issue, the developed simulation tool will provide the key information in the preplanning phase.

The research credit was shared with many colleagues and collaborators. Hermes Kamimura, PhD (Biomedical Engineering, Columbia University) performed the study in mice and assisted the simulation in NHP. Sergio Jimenez, M.S. (Universidad Politecnica de Valencia, Spain) and Francisco Camarena Femenia, PhD (Universidad Politecnica de Valencia, Spain) helped investigate the targeting effect in the simulation in humans. Fabrice Marquet, PhD (Biomedical Engineering, Columbia University), Tobias Teichert, PhD (Neuroscience, Columbia University), and Yao-Sheng Tung, PhD (Biomedical Engineering, Columbia University) mentored and assisted the in vivo NHP experiments.

Chapter 3

Acoustic Monitoring to Assess Drug Delivery with Customized Mediators

3.1 INTRODUCTION

In Chapter 2 it has been shown that ultrasound at 0.5 MHz can be applied through mice, monkey and human skull. While to achieve BBB opening and drug delivery, cavitation plays the key role. Proper acoustic agents and acoustic monitoring through passive cavitation detection (PCD) are thus crucial to ensure a safe and effective treatment outcome. Since the commercially available agents were designed for imaging purpose, their use in BBB opening and drug delivery often results in low delivery efficiency which is even more difficult for large molecules (> 1 kDa). In this chapter, acoustic agents with different properties including microbubbles and nanodroplets were designed and tested in mice, with PCD monitoring to assess their physical mechanisms for drug delivery. Three schemes were postulated with PCD monitoring of the efficacy and the safety to the cellular level evaluated.

1) The microbubble shell physiochemical properties
2) Fluorescently-tagged microbubbles as pseudo drug-loaded microbubbles
3) Acoustically-activated nanodroplets

Lipid-shelled microbubbles have been used in ultrasound-mediated drug delivery. The physicochemical properties of the microbubble shell could affect the delivery efficiency since they determine the microbubble mechanical properties, circulation persistence, and dissolution behavior during cavitation. Therefore, the first objective was to investigate the shell effects on drug delivery efficiency in the brain via BBB opening *in vivo* using monodisperse microbubbles with different phospholipid shell components. The physicochemical properties of the monolayer were varied by using phospholipids with different hydrophobic chain lengths (C16, C18, and C24). The dependence on the molecular size (3 kDa and 40 kDa dextran been delivered) and acoustic energy (both pressure and pulse length) were investigated. The different shelled microbubble dynamics *in vivo* were also captured during insonification using passive acoustic cavitation detection (PCD) in order to potentially uncover the physical mechanisms affecting the delivery efficiency such as micro-streaming and micro-jetting. The signal recorded by PCD is the acoustic emission from the cavitating bubbles, which represents the cavitation intensity with the signature of stable and/or inertial cavitation. Stable cavitation (bubble oscillation) and inertial cavitation (violent bubble oscillation to bubble collapse) relates to micro-streaming and micro-jetting, respectively [18], and both are thought to contribute to ultrasound-mediated drug delivery.

In the second scheme, microbubbles loaded with fluorophore 5-dodecanoylaminfluorescein (C-12) on the lipid shell through covalent bond were used as vectors for localized drug delivery into the brain, with PCD monitored for all the experiments to investigate the physical mechanisms. Although drug-loaded microbubbles have been widely used for targeted drug delivery [141-143], their physical mechanisms of delivery during sonication have not been investigated. These mechanisms could provide important information for the design of drug-loaded microbubbles.

Lastly, acoustically-activated nanodroplets were used as a new class of contrast agents to mediate FUS-induced BBB opening in order to study the feasibility of utilizing these nanoscale phase-shift particles for targeted drug delivery (3 kDa and 40 kDa dextran) in the brain. Customization of nanodroplets for the sensitivity to acoustic energy have been explored through modification on the boiling point of the perfluorocarbon liquid core. Again, PCD was used to monitor the vaporization and bubble activities and compared with the drug delivery results. Our findings offered a new means of developing the FUS-induced BBB opening technology for potential extravascular targeted drug delivery in the brain, extending the potential drug delivery region beyond the cerebral vasculature.

3.2 METHODS

3.2.1 Ultrasound System

The experimental setup, as shown in Fig. 3.1A, was used as previously described [78]. A single-element, ring-shaped focused ultrasound (FUS) transducer (center frequency: 1.5 MHz, focal depth: 60 mm; Imasonic, Besancon, France) was driven by a function generator (33220A; Agilent Technologies, Palo Alto, CA, USA) through a 50 dB power amplifier (325LA; E&I, Rochester, NY, USA). A pulse-echo transducer (center frequency: 10 MHz, focal length: 60 mm; Olympus NDT, Waltham, MA, USA) confocally and coaxially aligned with the FUS transducer was used for both targeting and passive cavitation detection (PCD) purposes. During the targeting procedure, the pulse-echo transducer was driven by a pulser receiver (Model 5800; Parametrics-NDT, MA, USA) in transmit-and-receive mode; while for PCD during sonication, it was switched in receive-

only mode with 20 dB of amplification. The signal was digitized in 50 MHz of sampling rate (CompuScope 1422, 14 bits; Gage Applied Technologies, Lachine, QC, Canada) and saved for offline processing.

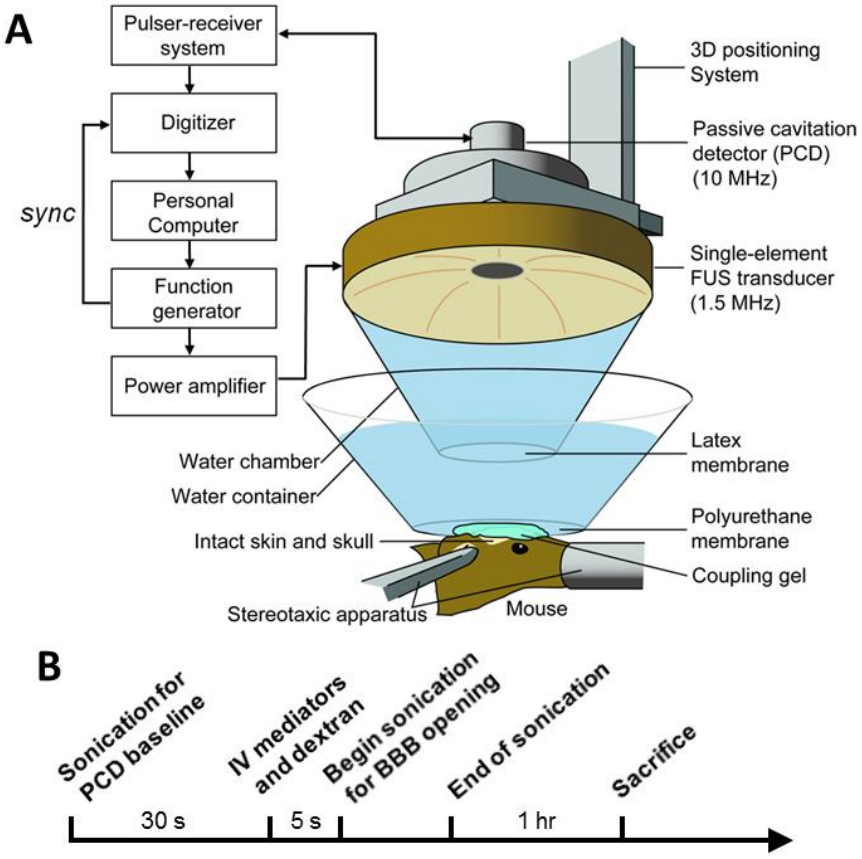

Figure 3.1. Experimental setup (A) and timeline (B) for FUS-induced BBB opening in mice *in vivo*. A focused ultrasound (FUS) transducer was used for sonication, while a pulse-echo transducer at the center of the FUS transducer was used for both targeting and passive cavitation detection (PCD) purposes. After the targeting procedure, a 30 s of sonication before microbubble injection was performed as a baseline control for PCD. The freshly diluted microbubble solution was then co-administered with dextran intravenously, and the sonication (1 min for microbubbles and 5 min for nanodroplets) for BBB opening started 5 s after injection. 1 hr after the end of sonication the mice was sacrificed using transcardial perfusion, and its brain was extracted and preserved for future processing.

The peak-rarefactional pressure profile used in the present study was estimated based on the calibration in degassed water with a bullet hydrophone (HGL-0400; Onda Corp., Sunnyvale, CA, USA), and the axial and lateral full-widths at half-maximum (FWHM) pressure of the focus were 10.6 mm and 1.3 mm, respectively. The pressure amplitudes were corrected to account for 18.1% attenuation through the murine skull as measured previously [89], and the derated peak-rarefactional pressure was reported in this study.

3.2.2 Generation and characterization of acoustic agents

3.2.2.1 Lipid-shelled microbubbles with various acyl chain lengths

All the lipids were purchased from Avanti Polar Lipids, Inc. (Alabaster, AL, USA), including 1,2-dipalmitoyl-sn-glycero-3-phosphocholine (DPPC or C16), 1,2-distearoyl-sn-glycero-3-phosphocholine (DSPC or C18), 1,2-dilignoceroyl-sn-glycero-3-phosphocholine (DLiPC or C24) and 1,2-distearoyl-sn-glycero-3phosphoethanolamine-N-[methoxy(polyethylene glycol)2000] (DSPE-PEG2000). The perfluorobutane gas (PFB, 99 wt% purity) used for microbubble generation was obtained from FluoroMed (Round Rock, TX, USA).

The lipid-coated microbubbles as shown in Fig. 3.2A were prepared at a 9:1 molar ratio of lipids and lipopolymers (DSPE-PEG2000). They were generated using the probe sonication method and size selected to 4-5 μm in diameter using differential centrifugation, as described elsewhere [134]. A Multisizer III particle counter (Beckman Coulter Inc., Opa Locka, FL, USA) with a 30-μm aperture was used to measure the microbubble size distribution (Fig. 3.2B-C) and concentration. The final size-isolated (4-5 μm) microbubble suspension was stored at 4 ºC till the

time of injection. All the microbubble samples used for this study were freshly prepared within 24 h to ensure experimental consistency.

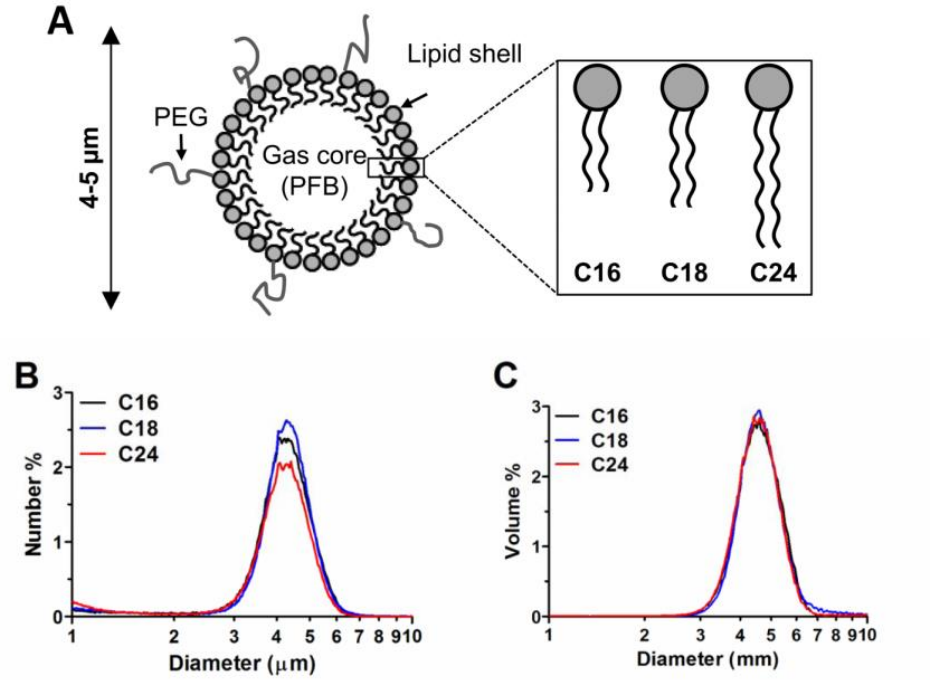

Figure 3.2. Schematic of the lipid-shelled microbubble used in this study (A) and their representative size distribution in number (B) and volume (C). Three different lipid acyl chain lengths (C16, C18, C24) were used to generate microbubbles of different physicochemical properties, while the emulsifier (DSPE-PEG2000), the molar ratio between the main lipid and the emulsifier (9:1), the gas core (PFB), and the size of the microbubbles (4-5 µm) were kept the same in order to focus on the effects of lipid hydrophobic chain length. The size of the different-shelled microbubbles was statistically the same. All microbubble suspensions were diluted to the same concentration (8×10^8 particle/mL) immediately prior to injection.

3.2.2.2 Fluorescently-tagged microbubbles

The fluorescent microbubbles were converted from the C18 microbubbles described previously with an addition of the lipophilic fluorescein probe, C-12 (Life technologies, Eugene, OR) (molecular weight 529.63 g/mol, maximum emission and excitation wavelengths 497±3 and 518±4

nm respectively) using a post-labeling technique. C-12 with a C_{12} alkyl chain (Fig. 3.3A) binds to the bubble shells with the fluorophore at the aqueous interface and the alkyl tail protruding into the lipid interior (Fig. 3.3B). C-12 was dissolved in pure ethanol at a concentration of 10 mM and put in direct contact with the microbubbles. Due to its amphiphilic nature, direct contact with the C-12 solution led to microbubbles binding to it. To allow the diffusion of C-12 to all the bubbles, the 1-mL syringe containing the suspension of microbubbles plus C-12 was incubated during two hours while it was rotated at 40 rpm. The size distribution and concentration of the fluorescent microbubbles were determined again with the Coulter Counter Multisizer III. Fig. 3.3C illustrates the appearance of the fluorescent microbubbles. It is clear that all the fluorescence is concentrated on the lipid shell.

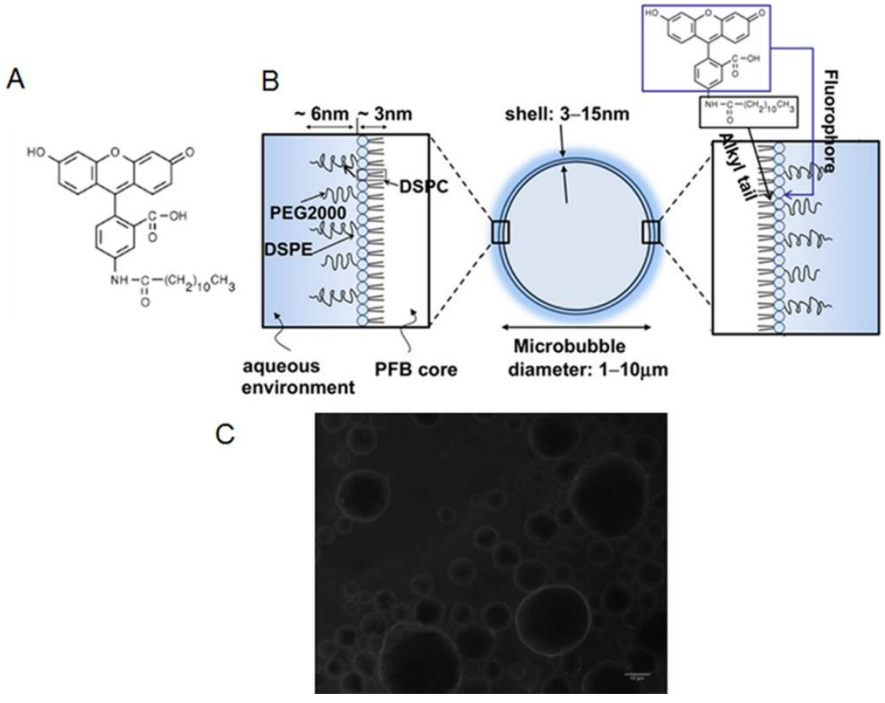

Figure 3.3. Fluorescently-tagged microbubble structure. (A) Molecular structure of 5-dodecanoylaminofluorescein (C-12). (B) Cartoon showing how the C-12 alkyl tail protrudes into the microbubble lipid shell converting the microbubble into a fluorescent drug carrier. (C) Epi-fluorescence image of a fluorescent microbubble sample. C-12 did not enter the core of the microbubbles; all the fluorescence is located at the lipid shell. The scale bar corresponds to 10 µm.

3.2.2.3 Nanodroplets

Through the condensation process with microbubbles (Fig. 3.4A), perfluorocarbon droplets with two different boiling-point gases (octafluoropropane or OFP: −36.7 °C, decafluorobutane or DFB: −1.7 °C) (FluoroMed, Round Rock, TX, USA) were fabricated as previously described [108, 144]. Briefly, 1,2-distearoyl-sn-glycero-3-phosphocholine (DSPC) and 1,2-distearoyl-sn-glycero-3-phosphoethanolamine-N-[methoxy(polyethylene glycol)2000] (DSPE-PEG2000) (Avanti Polar Lipids, Alabaster, AL, USA) were combined in a 9:1 molar ratio and dissolved in a phosphate-buffered saline (PBS)-based excipient solution containing 15% (v/v) propylene glycol and 5% (v/v) glycerol for a final lipid concentration of 1.0 mg/mL. The resultant lipid solution (1.5 mL) was added to 3 mL glass vials, and the headspace air was exchanged with OFP or DFB gas. Followed by vigorous shaking of the lipid-filled vials, precursor microbubbles were formed using a Vialmix mixer (Bristol-Myers-Squibb, New York, NY, USA). The nanodroplets were then generated via microbubble condensation under reduced temperature and increased ambient pressure. Vials of microbubbles were immersed in an isopropanol/CO_2 bath maintained between -8°C and -13°C for approximately 2 minutes. The vials were then attached to an adjustable pressure source, and the headspace pressure was increased until condensation was observed.

The size distribution and concentration of nanodroplets (Fig. 3.4B) were measured using a Malvern NanoSight NS500 (Malvern, Worcestershire, UK) in comparison to their precursor microbubbles (Fig. 3.4C). This instrument measures nanoparticle size based on their Brownian motion and is able to detect particles between 30 and 2000 nm. Number weighted size distributions and particle concentrations were measured for three vials of OFP- and DFB-filled nanodroplets.

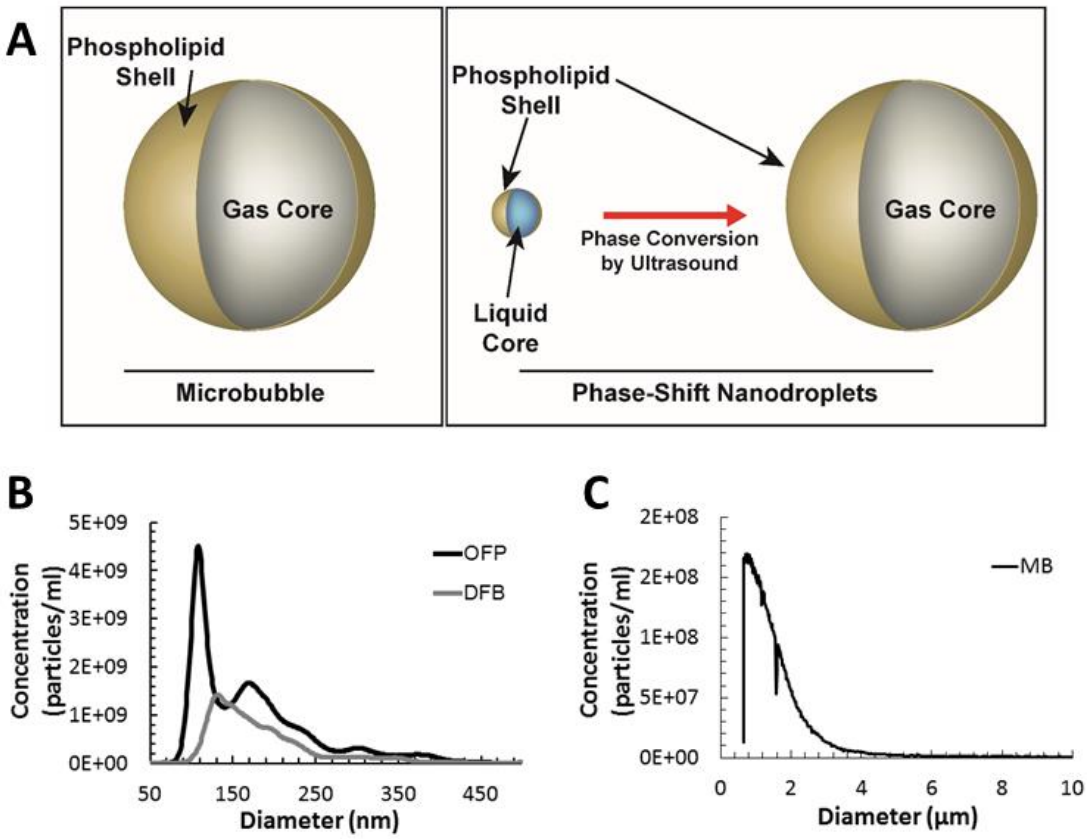

Figure 3.4. Nanodroplet characteristics. (A) Schematics of phase-shift nanodroplets through condensation process using microbubbles. The average size distribution of (B) the nanodroplets and (C) their precursor microbubbles. The average concentration and the median size for DFP droplets were 2.8×10^{11} particles/mL and 171 nm, respectively; those for DFP droplets were 1.3×10^{11} particles/mL and 183 nm, respectively.

3.2.3 In vitro experiments using high-speed camera

Droplet vaporization characteristics including the pressure threshold and relative vaporization efficiency (i.e., number of bubbles generated with given acoustic parameters in the measurement field per nanodroplets) were investigated in vitro using a previously described high-speed optical microscopy setup [78]. Briefly, an inverted microscope with a 100X objective (Olympus IX71; Center Valley, PA, USA) was mounted with a water bath filled with degassed water at 37°C and interfaced with an ultra-high-speed framing camera (20 million fps with 24-frame buffer, SIMD24;

Specialised Imaging, Simi Valley, CA) to study the vaporization threshold or a high-speed camera (1000 fps, FastCam SA1.1; Photron Inc., San Diego, CA, USA) to study the vaporization efficiency. A spherically focused transducer (A305S; Panametrics, Inc., Waltham, MA, USA) with a focal size of 0.75 mm laterally and 2 mm axially was used to activate the droplets by sending 1.5-MHz, 50-cycle sinusoidal pulses at 150-900 kPa driven by an arbitrary waveform generator (AWG 2021; Tektronix, Inc., Beaverton, OR, USA) through a RF amplifier (A500; ENI, Rochester, NY, USA).

Before the experiment, the transducer focus was calibrated and aligned with the optical focus using a calibrated needle hydrophone (HNA-0400; ONDA Corp., Sunnyvale, CA, USA). The hydrophone at the center of focus was then replaced with a nearly optically and visually transparent microcellulose tube (200 µm in diameter, Spectrum Laboratories INC., Greensboro, NC, USA), which was aligned with the microscope field of view using a micropositioner (MMO-203; Narishige Group, East Meadow, NY, USA). Nanodroplets (both OPF and DFB) were diluted by 50% in PBS and flowed through the microcellulose tube for visualization. At each sonication, a trigger pulse was transmitted from the waveform generator to the high-speed camera to allow synchronized video recording of the droplet vaporization events.

After the experiments, the videos for the behavior of nanodroplets vaporization was analyzed offline to determine the pressure threshold for consistent vaporization, and to count the number of bubbles generated in the microscope field of view (an estimate of vaporization efficiency). Bubbles were counted using a custom image processing code in MATLAB (Mathworks Inc., Natick, MA, USA) based upon a Hough transform for circle pattern recognition (Supplementary Fig. 1) [145, 146]. The lighting in the setup allowed for good contrast between the background and the formed bubbles (shown as black shadows). Although the bubbles were

formed in and out of imaging plane due to the stochastic nature of vaporization process, the use of the Hough transform for circle recognitions allowed for accurate identification of bubbles since the principal radius component was chosen through an ordered voting process. Bubbles vaporized within a finite width slice around the plane of focus of the camera were counted, while those completely out of focus become part of the background and were therefore not counted. Since this plane remained the same between OFP and DFB experiments, our quantification gave a relative vaporization efficiency between OFP and DFB nanodroplets activated *in vitro*.

3.2.4 In vivo mice experiments

Pulsed FUS (parameters summarized in Table 3.1) was applied transcranially to the targeted left hippocampus of the mouse brain while the right hippocampus served as the control without FUS. After the FUS transducer was aligned with the targeted region following the procedure described previously [89], the sonication procedure as illustrated in Fig. 3.1B was then followed. A 30 s of sonication was performed before microbubble injection as a baseline control for PCD. While at the same time the microbubble and dextran solution was prepared for the sonication with microbubble injection. The microbubble samples were freshly diluted to a final concentration of 8×10^8 bubbles/mL using sterile saline, and a 30 µL of the diluted microbubble suspension was co-administered with 50 µL dextran solution (40 kDa, fluorescently tagged with Texas Red, 40 mg/mL of weight concentration) via bolus injection through the tail vein 5 s prior to the start of sonication. Likewise, the nanodroplets (25 µL for OFP droplets and 100 µL for DFB droplets based on their concentration and vaporization efficiency difference) were co-injected with the same amount of dextran for the nanodroplets study. In addition, two sham cohorts without

sonication were injected with dextrans to serve as the basis for comparison of successful drug delivery in the fluorescence imaging analysis.

A 1-h period was allowed after sonication to enable the dextran to circulate throughout the vasculature and to diffuse into the brain parenchyma. At the end of the allotted time, the animal was sacrificed by transcardial perfusion using 30 mL phosphate buffer saline (PBS) for 5 min followed by 60 mL 4% paraformaldehyde for 8 min. The mouse brain was extracted from the skull, post-fixed in 4% paraformaldehyde overnight before sectioning for either fluorescence imaging or hematoxylin or eosin (H&E) staining in order to evaluate drug delivery efficiency and safety, respectively.

Table 3.1 Acoustic parameters used in each project.

Projects	**Acoustic agents**	**Pressure (kPa)**	**Pulse lengths (cycles)**	**PRF (Hz)**	**Duration (min)**	**Molecular size delivered (kDa)**
Microbubble shell	C16,C18,C24 microbubbles	225-600	100, 1000	5	1	3, 40
Fluorescent microbubbles	Fluorescently-tagged microbubbles	450-750	10000	5	5	-
Nanodroplets	DFB droplets, OFB droplets, Polydisperse microbubbles	150-900	10000	5	5	3, 40

3.2.5 Quantification of Acoustic Cavitation Emission

Three types of cavitation dose (SCD_h, stable cavitation dose using harmonics; SCD_u, stable cavitation dose using ultraharmonics; ICD, inertial cavitation dose) were quantified. First, each pulse of the PCD signal was calculated into the frequency spectrum in MATLAB (Mathworks Inc.,

Natick, MA, USA). Second, after taking the root mean square (rms) of the voltage spectral amplitude, the harmonic signal (n*f; n = 3, 4, 5, 6; f = 1.5 MHz; maximum amplitude within a bandwidth of 20 kHz around the harmonic frequency), ultraharmonic signal (n*f+0.5*f; n = 2, 3, 4, 5; f = 1.5 MHz; maximum amplitude within a bandwidth of 20 kHz around the ultraharmonic frequency), and the broadband signal in 3-9 MHz between them (applying a comb filter to suppress the harmonic and ultraharmonic signal with rejection bandwidths of 350 kHz and 100 kHz, respectively) were separately extracted. Third, the mean harmonic, ultraharmonic, and broadband signal were taken for each pulse and summed up over all pulses received during sonication to acquire SCD_h, SCD_u, and ICD, respectively. Lastly, the differential cavitation doses were computed by subtracting the normalized baseline cavitation doses (30s of sonication before microbubble injection). The cavitation doses reported in this study were the differential cavitation doses.

3.2.6 Fluorescence imaging and analysis for BBB opening and drug delivery

Followed by post-fixation process, the brains for delivery efficiency analysis were cryoprotected (30% of sucrose for 48 hr) and then sectioned horizontally using a cryostat (Leica RM2255; Leica Microsystems Inc., Buffalo, IL, USA) into 60-μm slices covering the hippocampi. The 60-μm frozen sections were used to quantify the relative fluorescence enhancement representing the ratio of dextran (in mass) been delivered to the targeted hippocampus through BBB opening relative to the contralateral hippocampus (unsonicated), since the dextran mass was kept constant for injection.

The epi-fluorescence images of the brain sections were captured for quantifying the fluorescence enhancement using an Olympus DP30BW digital camera mounted on an up-right

Olympus BX61 microscope (Melville, NY, USA). Briefly, a section representing the ventral-dorsal midline, as determined by anatomical landmarks, was first selected, and four adjacent sections were then selected on both the ventral and the dorsal side of the midline. The left (sonicated) and the right (unsonicated control) hippocampus were manually delineated using MATLAB (Mathworks Inc., Natick, MA, USA), and the fluorescence intensity increase as well as the BBB opening area in the region of interest (ROI) were calculated [147]. The relative fluorescence intensity increase was calculated by dividing the difference in fluorescence intensity between the left and the right ROIs (removing the auto-fluorescence) by the fluorescence intensity in the background (the spatial average of the background signal adding three times its standard deviation). For each brain, the reported fluorescence intensity increase was thus equal to the sum of all nine sections. The BBB opening area (intensity > background) was calculated as a percentage normalized to the sonicated ROI. A successful dextran delivery for an individual brain was concluded if both the fluorescence intensity increase and the BBB opening area were higher by two standard deviations relative to the average of the corresponding sham cohort.

3.2.7 Histological evaluation for safety

The histological examination for safety assessment of the entire hippocampi (both left and right) was performed via hematoxylin and eosin (H&E) staining, which can be used to identify damaged neurons (dark neurons showing shrunken and triangulated cell bodies) and red blood cell extravasations (hemorrhage) [148]. Followed by post-fixation process, the brains in the safety assessment study were paraffin-embedded and then sectioned horizontally into 6-μm slices with 180-μm gaps covering the hippocampi. The bright field images of the stained slices were captured using the same microscope as mentioned previously. This histological examination was double-

blinded, i.e., without knowledge of the microbubble type, the FUS exposure parameters, or the sonicated side.

3.3 RESULTS

3.3.1 Microbubble shell effects on drug delivery

Number of animals in each cohort is summarized in Table 3.2

Table 3.2 Summary of the experimental groups in the microbubble shell study**.**

Group	Microbubble	Dextran (kDa)	Pulse Length (#Pulses)	Number of mice per experimental condition				
				Acoustic pressure (kPa)				
				Sham	225	300	450	600
1	DPPC (C16)	3	10^2	-	3	3	3	4[a]
	DSPC (C18)			-	3	3	3	4[a]
	DLiPC (C24)			-	3	3	3	4[a]
2	DPPC (C16)	40	10^2	-	3	3	3	3
	DSPC (C18)			-	3	3	4	3
	DLiPC (C24)			-	3	3	3	3
3	DPPC (C16)	40	10^3	-	3	3	3	4[a]
	DSPC (C18)			-	3	3	3	4[a]
	DLiPC (C24)			-	3	3	3	4[a]
4	-	3	-	5	-	-	-	-
5	-	40	-	3	-	-	-	-

[a] Number shown including 1 mouse per experimental condition used for histology examination.

3.3.1.1 Drug delivery efficiency

Using fluorescently-labeled dextrans as model drug molecules, the delivery efficiency due to FUS-induced BBB opening could be quantified as the relative fluorescence enhancement in the sonicated hippocampus over the control. The two sham cohorts (Group 4 for 3-kDa dextran, Group

5 for 40-kDa dextran), for which no ultrasound was applied and no microbubbles were injected, did not show any change in fluorescence intensity between the two hemispheres (Suppl. Fig. 1). Quantified fluorescence enhancement results confirmed this observation as no detectable increase in fluorescence intensity between the two ROIs was acquired. For the rest of the 36 experimental conditions, the measured fluorescence enhancement was compared to their corresponding sham cohort in order to determine whether sufficient amount of dextran molecules were delivered to the targeted region. To study the shell effect on delivery efficiency with various drug molecule sizes, 3-kDa (Group 1) and 40-kDa (Group 2) dextrans were used as model drugs after FUS-induced BBB opening using 100-cycle (67 μs) pulses. To study the shell effect with various sonication pulse lengths, results of 100-cycle pulses (Group 2) and 1000-cycle pulses with 40-kDa dextrans (group 3) were compared.

Fig. 3.5 shows both the representative fluorescence images and the quantified enhancement results for Group 1 (3-kDa dextrans with 100-cycle pulses) after BBB opening. Due to the small molecular size, successful BBB opening was easily achieved at the lowest pressure level (225 kPa): 100% BBB opening efficiency was obtained for all mice regardless of the microbubble shell composition, with the exception of 1 mouse from the C24 microubbble/225 kPa cohort. The representative fluorescence images showed homogeneous dextran diffusion within the sonicated locations with a fluorescence signal detected not only within or near large vessels, but also diffusely distributed across the entire hippocampi as the pressure increased (Fig. 3.5C-D, G-H, K-L). However, the difference was found to be statistically insignificant between shells (Fig. 3.5M).

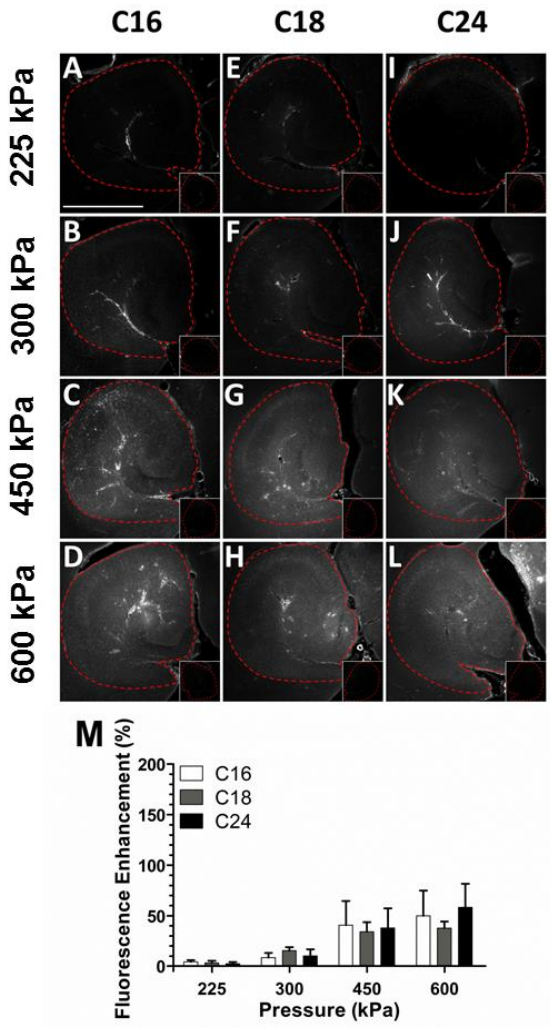

Figure 3.5. Effects of lipid hydrophobic chain length on delivery efficiency for 3-kDa dextran after FUS-induced BBB opening using 100-cycle (67 µs) pulses. (A-L) Representative fluorescence images comparing the targeted and the control (insets) hippocampi when C16, C18 or C24 microbubbles were used to mediate BBB opening at various pressures. The scale bar in A depicts 1 mm. (M) The quantified fluorescence enhancement between the sonicated and the control ROIs showed no significant shell effect on the 3-kDa dextran delivery across the BBB.

Fig. 3.6 shows the representative fluorescence images for Group 2 (40-kDa dextrans with 100-cycle pulses). Under the same acoustic exposures regardless of the microbubble shell type, BBB opening was obtained in 100% of the mice sonicated using pressures at or above 300 kPa. However, at the lowest pressure level (225 kPa), successful BBB opening was not consistently achieved: 1 out of 3 mice sonicated using C16 microbubbles and 2 out of 3 mice sonicated using C24 microbubbles did not show significant fluorescence enhancement. C16 microbubbles mediated the smallest dextran diffusion within the targeted hippocampi at all pressure levels. Moreover, the detectable dextran signal was predominantly contained within the blood vessels

even when some diffuse fluorescence enhancement within the targeted location was obtained as the pressure was increased above 300 kPa (Fig. 3.6C-D). On the other hand, significantly higher and more diffuse dextran distribution was induced using C18 and C24 microbubbles, especially at higher pressures (Fig. 3.6G-H, 3.6K-L). The quantified fluorescence analysis supported this finding (Fig. 3.6M). At 450 and 600 kPa, significantly higher 40-kDa dextran delivery was detected with both C18 and C24 microbubbles compared to C16 microbubbles. In addition, C24 microbubbles induced significantly more fluorescence enhancement at 600 kPa compared to C18 microbubbles.

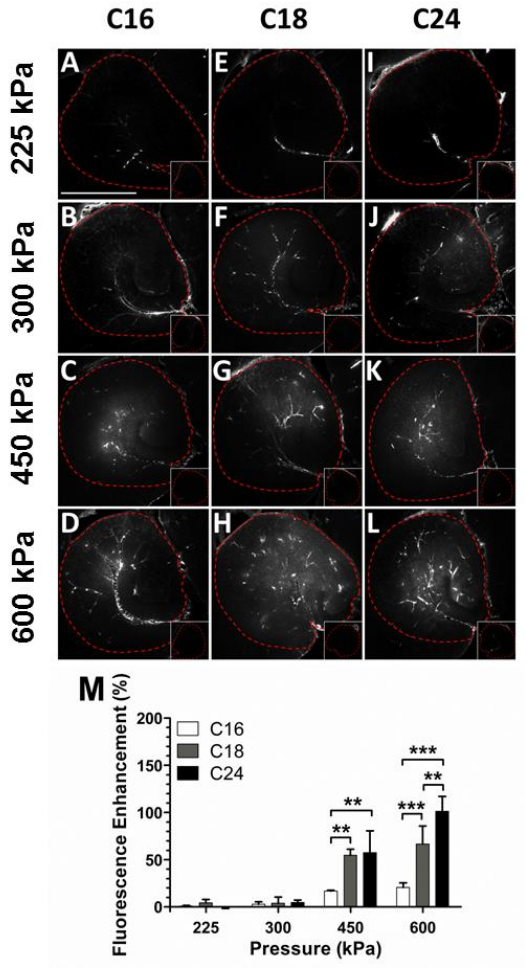

Figure 3.6. Effects of lipid hydrophobic chain length on delivery efficiency of 40-kDa dextran after FUS-induced BBB opening using 100-cycle (67 µs) pulses. (A-L) Representative fluorescence images compare the targeted and the control (insets) hippocampi when C16, C18 or C24 microbubbles were used to mediate BBB opening at various pressures. The scale bar in A depicts 1 mm. (M) The quantified fluorescence enhancement between the sonicated and the control ROIs showed significant shell effects on the 40-kDa dextran delivery across the BBB at higher pressures.

Fig. 3.7 shows the representative fluorescence images for Group 3 (40-kDa dextrans with 1000-cycle pulses). 100% BBB opening efficiency was obtained in all animals regardless of the microbubble lipid chain length. Based on the fluorescence images (Fig. 3.7A-L), in stark contrast with the 100-cycle BBB opening findings, the longer acoustic pulses produced significantly more homogeneous diffusion of the 40-kDa dextran, especially with the longer C18 and C24 acyl chain lengths. Punctate clusters of dextran were still visible within the vessels at all pressure levels. The quantified fluorescence enhancement results showed significantly more dextran accumulation within the targeted hippocampi after BBB opening using C24 microbubbles at 450 and 600 kPa (Fig. 3.7M). On the other hand, no statistical difference in dextran delivery was detected between the C16 and C18 microbubbles across all pressure levels.

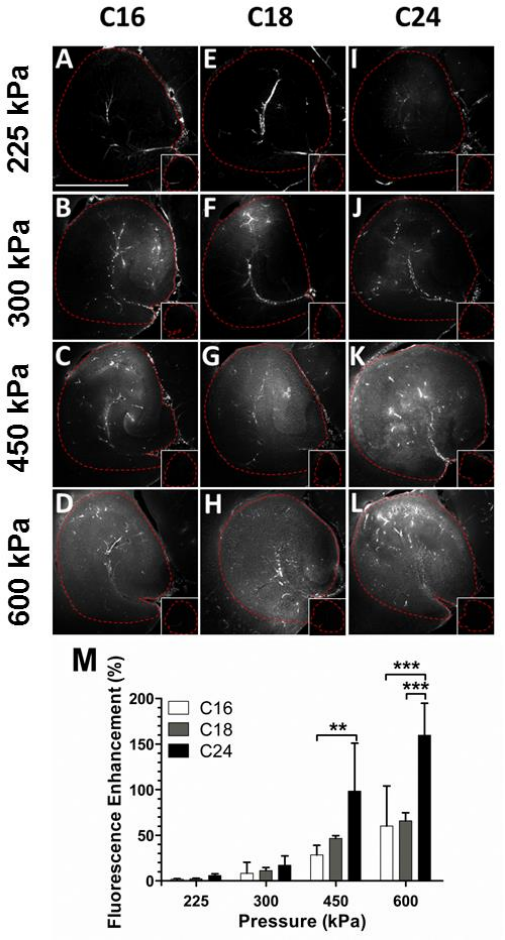

Figure 3.7. Effects of lipid hydrophobic chain length on delivery efficiency of 40-kDa dextran after FUS-induced BBB opening using 1000-cycle (670 µs) pulses. (A-L) Representative fluorescence images compare the targeted and the control (insets) hippocampi when C16, C18 or C24 microbubbles were used to mediate BBB opening at various pressures. The scale bar in A depicts 1 mm. (M) The quantified fluorescence enhancement between the sonicated and the control ROIs showed significant shell effects with C24 microbubbles on the 40-kDa dextran delivery across the BBB at higher pressures.

3.3.1.2 Acoustic cavitation emission

Three different types of cavitation dose (SCD_h, ICD, SCD_u) were separately quantified representing different bubble activities. Stable cavitation dose with harmonics (SCD_h) was for volumetric oscillation; inertial cavitation dose (ICD) identified drastic bubble oscillation and bubble collapse; stable cavitation dose with ultraharmonics (SCD_u) was thought to identify asymmetric oscillation and shell waves [70]. Fig. 3.8 shows the quantified acoustic cavitation dose during BBB opening using 100-cycle pulses (Fig. 3.8A-C) and 1000-cycle pulses (Fig. 3.8D-F). Using 100-cycle pulses, the SCD_h (Fig. 3.8A) for C18 and C24 was significantly higher than that of C16 at higher pressures, and the ICD and SCD_u for C24 was the highest (Fig. 3.8B-C). These results indicated that both C18 and C24 had stronger volumetric oscillation, and C24 had the strongest asymmetric oscillation potentially and bubble collapse over the others, corresponding to the 40-kDa dextran delivery efficiency in Fig. 4. By increasing the pulse length to 1000 cycles (Fig. 3.8D-F), the cavitation difference among shells was compensated at lower pressures except at 600 kPa where the cavitation dose for C24 was still the highest, corresponding to the 40-kDa dextran delivery efficiency in Fig. 3.7.

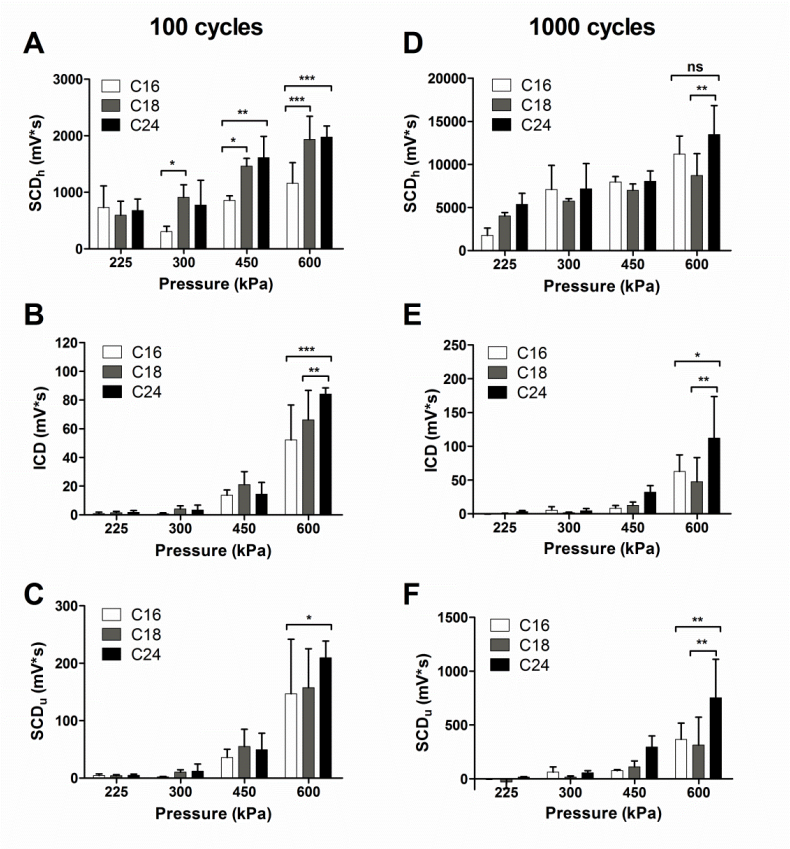

Figure 3.8. Quantified acoustic emission detected during BBB opening at various pressures and pulse lengths. For 100-cycle pulses, stable cavitation dose with harmonics (SCD_h) (A), inertial cavitation dose (B), and stable cavitation dose with ultraharmonics (SCD_u) (C) was calculated. The three types of cavitation dose for 1000-cycle pulses were also quantified (D-F).

3.3.1.3 Safety

Histological evaluation was performed in order to assess for potential tissue damage 1 hr after insonification. Fig. 3.9B shows the representative images obtained from all brain samples sonicated at the highest pressure (600 kPa). This pressure was selected since it represented the highest amount of exposed acoustic energy among all three groups. Examination at higher magnification did not reveal any discrete damage sites, such as clusters of dark neurons, small erythrocyte extravasations, hemorrhage or microvacuolations for brains sonicated with C16

microbubbles. While a few petechial hemorrhages were observed within the brain parenchyma sonicated with C18 microbubbles. The most discernible abnormalities occurred in the C24 microbubble cohorts, for which a larger degree of microscopic perivascular hemorrhages was detected. However, the damage to the brain parenchyma was negligible. The severity of all observed tissue damages was concluded to be Category 1 to 2 with Category 0 representing no damage based on the criteria provided by Hynynen *et al.* [149].

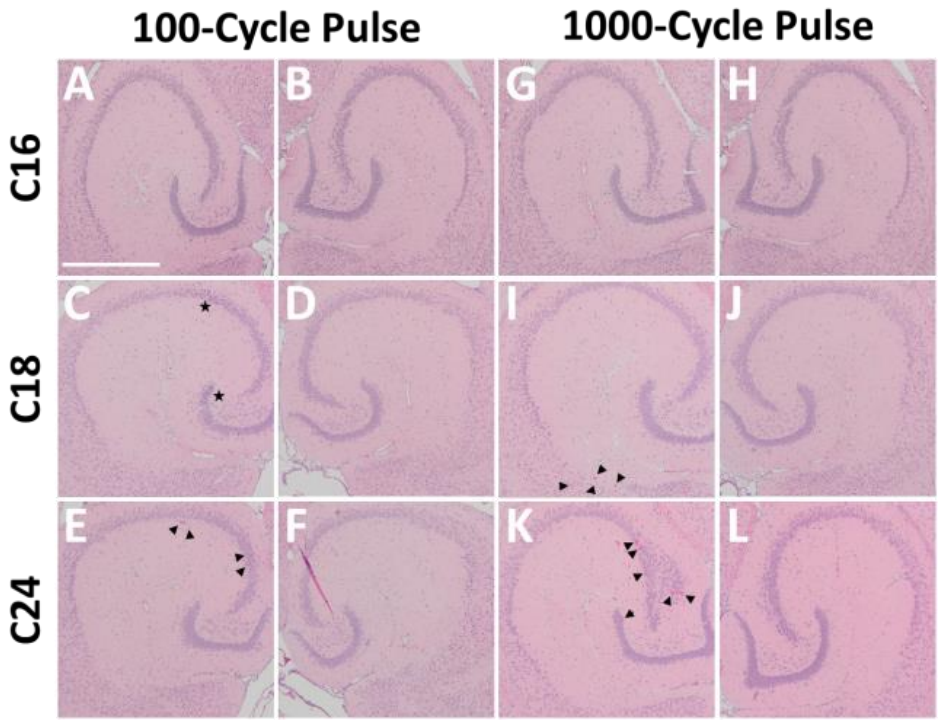

Figure 3.9. Representative histological images of the targeted (left) and control (right) hippocampi using 100-cycle (A-F) and 1000-cycle pulses (G-L) at 600 kPa. No erythrocyte extravasation, dark neurons, gross hemorrhage or microvacuolations were observed when C16 microbubbles were used to mediate BBB opening using either 100-cycle (A-B) or 1000-cycle (G-H) pulses. Small clusters of dark neurons (indicated with stars) were identified when C18 microbubbles were used with 100-cycle pulses (C-D), while a few petechial hemorrhages (indicated with triangles) were observed with 1000-cycle pulses (I-J). Larger degree of perivascular hemorrhages was seen with C24 microbubbles regardless of the pulse length (E-F, K-L). The scale bar in A depicts 1 mm.

3.3.1.4 Assessment of opening outcome using acoustic cavitation detection

The acoustic cavitation emission has been used to assess the drug delivery efficiency with acoustic responsive agents. In order to investigate whether the cavitation dose for different shelled microbubbles followed the same trend for assessing the BBB opening outcomes and drug delivery efficiency, both qualitative classification and quantitative analysis were performed as shown in Fig. 3.10. The total stable cavitation dose (SCD_{h+u}, sum of SCD_h and SCD_u) was adopted since it has been reported to correlate well with the drug delivery efficiency [78]. For the qualitative analysis (Fig. 3.10A), the SCD_{h+u} was separated into groups of no opening and opening based on the fluorescence results, and into groups of no damage and damage based on the histological findings. Despite the overlap, the SCD_{h+u} of the opening group was significantly higher than that of the no opening group for both 100-cycle and 1000-cycle pulses. The SCD_{h+u} of the no damage group was lower than that of the damage group. For quantitative analysis (Fig. 3.10B), the fluorescence enhancement was positively correlated with SCD_{h+u} for both 100-cycle and 1000-cycle pulses. The correlation curve of the SCD_{h+u} for different shelled microbubbles showed no difference.

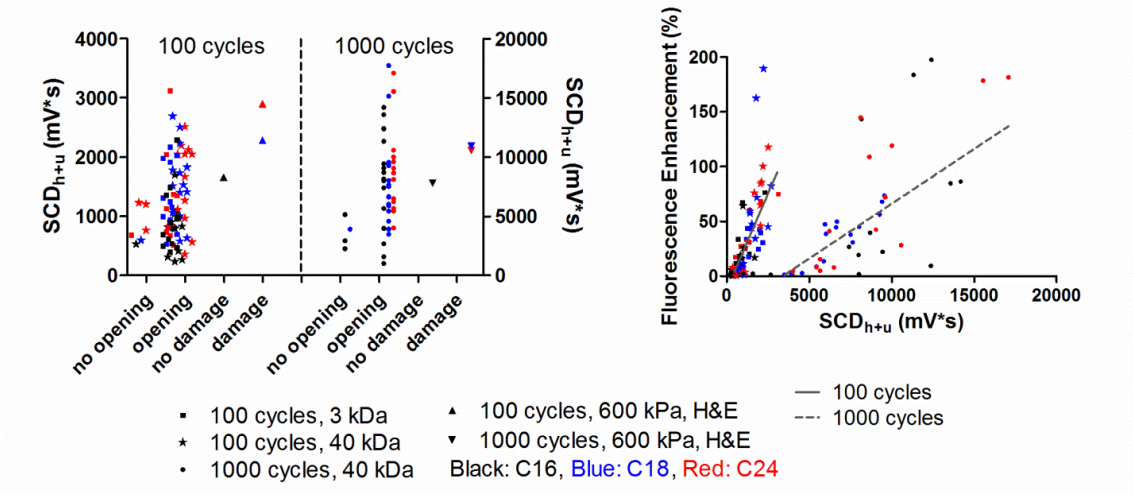

Figure 3.10. Using stable cavitation dose ($SCD_{h+u} = SCD_h + SCD_u$) to evaluate the opening outcomes qualitatively for classification (A) and quantitatively for delivery efficiency assessment (B). In the qualitative analysis (A), the SCD_{h+u} was separated into groups of no opening and opening (fluorescence enhancement was higher than the mean plus 2 times of standard deviation of the sham cohort), while based on the histological results it was separated into groups of no damage and damage (erythrocyte extravasation or dark neurons appeared). In the quantitative analysis (B), the fluorescence enhancement was positively correlated with the SCD_{h+u}, with a R^2 of 0.63 and 0.61 using linear fitting for 100-cycle pulses and 1000-cyle pulses, respectively.

3.3.2 Fluorescently tagged microbubbles for drug delivery

Table 3.3 summarizes the number of animals used in each experimental groups. BBB opening was validated with contrast-enhanced T1-weighted imaging (method described in Chapter 2.2), and all groups showed successful delivery. While the fluorescence enhancement was only successful at pressures of 600 and 750 kPa (Fig. 3.11), revealing a higher pressure threshold for drug delivery using drug-loaded microbubbles. The PCD monitoring showed that inertial cavitation was accompanied with cases of successful fluorescence delivery (Fig. 3.12). Therefore, disruption of microbubbles is crucial to for drug delivery using drug-loaded microbubbles.

Table 3.3 Summary of experimental groups and the fluorescence delivery results.

Group	**Pressure (kPa)**	**Successful BBB opening**	**Successful delivery**	**Fluorescence enhancement (A.U.)**
1	450	4/4	0/4	0
2	600	15/15	3/9	4.63 ± 2.58
3	750	6/6	3/5	8.99 ± 6.85

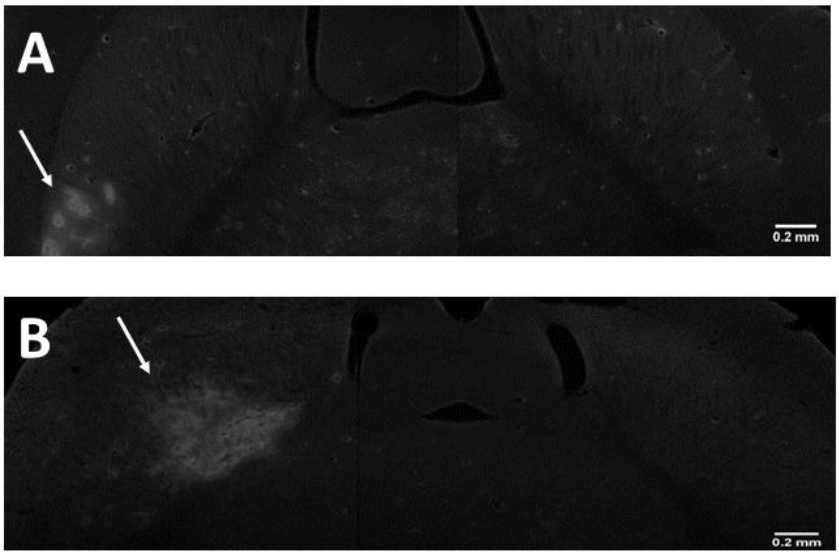

Figure 3.11. Fluorescence enhancement in the sonicated region showed successful drug delivery at (A) 600 kPa and (B) 750 kPa.

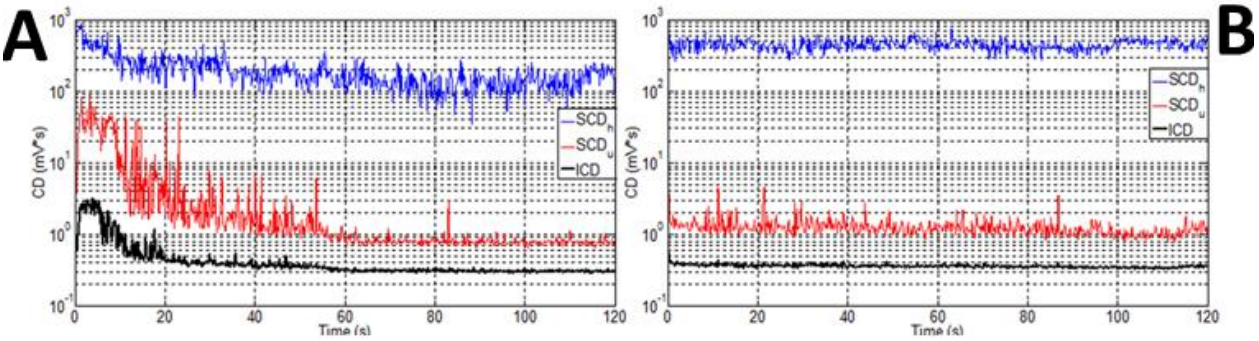

Figure 3.12. PCD monitoring of the cavitation doses in the cases of (A) significant and (B) insignificant fluorescence delivery.

3.3.3 Feasibility of drug delivery using Nanodroplets

Table 3.4 summarizes the number of animals used in each experimental groups.

Table 3.4. Summary of the experimental groups.

Group	Contrast agent	Number of mice per experimental condition [1]					
		Sham	Acoustic pressure (MPa)				
			0.15	0.225	0.30	0.45	0.60
1	DFB nanodroplet	6	6	6	7	7	8
2	Microbubble	5	7	7	7	7	7

[1] Number shown including up to 2 mice per experimental condition used for histology examination.

3.3.3.1 Nanodroplet vaporization threshold

In order to confirm the nanodroplets generated via microbubble condensation were acoustically vaporizable, high-speed optical microscopy was used to visually verify the vaporization of individual stationary droplets at pressures relevant to our *in vivo* experiment. Fig. 3.13 shows that at peak-rarefactional pressure of approximately 0.35 MPa, no detectable number of vaporized bubbles appeared within the focal plane. However, when the pressure amplitude was increased to 0.45 MPa, vaporized bubbles were observed almost immediately upon exposure to the ultrasound beam. These acoustically activated bubbles were within the micrometer size range and appeared to be acoustically responsive (i.e., they could expand and contract according to the pressure change during a single pulse). The activation of sub-micron droplets was also repeatedly observed at higher pressures (up to 1.1 MPa tested in the current study) using the *in vitro* setup, complementing our finding of the *in vivo* pressure threshold of BBB opening using nanodroplets (see discussion below).

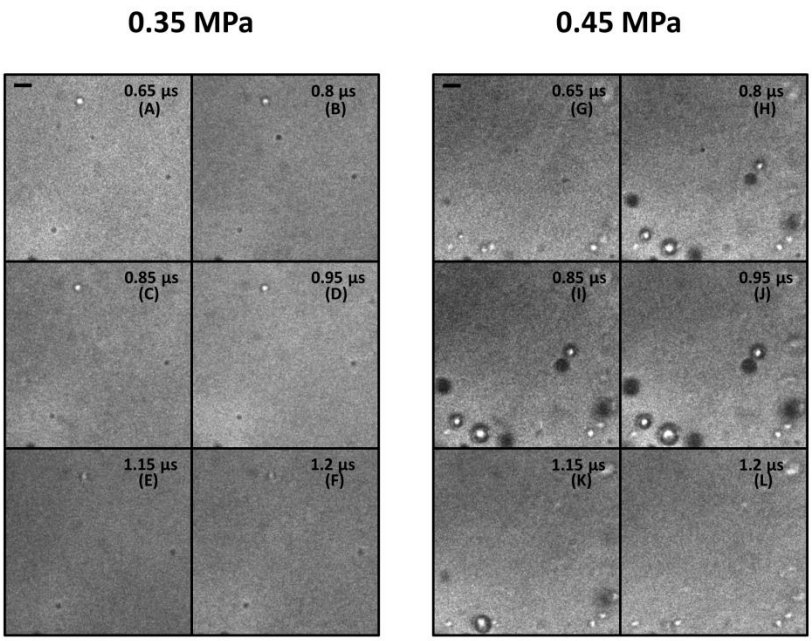

Figure 3.13. Still-frame images showing nanodroplet activation within the first two cycles of the pulse as a function of sonication pressure. Frames A-D and G-J were taken in the first rarefactional half-cycle, while E-F and K-L were taken in the following compressional cycle. No nanodroplet vaporization was detected at 0.35 MPa (left) while micron-scale acoustically-responsive bubbles were seen expanding in the rarefactional cycle at 0.45 MPa (G-J). When transitioned to the next positive pressure cycle (K, L), the newly formed bubbles were observed to respond to the acoustic pressure by compressing until no longer visible in the field of view. Times shown are relative to the start of the pulse, and the scale bars indicate 5 µm.

3.3.3.2 Delivery of small molecules

Using fluorescently-labeled 3 kDa dextran as a model drug molecule, the extent of the FUS-induced BBB opening could be quantified as the relative fluorescence enhancement in the sonicated hippocampus over the control. The two sham cohorts, for which no ultrasound was applied, did not show any change in fluorescence intensity between the two hemispheres. Quantified fluorescence enhancement results confirmed this observation as no detectable increase in fluorescence intensity between the two ROIs was calculated. For the rest of the 12 experimental conditions, the measured fluorescence enhancement was compared to their corresponding sham

cohort in order to determine whether sufficient amount of dextran molecules were delivered into the targeted region.

Following the systemic administration of nanodroplets and subsequent BBB opening, a significant increase in dextran delivery in the targeted ROI was observed at 0.45 and 0.60 MPa (60% opening efficiency with $P=0.047$ and 100% opening efficiency with $P=0.0002$, respectively) while only up to 33% of the animals evaluated showed a significant fluorescence enhancement when sonicated at pressures below 0.45 MPa. Due to the inconsistency across animals, there was no statistically significant ($P>0.56$) increase in fluorescence enhancement to clearly indicate BBB opening with dextran delivery for sonication pressures ranging between 0.15 and 0.30 MPa (Fig. 3.14A). At pressures above 0.45 MPa, fluorescence was observed not only within or near large vessels, but also diffusely distributed across the hippocampi (Figs. 3.15D and 3.15E).

Following the systemic administration of microbubbles and subsequent BBB opening, a significant fluorescence enhancement was detected for all mice when sonicated at pressures including and above 0.30 MPa ($P<0.0050$). A similar inconsistency of dextran delivery across animals was seen at 0.225 MPa that only 3 out of 5 mice showed significant fluorescence enhancement in the targeted ROI. Thus, no sufficient statistical difference ($P>0.16$) could be obtained to unequivocally show BBB opening at pressures below 0.30 MPa (Fig. 3.14B). The detectable fluorescence signal was predominately contained within vessels at 0.30 MPa but more diffusely distributed throughout the targeted region at 0.45 MPa, indicating a more homogenous distribution of dextran molecules (Figs. 3.15H and 3.15I). At 0.60 MPa, heterogeneous spots of particularly high levels of fluorescence in combination with diffusely distributed fluorescence was observed (Fig. 3.15J).

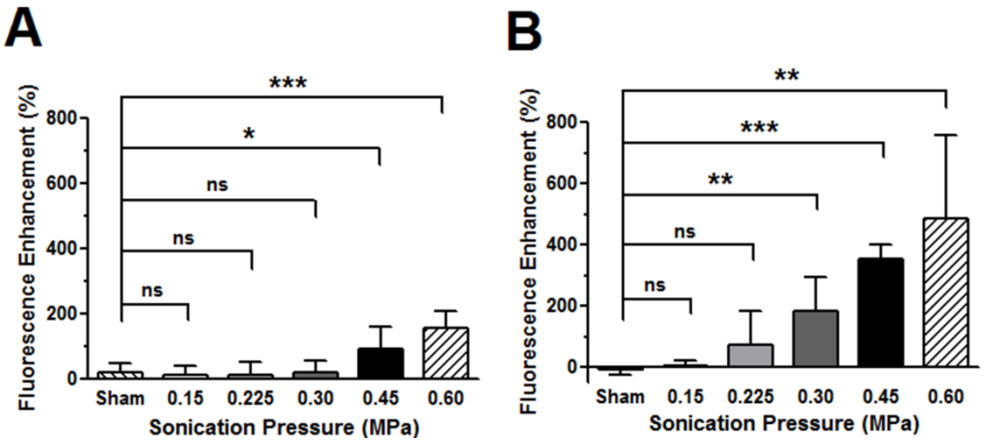

Figure 3.14. Normalized fluorescence enhancement between the targeted and the control hippocampi using either nanodroplets (A) or microbubbles (B) to mediate BBB opening at distinct sonication pressures. The normalized fluorescence enhancement with pressure followed a linear relationship with correlation coefficient R^2 being 0.76 and 0.94 for nanodroplets and microbubbles, respectively. Significant dextran delivery was observed at pressures higher than 0.45 MPa using nanodroplets while the BBB opening threshold was decreased down to 0.30 MPa when microbubbles were administered. All numbers are reported as mean ± standard deviation. (ns: not significant; *: P<0.05; **: P<0.01; ***: P<0.001)

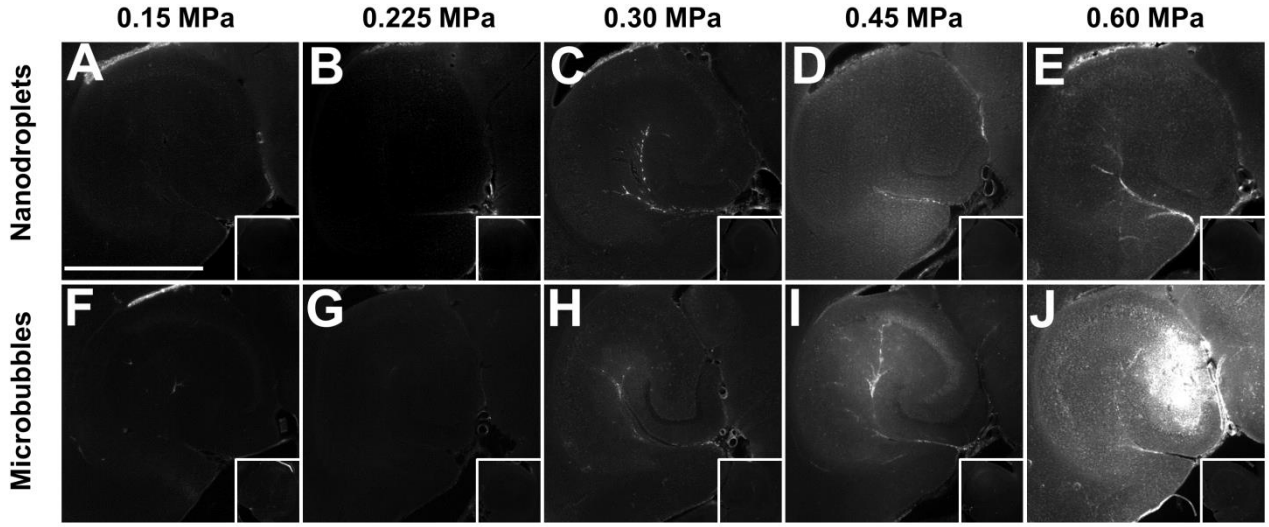

Figure 3.15. Representative fluorescence images comparing the targeted and the control (insets) hippocampi when nanodroplets (top) or microbubbles (bottom) were used to mediate BBB opening at various sonication pressures. The left hippocampus was sonicated in the presence of either nanodroplets or microbubbles and fluorescently-labeled 3-kDa dextran. Sonications were achieved at distinct peak-rarefactional pressures: 0.15 MPa (A&F), 0.225 MPa (B&G), 0.30 MPa (C&H), 0.45 MPa (D&I) and 0.60 MPa (E&J). The scale bar in A depicts 1 mm.

For each acoustic pressure, microbubbles produced greater fluorescence enhancement compared to nanodroplets. The normalized fluorescence enhancement with pressure amplitude followed a linear relationship with correlation coefficients at 0.76 and 0.94 for nanodroplets and microbubbles, respectively. The pressure threshold, at which significant fluorescence enhancement was detected in comparison to the sham animals, was higher for the nanodroplets (0.60 MPa) than that for the microbubbles (0.30 MPa), although the percent enhancement values at the threshold pressures were not statistically different (P=0.56).

3.3.3.3 PCD monitoring to assess drug delivery

Fig. 3.16 shows the quantitative acoustic emission results detected before and after the contrast agent administrations at various sonication pressures. For nanodroplets, the quantified SCD showed significant increase (P<0.0001) at 0.60 MPa (Fig. 3.16A), corresponding to the significant dextran delivery detected based on fluorescence microscopy. However, no statistical difference was determined at 0.45 MPa (P=0.21) despite a 90% mean signal increase after nanodroplet administration owing to the large variations among different mice. The SCD increase followed a linear relationship with the sonication pressure (R^2=0.99). The quantified ICD, on the other hand, showed no detectable inertial cavitation dose across all pressures (Fig. 3.16B), implying that no significant vaporized nanodroplet fragmentation was detected during sonication.

The acoustic emission results for the microbubble group are shown in Figs. 3.16C-D. Interestingly, the SCD showed significant increase (P<0.0005) for all pressure levels after microbubble injections regardless the outcome of the BBB opening (Fig. 3.16C). Similar to the nanodroplet group, the SCD increase followed a linear correlation with the FUS pressure amplitude (R^2=0.93). The ICD measurement showed significant signal increase after microbubble

injection at 0.60 MPa (P=0.017) but not at other pressure levels, indicating microbubbles underwent inertial cavitation during sonication only at the highest acoustic energy exposure (Fig. 3.16D).

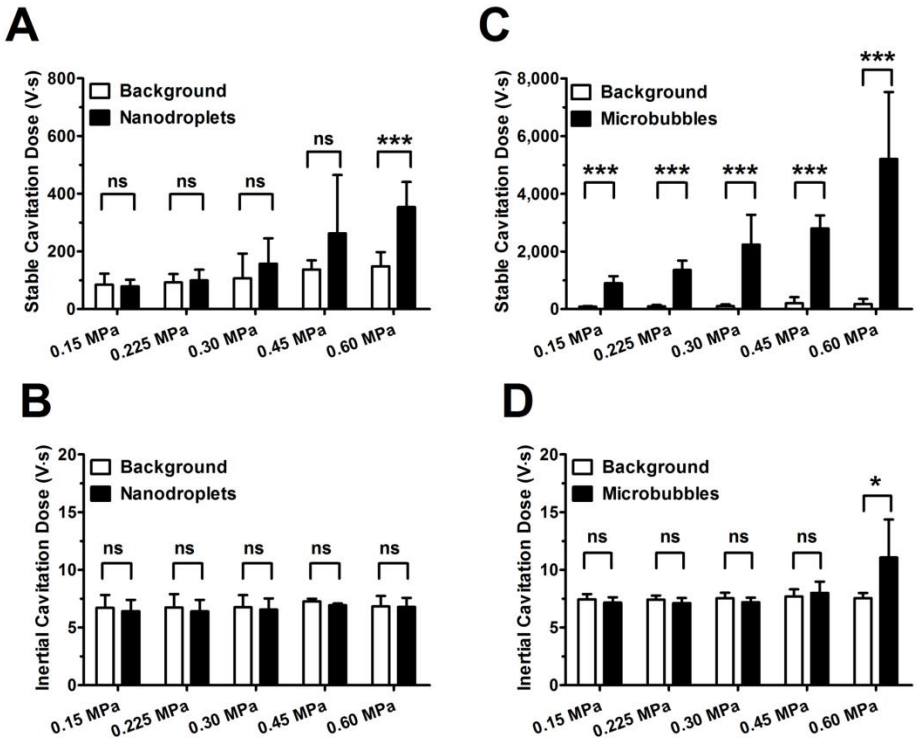

Figure 3.16. Quantified acoustic emission detected during BBB opening at various sonication pressures. Stable cavitation implied that vaporized nanodroplets or microbubbles underwent stable nonlinear oscillation during sonication, while inertial cavitation signified particle fragmentation. Significant SCD increase was detected after nanodroplet injection at the highest pressure level (A), but no significant ICD increase was measured (B). On the other hand, significant increase of SCD was detected for all pressures after microbubble administration (C), and ICD increase was detected at the highest acoustic exposure level (D). All numbers are reported as mean ± standard deviation. (ns: not significant; *: $P<0.05$; ***: $P<0.001$)

In order to test whether acoustic emissions could be used to predict the magnitude of the BBB opening, the relative fluorescence enhancement was plotted against the SCD for all sonications using each contrast agent (Fig. 3.17). Both agents showed relatively good linear correlations between these two parameters (R^2=0.74 for nanodroplets and R^2=0.67 for

microbubbles). A cavitation dose opening threshold can also be derived when SCD was grouped based on whether significant dextran delivery was detected based on fluorescence enhancement [150] (Fig. 3.18). For the mice sonicated in the presence of nanodroplets, a statistically higher ($P<0.0001$) stable cavitation emission was detected for cases where significant fluorescence enhancement was measured. The highest SCD value, at which no evidence of dextran delivery was detected, was 74 V·s. Out of the 10 animals that showed significant fluorescence increase, 3 mice (30%) had their SCD lower than 74 V·s, suggesting that this level could be used as the threshold for predicting successful FUS-induced BBB opening using nanodroplets as the contrast agents.

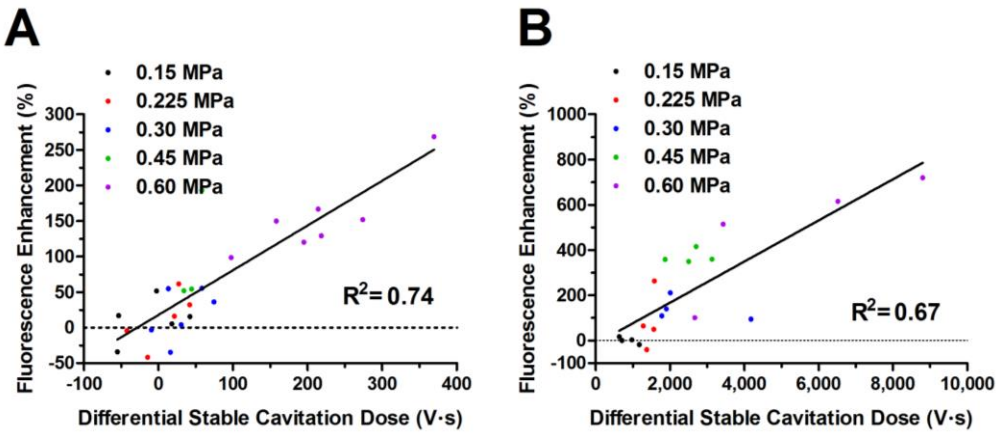

Figure 3.17. Correlation between differential stable cavitation dose (SCD) and fluorescence enhancement. The SCD was normalized based on the background emission signal measured prior to contrast agent injection. Linear correlations were obtained for both (A) nanodroplets ($R^2=0.74$) and (B) microbubbles ($R^2=0.67$).

Interestingly, the acoustic threshold of BBB opening appeared to be contrast agent dependent. For the microbubble group, the highest SCD value, for which no detectable dextran delivery was observed, was 1.4 kV·s, significantly higher ($P<0.0001$) than the SCD threshold found for the nanodroplet group. A much more prominent threshold was held for group #2, for 1

out of 15 mice (6.7%) with significant fluorescence enhancement had a SCD lower than 1.4 kV·s. Despite the wider range of the calculated SCDs, in which successful BBB opening was detected, a statistical difference was obtained (P=0.04) between cases with or without significant dextran delivery. The threshold for predicting FUS-induced BBB opening in the presence of microbubbles was therefore concluded to be 1.4 kV·s (Fig. 3.18).

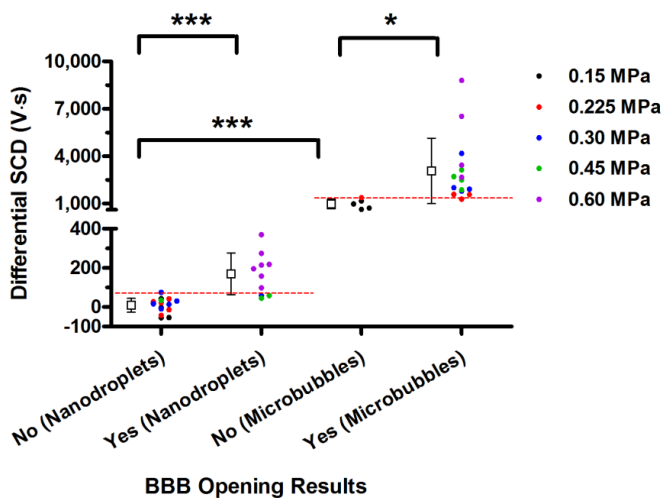

Figure 3.18. Stable cavitation dose (SCD)-indicated BBB opening threshold. The SCD was grouped based on whether significant dextran delivery was detected. Each individual brain was concluded to have significant BBB opening when the difference in fluorescence intensity between the sonicated and the control hippocampi was two standard deviations greater than the average value obtained for the corresponding sham group. Sonication using microbubbles as the contrast agents produced a much wider range of SCD values comparing to when nanodroplets were used. The SCD threshold for predicting BBB opening appeared to be contrast agent dependent. 7 out of 10 mice showed significant dextran delivery with SCD values greater than 74 V·s using nanodroplets while 92.3% of the animals showed significant dextran delivery at SCD above 1.4 kV·s using microbubbles. The slightly weaker threshold for the nanodroplet group indicated secondary mechanism other than cavitation could induce the BBB opening. (*: P<0.05; ***: P<0.001)

3.3.3.4 Safety

Histological evaluation was performed in order to assess for potential tissue damage caused by the procedure. Fig. 3.19 shows the bright-field microscopic images taken of representative brain samples at 0.45 and 0.60 MPa. These two pressure amplitudes were chosen since relatively consistent BBB opening was detected only at these pressure levels for both nanodroplet and microbubble groups. Close examinations did not reveal any discrete damage sites, such as clusters

of dark neurons, small erythrocyte extravasations, hemorrhage or microvacuolations at 0.45 MPa for either the nanodroplet or the microbubble group (Fig. 3.19 top). A few (<10) dark neurons were identified from 3 nonadjacent sections of the representative brain sample that was sonicated at 0.30 MPa using nanodroplets. No other tissue damage indicators were observed, indicating that this could be an artifact due to inadequate perfusion-fixation [151]. However, small clusters of extravasated erythrocytes in addition to a few dark neurons were observed for a sample from the microbubble/0.60 MPa cohort (Fig. 3.19O). Less than 10 clusters were found throughout the sonicated region across all sections, indicating minor tissue damage. The larger portion of the targeted hippocampus appeared to be normal and the neurons appeared to be unaffected (Fig. 3.19M).

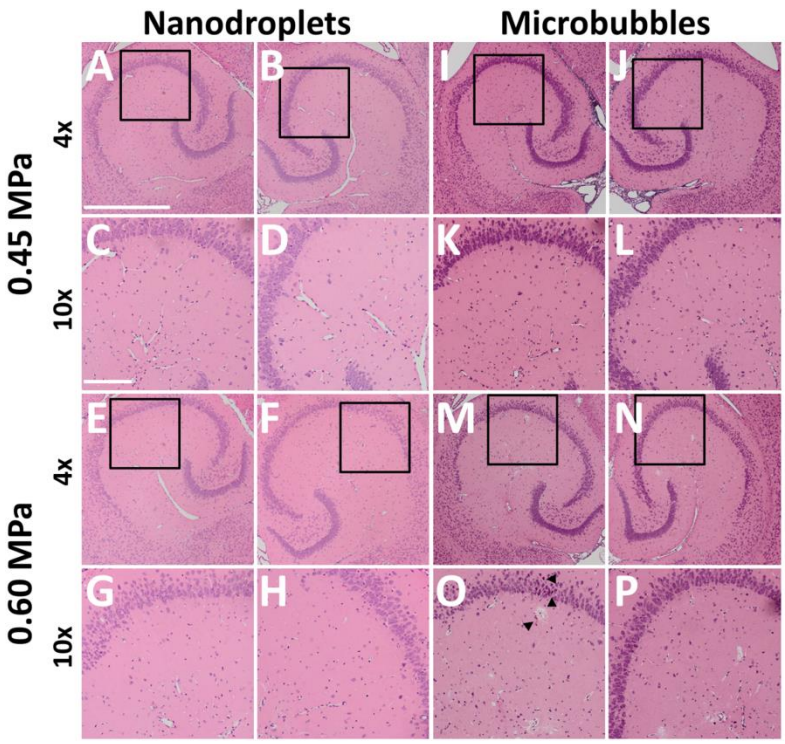

Figure 3.19. Representative histological images of the targeted and control hippocampi. The animals were sacrificed 1 h after sonication. (Left) No erythrocyte extravasations, dark neurons, gross hemorrhage or microvacuolations were observed when nanodroplets were used to mediate

BBB opening at either 0.45 MPa or 0.60 MPa. (Right) When microbubbles were used, erythrocyte extravasations or dark neurons were not seen at 0.45 MPa. However, small clusters of erythrocyte extravasations and a few dark neurons were observed (arrow heads in O), indicating minor damage, after sonication at 0.60 MPa. The boxed regions in all 4x images are further zoomed into 10x. The scale bars in A and C depict 1 mm and 100 μm, respectively.

3.3.4 Efficient drug delivery using highly-volatile nanodroplets

The number of animals in each cohort is summarized in Table 3.5.

Table 3.5. Summary of the experimental groups.

Group	Mediators	Number of mice per experimental condition					
		Sham	Acoustic pressure (kPa)				
			150	300	450	750	900
1	OFP droplets	4	3	7*	8*	-	-
2	DFB droplets	-	-	-	-	4	7*
3	Microbubbles	-	-	-	5	-	-

* Number shown including 3 mice per experimental condition used for histological examination.

3.3.4.1 Nanodroplet vaporization efficiency

Three different vials of each type of droplets were taken for measuring the size distribution and the concentration (Fig. 3.4B). The mean, median, and mode size of the OFP droplets were 171.2 nm, 153.3 nm, and 109.1 nm, respectively; those for the DFB droplets were 182.5 nm, 145.1 nm, and 163.4 nm, respectively. The average concentration for OFP droplets was 2.8×10^{11} particles/mL, and 1.3×10^{11} particles/mL for DFB droplets. The droplet distributions were polydisperse since they were condensed from polydisperse microbubbles.

In order to investigate the acoustic vaporization threshold and the relative vaporization efficiency for the droplets, the high speed camera with optical microscopy was used with a focused transducer exciting at the same excitation frequency and pressure as for the in vivo experiments.

As shown in the images before and after sonication (Fig. 3.20A-B), OFP droplets vaporized to microbubbles at pressures of 300 kPa and above, while DFB droplets required higher pressures for vaporization (600 kPa and above). On the other hand, the number of bubbles been vaporized were counted for estimating the nanodroplet vaporization efficiency. For OFP droplets, an average of 11±7 (mean ± standard deviation) bubbles were generated in the microscope field of view at 300 kPa. This was nearly doubled (25±7 bubbles) when the pressure was increased to 450 kPa. Qualitatively, we observed more bubbles being generated at even higher pressures (600-900 kPa) for OFP droplets. However, the number of bubbles formed from DFB droplets was lower, although the bubble size could be larger (>10 μm). On average, 0.4±0.7, 3±2, and 2±1 bubbles were generated at 600, 750, and 900 kPa, respectively. After normalizing with the nanodroplet concentration, the vaporization efficiency (number of bubbles formed in the microscope field of view divided by the concentration/10^{11}) was found to be higher for OFP droplets than for DFB droplets as shown in Fig. 3.20C.

Through *in vitro* experimentation, it was confirmed that more microbubbles were generated from OFP droplets compared to DFB droplets when using the relevant acoustic pressures for the same dilution factor. Therefore, OFP droplets were deemed as more efficient acoustic mediators. We hypothesized that a lower dose of OFP droplets (1/4 volume of the DFB droplets) would be sufficient for BBB disruption and drug delivery *in vivo* compared to DFB droplets.

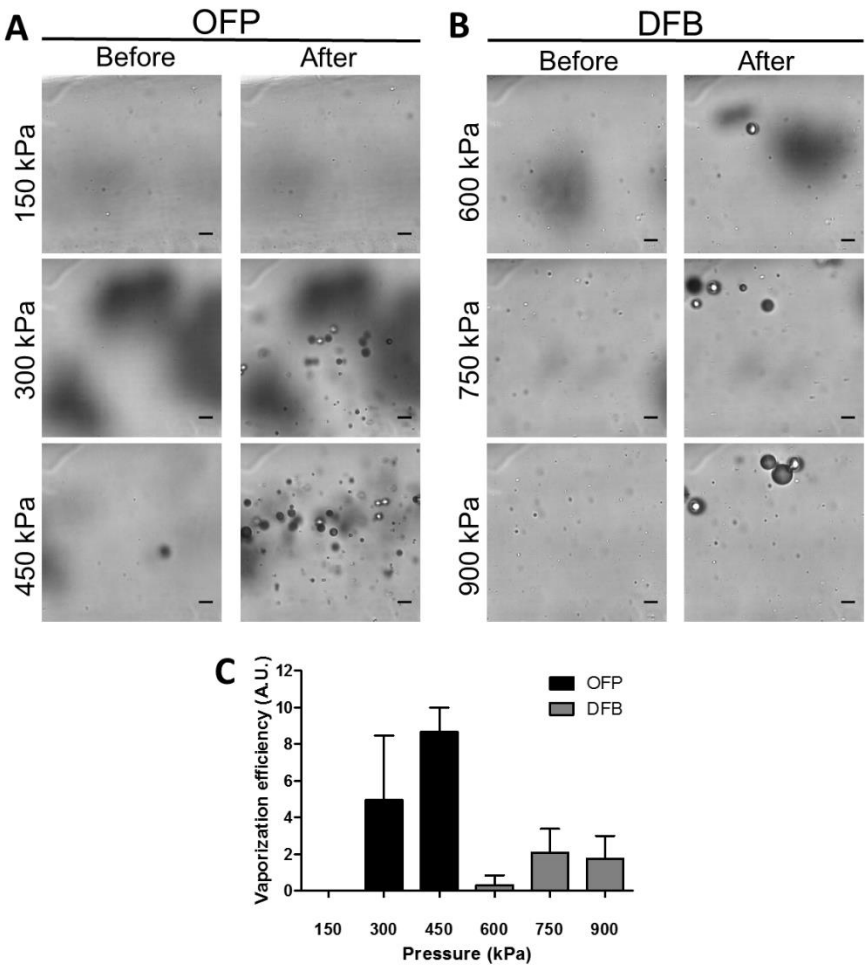

Figure 3.20. Detection of acoustic droplet vaporization using high-speed optical microscopy. (A) OFP-filled droplets were found to vaporize at pressures at and above 300 kPa, but not at 150 kPa. (B) DFB droplets were found to vaporize inconsistently at 600 kPa (vaporization did not occur with every activation pulse). Vaporization was consistently observed at 750 kPa and 900 kPa for DFB droplets. On average, more bubbles were generated from OFP droplets at low pressures (300-450 kPa) compared to those generated from DFB droplets at higher pressures (750-900 kPa). Scale bar represents 10 μm. (C) The vaporization efficiency defined as the number of bubbles formed in the field of view after normalized by the nanodroplets concentration was calculated. The vaporization efficiency of OFP droplets was higher than that of DFB droplets.

3.3.4.2 Delivery of large molecules

The *in vivo* drug delivery outcomes (40 kDa dextran) after BBB opening were quantified with fluorescence microscopy comparing the fluorescence enhancement in the sonicated hippocampus

to the contralateral side (Fig. 3.21). With the OFP droplets, successful delivery was found to be at 300 kPa (75%, 3 out of 4 mice)(Fig. 3.21A) and 450 kPa (100%, 5 out of 5 mice)(Fig. 3.21B), and no delivery for the 150 kPa group (0 out of 3 mice). Similar to OFP droplets at 450 kPa, 100% of successful delivery (5 out of 5 mice) was achieved using microbubbles at 450 kPa (Fig. 3.21C). For the DFB droplets, successful delivery was found to be at 900 kPa (100%, 4 out of 4 mice) (Fig. 3.21D), whereas no delivery was detected at 750 kPa (0 out of 4 mice). As shown in the stacked images, the 40-kDa dextran was delivered locally over the entire sonicated hippocampi for both OFP droplets at 450 kPa (Fig. 3.21E), microbubbles at 450 kPa (Fig. 3.21F), and DFB droplets at 900 kPa (Fig. 3.21G), with the opening area similar to the FUS focal size (1.3 mm laterally and 10.6 mm axially).

The quantitative results showed similar results for OFP droplets at 300 kPa to DFB droplets at 900 kPa ($p>0.05$), and for OFP droplets to microbubbles at 450 kPa ($p>0.05$) in both the area of BBB opening (Fig. 3.21H) and the fluorescence intensity increase (Fig. 3.21I). Thus, the pressure required for same amount of delivery using OFP droplets was 2-3 times lower than that using higher dosage of DFB droplets, which corresponded to the vaporization measurement detected in vitro. Furthermore, OFP droplets could achieve the same delivery outcomes as the microbubbles in a relatively smaller region based on the fluorescence intensity increase.

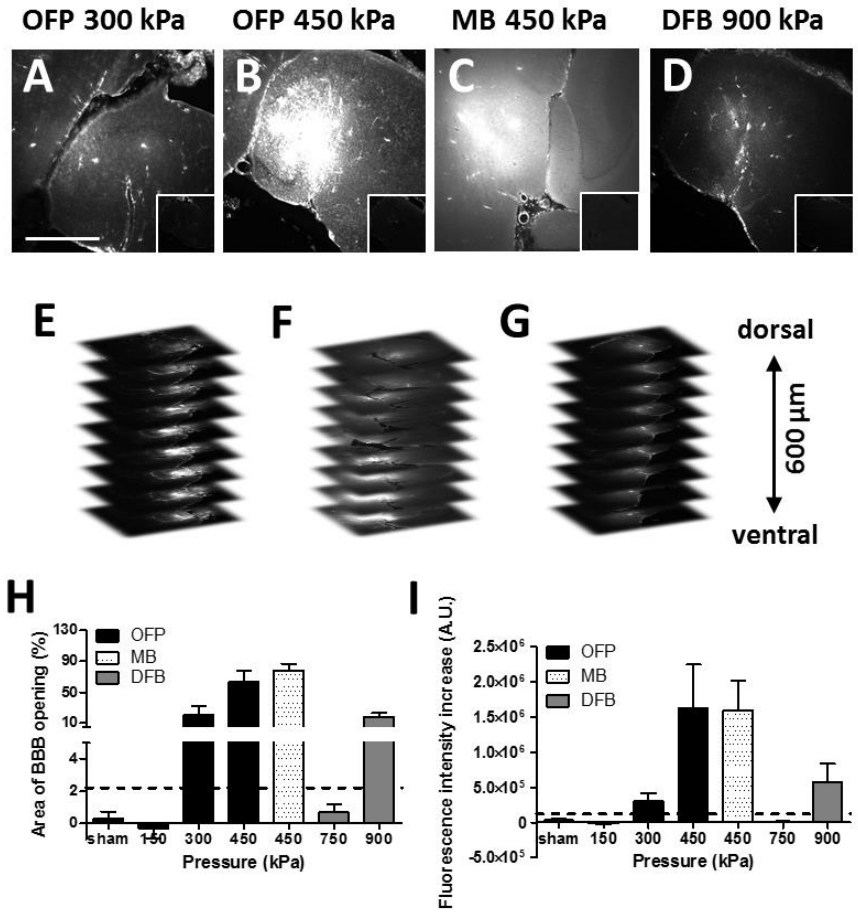

Figure 3.21. Delivery efficiency (40 kDa dextran) using fluorescence microscopy after BBB opening. Fluorescence images of sonicated vs. non-sonicated hippocampi (insets) using (A) OFP droplets at 300 kPa, (B) OFP droplets at 450 kPa, (C) microbubbles at 450 kPa, and (D) DFB droplets at 900 kPa. The stacked slices showed localized delivery across the entire sonicated hippocampi for (E) OFP droplets at 450 kPa, (F) microbubbles at 450 kPa, and (G) DFB droplets at 900 kPa. (H) The mean BBB opening area (normalized to the entire hippocampus) and (I) mean fluorescence intensity increase for all cohorts, with a dash line representing the threshold of successful delivery defined by the sham group (mean plus 2 time of the standard deviation). Successful delivery was found to be at and above 300 kPa for OFP droplets, and 900 kPa for DFB droplets.

3.3.4.3 PCD monitoring to assess drug delivery

Transcranial cavitation monitoring was performed in all experiments in order to investigate the behavior of droplet vaporization and cavitation determining drug delivery and safety.

Representative monitoring findings from the six cohorts were shown in Fig. 4 after nanodroplets or microbubble injection. The left panel represented the temporal variation of frequency spectra in the beginning 0.3 ms of the first pulse, and the right panel showed the evolution of the stable (SCD_h with harmonics and SCD_u with ultraharmonics) and inertial (ICD) cavitation level during the entire sonication. In the cases with significant dextran delivery (Fig. 3.22B, C, D, F for OFP at 300 kPa, OFP at 450 kPa, microbubbles at 450 kPa, and DFB at 900 kPa, respectively), the cavitation events for SCD_u, and ICD were significantly more frequent with higher intensity compared to the cases without delivery (Fig. 3.22A, E for OFP at 150 kPa and DFB at 750 kPa, respectively).

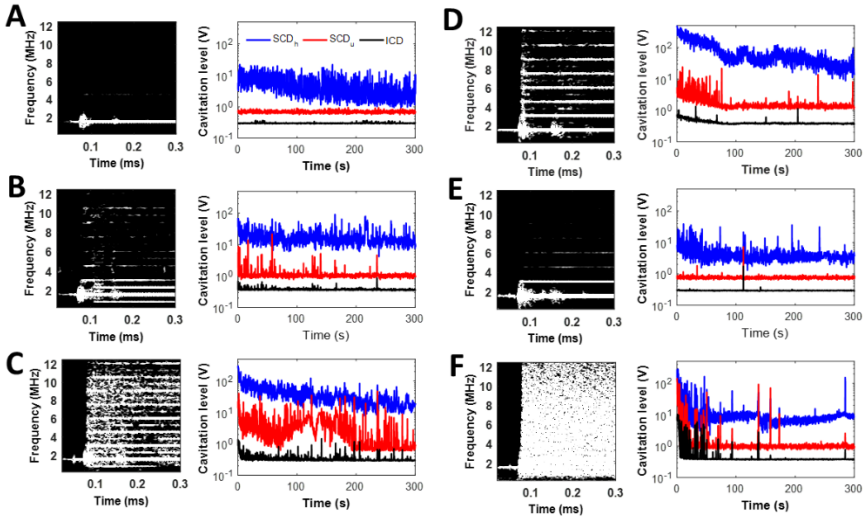

Figure 3.22. Passive cavitation detection during the sonication for BBB opening, with the cavitation evolution within a pulse (spectrograms) and within the whole sonication duration (cavitation level for stable cavitation dose SCD_h, SCD_u, and inertial cavitation dose ICD) shown on the left panel and the right panel, respectively. (A) OFB droplets at 150 kPa without delivery. (B) OFP droplets at 300 kPa with delivery. (C) OFP droplets at 450 kPa with delivery. (D) Microbubbles at 450 kPa with delivery. (E) DFB droplets at 750 kPa without delivery. (F) DFB droplets at 900 kPa with successful delivery. Strong and abundant cavitation events including both stable and inertial cavitation were observed in cases with successful delivery (B, C, D, F).

The overall cavitation dose representing the accumulative cavitation intensity for each sonication was calculated and shown in Fig. 3.23. For the OFP droplets, the SCD_h was significantly

higher at pressures with successful dextran delivery; the significantly higher SCD_u appeared only at the pressure causing higher amount of delivery (450 kPa); whereas the ICD showed no significance. Similarly, microbubbles at 450 kPa showed significantly higher SCD_h and SCD_u with insignificant ICD. For DFB droplets, although the SCD_h was insignificant due to the low volumetric bubble oscillation at high pressures, the SCD_u and the ICD showed statistical significance at 900 kPa with successful delivery. Interestingly, although the SCD_h for microbubbles was much higher than that for droplets, the SCD_u was at the same level or even slightly lower. Since both types of the stable cavitation dose was detectable for OFP droplets, their sum ($SCD_{h+u} = SCD_h + SCD_u$) was then plotted against the area of BBB opening (Fig. 3.23D) as well as the fluorescence intensity increase representing the delivery efficiency (Fig. 3.23E). In both of them, good agreement ($R^2 = 0.74, 0.92$) was found in cases of successful delivery, similar to the DFB droplets [78].

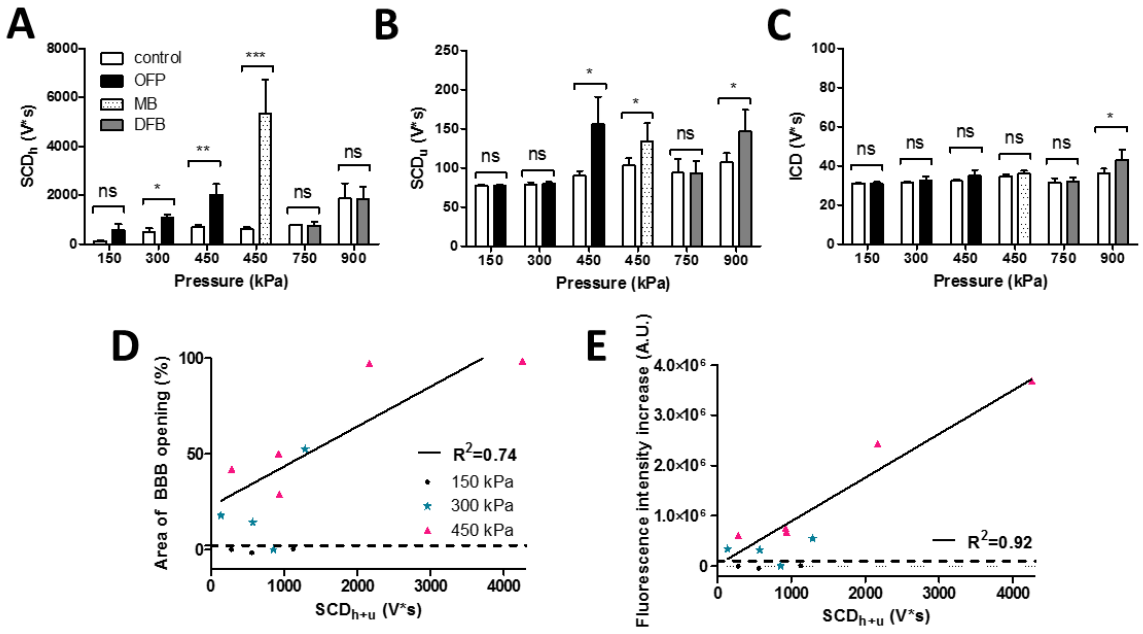

Figure 3.23. Cavitation dose of the entire sonication. (A) SCD_h or stable cavitation dose with harmonic emissions. (B) SCD_u or stable cavitation dose with ultraharmonic emissions. (C) ICD or inertial cavitation dose with broadband emissions. (D) The area of BBB opening and (E) the

fluorescence intensity increase using OFP droplets was linearly correlated with the total stable cavitation dose (SCD_{u+h} = SCD_h + SCD_u) for the cases with successful delivery. The dash line represents the threshold of successful delivery defined by the sham group (mean plus 2 times of the standard deviation).

3.3.4.4 Safety

The histological (H&E) staining was performed in the cohorts with successful delivery (3 mice from each group: OFP at 300 kPa, OFP at 450 kPa, DFB at 900 kPa) in order to assess the potential tissue damage occurred 1 h after sonication (Fig. 3.24). The results showed no damage, i.e., no red blood cell extravasations or dark neurons, using OFP droplets at the pressures leading to successful delivery for all the animals (Fig. 3.24A-D). These results indicate a safe and effective drug delivery for relatively large molecules that could be achieved using OFP droplets. For DFB droplets at 900 kPa, 2 out of 3 animals showed no damage while 1 had more dark neurons on the treated hippocampus (Fig. 3.24E-F), which was corresponded to the statistically significant inertial cavitation during sonication (Fig. 3.23C).

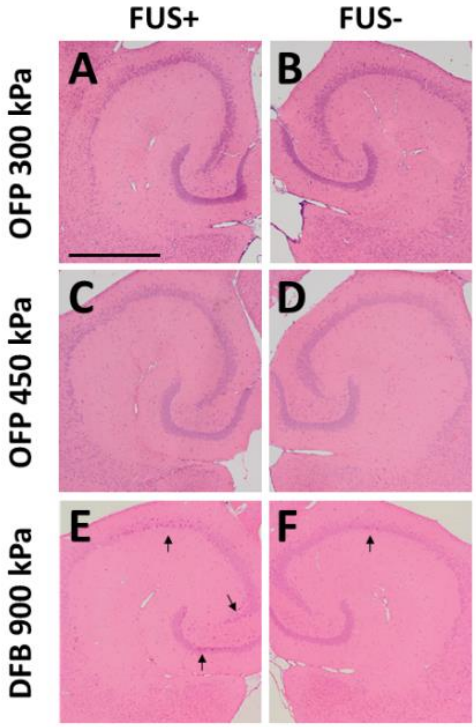

Figure 3.24. Safety assessment using histological staining (H&E). Sonicated (A, C, E) and nonsonicated (B, D, F) hippocampi using OFB at 300 kPa (A, B), 450 kPa (C, D), and DFB at 900 kPa (E, F). The results showed no damage (erythrocyte extravasations or dark neurons) using OFP droplets. For DFB droplets at 900 kPa, only 1 out of 3 animals showed an increased amount of dark neurons on the hippocampi. The scalebar in (A) represents 1 mm.

3.3.4.5 Extravascular delivery of fluorescently-tagged nanodroplets

Fluorescently-tagged nanodroplets were used for BBB opening and delivery (Dil OFP, 4 mice), and for drug delivery after BBB opening with OFP droplets (OFP + Dil OFP, 4 mice) at 450 kPa. As shown in Fig. 3.25, there were slightly more fluorescence enhancement in the sonicated side in the OFP+Dil OFP group, while no statistical significance was found. It could be due to the size of OFP droplets (a mean diameter of 171.2 nm) requiring a higher pressure for delivery.

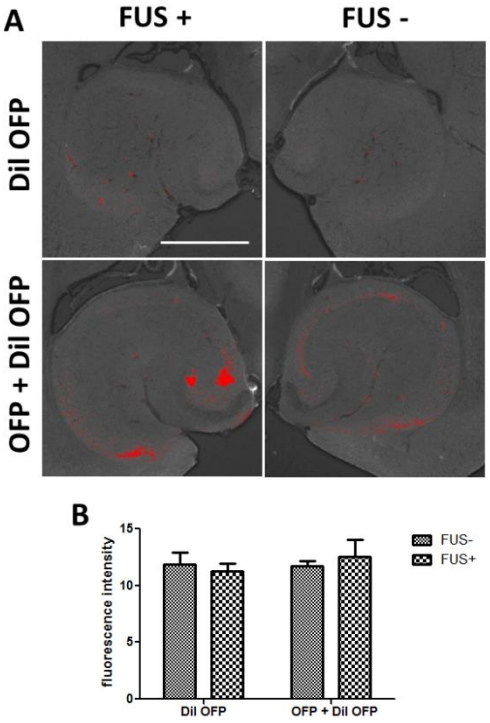

Figure 3.25. Extravascular delivery using fluorescently tagged nanodroplets. OFP droplets were used at 450 kPa. (A) Fluorescent microscopy showed low or no delivery on the sonicated side compared to the control. (B) The quantified fluorescence intensity showed no statistical significance. Therefore, higher pressures would be required to delivery nanodroplets to the brain.

3.4 DISCUSSION

In this chapter, different types of acoustic agents including lipid-shelled microbubbles and nanodroplets were customized for enhanced delivery through BBB opening in mice, and the amount of delivery was positively correlated with the cavitation dose given any types of mediators used. PCD served as a tool to monitor and to shed light on the physical mechanisms for drug

delivery during in vivo BBB opening. For example, C24 microbubbles had stronger stable and inertial cavitation intensity that also resulted in higher amount of delivery and the likelihood of damage. Drug-loaded microbubbles required bubble disruption for delivery. OFP droplets had more persistent stable cavitation at lower pressures that resulted in higher amount of delivery without damage. Therefore, PCD could be used with various acoustic agents to assess drug delivery and safety.

3.4.1 Microbubble shell physicochemical properties determined the drug delivery efficiency

Enhanced drug delivery with hydrophobic chain length in lipid-shelled microbubbles could be caused by the differences in (i) mechanical properties of the microbubbles, (ii) lipid buildup and shedding behavior, and (iii) microbubble persistence. Although the study was performed in FUS-induced BBB opening, the same concept may be applied to focused ultrasound and microbubble mediated drug delivery applications in general.

First, the difference in microbubble mechanical properties may affect the drug delivery efficiency by changing the force applied on the cell membrane through micro-streaming and micro-jetting during cavitation. For a lipid-shelled microbubble with longer hydrophobic chain length, the surface shear viscosity and surface yield shear were both higher, meaning that the shell became more rigid as the resistance to the shear deformation increased [97]. Besides, the microbubble stiffness may vary by adjusting the shell composition. As reported by Chen et al. using atomic force microscopy [100], the stiffness of C18 microbubbles in 4-5 μm was 15 mN/m, and adjustment of the shell composition could affect the overall stiffness [152]. Those differences

could result in different shear stress on the cell membrane during cavitation as reported in simulation [98, 99].

Second, lipid buildup and shedding for microbubbles with longer hydrophobic chain length during cavitation could influence the process of drug delivery. Using high-speed microscopy, Borden *et al.* showed that microbubbles coated with longer hydrophobic chains had more cohesive shells and thus showed a higher probability of lipid buildup on their shells during sonication [93]. Therefore, it was possible that C18 and C24 microbubbles underwent a significant increase of the surface area through lipid buildup that has led to an increased contact area with the capillary endothelium during insonification. This induced higher shear stress along the vessel walls that may have led to more efficient drug delivery than with C16 microbubbles. In addition, the potentially increased shear stress could also explain the increased likelihood of minor petechial erythrocyte extravasation observed based on histological examination (Fig. 3B). On the other hand, although microbubbles with shorter hydrophobic chains had lower delivery efficiency, their lipid shedding mechanism may benefit the drug delivery applications using drug-loaded microbubbles [153-155]. C16 and C18 microbubbles with less cohesive shells could experience quasi-continuous to discrete phases of excessive lipid shedding and are capable of generating new micron-scale or smaller lipid vesicles [92, 93]. This mechanism has been used for multimodality imaging by converting microbubbles to nanoparticles after applying ultrasound [156]. Those small vesicles if carrying drugs could potentially be delivered to the cell as drug-loaded nanobubbles [157, 158].

Third, higher persistence for microbubbles with longer hydrophobic chain lengths during cavitation and circulation *in vivo* may enhance the drug delivery efficiency as well. It was reported that longer-acyl-chain (C18 or C24) microbubbles had higher resistance to natural gas permeation [92], acoustic dissolution and monolayer collapse due to the increased intermolecular cohesiveness

of the shell [93-95]. Therefore, it is plausible to assume that the increased monolayer stability for microbubbles coated with longer acyl chains could prolong the *in vivo* microbubble persistence during circulation and insonification, which could ultimately lead to increased dextran delivery. Even though Garg *et al.* showed that a hydrophobic mismatch could reduce the circulation time of DLiPC:DSPE-PEG5000 microbubbles [159], we did not observe any significant decrease in persistence of our C24 microbubbles based on the cavitation signal acquired during sonication when compared to C16 or C18 microbubbles. We attribute the discrepancies between these two studies to the differences in the experimental designs, including microbubble dosage, sonication and detection duration, signal detection methods including targeting organs (brain through the skull vs. kidney) as well as acoustic pulse sequences (different mechanical indexes, pulse lengths, pulse repetition frequencies).

The observed microbubble shell effect appeared to be molecular size-dependent. Based on fluorescence analysis, there was no significantly different delivery amount detected for 3 kDa dextran among the various microbubble shells at each pressure (Fig. 3), while a difference was obtained at 40 kDa dextran delivery at pressures causing microbubble destruction or inertial cavitation (450 kPa and 600 kPa) (Fig. 4 and Fig. 5). This suggests that the microbubble shell effects were only dominant if the delivered agent has a size above that threshold, since a large amount of small molecules could easily permeate across the BBB in a short time until reaching saturation. Moreover, it also indicates that microbubbles of longer hydrophobic chain (C24) could be used to enhance the delivery efficiency of large molecules. This is promising since delivering large molecules has been shown challenging after BBB opening [60, 114].

3.4.2 Acoustic energy (by varying pressure and pulse length) modulated the shell effects

The shell effects occurred most significantly at pressures causing microbubble destruction or inertial cavitation (450 kPa and 600 kPa) (Fig. 4 and Fig. 5) may be due to more lipid buildup that cause higher shear stress generated on the cell membrane. The lipid buildup behavior during insonification may be dominant at intermediate or high pressures since the bubble oscillation amplitude is higher. This is consistent with the previous study using a pressure of 400 kPa or higher to observe lipid buildup in the microbubble shell with a high-speed camera [93].

Increasing the pulse length did not alter the general trend of the microbubble shell effect although the difference in fluorescence enhancement between C16 and C18 microbubbles became statistically insignificant (Fig. 5). As shown in previous studies, the drug delivery efficiency increased with the pulse length until it reached to a plateau [160, 161]. This principle could also be applied to microbubbles of various hydrophobic chain lengths. The more significant pulse length effect for C24 microbubbles may be due to their higher persistence to dissolution *in vivo* as the delivery efficiency remained significantly higher than others. Our data suggests that the increased pulse length could be used to compensate for the microbubble shell effects when the hydrophobic chain lengths were close (e.g., C16 and C18). Furthermore, using microbubbles of longer hydrophobic chain length in combination with longer pulse length could maximize the delivery efficiency for large molecules.

Overall, it is possible that the shell effects on drug delivery efficiency were dependent on the interactions between the acoustic energy and the drug properties, such as molecular size, molecular structure (linear vs. globular), and hydrophobicity (water-soluble vs. lipid-soluble). In the future, additional systematic and parametric studies could be performed to determine the optimal ultrasound and microbubble combination that achieves optimal delivery dose for various drugs without compromising safety.

3.4.3 Acoustic cavitation detection revealed the microbubble shell effects

Passive cavitation detection (PCD) revealed the possible physical mechanisms behind the *in vivo* microbubble shell effects. PCD offers an indirect way to record the microbubble dynamics *in vivo* both noninvasively and transcranially, in which other methods such as high-speed camera or B-mode imaging could hardly achieve. PCD records cavitation signatures including stable and inertial cavitation causing micro-streaming and micro-jetting [18]. The quantified SCD_h could be related to microbubble circulation persistence which is usually measured with B-mode imaging, ICD to shock wave or force generated by microbubble collapse, and both SCD_h and SCD_u (SCD_{h+u}) to the shear stress applied on the cell membrane, which were thus used to assess the BBB opening outcome (Fig. 8). In these scenarios, the circulation persistence and the strength from microbubble collapse for C24 may surpass other microbubbles, thereby delivering more 40kDa dextrans to the brain.

3.4.4 Nanodroplets as new acoustic agents for drug delivery to the brain

The current study utilized acoustically-activated nanodroplets as a new class of contrast agents to facilitate targeted drug delivery in the brain after FUS-induced BBB opening in mice. Though similar agents have been used in other therapeutic applications, to the best of our knowledge, this is the first study that has explored the benefits of a nanodroplet-based approach to FUS-induced BBB opening. Using fluorescent dextran as a model drug, the extent of the BBB opening was quantified and compared between nanodroplets and the conventional contrast agent, i.e., microbubbles. The two agents were compositionally the same – having lipid-encapsulated perfluorobutane cores - but the nanodroplet approach afforded taking advantage of the benefits of

both the liquid and gaseous state of the cores. The acoustic emission generated from the contrast agents during sonication was recorded and analyzed in order to gain insights to their cavitation characteristics. A linear correlation between BBB permeabilization, as indicated by the relative fluorescence enhancement within the targeted hippocampus, and the acoustic emission, as characterized by the SCD, was found for both nanodroplets ($R^2 = 0.74$) and microbubbles ($R^2 = 0.67$). Interestingly, the acoustic threshold, at which significant dextran delivery was observed, appeared to be contrast agent dependent. Our results suggested future contrast agent-specific monitoring during FUS-induced BBB opening might be needed.

The high-speed microscopy results confirmed that the nanodroplet samples were acoustically vaporizable at exposure conditions similar to that used during BBB opening *in vivo*. The vaporization pressure threshold detected *in vitro* corresponded to our *in vivo* estimation remarkably well. While it was possible that nanodroplet vaporization at pressures lower than 0.45 MPa could still occur, it was more likely that the number of activated nanodroplets was too low to cause any detectable fluorescence enhancement. Thus, nanodroplet-mediated dextran delivery to the targeted hippocampus could not be consistently achieved until the sonication pressure was higher than 0.45 MPa. For the purpose of direct comparison, the droplets used in this study were formed from perfluorobutane. While the pressures used were sufficient to cause some droplet vaporization, other studies have shown that highly efficient vaporization at frequencies near 1 MHz required pressures on the order of 1 MPa or greater [108, 162]. Further studies are needed to develop different nanodroplet formulations in order to decrease the *in vivo* vaporization threshold by incorporating more volatile perfluorocarbons, such as perfluoropropane [144]. Additionally, the not-yet-optimized droplet formulation could also explain the lower fluorescence

enhancement observed using nanodroplets than that of microbubbles even though the injection amount of the former was much greater.

3.4.5 Improved drug delivery with highly volatile nanodroplets

Nanodroplets are promising for highly targeted extravascular applications in the brain, while the delivery of small molecules to the brain was poor with DFB droplet in the first attempt. Here we showed that high amount of delivery for large molecules was achievable by modulating the droplet's sensitivity to acoustic energy. OFP droplets hold high vaporization efficiency at low acoustic pressure, and could safely deliver large molecules to the brain with the amount of delivery comparable to conventional gaseous microbubbles. They were also safer compared to DFB droplets as they can be vaporized and cavitate stably at lower pressures. The excellent correlation of drug delivery to the cavitation monitoring also demonstrated high predictability of nanodroplets through acoustic cavitation monitoring for safe and effective FUS treatment.

The droplet's sensitivity to acoustic energy could be tailored through the PFC core [144] and the lipid chain length of the shell [103], that determined the number of bubbles been vaporized after applying ultrasound in the body temperature. After microbubble condensation at high pressures, the nanodroplets maintain metastable due to the pure superheated fluid to homogeneous nucleation [103]. Once experiencing temperature change or acoustic energy deposition, the droplets then vaporized to bubbles for contrast enhancement in imaging or cavitation for drug delivery or ablation. Due to extremely low boiling point of OFP, the droplets were highly efficient to form significantly more bubbles at and above 300 kPa than DFB droplets at 900 kPa. Furthermore, the formed OFP bubbles were more stable against dissolution than DFB bubbles,

although OFP droplets were more sensitive to the temperature (90% of them vaporized at 40°C compared to 75°C for DFB droplets) [103]. Because of these advantages, the OFP droplets could achieve tremendously higher amount of delivery for large molecules in vivo even with only one fourth dosage of the DFP droplets.

The in vivo drug delivery outcomes (Fig. 3) were found to associate with the in vitro vaporization efficiency (Fig. 2). For OFP droplets, the pressure threshold for successful drug delivery was the same as the vaporization threshold (300 kPa), and the drug delivery outcomes correlated with the vaporization efficiency. For DFB droplets, low number of bubbles formed resulted in no or low delivery. The pressure threshold for successful drug delivery (900 kPa) was higher than the vaporization threshold (600 kPa) due to the difficulty in delivering large molecules with fewer bubbles. High vaporization efficiency of OFP droplets not only dramatically improved the drug delivery outcomes to be comparable to microbubbles. The use of nanodroplets also avoids the microbubble shielding effects which reduces spatial specificity of acoustic energy deposition. In turn, more focused and effective cavitation leads to more precise cavitation monitoring. A similar reason was attributed to the more effective ablation without off-target surface heating compared to microbubbles [163].

The acoustic emission during BBB opening (Fig. 4, 5) reflected the behavior of droplet vaporization to cavitation associated with drug delivery and safety. A significant stable cavitation dose (either SCD_h for volumetric oscillation or SCD_u for surface oscillation) was detected in groups with successful delivery, meaning that cavitation was effective to achieve drug delivery due to highly localized and strong shear stress applied on the vessel wall after droplet vaporization. Harmonic emission was detected in the cases of the OFP droplets but not for DFB droplets possibly because the bubbles were rapidly disrupted after vaporization at high pressures (e.g. 900 kPa).

Nevertheless, ultraharmonics were detected for both OFP and DFB droplets since they were less affected by the nonlinear effect generating harmonics from the skull or tissue. Interestingly, stronger ultraharmonics were found in droplets with 100% successful delivery (OFP droplets at 450 kPa and DFP droplets at 900 kPa) compared to microbubbles. This implied that irregular oscillation with bubbles after nanodroplet vaporization were effective in increasing BBB permeability, and may be due to the larger bubbles were more compliant and more prone to irregular oscillation than the small bubbles [100].

Safety can be assessed by inertial cavitation with droplets, similar to what has been reported with microbubbles [76]. Significant inertial cavitation occurred at 900 kPa for DFB droplets demonstrated that the bubbles were disrupted right after droplet vaporization, and these strong shock waves and microjets may cause damage (Fig. 6). On the other hand, OFP droplets did not cause any damage since the bubbles were mainly undergoing stable cavitation at 300-450 kPa after vaporization, as demonstrated by insignificant broadband emission (ICD). Therefore, for delivering large molecules, OFP droplets were safer than DFB droplets due to the OFP vaporization threshold falling in the regime of stable cavitation. Nevertheless, the benefits of low vaporization threshold and high vaporization efficiency with lower dosage of OFP droplets demonstrated a safer, more effective, and more predictable drug delivery over microbubbles and DFB droplets.

The restriction to use highly-efficient nanodroplets is the care of spontaneous vaporization due to the nature of highly volatile OFP. This spontaneous vaporization may occur at higher temperature (> 4 °C) once been thawed, with a speedily temperature change such as been taken out from -80 °C freezer to be thawed in the room temperature (as comparison to be thawed in the 4°C fridge), or even during injection to the bloodstream. Therefore, low OFP droplet concentration

should be chosen in order to avoid embolism from spontaneous vaporization upon injection, and handled speedily with care because of their lower stability in room temperature (10 min. for OFP droplets vs. 1 h for DFB droplets [144]). Although the spontaneous vaporization was observed in the in vitro experiment, its effect on drug delivery in this study may be insignificant with the current dosage, as the SCD_h is sensitive especially at lower pressures with microbubbles was insignificant with OFP droplets at 150 kPa and remained low at 300 kPa.

Future applications for utilizing nanodroplets for drug delivery to the brain could be based on the characteristics of smaller size and the ability to encapsulate drugs. Owing to the small size, the nanodroplets could possibly enter the parenchyma after BBB opening or through intranasal delivery [147]. Their presence in the brain parenchyma could enhance drug delivery through sonoporation, or facilitate thermal ablation or occlusion therapy for droplets accumulated in tumors or other tissues in the brain. Moreover, nanodroplets could serve as drug carrier for targeted delivery and possibly achieve more effective drug delivery due to the higher drug payload in the liquid core.

3.5 CONCLUSION

The entire sonication for BBB opening was monitored using passive acoustic cavitation detection (PCD) in order to shed light on the physical mechanisms behind cavitation with microbubbles and nanodroplets in mice. Modification of microbubble's shell properties and droplet's vaporization efficiency could significantly affect the outcomes of drug delivery. Furthermore, acoustic

cavitation detection showed a good correlation between the delivery efficiency and tissue damage using various acoustic agents in this chapter.

First, the effects of the microbubble shell physicochemical properties on drug delivery efficiency using ultrasound have been characterized using microbubbles of three phospholipids with increasing hydrophobic chain lengths (C16, C18, C24) for drug delivery to the brain through BBB opening. The entire process was monitored using passive acoustic cavitation detection (PCD) in order to shed light on the physical mechanisms behind the shell effects. The dependence on both the molecular size and acoustic energy (by varying pressure and pulse length) were studied. We showed that relatively small changes in lipid hydrophobic chain length resulted in a significant increase for large (40 kDa) but not for small (3 kDa) dextran delivery, and the acoustic energy modulated the shell effects on the delivery efficiency. The C24 microbubble was deemed to be the most efficient for large-molecule delivery. Acoustic cavitation detection revealed possible mechanisms with different shells, and the findings showed a good correlation between the delivery efficiency and tissue damage for different shelled microbubbles.

Second, in the initial feasibility study to explore the utilization of phase-shift nanodroplets for targeted drug delivery in the brain with FUS-induced BBB opening, significant dextran delivery was achieved in the mouse hippocampus using acoustically-activated nanodroplets at clinically relevant pressure amplitudes. Passive cavitation detection was used in the attempt to establish a correlation between the amount of dextran delivered in the brain and the acoustic emission recorded during sonication. Conventional microbubbles with the same lipid shell composition and perfluorobutane core as the nanodroplets were also used to compare the efficiency of FUS-induced dextran delivery. It was found that nanodroplets had a higher BBB opening pressure threshold but a lower stable cavitation threshold than the microbubbles. More

homogeneous dextran delivery within the targeted hippocampus was achieved using nanodroplets without inducing inertial cavitation or compromising safety. Our results offered a new means of developing the FUS-induced BBB opening technology for potential extravascular targeted drug delivery in the brain.

Nanodroplets can also be customized to enhance drug delivery to the brain for extravascular interrogation. The findings showed drug delivery outcomes were directly associated with the nanodroplet vaporization efficiency, i.e., the number of bubbles formed after vaporization. OFP nanodroplets after vaporization could deliver large molecules across the BBB with the outcomes comparable to microbubbles. Furthermore, the delivery with OFP nanodroplets was safer than with DFB droplets due to the lower vaporization threshold. While the restriction to use highly-volatile nanodroplets is the care of spontaneous vaporization, low concentration with slow injection could ensure safety. Our results provided information for customizing nanodroplets in delivering large molecules to the brain.

3.6 SIGNIFICANCE & CONTRIBUTION

Cavitation monitoring is the only way to study the physical mechanisms of BBB opening in vivo, and the feasibility using it as a tool to investigate the customization of various acoustic agents for BBB opening remained unknown. In this chapter, cavitation monitoring for assessing BBB opening has been studied with various acoustic agents from conventional microbubbles to phase-shift nanodroplets in mice, and the customization of the agents includes shell and core modification. Our lab built the system to detect cavitation previously. Here, the quantification method for

different types of cavitation has been established and both the stable and inertial cavitation dose were found to be associated with BBB opening effectiveness and safety using modified microbubbles and nanodroplets. This study showed that cavitation monitoring could elicit the difference in physical response that affects the BBB opening outcomes in customized acoustic agents. Moreover, large molecules were difficult to be delivered were found been able to cross the BBB at ease for the first time using microbubbles of long acyl chain and nanodroplets of low boiling-point core, owing to the high stable cavitation dose imposing high shear stress on the vessel wall.

The research contribution was shared with many colleagues and collaborators. Cherry Chen (PhD, Biomedical Engineering, Columbia University) and Yao-Sheng Tung, (PhD, Biomedical Engineering, Columbia University) assisted and mentored the microbubble shell study. Cherry Chen performed in part and mentored the nanodroplet study, and Paul Dayton (PhD, University of North Carolina) and his team provided the nanodroplets and assisted the in vitro experiments. Carlos Sierra Sanchez (PhD, Biomedical Engineering, Columbia University) performed the fluorescently-tagged microbubble study. Oluyemi Olumolade (B.A., Biomedical Engineering, Columbia University) assisted the tissue sample handling.

Chapter 4

Acoustic Monitoring to Characterize BBB Opening & Drug Delivery in Primates

4.1 INTRODUCTION

As shown in Chapter 3, transcranial passive cavitation detection (PCD) provides methodology of monitoring the treatment. Acoustic cavitation monitoring could potentially serve as an on-line tool to assess and control the treatment. While it demonstrated a strong correlation in small animals, its translation to primates remains in question due to the thicker skull attenuating cavitation signal for monitoring, the anatomically different and highly heterogeneous brain structures with gray, white matter and dense vasculature. In this chapter, three objectives were achieved to address the above questions. All these new findings are critical in primates and provide essential information for clinical applications.

1) The PCD performance through the primate skull was assessed both in vitro and in vivo. We investigated the sensitivity, reliability, and limitations of PCD through primate (macaque and human) skulls in vitro. The results were further correlated with the in vivo macaque studies including the transcranial PCD calibration. The stable cavitation doses using harmonics (SCD_h) and ultraharmonics (SCD_u), the inertial cavitation dose (ICD), and the cavitation signal-to-noise ratio (SNR) were quantified based on the PCD signals.

2) Real-time cavitation monitoring during BBB opening in primates was developed in order to determine how the cavitation activity was correlated with the BBB opening volume, the amount of model drug (gadolinium) delivered through the barrier and its delivery efficiency in NHP. All types of cavitation doses (SCD_h, SCD_u, and ICD) and the frequency spectra can be monitored in real time to ensure treatment effectiveness. They were used to investigate the inter- and intra-animal variability in BBB opening. This study aimed at determining how cavitation activity can be reliably monitored through the primate skull, and how it is correlated with the amount and concentration of gadolinium delivered through the BBB and its associated delivery efficiency as well as the BBB opening volume in non-human primates.

3) The heterogeneous brain effects on PCD monitoring were investigated, including gray and white matter and vasculature. The finding entails the effect of heterogeneous brain anatomy and vasculature of a primate brain, i.e., presence of large cerebral vessels, gray and white matter will also affect the cavitation activity associated with variation of BBB opening in different tissue types, which is not seen in small animals.

In achieving the first objective, both in vitro macaque and human skull experiments as well as in vivo skull effects and real-time monitoring in BBB opening of macaques were performed in this study. Three types of cavitation doses and the cavitation SNR were quantified and used to address the characteristics of cavitation, skull attenuation, and detection limit. The stable cavitation dose (SCD) representing the overall extent of stable cavitation is defined as the cumulative harmonic or ultraharmonic emission. The inertial cavitation dose (ICD) represents the overall extent of inertial cavitation, and is defined as the cumulative broadband acoustic emission [164]. The cavitation SNR is defined as the ratio of the post- to pre-microbubble administration cavitation

doses. The quantification of cavitation dose and SNR in this study is based on the detected signals, emitted by acoustic cavitation.

For objective 2 and 3, real-time transcranial cavitation monitoring of the stable and inertial cavitation doses was performed in four macaque monkeys during BBB opening through stereotactic targeting. For the quantitative analysis of BBB opening volume and drug delivery efficiency, T_1-weighted (T_{1w}) imaging and variable flip-angle (VFA) T_1 mapping in magnetic resonance imaging (MRI) were performed 1 h following BBB opening. These opening outcomes were then correlated with the acquired acoustic monitoring findings in order to assess the PCD predictability value among animals. The effect of gray and white matter on BBB opening and cavitation was analyzed after tissue segmentation. The vasculature effect on cavitation monitoring was evaluated by targeting a region proximal to the medial cerebral artery (MCA) with a monotonically increasing pressure for PCD calibration. The effect of the incidence angle with respect to the skull on cavitation monitoring was evaluated by varying the targeting angle with PCD calibration as well.

4.2 METHODS

4.2.1 Ultrasound System

A single-element FUS transducer (H-107, Sonic Concepts, WA, USA) operated at 0.5 MHz with a -6-dB focal width by length equals to 5.85 mm by 34 mm and a geometric focal depth of 62.6 mm was used for sonication. A spherically focused, flat-band hydrophone made of polyvinylidene fluoride (PVDF) (Y-107, Sonic Concepts, WA, USA; sensitivity: 10 kHz to 15 MHz; mean absolute

characterization in 1.25 MHz to 5 MHz: 32.5 dB Volts/MPa) was coaxially and confocally aligned with the transducer and served as the passive cavitation detector. A PC work station (model T7600, Dell) with a customized program in MATLAB® (Mathworks, MA, USA) was developed to automatically control the sonication through a function generator (model 33220A, Agilent Technologies, CA, USA) followed by a 50-dB amplifier (A075, ENI, NY, USA). The PCD signal acquisition was performed at a 14-bit analog-to-digital converter (Gage Applied Technologies, QC, Canada) (sampling rate: 100 MHz and 50 MHz in vitro and in vivo, respectively). A 20-dB amplification was applied throughout the macaque experiments, while 10 dB was applied for the human skull due to large reflection. The electronic noise level and variance of the system in 1.25-5.00 MHz was 1.20 μV and 0.66 μV, respectively. The PCD signals acquired in vivo including the frequency spectra and cavitation doses were monitored in real time.

4.2.2 Quantification of Acoustic Cavitation Emission

The PCD signals, frequency spectra, and spectrograms (8-cycle Chebyshev window, 98% overlap, 4096-point Fast Fourier Transform) were used to monitor the cavitation using MATLAB®. In order to quantify the cavitation level−time derivative of the cavitation dose, the harmonic, ultraharmonic, and the broadband signals in the spectra for each pulse were separately filtered. The stable cavitation level based on harmonics only ($dSCD_h$) was the root-mean squared amplitude of the harmonic signals in a single pulse, with the harmonic signals defined as the maxima in the 20-kHz (-6-dB width) range around the harmonic frequency (multiples of the excitation frequency) in the frequency spectrum. The stable cavitation level based on ultraharmonics only ($dSCD_u$) was the root-mean squared amplitude of the ultraharmonic signals in a single pulse, with the ultraharmonic signals defined as the maxima in 20 kHz around the ultraharmonic frequency (multiples plus a half

of the excitation frequency) in the frequency spectrum. The inertial cavitation level (dICD) was the root-mean squared amplitude of the frequency spectrum after excluding the harmonics (360 kHz around the harmonic frequency) and ultraharmonics (100 kHz around the ultraharmonic frequency).

The cavitation dose for each sonication was the cumulative sum of the cavitation level in 1.25-5.00 MHz for every pulse.

$$Cavitation\ dose\ (CD) = \sum_{t=0-T} dCD_t = \sum_{t=0-T} \sqrt{\overline{S^2}}_t$$

$$Cavitation\ SNR = 20\log(CD_{post}/CD_{pre})$$

where t is the time for each pulse; T, the sonication duration; CD, the cavitation dose (SCD_h, SCD_u, and ICD for harmonics, ultraharmonics, and broadband emissions, respectively); dCD_t, the cavitation level for the pulse at time t ($dSCD_h$, $dSCD_u$, and dICD for harmonics, ultraharmonics, and broadband emissions, respectively); $\sqrt{\overline{S^2}}_t$ the root-mean squared amplitude of the harmonic/ultraharmonic/broadband signals in the frequency spectrum for the pulse at time t; CD_{post}, the post-microbubble administration cavitation dose; CD_{pre}, the pre-microbubble administration cavitation dose.

The frequency range used to quantify the cavitation level was 1.25-5.00 MHz in order to cover the strong harmonics, ultraharmonics, and broadband emission, while suppressing the linear and nonlinear scattering from the tissue and the skull. Moreover, the acoustic measurement in this frequency range is less dependent on the system or FUS frequency used in comparison to using a narrow frequency range. The quantification of the SCD_h and the SCD_u was based on the acoustic emissions generated by stable cavitation including harmonics and ultraharmonics, while the ICD was based on the broadband emission (after filtering the harmonics and ultraharmonics) emitted

from inertial cavitation. The harmonics and ultraharmonics were quantified separately due to the large difference of the spectral amplitudes. In addition, their physical mechanisms are assumed to be different: the harmonics is the result of volumetric oscillation, while the ultraharmonics and subharmonics may relate to the nonspherical bubble oscillation [18, 165]. For ICD quantification, the width of the spectral window for the broadband signals was chosen in order to minimize both the electronic noise and the increase due to the harmonic peaks (i.e., the window width is large enough to minimize the electronic noise by averaging and not to cover the broadening part of harmonic peaks).

The SCD based on subharmonics (SCD_s) was excluded in the present study due to the intrinsic low-frequency noise. In addition, since the excitation frequency used in this study was low, the subharmonics were overlapping with the linear scattering whose amplitude increased even more with the scattering of the skull.

4.2.3 In vitro skull experiments

The desiccated macaque skull was purchased from Skulls Unlimited (Macaca mulatta, OK, USA) and sectioned to keep the cranial part (including the frontal bone, the parietal bones, and the occipital bone) (Fig. 1). Its average thickness in the ultrasound beam path was 3.09 mm using a caliper at five points of the skull lined in a cross below the transducer, and was degassed for 24 h prior to the experiment. The desiccated human skull was purchased from The Bone Room (CA, USA), and sectioned to keep the frontal and the parietal bones (Fig. 1) with an averaged thickness of 4.65 mm using the same measuring method described above. It was degassed for 48 h prior to the experiment. The pressures at the focus of the FUS transducer with and without the skulls were calibrated using a bullet hydrophone [133].

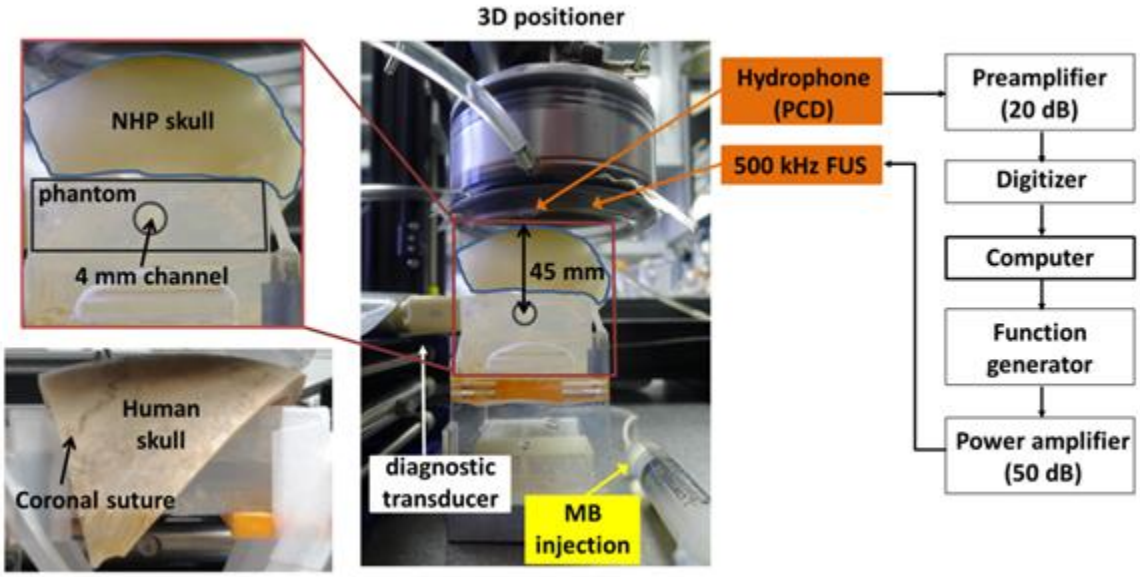

Figure 4.1. In vitro experimental setup. A focused ultrasound (FUS) transducer was used for sonication, while a flat-band hydrophone at the center of the FUS transducer was used for passive cavitation detection (PCD). The cranial part of the macaque skull (including frontal bone, parietal bones, and occipital bone) was 3.09-mm thick in average of the beam-path region, and the human skull (including the frontal and the parietal bones) was 4.65-mm thick.

Table 4.1. Number of in vitro sonications at each pressure.

			Without microbubbles	**With microbubbles**
Skull effect (100 cycles)	**Macaque**	No skull	41	49
		Skull	33	46
	Human	No skull	60	60
		Skull	70	81
Pulse length effect (5000 cycles)		No skull	20	20

The experimental setup is shown in Fig. 4.1 and the number of sonications is summarized in Table 4.1. In-house, lipid-shell, monodisperse microbubbles [134] (median diameter: 4-5 μm) were diluted to 2×10^5 bubbles/mL and injected to the 4-mm-in-diameter channel in the acrylamide

phantom before and after placing the skull on the phantom. The channel was roughly 45 mm and 25 mm below the macaque and human skulls, respectively. The PCD with the hydrophone and the diagnostic B-mode imaging system (Terason, MA, USA) were separately used to monitor the sonication (peak negative pressure (PNP): 50-450 kPa, pulse length: 100 cycles (0.2 ms) and 5000 cycles (10 ms), pulse repetition frequency (PRF): 10 Hz, duration: 2 s) in order not to interfere the PCD. B-mode images of bubble disruption were acquired to ensure the FUS focusing at the channel, which was performed through a linear array transducer (10L5, Terason, MA, USA; center frequency: 5.1 MHz) placed transversely to the FUS beam. Before each sonication, the microbubbles were injected and the old microbubbles were flushed out, which ensured the independence between each sonication and experiment. During the experiments for PCD only, the microbubbles were constantly replenished at around 0.25 mL/s in order to mimic the replenishment of the microbubbles in the brain.

The in vitro experimental setup was designed to mimic the in vivo conditions in terms of targeting through the skull. Specifically, FUS was applied through the parietal bone next to the sagittal suture, which corresponding to the position for targeting the thalamus, putamen, and caudate nucleus in the present and previous studies [65, 66]. The 4-mm channel was chosen to accommodate the area of bubble disruption at the highest pressure (450 kPa). The low microbubble concentration was chosen in order to minimize the bubble-bubble interaction (the mean distance between bubbles is 58.5 mm) while still capable of being captured for B-mode visualization. The sonication parameters (pulse length, PRF, duration) were set based on our previous mouse skull study [166], in which no changes in the detection threshold were found. Sonication using 5000-cycle pulses without the skull in place was also performed in accordance to the in vivo BBB opening experiment.

4.2.4 In vivo NHP experiments

In accordance with the National Institutes of Health Guidelines for animal research, all procedures for the animal experiments were reviewed and approved by the Institutional Animal Care and Use Committee at Columbia University and the New York State Psychiatric Institute. Four male rhesus macaques (Macaca mulatta, weight: 7-10 kg, age: 8-20 yo) were used in this study. Each animal was sedated with ketamine (5-15 mg/kg in conjunction with 0.04 mg/kg of atropine through intramuscular injection) for placement of an endotracheal tube and an intravenous catheter in the saphenous vein, and was under anesthesia using 1-2% isoflurane-oxygen mixture with vital signs (electrocardiography, heart rate, blood pressure, SpO_2, breathing rate, end-tidal CO_2) monitored during the entire experiments. No animals were euthanized in this study.

Three separate sets of experiments were performed in non-human primates, i.e., one set for the in vivo skull effect, one for the heterogeneous brain effects, and the other for BBB opening. The same type of in-house microbubbles was intravenously injected, and the total number of microbubbles administered was calculated based on the animal's weight. For the purpose of BBB opening brain, a bolus of microbubbles (2.5×10^8 bubbles/kg) was injected and the sonication (PNP: 200-600 kPa, pulse length: 10 ms, PRF: 2 Hz, duration: 2 min) started at the beginning of injection (N = 43). In order to study the in vivo skull effect, a bolus of microbubbles (1.25×10^8 bubbles/kg) was injected immediately after the BBB opening sonication (N = 22). 10 s after injection when the microbubbles perfused to the brain, a consecutive sonication at ramp-up pressures was started (PNP: 50-700 kPa, pulse length: 100 cycles (0.2 ms) or 5000 cycles (10 ms), PRF: 2 Hz, duration: 10 s). This PCD calibration method was also used to investigate the effects of heterogeneous primate brain (N = 31) (a 5-s consecutive sonication at monotonically increasing pressures ranging

within 100-600 kPa starting at 10 s after re-injecting half the dose of microbubbles)[70] was performed after the regular sonication for BBB opening. The targeted regions were the caudate nucleus and putamen using the steretactic targeting technique shown in Fig. 4.2 [69].

After the FUS procedure, the animal was transferred to the MRI suite for assessing the BBB opening and safety within 1 h.

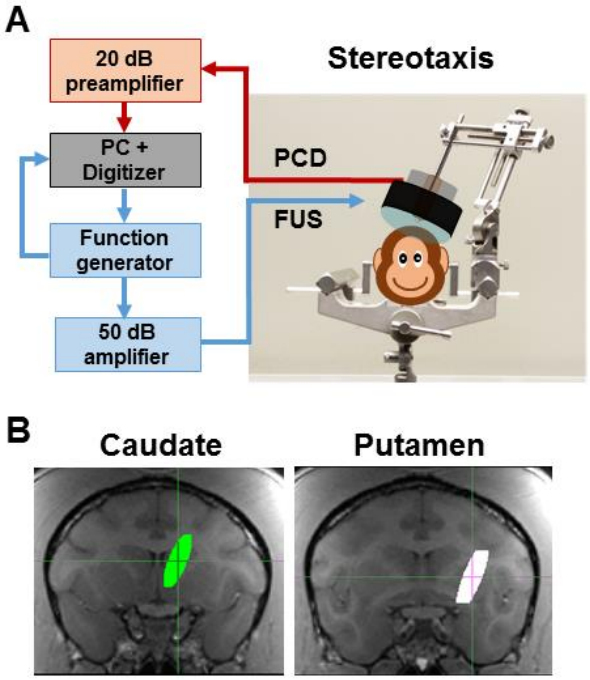

Figure 4.2. In vivo NHP experimental setup. (A) A focused ultrasound (FUS) transducer was used for sonication and a hydrophone coaxially and confocally aligned with the FUS transducer served for passive cavitation detection (PCD). (B) Targeting was performed using stereotaxis with pre-planning for focusing at the caudate nucleus (left) or putamen (right) based on the preoperative MRI scan with a stereotax.

4.2.5 MRI for validating BBB opening and safety

A 3.0 T MRI system (Achieva, Philips Medical Systems, USA) with an eight-channel head coil was used for assessing safety and BBB opening. T_{1w} imaging was used for BBB opening detection

and opening volume quantification because of its higher sensitivity, while T_1 mapping was for quantifying the amount of delivered MR contrast agents and the delivery efficiency. For assessing BBB opening, both pre- and post- contrast agent T_1-weighted (T_{1w}) images and T_1 maps using the variable flip-angle (VFA) SPGR method were acquired. The contrast agent used in this study was Gd-DTPA-BMA as the model drug (gadodiamide or Gd, molecular weight = 573.66 Da; Omniscan®, GE Healthcare, NJ, USA) with the same dosage suggested for patients (0.2 mL/kg or 0.1 mmol/kg of body weight). Pre- and post-Gd (40 min after injection) T_{1w} images using 3D spoiled gradient echo (SPGR) sequence (TR/TE = 8.5/4.8 ms, FA = 8º, SR = 0.97×0.97×1 mm^3) were acquired for detecting the opening and analyzing the opening volume. For quantitative analysis of the Gd concentration and delivery efficiency, pre- and post-Gd (20 min after injection) T_1 maps were acquired using a series of 3D SPGR sequence with five flip angles (TR/TE = 10/4 ms, FAs = 5°/10°/15°/20°/35°, SR = 0.89×0.89 mm^2, SL = 1 mm). For detecting edema, T_2-weighted (T_{2w}) images were acquired using 3D Turbo Spin Echo sequence (TR/TE = 3000/80 ms, flip angle or FA = 90º, resolution = 0.42×0.42×2 mm^3). For detecting hemorrhage, susceptibility-weighted imaging (SWI) was performed (TR/TE = 19/27 ms, FA = 15º, resolution = 0.44×0.44×1 mm^3). Magnetic resonance angiography (MRA) was conducted in order to visualize the size and orientation of blood vessels using 3D time-of-flight SPGR sequence (TR/TE = 23/3.4 ms, FA = 15°, resolution = 0.89×0.89×1 mm^3) in a separate 3.0 T scanner (Signa, GE Healthcare, USA) with a customized two-channel head coil.

4.2.6 Quantification for BBB Opening volume and delivery efficiency

The BBB opening volume was quantified using pre- and post-Gd T_{1w} images in Matlab with custom-built programs[70]. In brief, both pre- and post-Gd images were first registered to the

individual stereotactically-aligned images (IST) with FSL's FLIRT toolbox[136], computing the ratio of post- to pre-Gd images as a measurement of contrast enhancement, which was normalized by linear scaling with reference to the unsonicated thalamus and the anterior cerebral artery (ACA) as shown in dashed and solid circle in the horizontal slice (Fig. 4.3A), respectively. In order to filter out the background contrast enhancement in the cerebral vessels and muscle tissue outside the brain for quantifying the BBB opening volume, the brain mask was applied (generated using pre-Gd T_{1w} images from the no-FUS sham cohort with FSL's Brain Extraction Toolbox[137]) and the enhancement images of the FUS-/MB- sham cohort for each individual was subtracted from the enhancement images (coronal slice in Fig. 4.3A), giving rise to Fig. Fig. 4.3B. Finally, the opening volume was calculated by applying a volume of interest (VOI, 10 × 10 × 32.5 mm^3) on the targeted region (solid box) subtracting the VOI on the contralateral side (dashed box) as shown in Fig. 4.3C. The threshold of BBB opening (80 mm^3) was defined by the average opening volume plus 3 times the standard deviation in the FUS+/MB- sham cohort.

Similarly, the Gd concentration maps [167, 168] provide quantification of the Gd amount that crossed the BBB. The delivery efficiency was calculated using the pre- (Fig. 4.3D) and post-Gd T_1 maps (Fig. 4.3E)[168]. First, the standard line fit method of VFA SPGR[169] was used to calculate the pre- and post-T_1 maps after registering the 3D SPGR images of various flip angles to the IST. Then, the Gd concentration map (Fig. 4.3F) was generated based on the following equation:

$$[Gd]_c = \frac{1}{r_1}\left(\frac{1}{T_1} - \frac{1}{T_{1,0}}\right), \quad (1)$$

where $[Gd]_c$ is the Gd concentration, r_1 is the relaxivity of the contrast agents (4 $s^{-1}mM^{-1}$ for Gd-DTPA-BMA[170]), T_1 is the post-Gd T_1 time, and $T_{1,0}$ is the pre-Gd T_1 time. Note that in the

$[Gd]_c$ map (Fig. 2F), the concentrations in the unopened brain tissue (thalamus, dashed circle), temporalis muscle (black solid circle), and anterior cerebral vessels (ACA, white solid circle) were also calculated and compared with that of the BBB opening area. In order to filter out the $[Gd]_c$ in the cerebral vessels and muscle tissue outside the brain for quantifying the delivered Gd due to BBB opening, the $[Gd]_c$ maps (coronal slice in Fig. Fig. 4.3F) were thresholded by setting the concentration higher than that in ACA to zero and applying the brain mask, giving rise to Fig. 4.3G. Finally, the amount of delivered Gd was calculated based on equation (2) by applying a volume of interest (VOI, 10 × 10 × 32.5 mm^3) on the targeted region (VOI_{ipsi} , solid box in Fig. 4.3H) subtracting the VOI on the contralateral side (VOI_{contra} , dashed box in Fig. 4.3H) for excluding the intrinsic Gd retention:

$$[Gd]_{BBB} = \left(\sum_{VOI_{ipsi}}[Gd]_c - \sum_{VOI_{contra}}[Gd]_c\right) \cdot V, \quad (2)$$

where $[Gd]_{BBB}$ is the amount of delivered Gd (mole) and V is the voxel volume in the T_1 map. The delivery efficiency was defined as the percentage of the amount of delivered Gd to the total amount of injected Gd (estimated to be 1 mmol).

The opening volume was separated by the tissue type (i.e., the gray matter, white matter, blood, cerebral spinal fluid) segmented based on the T_1 time in the pre-Gd T_1 map. The T_1 time for blood is between 1 ms to 700 ms, 700 ms to 1170 ms for white matter, 1170 ms to 1800 ms for gray matter, and 1800 ms to 5000 ms for cerebral spinal fluid based on our measurement in the NHP and the previous study in human[169].

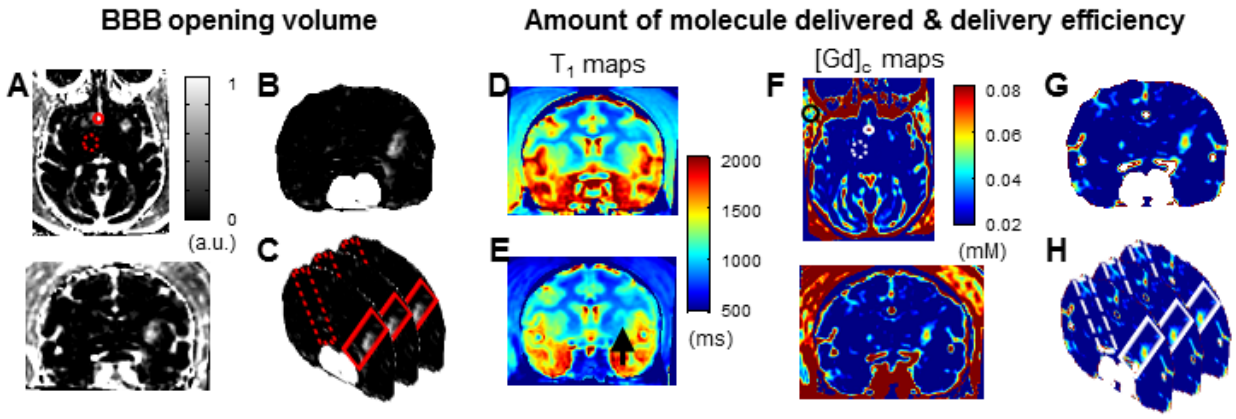

Figure 4.3. Pipeline for BBB opening volume quantification and drug delivery analysis based on MRI processing. (A) To quantify BBB opening volume, the contrast enhancement map (upper: horizontal slice, lower: coronal slice) were used after dividing the post-Gd T_1 images by the pre-Gd images. Then, after applying the brain mask and the vessel mask in order to filter out the contrast enhancement outside of the BBB opening area (B), the opening volume was calculated by subtracting the VOI in the contralateral area (dashed rectangle) from the targeted area (solid rectangle) (C). On the other hand, the pre- Gd $T_{1,0}$ (D) and post-Gd T_1 maps (E) were used to quantify the amount of Gd delivered and its delivery efficiency since the Gd shorted the T1 time after diffused the BBB opening region (arrowhead). The Gd concentration map (F)(upper: horizontal slice, lower: coronal slice) was acquired by calculating the change of T_1 time between pre- and post-Gd T_1 maps. After applying the brain mask and excluding the Gd retention in the vessels by thresholding (G), the amount of Gd delivered was calculated by subtracting the VOI in the contralateral area (dashed rectangle) from the targeting area (solid rectangle) (H).

4.3 RESULTS

4.3.1 Performance assessment of transcranial PCD

4.3.1.1 In vitro skull effects

Fig. 4.4 shows the PCD spectrograms before and after placing the skull. Before placing the skull, the amplitude of harmonics, ultraharmonics as well as the broadband signals increased significantly with pressure after microbubble administration (Fig. 4.4B) when compared to the control (Fig.

4.4A), in which the second harmonic became significant at and above 150 kPa. The broadband signals increased mostly within the range of 3-5 MHz according to the results at 150 kPa and 200 kPa in Fig. 4.4B. In the case of the macaque skull (Fig. 4.4C), the high frequency components were attenuated, while the signals remained detectable at the lowest pressure (50 kPa). In the case of the human skull (Fig. 4.4D), the frequency components below 3 MHz were detected only at or above 150 kPa. The cavitation emissions occurred at 0.05-0.10 ms (the echo arrival time to the focus (62.9 mm)) after microbubble administration (Fig. 4.4 B-D).

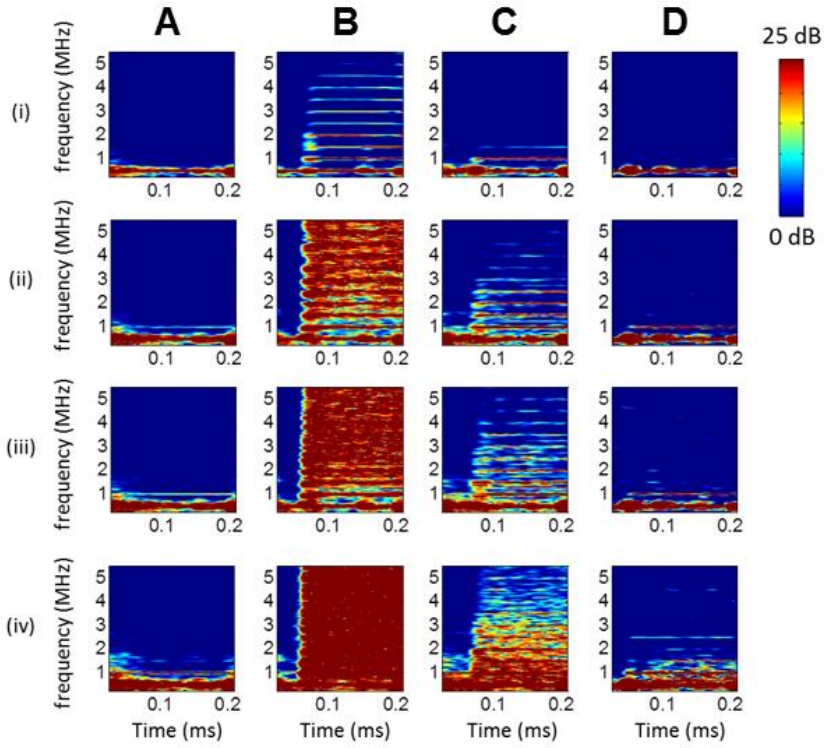

Fig. 4.4. In vitro cavitation monitoring: spectrograms. (A) Sonicating water without the skull in place. (B) Sonicating microbubbles without the skull in place. (C) Sonicating microbubbles with the macaque skull in place. (D) Sonicating microbubbles with the human skull in place. (i), (ii), (iii), and (iv) represents 50 kPa, 150 kPa, 200 kPa, and 450 kPa, respectively. The colorbar shows the intensity of the spectra, with a dynamic range of 25 dB and 15 dB for the macaque and human skull experiments, respectively, based on the preamplification (macaque: 20 dB, human: 10 dB).

B-mode cine-loops were also used to monitor the cavitation separately. Fig. 4.5 shows the images of the microbubbles in the channel phantom after sonication. The microbubbles were found to dissolve or fragment at or above 200 kPa as evidenced by the loss of echogenicity in the focal region in all experimental conditions, i.e., cases without (Fig. 4.5A), with the macaque (Fig. 4.5B) and the human (Fig. 4.5C) skull, and using longer pulses without the skull (5000 cycles in Fig. 4.5D). The mean diameter of the hypoechogenic area at 200 kPa and 450 kPa was 1.3 mm and 4 mm, respectively.

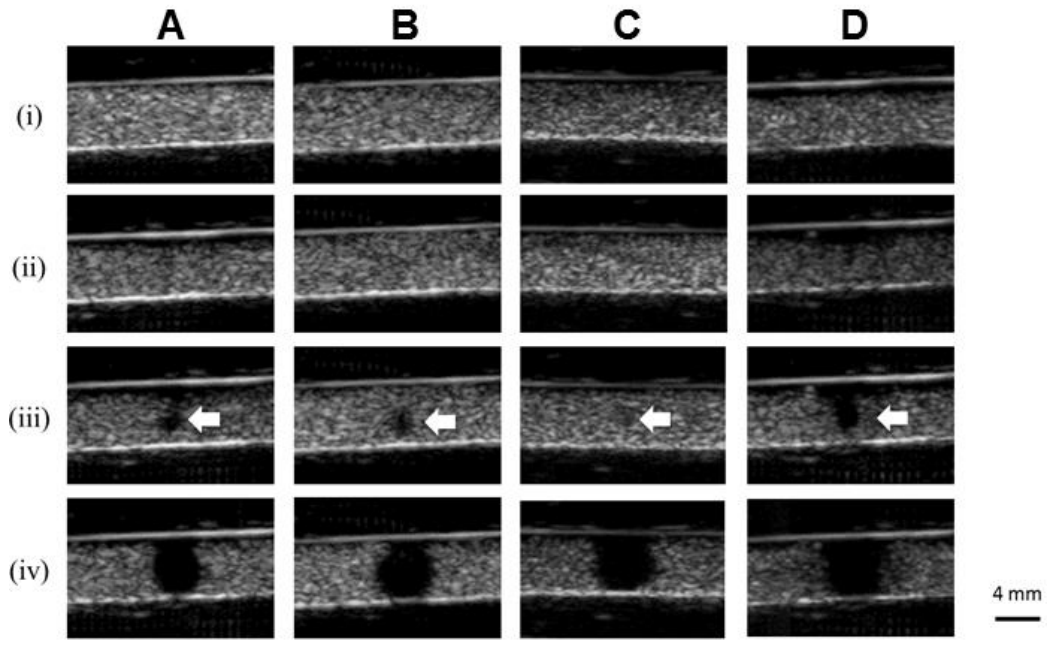

Figure 4.5. In vitro cavitation monitoring: B-mode images in transverse plane after the sonication. (A) Without the skull in place using 100 cycles. (B) With the macaque skull in place using 100 cycles. (C) With the human skull in place using 100 cycles. (D) Without the skull in place using 5000 cycles. (i), (ii), (iii), and (iv) represents 50 kPa, 150 kPa, 200 kPa, and 450 kPa, respectively. The arrows indicate the spot losing echogenicity at the pressure threshold (200 kPa). The images showed good focal alignment to the channel and the bubbles lost the property of contrast enhancement at or above 200 kPa. The shape to the hypoechogenitic area was roughly a circle with an averaged diameter of 1.3 mm at 200 kPa and 4 mm at 450 kPa.

Fig. 4.6 shows cavitation doses with and without the skull in place using 100-cycle pulses. In the macaque skull experiments (Figs. 4.6A-C), the SCD_h, the SCD_u, and the ICD without placing the skull were significantly higher ($p < 0.05$) than the control at and above 50 kPa, which also increased monotonically with pressure. After placing the macaque skull, the SCD_h was detectable ($p < 0.05$) at all pressures, whereas the detection pressure threshold for both the SCD_u and the ICD increased to 150 kPa. In the human skull experiments (Figs. 4.6D-F), the SCD_h was detectable at and above 100 kPa after placing the skull. For the SCD_u, the detection pressure threshold increased to 250 kPa. For the ICD, it became 350 kPa. The SCD_h at or above 400 kPa was undetected since the control signal with the human skull was strong. While the detection pressure threshold slightly changed after placing the macaque and the human skull, the sensitivity of cavitation doses to pressure changes remained the same.

The pulse length effect on the cavitation dose was also studied. Figs. 4.6G-I show the cavitation doses with 100-cycles and 5000-cycle pulse lengths. The SCD_h using 100-cycle pulses increased monotonically with pressure increase, whereas the SCD_h with 5000-cycle pulses reached a maximum at 300 kPa and started to decrease at pressures above 300 kPa. Similar to the SCD_h, the SCD_u using 100-cycle pulses increased monotonically with pressure, while the SCD_u using 5000-cycle pulses reached a plateau at 250 kPa and started to decrease at higher pressures. The ICD using 100-cycle and 5000-cycle pulses both increased monotonically with pressure increase, and the latter increased at a faster rate. All of the cavitation doses of 5000-cycle pulses were higher than that of 100-cycle pulses.

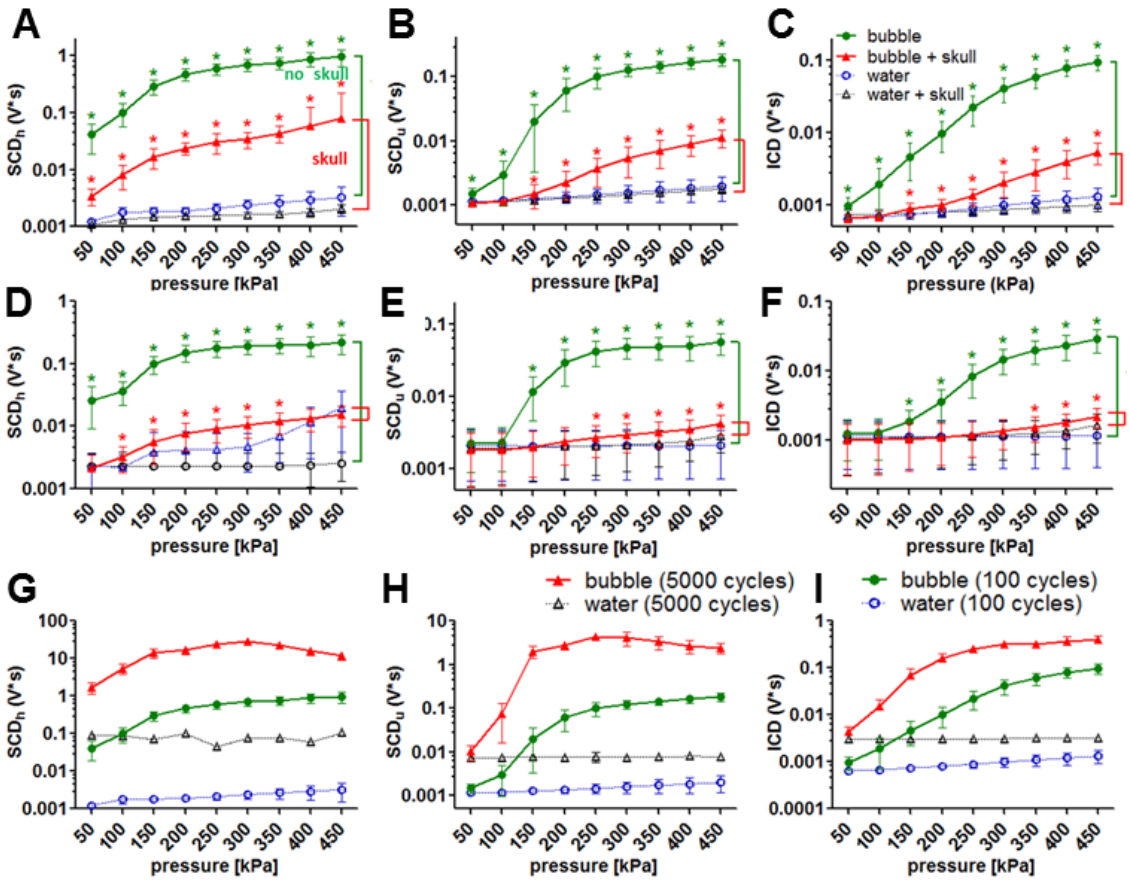

Figure 4.6. In vitro cavitation doses. (A) SCD_h, (B) SCD_u, and (C) ICD for the macaque skull experiments using 100-cycle pulses. (D) SCD_h, (E) SCD_u, and (F) ICD for the human skull experiments using 100-cycle pulses. (G) SCD_h, (H) SCD_u, and (I) ICD without the skull in place using 100- and 5000-cycle pulses. The error bar shows the standard deviation. *: $p<0.05$. Green *: comparison made in the cases without the skull in place. Red *: comparison made in the cases with the skull in place. All of the comparisons in (G)-(I) showed statistical significance. All of the cavitation doses became detectable at 50 kPa, while this detectable pressure threshold may change after placing the skull. The nonlinear effect of the skull was seen after placing the human skull at high pressures as the SCD_h increased significantly. Applying long pulses (5000 cycles) was effective in generating high cavitation doses at low pressures when compared with applying short pulses (100 cycles).

Fig. 4.7 shows the cavitation SNR, which was used to study the sensitivity of PCD using the pulse length, the detection limit, and skull attenuation. Before placing the skull, the cavitation SNR for the SCD_h, SCD_u, and ICD using 100-cycle pulses (Fig. 4.7A) ranged within 28.6-49.1 dB,

2.1-38.9 dB, and 3.1-37.0 dB, respectively. Followed by the SCD_u and the ICD, the cavitation SNR for the SCD_h was the highest. The cavitation SNR for the SCD_h, SCD_u, and ICD using 5000-cycle pulses (Fig. 4.7B) ranged within 24.8-54.6 dB, 2.2-54.8 dB, and 2.9-41.9 dB, respectively. Both the cavitation SNR for the SCD_h, SCD_u reached a plateau at 250 kPa, while it increased monotonically for the ICD.

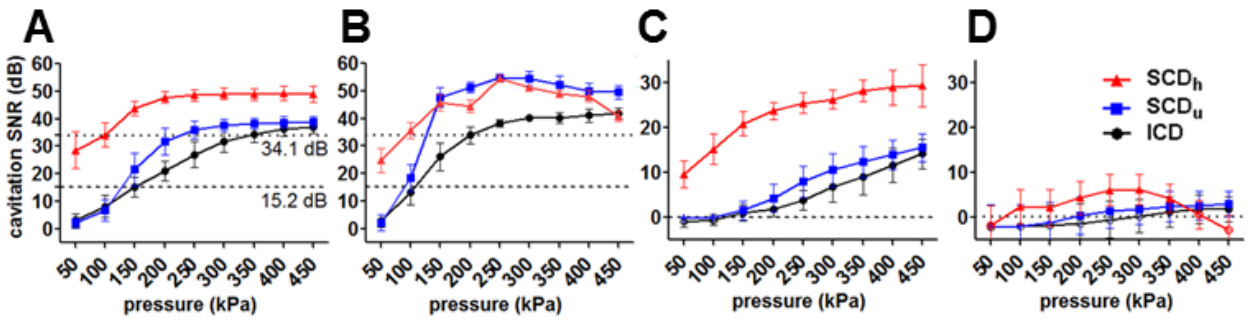

Figure 4.7. In vitro cavitation SNR (a) without the skull in place using 100-cycle pulses, (b) without the skull in place using 5000-cycle pulses, (c) with the macaque skull in place using 100 cycles, and (d) with the human skull in place using 100 cycles. The error bar shows the standard deviation. The dash lines in (a) represent the SNR threshold for surpassing the skull attenuation (macaque: 15.2 dB, human: 34.1 dB). For SNR higher than 1 dB, the detected cavitation doses were significantly higher than that of control. This 1 dB was deemed as the detection threshold with and without the skull.

Figs. 4.7C-D show the cavitation SNR using 100-cycle pulses through the skull. The cavitation SNR through the macaque skull (Fig. 4.7C) ranged within 9.7-29.4 dB, 1.6-15.6 dB, and 1.1-14.1 dB, respectively, corresponding to the statistically significant SCD_h, SCD_u, and ICD through the macaque skull compared to the control (Fig. 4.7A-C). The cavitation SNR through the human skull (Fig. 4.7D) ranged within 2.4-6.2 dB, 1.4-3.0 dB, and 1.2-1.9 dB, respectively, corresponding to the statistically significant SCD_h, SCD_u, and ICD through the human skull compared to the control (Fig. 4.7D-F). For the cavitation SNR with the skull lower than 1 dB, the corresponding cavitation doses failed to reach statistical significance ($p < 0.05$) compared to the

control. This 1 dB was deemed as the detection limit (or SNR limit), meaning that the PCD was reliable when the cavitation SNR exceeded 1 dB.

As described above, by correlating the cavitation SNR with the skull (Fig. 4.7C-D) to the cavitation doses with the skull (Fig. 4.6A-F), it was found that when the cavitation SNR exceeded 1 dB−defined as the detection limit for PCD−the transcranially acquired cavitation doses were statistically significant compared to the control. In order to assess the skull attenuation, the cavitation SNR without the skull (Fig. 4.7A) was then compared against the cases with the skull surpassing the 1-dB SNR limit (Fig 4.7C-D). It was found that the SNR without the skull should be higher than 15.2 dB and 34.1 dB (Fig. 4.7A) in order to be detected through the macaque (Fig. 4.7C) and the human skull (Fig. 4.7D), respectively. In other words, for cavitation SNR higher than 15.2 dB and 34.1 dB without the macaque and human skull, respectively (Fig. 4.7A), the cavitation SNR through the skull (Fig. 4.7C-D) would be higher than 1 dB and the corresponding cavitation doses with the skull would be significantly higher than those of the control ($p < 0.05$). The skull attenuation was then calculated by dividing by the measured skull thickness: 4.92 dB/mm and 7.33 dB/mm for the macaque and human, respectively.

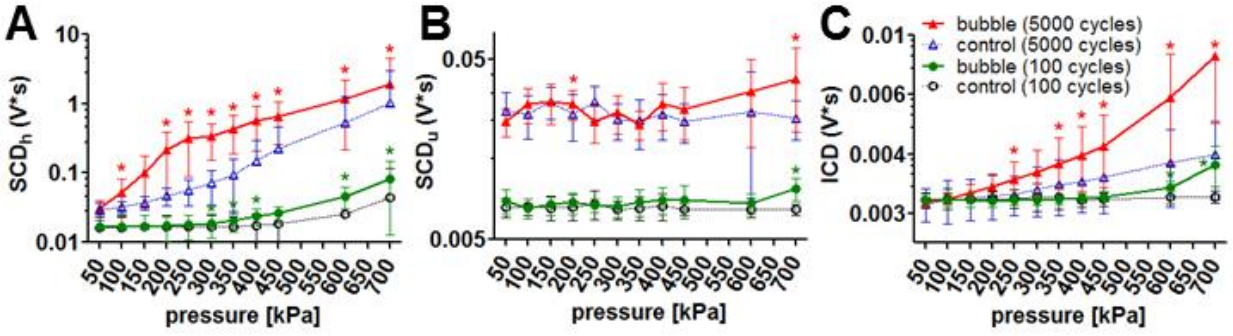

Figure 4.8. In vivo cavitation doses using 100- and 5000-cycle pulses. (A) SCD_h. (B) SCD_u. (C) ICD. *: $p<0.05$. The error bar shows the standard deviation. When using 5000-cycle pulses, the SCD_h became detectable transcranially at 100 kPa; for the ICD, 250 kPa; while the SCD_u was unrealiable and could be detected at high pressures. When using 100-cycle pulses, the pressure threshold in detecion increased.

4.3.1.2 In vivo skull effects

In vivo skull effects at different pressures and different pulse lengths were studied and compared with the in vitro findings. Fig. 4.8 shows the cavitation doses using 100- and 5000-cycle pulses. When applying 100-cycle pulses, the SCD_h, SCD_u, and ICD were significantly higher than the control at and/or above 300 kPa, 700 kPa, and 600 kPa, respectively. When applying 5000-cycle pulses, the SCD_h, SCD_u, and ICD were significant compared to the control at pressure lower than that for the 100-cycle pulses: at and above 100 kPa, at 200 kPa and 700 kPa, and at and above 250 kPa, respectively. The cavitation dose when applying 5000-cycle pulses was higher than that with 100-cycle pulses. In either case, the cavitation doses increased monotonically with pressure. Besides, the SCD_h using 100-cycle pulses at 450 kPa, the SCD_h using 5000-cycle pulses at 150 kPa, and the ICD using 5000-cycle pulses at 300 kPa showed no significance compared to the control ($0.05 < p < 0.06$) due to their higher variability.

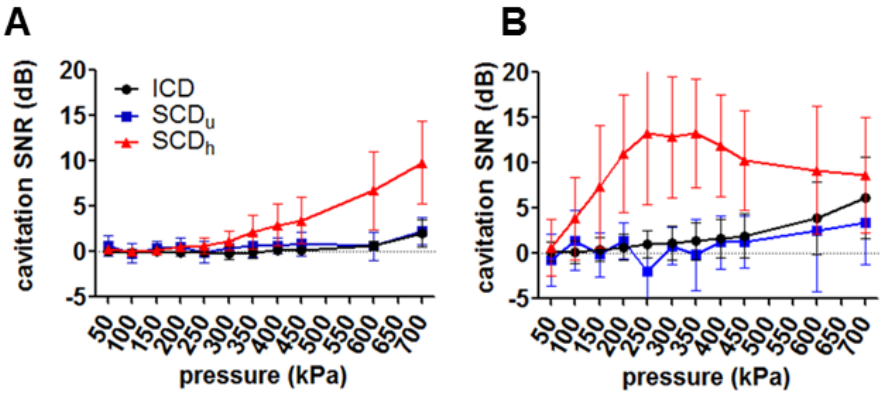

Figure 4.9. In vivo cavitation SNR using (A) 100-cycle and (B) 5000-cycle pulses. The error bar shows the standard deviation. The cavitation SNR using 100-cycle pulses increased with pressure. When using 5000-cycle pulses, the SNR of the SCD_u and ICD increased with pressure, while it for the SCD_h reached plateau due to the nonlinear effect of the skull at high pressures.

Fig. 4.9 shows the cavitation SNR for the skull effect using 100- and 5000-cycle pulses. When applying 100-cycle pulses (Fig. 4.9A), the cavitation SNR for the statistically significant SCD_h, SCD_u, and ICD compared to the control ranged within 1.2-9.8 dB, 2.3 dB, and 0.7-2.1 dB, respectively. It increased monotonically for the SCD_h and ICD, whereas it fluctuated for the SCD_u. When applying 5000-cycle pulses (Fig. 4.9B), the cavitation SNR for the SCD_h, SCD_u, and ICD ranged within 3.8-13.3 dB, 1.4-3.5 dB, and 1.0-6.1 dB, respectively. It reached a plateau for the SCD_h at 250 kPa and then started to decrease at 400 kPa. In the SCD_h case, it fluctuated at low pressures and then increased monotonically at and above 400 kPa. In the ICD case, it increased monotonically without fluctuating or reaching a plateau. The cavitation SNR at pressures where significant cavitation signals were detected compared to the control was above the 1-dB SNR limit, with the exception for SCD_u (57% of the measurements beyond the detection limit were statistically insignificant compared to the control). This result was remarkably consistent with our in vitro findings.

4.3.2 Real-time PCD monitoring during BBB opening in NHP

Real-time PCD monitoring during BBB opening was achieved. Fig. 4.10 shows four cases of PCD monitoring and the corresponding opening results in MRI at different pressures. The MRI showed BBB opening in two macaques in the thalamus and the putamen at pressures ranging from 250 kPa to 600 kPa, with the opening volume of 494.7, 230.9, 112.9, and 299.2 mm^3, respectively. The volume increased with pressure in the same macaque (Fig. 4.10B-D) in general, and its range varied across animals. The $dSCD_h$ reached a plateau in 10-30 s after injecting microbubbles and was kept at the same level for the rest of sonication duration. The $dSCD_u$ remained mostly

undetected. The dICD increased by 3.18 dB at 350 kPa and 0.19 dB at 450 kPa as compared the end of the sonication to the beginning, while it remained unchanged at 275 kPa and 600 kPa.

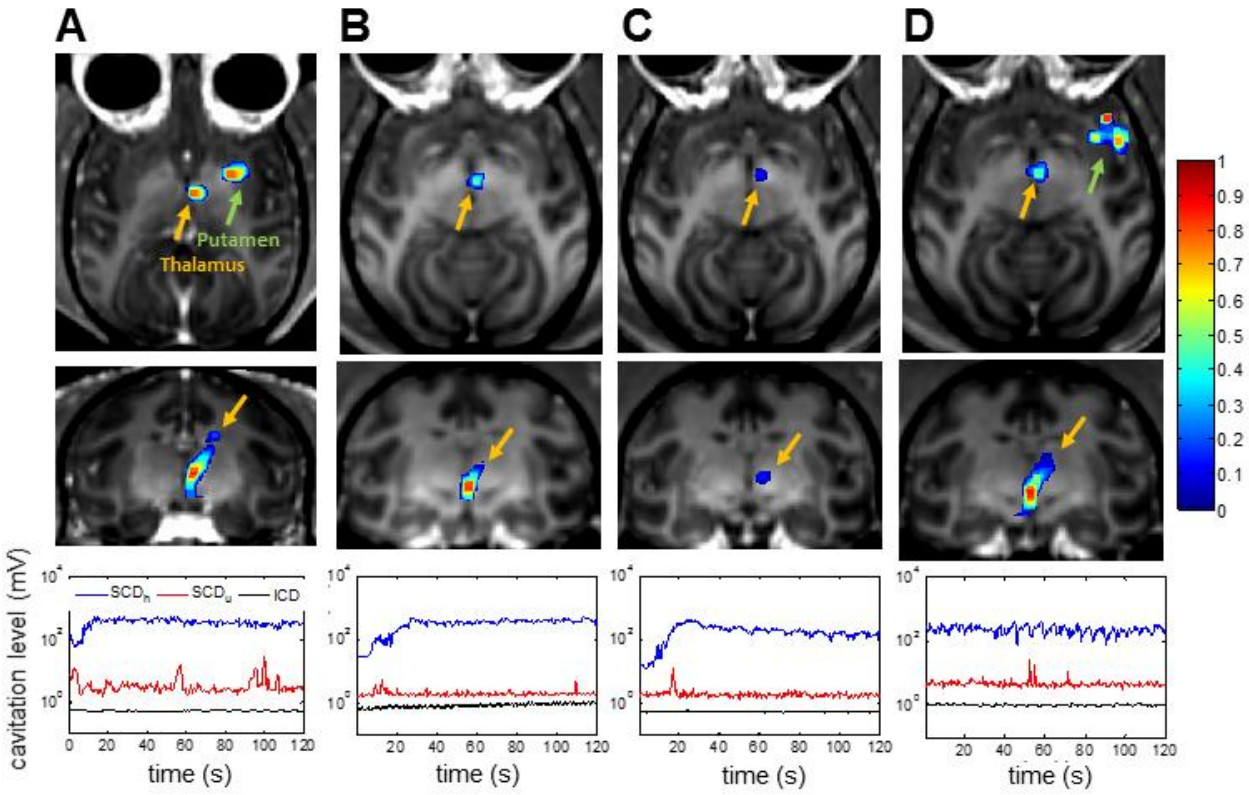

Figure 4.10. Real-time cavitation monitoring during in vivo BBB opening at (a) 275 kPa, (b) 350 kPa, (c) 450 kPa, and (d) 600 kPa in the thalamus (orange arrow) or the putamen (green arrow). The upper and middle rows show the post-contrast T1 weighted images with calculated enhancement (with colorbar) in axial and coronal view, respectively. The opening volume of (a) to (d) was 494.7, 230.9, 112.9, and 299.2 mm^3, respectively. The bottom row shows the real-time monitoring of the SCD_h, SCD_u, and ICD for sonicating the thalamus. Note that in (d) the microbubbles were injected before the sonication was started. Case (b)-(d) were performed in the same macaque.

Finally, Fig. 4.11 shows the corresponded safety assessment using T2-weighted MRI and SWI corresponding to the four BBB opening cases in Figure 8. No edema or hemorrhage was

detected in any of the animals used, corresponded to the PCD monitoring results for which minimum or no ICD increase was recorded during sonication.

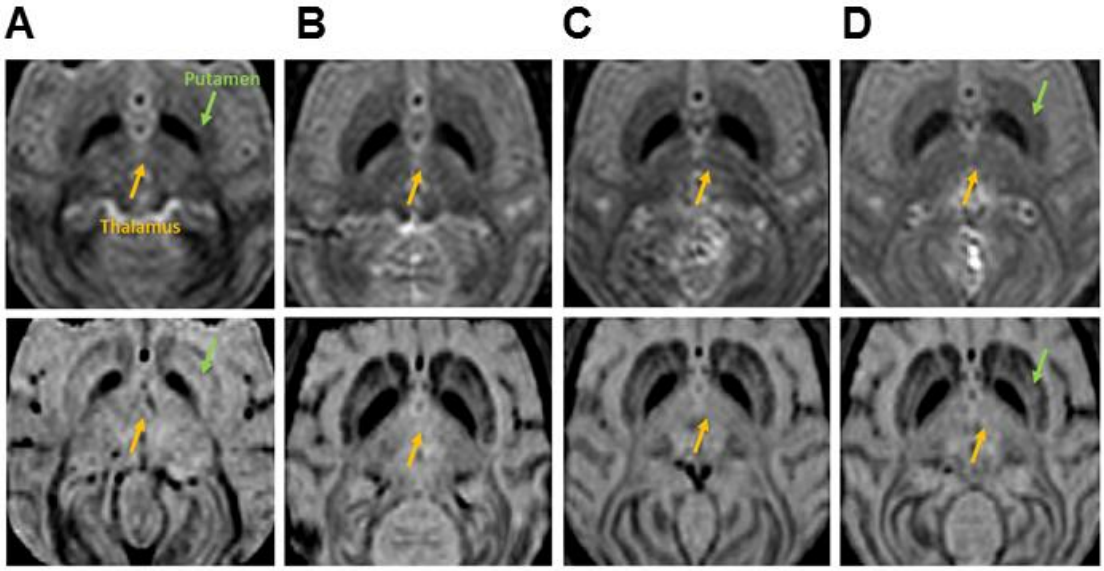

Figure 4.11. Safety assessment using MRI at (a) 275 kPa, (b) 350 kPa, (c) 450 kPa, and (d) 600 kPa. The upper row shows the T2-weighted images (coronal view) for detecting the edema, which is lighter if occurred. The lower row shows the SWI (coronal view) for detecting the hemorrhage, which is darker if occurred. In all cases, no hemorrhage and edema was detected.

4.3.2.1 BBB opening reproducibility and variability

The BBB opening in NHP was achieved with the opening volume and delivery efficiency quantified following the pipeline in Fig. 4.3 through pre- and post-contrast (Gd, gadolinium) T_{1w} imaging and T_1 mapping for Gd concentration ($[Gd]_c$) as the Gd, a paramagnetic particle does not cross the BBB, perfused the BBB opening region and shortened the relaxation time of the tissue. Fig. 4.12 showed representative BBB opening findings in two NHPs with acoustic monitoring of the cavitation dose (SCD_h: stable cavitation dose with harmonics, SCD_u: stable cavitation dose with ultraharmonics, ICD: inertial cavitation dose with broadband emission). BBB opening was

revealed in both T_{1w} imaging (Fig. 4.12A-B) and the $[Gd]_c$ map (Fig. 4.12C-D) in both gray and white matter (Fig. 4.12E-F) after a significant increase of SCD_h (Fig. 4.12G-H). In NHP 2 (300 kPa on the right putamen), an opening volume of 298 mm^3 was achieved with the highest $[Gd]_c$ in the opening area reached 0.07 mM, and the amount of Gd delivered was 10.7 nmol. The BBB opening volume was 393 mm^3 in NHP 3 (600 kPa on the left putamen) with the highest $[Gd]_c$ reached 0.06 mM, and the amount of Gd delivered was 8.7 nmol. The $[Gd]_c$ was higher in gray matter than that in white matter in the BBB opening area. While comparing to the Gd retention of the unsonicated tissue (Table 4.2), the $[Gd]_c$ at the center of the opening was higher than that in the unopened brain parenchyma (0.01-0.02 mM), similar to that of the muscle (0.06-0.07 mM), and lower than that of the vessel (0.14-0.15 mM).

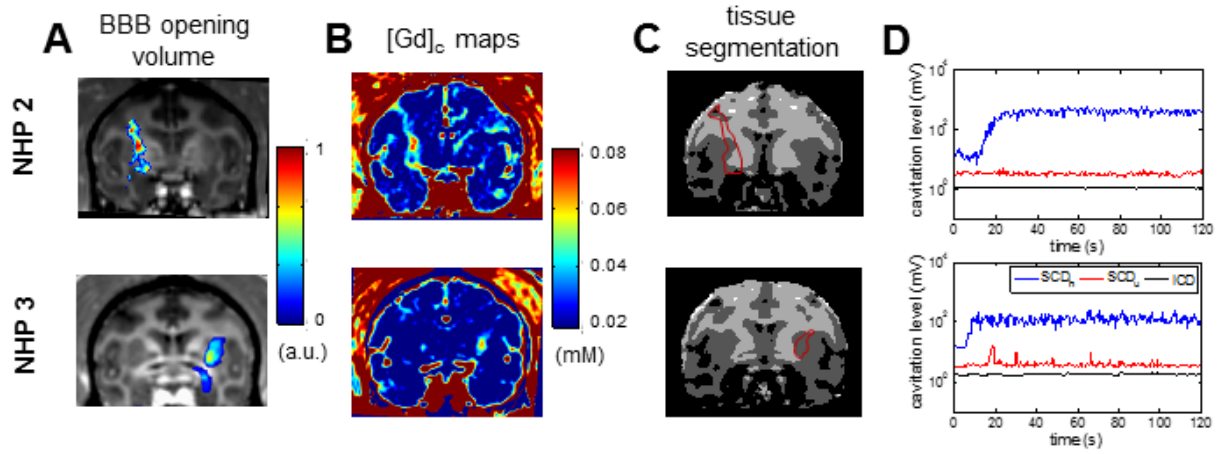

Figure 4.12. BBB opening with real-time acoustic cavitation monitoring in two NHPs. FUS-induced BBB opening in NHPs was visualized in T_{1w} images after overlaying the contrast enhancement onto the post-Gd T_{1w} image (A-B) (A: NHP 2 at 300 kPa; B: NHP 3 at 600 kPa). The corresponded Gd concentration map ($[Gd]_c$) (C-D) showed the variation of Gd delivered in gray and white matter according to the tissue segmentation map based on the pre-Gd T_1 map (E-F)(dark gray: gray matter, light gray: white matter, black: blood, white: CSF). The acoustic cavitation emission were recorded and calculated in real time. (G-H). The BBB opening of NHP 2 and 3 showed an inter-animal variation and may be due to the skull.

Table 4.2. Gd retention in different tissues after Gd injection (without applying FUS)

	Thalamus (mM)	**Muscle (mM)**	**ACA* (mM)**
NHP 2	0.017 ± 0.005	0.071 ± 0.008	0.153 ± 0.022
NHP 3	0.012 ± 0.004	0.060 ± 0.009	0.142 ± 0.014

*anterior cerebral artery

Both intra- and inter-animal variation in BBB opening were observed in the quantitative results (Fig. 4.13). In repeated sonication in NHP 1 (275 kPa at putamen, Fig. 4.13A) to estimate intra-animal variation, the coefficient of variation in the opening volume was 22% (ratio of the standard deviation to the mean). Inter-animal variation was observed in the pressure threshold for BBB opening after applying an estimate of 50% pressure increase to compensate the skull attenuation. As shown in Fig. 4.13B, the pressure threshold for NHP 1 and 2 was lower (250 kPa) than that in NHP 3 (350 kPa) with the same range of vital signs during sonication (Supplementary Table S1). This discrepancy was also observed in the $[Gd]_c$ map analysis performed in NHP 2 and NHP 3 (Fig. 4.13C), showing that the amount of Gd delivered and the delivery efficiency in NHP 2 was higher than that in NHP 3 using the same pressure. This inter-animal variation may be due to the difference in skull and tissue attenuation. Nevertheless, an opening volume of 400 mm^3 and 15 nmol of Gd delivered (0.0015% of delivery efficiency) could be achieved.

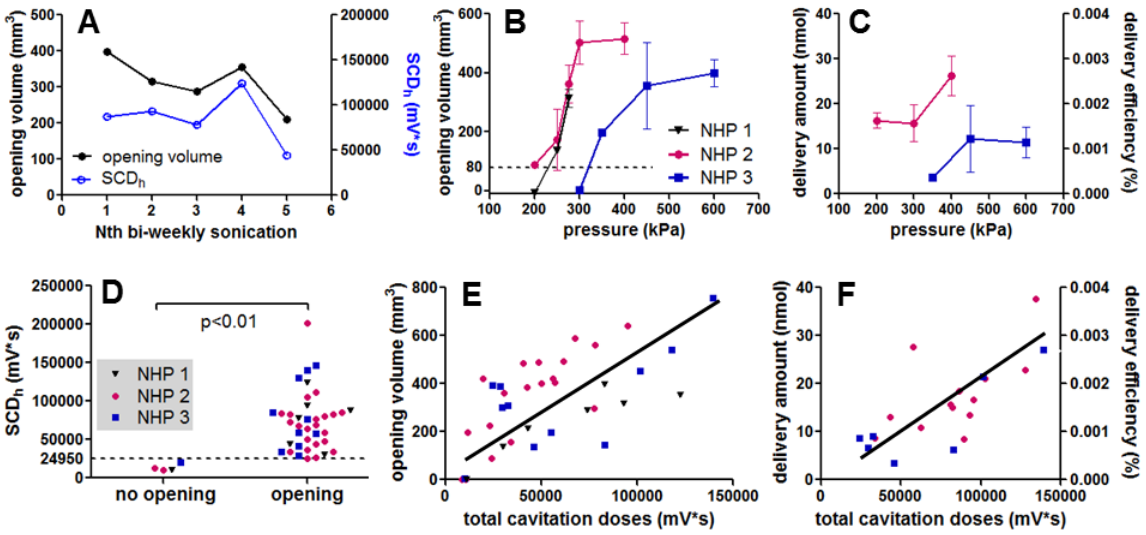

Figure 4.13. Cavitation monitoring in assessing the BBB opening and drug delivery. (A) In order to study the intra-animal variation, NHP 1 was sonicated with the same targeting (putamen) and acoustic parameters (275 kPa) in a bi-weekly basis five times. FUS-induced BBB opening was performed in three NHPs with the opening volume (B), and the drug delivery analysis was performed in two NHPs for the amount of Gd delivered and the delivery efficiency (C). NHP 1 to NHP 3 were sonicated 7, 12, and 24 times, respectively, and the error bar represents standard deviation. Both (B) and (C) showed an inter-animal variation as the BBB opening threshold for NHP 1 and 2 were lower than that for NHP 3. Quantified cavitation doses (SCD_h: stable cavitation dose with harmonics, SCD_u: stable cavitation dose with ultraharmonics, ICD: inertial cavitation dose) were correlated with the BBB opening outcomes. The SCD_h can be used to detect the effectiveness of BBB opening (D). For a quantitative assessment, the opening volume (E), the amount of delivered Gd and delivery efficiency (F) was positively correlated with the total cavitation dose (SCD_h + SCD_u + ICD). (The R^2 of the linear fitting in (E) for NHP 1 to 3 and all experiments across animals was 0.81, 0.63, 0.50, and 0.47, respectively; that in (F) for NHP 2, 3, and all experiments across animals was 0.52, 0.71, and 0.61, respectively.)

4.3.2.2 Cavitation monitoring characterizing BBB opening

Cavitation monitoring characterized BBB opening without significant intra- and inter-animal variation, and could be used to predict BBB opening volume, amount of delivered Gd and its delivery efficiency. The cavitation monitoring was positively correlated with the BBB opening volume given the intra-animal variation (Fig. 4.13A), suggesting the possibility of using cavitation

monitoring as a feed-back loop to control the FUS treatment in NHPs. Moreover, the SCD_h (sensitive to bubble activity at low pressures) was found to be an indicator of the effectiveness of the FUS procedure among animals (Fig. 4.13D, $p < 0.01$). The total cavitation doses ($SCD_h + SCD_u$ + ICD) was positively and linearly correlated with the opening volume (Fig. 4.13E, $R^2 = 0.47$), amount of delivered Gd and delivery efficiency (Fig. 4.13F, $R^2 = 0.61$), and could serve as a surrogate for MRI-based treatment evaluation. No significant difference was found among animals, while the R^2 of each individual varied. The total cavitation doses was adopted since it best correlated with the opening outcomes as the SCD_h and SCD_u may reach a plateau at high pressures while the ICD was detected[70]. Transcranial cavitation monitoring showed insignificant intra-animal variation may be because the recorded cavitation signal reflected the in situ pressure after attenuation.

4.3.3 Effect of brain heterogeneity

4.3.3.1 Gray and white matter

The effect of brain heterogeneity on BBB opening, drug delivery, and cavitation monitoring was separated into two parts: the effect of gray and white matter, and the effect of large vessels. In studying the effect of gray and white matter (Fig. 4.14), three animals were sonicated at the caudate nucleus and putamen at pressures causing a BBB opening volume of 400 mm^3 (300 kPa for NHP 2, and 450 kPa for NHP 3 and 4 due to the inter-animal variation). The opening volume in the caudate nucleus was the same or slightly smaller than that in the putamen in the same animal without statistical significance (Fig. 4.14A), and the cavitation response revealed the same trend (Fig. 4.14B). Although the gray-and-white matter composition in the sonicated area was about 1:1

(Fig. 4.14C), the gray matter contributed 68.8% of the BBB opening in comparison to 21.4% for the white matter (Fig. 4.14D), meaning that the gray matter had the probability of BBB opening three times higher than that of the white matter. In order to investigate the capability of cavitation monitoring on the gray and white matter, their opening volume were delineated for correlating with the total cavitation dose. As shown in Fig. 4.14E, a better correlation of cavitation dose to the total opening volume was found ($R^2 = 0.51$, $p < 0.001$) compared with the volume of gray matter only ($R^2 = 0.15$, $p = 0.05$), suggesting that the cavitation was detected in both the gray and white matter and caused BBB opening in both.

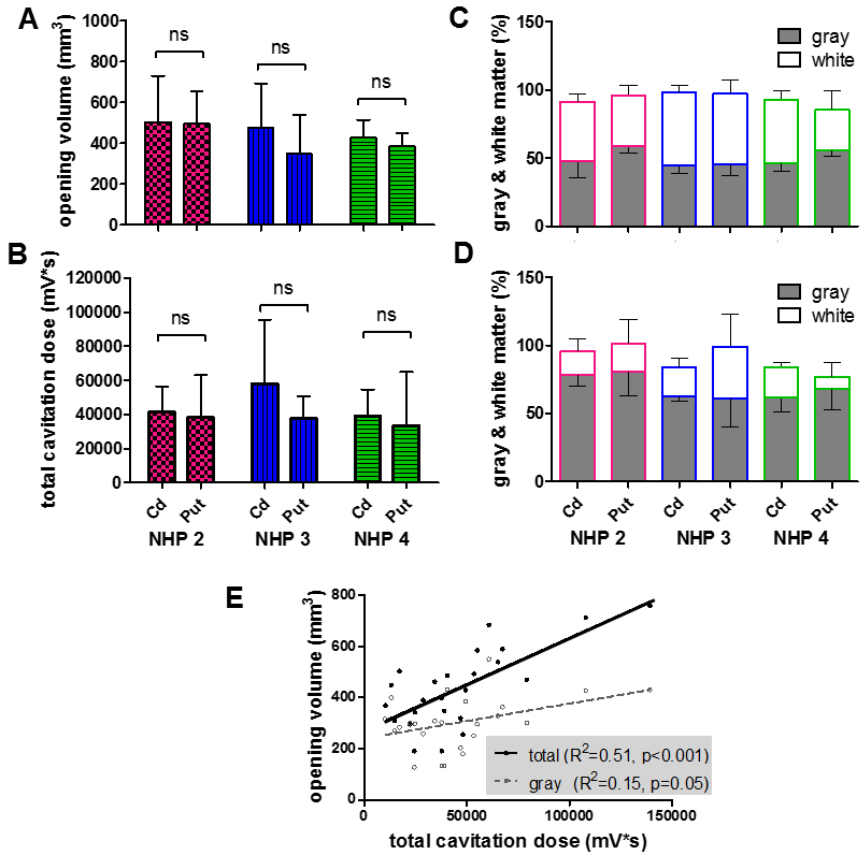

Figure 4.14. Effect of gray and white matter. FUS was applied in the caudate and putamen in three animals causing a BBB opening volume close to 400 mm^3 (300 kPa for NHP 2, 450 kPa for NHP 3 and 4). The opening volume was shown in (A), and the total cavitation dose in (B). Based

on the tissue segmentation, the gray-and-white matter composition in the sonicated area (C) and in the BBB opening area (D) were calculated. The correlation of total cavitation dose to the BBB opening volume was calculated in (E), in which it was better correlated with the total opening volume than with the volume in gray matter.

4.3.3.2 Vasculature

The effect of the large vessel (diameter ≥ 1 mm) in the BBB opening and cavitation monitoring were investigated by targeting a region (putamen) close or including the middle cerebral artery (MCA) in NHP 4. As shown in the MRA (Fig. 4.15A-C), the NHP brain is rich in cerebral blood vessels of different sizes. When applying FUS at 450 kPa, the BBB opening was found to be successful regardless of the distance to MCA in the four cases in Fig. 5D (opening volume: 309, 469, 443, and 758 mm^3 and angle of incidence to the skull: 24°, 18°, 35°, 41° for case i to iv, respectively). However, the cavitation response was significantly enhanced as the focus drew closer to the MCA. Interestingly, the spontaneous SCD_u and ICD were found to be reliably detected when targeting a region including MCA, and a periodicity of the cavitation level was similar to the breathing rate in certain cases where large vessels were in the focus. This increased cavitation response was also observed in the PCD calibration assessing the cavitation level (the cavitation dose of one single pulse) at different pressures (Fig. 4.15E-G) after the BBB opening in Fig. 4.15D. The ICD increased monotonically with pressure (Fig. 4.15G) while the SCD_h (Fig. 4.15E) and SCD_u (Fig. 4.15F) increased until a plateau was reached at higher pressures. Furthermore, although the opening volume in cases ii and iii were similar, the cavitation level of SCD_h, SCD_u, and ICD in the PCD calibration followed a different variation. The SCD_h was slightly lower at pressures above 300 kPa while the SCD_u and ICD were higher in case iii (MCA in the focus) compared to case ii (Fig. 4.15D).

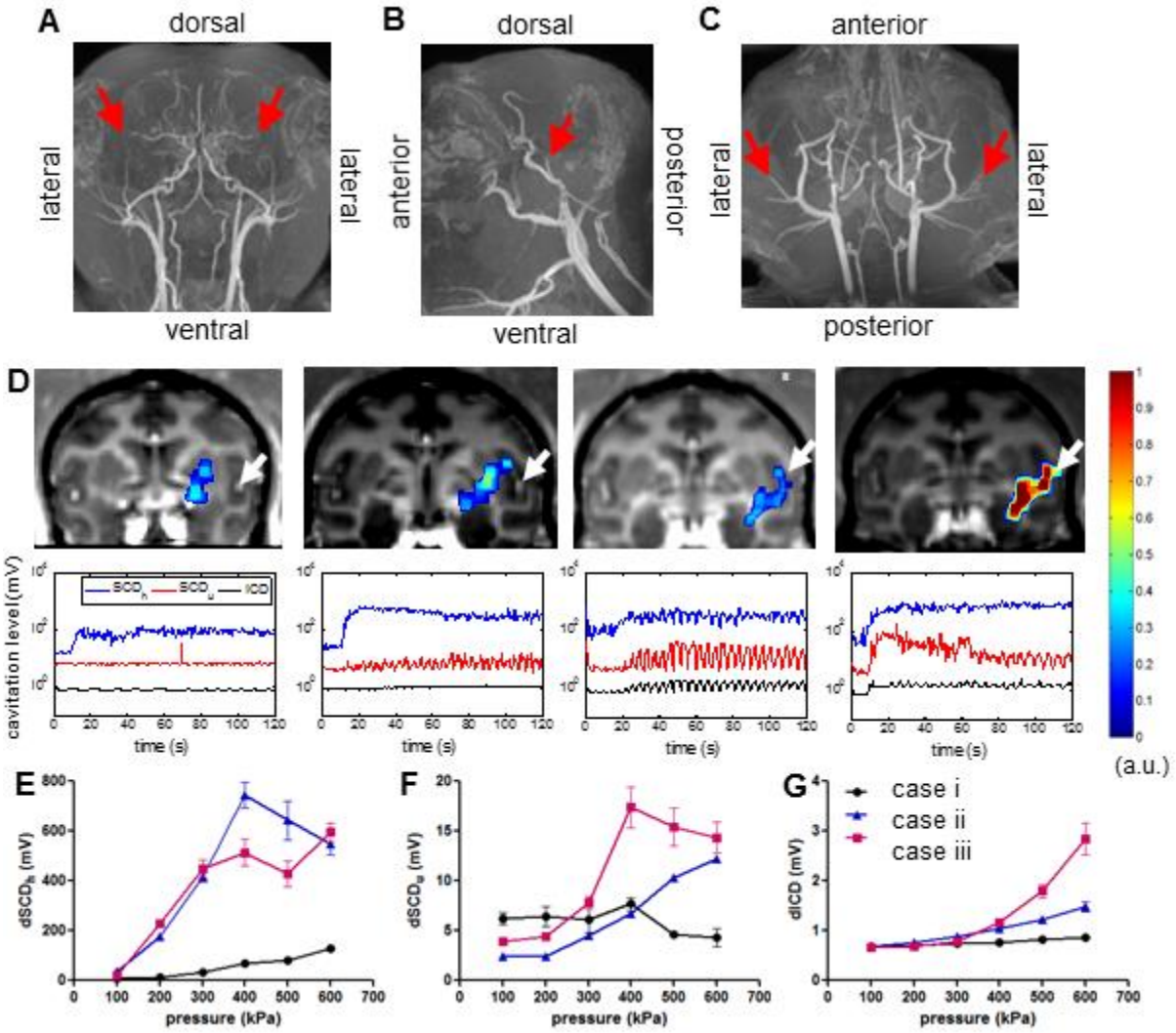

Figure 4.15. Vasculature effect. MR angiography (MRA) in NHP in (A) coronal, (B) sagittal, and (C) horizontal view, and the middle cerebral artery (MCA) was indicated by an arrowhead. (D) Four BBB opening cases targeting regions proximal to the MCA (arrowhead) at 450 kPa in NHP 4, where the upper row showed the opening volume overlaying onto the post-Gd T_{1w} images and the lower row was the cavitation response along the sonication time. PCD calibration (E-G) after BBB opening in cases i-iii was performed in order to assess the cavitation level at different pressures (10 pulses per pressure) with targeted regions near or include the MCA (E: SCD_h, F: SCD_u, G: ICD), and the errorbar represented the standard deviation of the 10 sonications. Note that the opening volume for case i to iv was 309, 469, 443, and 758 mm^3 and angle of incidence to the skull: 24°, 18°, 35°, 41°, respectively. The cavitation level varied as the targeted region approached the MCA that was correlated with the opening volume but was found to be independent of the incidence angle.

4.3.4 Safety for large BBB opening cases

The safety of the FUS procedure was evaluated in all experiments using MRI in 1 h (edema in hyper-intensity of T_{2w} imaging, and hemorrhage in hypo-intensity of SWI). No edema, hemorrhage, or any kind of macroscopic damage was detected in any of the animal in this study. Representative cases with large BBB openings in the four animals were shown in Fig. 4.16. For NHP 1, one sonication was performed at 275 kPa (putamen, opening volume: 397 mm^3), two for NHP 2 at 400 kPa (caudate and putamen, opening volume: 783 mm^3 and 436 mm^3, respectively), one for NHP 3 at 450 kPa (putamen, opening volume: 845 mm^3), and two for NHP 4 at 600 kPa (caudate and putamen, opening volume: 623 mm^3 and 539 mm^3, respectively). In addition, no damage was detected in the experiments for the vasculature effect (Fig. 4.15) despite the high cavitation response. The damage, if occurred, might be microscopic and insignificant in histological examination for sonications without detectable damage in MRI [67].

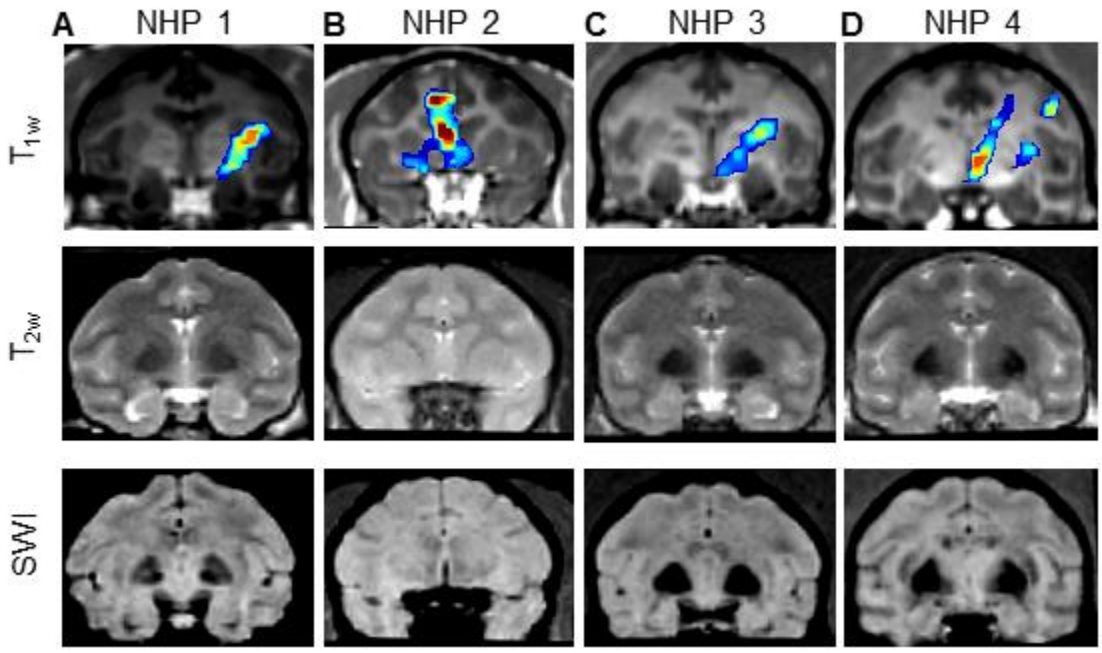

Figure 4.16. Safety assessments in the MRI. (A) NHP 1 targeting putamen at 275 kPa. (B) NHP 2 targeting caudate nucleus and putamen at 400 kPa. (C) NHP 3 targeting putamen at 450 kPa. (D) NHP 4 targeting caudate nucleus and putamen at 600 kPa. No edema or hemorrhage was detected in any of the cases. 1st row: contrast enhancement of the BBB opening overlaying onto the post-Gd T_{1w} imaging; 2nd row: T_{2w} imaging for edema; 3rd row: susceptibility-weighted imaging (SWI) for hemorrhage.

4.4 DISCUSSION

In this chapter, we have demonstrated the primate skull affecting the PCD performance using short and long pulses. Its sensitivity, reliability, and transcranial cavitation detection limit in macaques and humans were investigated, by performing in vitro macaque and human skull experiments as well as in vivo experiments in macaques with BBB opening. The in vitro study allows extensive investigation of the cavitation characteristics and the primate skull effects, while the in vivo study confirmed the in vitro findings using realtime PCD monitoring. The transcranial PCD was found sensitive to detect cavitation signals at pressures as low as 100 kPa in vivo. The transcranial detection limit (1-dB SNR limit) served as a criterion to guarantee reliable detection. Realtime PCD monitoring was performed during BBB opening, in which safe opening and reliable detection was achieved using long pulses.

Moreover, our in vivo findings presented have provided a link in transcranial cavitation detection from small animals to primates through the use of both stable and inertial cavitation dose. We have demonstrated the primate skull effects in PCD both in vitro and in vivo, the detection threshold for harmonics, ultraharmonics, broadband emission to achieve reliable detection. The in vivo findings demonstrated a clear relationship between the cavitation measures and the BBB opening characteristics in non-human primates such as opening volume, the drug amount delivered

and the delivery efficiency. Cavitation was detected in both gray and white matter and was correlated with the BBB opening in both, while the cavitation response varied by the large cerebral vessels due to the change of cavitation threshold.

4.4.1 B-mode imaging vs. PCD

B-mode imaging was used to visualize the cavitation, ensuring the focal alignment to the channel and confirming the loss of echogenicity became detected at 200 kPa with and without the skull. It visualized cavitation by the maintenance or loss of echogenicity, representing stable or inertial cavitation, respectively. It also confirmed good focal alignment to the channel before and after placing the skull by detecting the bubble collapse at the center of the channel. In addition, it confirmed that the loss of echogenicity became detectable at 200 kPa in the presence of the skull.

In contrast to the active visualization of B-mode imaging, the PCD served as an indirect monitoring tool. The PCD was shown to be more sensitive than B-mode imaging in this study since it detected inertial cavitation at 50 kPa, lower than the lowest pressure losing echogenicity (200 kPa). Detecting bubble destruction in B-mode imaging is limited by its spatial and contrast resolution, which failed to detect a smaller amount of bubble destruction at pressures lower than 200 kPa. Therefore, B-mode imaging was used to supplement to the PCD results rather than to determine the inertial cavitation threshold. This result−PCD was more sensitive than B-mode imaging−was different from a previous study [171], which may due to the different excitation frequency and microbubbles used as well as different sensitivity of the imaging and PCD systems. On the other hand, the inertial cavitation occurred at 50 kPa in our study due to low excitation frequency, long pulse lengths [172], and low stiffness of the in-house microbubbles with a 4-5 μm

diameter [100]. This threshold is comparable to experimental results reported by other groups [172-174] as well as numerical simulation [175].

4.4.2 Cavitation doses without and with the skull

There is a need to define a quantity that could be used to assess the FUS treatment outcome. Since both thermal and non-thermal based FUS treatment outcomes are closely related to the extent of cavitation [48, 176-178], which is typically reflected by the nonlinear emissions including harmonics, ultraharmonics, and broadband emissions, the quantity "cavitation dose" was employed here. The quantification of cavitation doses is based on the detected signals, emitted by acoustic cavitation and attenuated by the brain or skull. Therefore, the true cavitation dose (or cavitation dose in situ) should be estimated by accounting for the skull or tissue attenuation.

The pulse length affected the characteristics of the cavitation dose (Fig. 4.6). Using 100-cycle pulses, the cavitation doses increased monotonically with pressure increase as the magnitude of bubble oscillation increased. Furthermore, using long pulses (5000 cycles) was found to be more effective in generating higher cavitation dose. This was not only due to the integration over long pulse duration, as the cavitation doses did not linearly increase with the pulse length. In fact, the ICD still increased monotonically with pressure increase, while the SCD_h and the SCD_u reached a plateau at 250 kPa. It could therefore be explained that under a long-pulse excitation, a larger number of microbubbles underwent stable and inertial cavitation. When most microbubbles were undergoing inertial cavitation and collapse immediately without contributing to stable cavitation, stable cavitation reached a plateau and started to decrease. We also speculate that the microbubbles undergoing stable cavitation diffused faster using longer pulses and failed to enhance the SCD_h.

Through the skull the trend of cavitation doses to pressure change remained the same, while the pressure threshold for the cavitation doses becoming detectable varied depending on the type of cavitation doses and the skull (Fig. 4.6). The monotonical increase of cavitation doses with pressure remained the same after placing the macaque and the human skull for signals surpassed the skull attenuation. On the other hand, the pressure threshold to detect the SCD_h through the macaque skull remained unchanged, while it increased for the SCD_h and ICD; for the human skull, the threshold increased for all three cavitation doses. In all types of cavitation doses, the pressure threshold for the SCD_h was the lowest, followed by the SCD_u and ICD. The SCD_h remained detectable through the skull at 50 kPa and 100 kPa for macaques and humans, respectively. For the SCD_u, the pressure threshold increased to 150 kPa and 250 kPa in the macaques and humans, respectively; for the ICD, 150 kPa and 350 kPa, respectively. This was due to the low signal intensity, even though the ultraharmonics and the broadband emissions occurred at 50 kPa.

The in vivo skull effect (Fig. 4.8) was supported by the in vitro findings, except that the in vivo SCD_u was unreliable. Using 100-cycle and 5000-cycle pulses, the SCD_h as well as the ICD increased monotonically with pressure like the in vitro cases, with the exception that the SCD_h for the 5000-cycle pulse did not reach a plateau. This could be due to the nonlinear scattering from the skull and possible air trapped between the transducer and the animal's skin. On the other hand, unreliable SCD_u was discerned due to the less frequent ultraharmonics as it was observed in real-time monitoring of BBB opening (Fig 4.10). It could be attributed to microbubble dynamics in the biological environment such as blood, capillary, and blood vessel, as those were the main differences between the in vivo and the in vitro experiments. The biological environment could presumably affect cavitation for different types of microbubbles with varied extents. In addition, the varying blood pressure could contribute to the variation of the SCD_u as well [179]. Finally, the

inertial cavitation was detected at and above 250 kPa, although it was possible that microbubble collapse could occur at lower pressures.

The cavitation SNR was defined and used to investigate the sensitivity and reliability of PCD under different conditions such as varied pressures and pulse lengths, and the skull effects on them. It served as a quantitative way to find the transcranial detection limit (1-dB SNR limit), the skull attenuation, and ways to improve the detection. In order to achieve reliable PCD, one may increase the cavitation SNR in two ways: increasing the pressure or the pulse length. Using long pulse lengths was found effective in increasing the cavitation SNR at low pressures, while the cavitation SNR for the SCD_h decreased at high pressures due to the cavitation characteristics and nonlinear skull scattering as described in the previous section for discussing the cavitation doses. Increasing the number of microbubbles injected could also improve the cavitation SNR since the inertial cavitation could be detected at low pressures (250 kPa) in the in vivo skull effect experiments after a second bolus injection of microbubbles, which was speculated that more microbubbles were circulating. Although safety could be a concern, no damages were reported in other studies using increased doses of microbubbles to induce BBB opening [160, 180].

The cavitation signals were reliable through the skull provided that the cavitation SNR was above 1 dB. This 1-dB SNR limit was acquired in the in vitro study and confirmed in the in vivo study. As in both studies, the cavitation doses showed statistical significance when satisfying this criterion with the only exception in SCD_u. In future applications, this transcranial detection limit provides us indication of inertial cavitation detected for the macaque experiments. In the clinical studies, it could give us an indication of reliable PCD for all types of cavitation doses.

Skull attenuation for macaques (4.92 dB/mm) and humans (7.33 dB/mm) in this study are comparable to previous studies [130, 181]. The attenuation by the human skull is higher than that in the macaque, which might be due to high skull density [182], strong nonlinear ultrasound transmission [183], strong reflections and different extents of mode conversion [184]. The attenuation measured in this study was averaged over 1.25-5.00 MHz. The attenuation decreases when using lower frequencies. However, the broadband emission may be filtered out if signals within 3-5 MHz were excluded in the cases of low pressures (Fig. 4.4B). Besides, harmonics from the skull and tissue nonlinearity may hinder the detection at low frequencies as described in the following paragraph. The appropriate frequency range is therefore a compromise between skull attenuation, nonlinear effects, and frequency distribution of the cavitation signals. In the future, one could estimate the in situ cavitation strength by combining the transcranial PCD measurements (provided they pass the transcranial detection limit) with the skull attenuation acquiring from simulation or ex vivo measurement in order to assess the treatment outcome.

In addition to the inherent skull attenuation, nonlinear ultrasound scattering due to the skull could further hinder the detection of harmonics. Nonlinear scattering from the human skull became apparent at and above 450 kPa (Fig. 4.7D), failing the detection of the harmonics (SCD_h) generated by the microbubble cavitation. It could be due to the fact that higher pressure was applied in order to compensate for the 80% of pressure attenuation through the human skull, causing inevitable nonlinear scattering. Second, the FUS focus was 25 mm below the human skull, which could cause stronger nonlinear effects compared to a deeper focus [183]. Third, although precautions were taken, trapped air could still be present. This phenomenon was also revealed in the in vivo macaque results (Fig. 4.8A), in which nonlinear scattering was significant using a 5000-cycle pulse. This

nonlinear effect could cause serious problems as it fails the detection of the SCD_h and may risk to overtreatment based on the monitoring.

4.4.3 Real-time PCD monitoring in BBB Opening

Real-time monitoring of the cavitation doses was performed during BBB opening using 5000-cycle pulses (Fig. 4.10), providing the information of bubble perfusion and the cavitation level. Furthermore, the use of long pulses enables reliable PCD monitoring and facilitate opening at low pressures, and this lower pressure threshold was also found in the study done in mice [161]. By monitoring the SCD_h, the time for microbubbles perfuse to the sonicated region as well as the microbubble persistence during the entire treatment could be monitored at and above 250 kPa. The lowest pressure for detecting the SCD_h was 100 kPa as was found in the in vivo skull experiments (Fig. 4.8A).

The SCD_u was detected when the microbubbles first perfused the brain in two (Fig. 8b-c) out of the three cases (Fig 4.10A-C), although the variability was high. Our finding was consistent with the other group [67, 180], in which not all cases showed significant ultraharmonics. Low SCD_u was affected by the noise from the system or the air trapped in the beam path. Therefore, in order to reliably detect the SCD_u a pressure as high as 700 kPa should be applied (Fig. 4.10B), which increases the probability of damage. This finding was also consistent with the method of detection and real-time feedback control based on ultraharmonics in mice by O'Reilly et al. [79]. However, this feedback control method based on ultraharmonics may not be optimal for large animals due to unreliable SCD_u and skull effects.

By monitoring the ICD, the safety of the treatment could be monitored in real time since low (SNR < 3dB) or no inertial cavitation was detected in the cases of safe BBB opening. Low or no ICD obtained during BBB opening experiments (Fig. 4.10) compared to the in vivo skull effect (Fig. 4.8) was most likely due to lower number of microbubbles circulating during FUS treatment, since significant increase of ICD was obtained in the same animal after a second bolus injection of microbubbles for in vivo skull effect.

Safe BBB opening was achieved at low pressures (250-600 kPa) in both the putamen and the thalamus (Fig. 4.10). No differences were observed between the putamen and the thalamus in terms of cavitation doses in this study. The opening volume varied across animals, but it increased with pressure in the same macaque as compare the 350-kPa case (Fig. 4.10B) with the 600-kPa case (Fig. 4.10D). The 450-kPa case had smaller opening volume than the 350-kPa case was expected based on the slightly decreasing SCD_h, which may due to the animal's physiological effect to the circulating microbubbles. For the safety threshold of ICD, a 3.18-dB (1.44 times above the background signal) SNR of ICD was detected in the case without damage (Fig 4.10B). This indicated that the ICD safety threshold was higher than 3.18 dB for the system used. This result was consistent with the study done by Arvanitis et al. using a lower excitation frequency [180], in which 6.33 dB (4.3 times above the background power signal) was reported with hemorrhage.

Studies correlating the cavitation dose to the opening volume based on single-element PCD should consider using the ICD instead of the SCD_h at relatively high pressures due to three reasons. First, the positive correlation of the ICD to pressure is independent of the pulse length which affected the cavitation characteristics. Second, the ICD is not affected by the nonlinear ultrasound scattering due to the skull (e.g. the human skull results in Fig. 4.6D-F). Third, the ICD can also provide safety assessment [180, 185]. One major challenge here is to achieve reliable ICD

detection by increasing the cavitation SNR. On the other hand, passive cavitation mapping [186, 187] including spatial information of cavitation could give us more precise estimation of opening volume and safety assessment using both the SCD_h and ICD. Further studies regarding the effects of brain heterogeneity and individual differences in cavitation doses and treatment outcome in large animals are crucial before clinical applications.

4.4.4 PCD to characterize BBB opening

Several new findings have been shown in this study in comparison to previous NHP studies. First, the cavitation monitoring was shown to be highly correlated with clinically relevant measures in the deeply seated subcortical structures, an improvement compared with the previous study using relative MRI enhancement in the cerebral cortex [180]. Second, cavitation monitoring was capable of detecting the delivery in both gray and white matter, while large vessels (diameter > 1 mm) resulted in saturated stable cavitation response and significantly higher inertial cavitation response at high pressures without detectable damage in the MRI. Third, the cavitation quantification using harmonics, ultraharmonics, and broadband emission could improve the correlation to the BBB opening and drug delivery via compensation of the effect of brain heterogeneity and the nonlinear skull effect. Although harmonics can be more easily detected, they could be hindered by nonlinear skull or large vessel effects at higher pressures and deteriorate the correlation with drug delivery and BBB opening. The primate skull is reported to contribute to harmonic signals at higher pressures, which decreased the cavitation signal-to-noise ratio[70]. Furthermore, harmonics from bubbles in the large vessels could reach a plateau at higher pressures (Fig. 4.15). These could be the reasons why the use of harmonics has previously failed in predicting the BBB opening volume[69], and that harmonics were correlated well mostly in the cerebral cortex in a small

juvenile monkey with respectively fewer large vessels and thinner skull producing insignificant skull effects[180].

Inertial cavitation reported to be indicative of vascular damage [67] or using ultraharmonics to control the treatment [79] should be considered with caution in large animals, since the large vessels can result in high ultraharmonics and broadband emission without detected damage in radiologic examination implying no significant damage in the histological examination [67]. This vascular effects in humans could prove even more important due to the larger sizes of cerebral vessels compared to smaller animals (e.g. the cerebral artery diameter for mice, monkey, and human is 0.2 mm [188], 1.2 mm [189], and 2.0 mm [190], respectively). The reason behind variable cavitation monitoring may lie in the fact that the microbubbles circulating in large vessels responded differently to FUS. As has been reported previously, the threshold of inertial cavitation was lower in larger vessels [191, 192], so more bubbles may be disrupted in large vessels without stable cavitation, resulting in the decrease of SCD_h and SCD_u at higher pressures with a monotonically increase of the ICD. Since larger vessels allow microbubbles to nonlinearly oscillate, the energy of volumetric oscillation (SCD_h) may convert to shell oscillation (SCD_u) and violent bubble oscillation leading to bubble collapse (ICD)[19]. The high broadband emission in this case may not cause vascular damage as the microjets may exert negligible forces towards the vessel wall due to the larger lumen space. Furthermore, large vessels composed of thicker walls and muscles may not easily be disrupted. Therefore, large vessels should be excluded from the FUS focal region for reliable cavitation monitoring.

For molecule delivery to the heterogeneous brain, the BBB opening results showed a localized delivery in both the contrast enhancement and the $[Gd]_c$ map (Fig. 2). The highest $[Gd]_c$ after BBB opening was the same as that of the epicranial muscle (Table 1), since the highest tissue

permeability after BBB opening was comparable to that of tissue without BBB [193]. Moreover, the highest delivery ($[Gd]_c$) occurred only at the center of the focus given a larger opening volume (298 or 393 mm^3) with a shape similar to that of the transducer focus. This suggests that the technique is suitable for region- or point-specific delivery with the highest efficiency. If a higher amount of delivery is required, increasing the injection dosage of the drugs could enhance the amount of delivery [167]. If a larger opening volume is desired, sonication at multiple locations would be necessary. However, the BBB opening occurred with greater ease in the gray than in the white matter [67] was confirmed in this study. BBB opening occurred in both gray and white matter with the probability in the gray matter three times higher than that for the white matter (Fig. 4.14), and the drug concentration (Gd) was significantly higher in the gray matter as well (Fig. 4.12). This may be due to the lower vascularity or higher attenuation in the white matter than that in the gray matter [130]. Moreover, since cavitation could be monitored in both tissue types, this discrepancy may be associated with blood accompanied by microbubbles during sonication. For example, the blood volume (1.5-1.8 times [194, 195]) or blood flow (1.7 times [196]) in the gray matter was higher than that of the white matter. Future studies regarding this issue would be required in optimizing this technique for various tissue types.

In addition, the BBB opening was achieved targeting a region including the large vessel MCA (Fig. 4.15). However, since microbubbles in circulation would attenuate ultrasound wave propagation at varying extents depending on the vessel distribution, size, and microbubble concentration [197], this microbubble shielding effect may impose potential difficulties in humans [41] as it was reported to hinder BBB opening in monkeys [66]. Therefore, large cerebral blood vessels should be avoided in the targeted region or acoustic path during FUS planning in order to avoid opening failure as well as monitoring discrepancies. MRA could be a useful tool for

visualizing the position and size of cerebral blood vessels during the pre-planning process. Furthermore, the use of nanodroplets to induce BBB opening could potentially minimize the shielding effect since nanodroplets vaporize into bubbles only in the focus and induce opening, which also strongly decreases variability in the relationship of cavitation dose to BBB opening [78].

Modelling bubble dynamics could potentially provide a priori knowledge for the safety and efficacy of BBB opening and drug delivery in various tissue types, as the mechanical effects of cavitation have long thought to associate with vascular permeability enhancement. A proper model is thus required for these emerging therapeutic purposes. Currently, modified or lumped-parameter models based on the Rayleigh-Plesset equation (free gas bubble model) have enabled us to investigate the behavior of coated microbubbles [198, 199] and the bubble-microvessel wall effects [200], assuming symmetric bubble oscillating in free space. However, a finite-element modelling (FEM) approach provides flexibility for both symmetric and asymmetric bubble oscillation while considering a variety of bubble and in vivo environmental properties [201]. Despite the findings obtained with this modelling approach, many efforts are also required to build a linkage to the in vivo BBB opening and drug delivery. First, the mechanical effects directly associated with the therapeutic effects need to be identified. Second, the in vivo properties must be measured, including the size, shell, stiffness [100], and distribution of bubbles as well as the shape, size, and wall elasticity of the microvessels. Third, the bubble-to-bubble interaction and the bubble behavior after rupture [199]. Once the simulation method is established, magnetic resonance angiography (MRA) may be used to construct the simulation model in order to compensate for the cavitation monitoring and predict the BBB opening outcomes more accurately.

4.5 CONCLUSION

To achieve transcranial cavitation monitoring in primates, in vitro macaque and human skull experiments as well as in vivo macaque experiments to study the skull effect and BBB opening were performed. It was found that through the macaque skull the pressure threshold for detecting the SCD_h remained the same, while it increased for SCD_u and ICD; through the human skull, it increased for all types of cavitation dose. The pressure threshold for detection the SCD_h was the lowest, followed by SCD_u and ICD. The positive or negative trend of cavitation doses to pressure increase remained the same through the skull, provided that the signal intensity surpassed the skull attenuation (macaque: 4.92 dB/mm, human: 7.33 dB/mm). The SNR for reliable detection for the PCD system used in this study is 1 dB. Using long pulses enabled reliable PCD monitoring and facilitates BBB opening at low pressures. The in vivo results showed that the SCD_h was detected at pressures as low as 100 kPa; the ICD, at 250 kPa and could occur at lower pressures; the SCD_u, at 700 kPa and was less reliable at lower pressures. Real-time monitoring of PCD was performed in vivo in macaques during BBB opening, and safe opening has been achieved at 250-600 kPa in both the thalamus and the putamen, with minimum or no inertial cavitation detected. Our study showed that transcranial PCD in macaques in vitro and in vivo as well as humans in vitro is reliable by improving the cavitation SNR to surpass the 1-dB detection limit.

The study presented in this chapter expanded the role of transcranial cavitation monitoring in NHPs in vivo and demonstrated a correlation with the BBB opening volume and the drug delivery efficiency with various the tissue types and targeting. The achieved BBB opening volume, amount of delivered molecules and delivery efficiency was as high as 800 mm^3, 40 nmol, and 0.004%, respectively, and could be predicted by the real-time cavitation monitoring. Quantitative

cavitation monitoring and drug delivery were achieved in both gray and white matter, with the probability of successful BBB opening three times higher in the gray matter than in the white matter. The targeting shift was 3.7 mm in the caudate and 7.5 mm in the putamen, and the incidence angle to the skull had negligible effects on the cavitation monitoring, showing the capability of cavitation monitoring for various targeting. The large cerebral vessels, however, may affect the cavitation monitoring, and should be excluded from the FUS path.

4.6 SIGNIFICANCE & CONTRIBUTION

In this chapter, a transcranial cavitation detection system for real-time calculating all types of cavitation dose during BBB opening has been established for the first time with performance assessed in monkeys in vitro and in vivo and humans in vitro. This monitoring technique was successfully used to assess the BBB opening volume and amount of gadolinium delivered in the heterogeneous monkey brain for the first time. The heterogeneous brain effects on BBB opening and monitoring including gray, white matter, and vasculature were extensively studied as well. In a nutshell, the results herein pave the way for clinical use of the monitoring system for BBB opening to ensure treatment effectiveness.

The research contribution was shared with colleagues. Yao-Sheng Tung (PhD, Biomedical Engineering, Columbia University) and Fabrice Marquet (PhD, Biomedical Engineering, Columbia University) and mentored the study. They together with Tobias Teichert (PhD, Neuroscience, Columbia University), Carlos Sierra Sanchez (PhD, Biomedical Engineering, Columbia University), Amanda Buch (B.S., Biomedical Engineering, Columbia University), and

Matthew Downs (PhD, Biomedical Engineering, Columbia University) assisted the in vivo experiments. Vincent Ferrera (PhD, Neuroscience, Columbia University) facilitated the animal experiments.

Chapter 5

Real-time Acoustic Mapping to Visualize Cavitation Events through Primate Skulls

5.1 INTRODUCTION

As shown in Chapter 4, passive cavitation detection (PCD) serves as the only online tool to real-time monitor FUS-induced BBB opening in ensuring effectiveness and safety. For a single-element detector as described in Chapter 3 and 4, it provides overall intensity of the treatment without spatial information. While the spatial information of the treatment outcome is critical to precisely control the treatment in desired location to achieve treatment efficacy and safety, especially with the need of multiple sonication for larger BBB opening volume.

With the passive beamforming algorithm based on time exposure acoustics (TEA) [82, 83], the spatial distribution of cavitation intensity could be reconstructed. This technique is known as cavitation mapping, using a conventional ultrasound imaging transducer as a PCD array to reconstruct the intensity and the spatial distribution of the cavitation. The concept behind TEA is from time-exposure photography in which the brightness of constant and low intensity light sources were enhanced by integration over time (long exposure time). For the adaptation to the applications of acoustics, a multi-dimensional array transducer with the passive beamforming technique is used by taking the time difference in the signals received by each element in the transducer into account regardless of the time origin. This technique is suitable for passive

cavitation mapping in therapeutic ultrasound including high-intensity focused ultrasound (HIFU) [83, 202, 203], BBB opening [187, 204], and drug delivery [205] owing to the use of long acoustic pulses and higher occurrence of cavitation emission relative to the background emission. This passive cavitation mapping in combining with a fast reconstruction algorithm called sparse matrix array beamforming [206] will be able to achieve real-time monitoring.

The objective of this chapter was thus to develop a cavitation mapping technique to real-time visualize the cavitation events in the primate brain during sonication. Real-time reconstruction of the cavitation maps was achieved by incorporating GPU computation to sparse matrix beamforming and time exposure acoustics – a breakthrough as conventional cavitation mapping takes hours to reconstruct. Its performance was assessed both in vitro through the primate skulls and in vivo during BBB opening in NHPs. In both experiments, cavitation mapping was achieved transcranially, granting a powerful FUS treatment monitoring tool for future applications.

5.2 METHODS

5.2.1 Experimental design

Both phantom experiments with NHP and human skulls, and the in vivo NHP experiments for BBB opening were performed. The phantom experiments were performed to access the performance of cavitation mapping such as spatial and contrast resolution and the correlation to cavitation visualized in B-mode imaging, and the sensitivity of transcranial cavitation mapping through the NHP and human skull. The in vivo experiments were to show the feasibility of real-time treatment monitoring in large animals.

5.2.2 Passive cavitation mapping algorithm and system

The purpose of cavitation mapping was to provide both the intensity and the spatial distribution of cavitation associated with BBB opening using a conventional ultrasound imaging transducer. This spatial distribution of cavitation intensity could be reconstructed with the passive beamforming algorithm used in ultrasound imaging and time exposure acoustics (TEA) [82, 83]. The concept behind TEA is from time-exposure photography in which the brightness of constant and low intensity light sources were enhanced by integration over time (long exposure time). In our application, several passive frames were reconstructed in one single FUS pulse acquired from a PCD array (the same as an array transducer used for ultrasound imaging) and were summed together as integration over time to enhance the cavitation signals in a spatial domain, as described in Fig. 5.1.

A programmable ultrasonic system (Vantage, Verasonics, WA) with a 128-channel linear array transducer (L7-4, Verasonics, WA) was used to passively detect cavitation signal (channel data) during sonication. The channel data were then reconstructed to the passive frames (cavitation maps in discrete time points) using dynamic receive beamforming ($\sum_{n=1}^{N} S_n(x_n, x, \tau)$) and then integrate ($\int_0^T |\cdot|^2 dt$) over a period of time T:

$$C(x) = \int_0^T |\sum_{n=1}^{N} S_n(x_n, x, t)|^2 dt,$$

$$S_n(x_n, x, \tau) = \alpha(d(x_n, x)) \cdot c_n(t + d(x_n, x)/c),$$

where N is the number of elements in the linar array, S_n the channel data for the n-th element, x_n the location of the n-th transducer element, x the location of the pixel to be reconstructed, t the

delay of the emission, T the duration of signal to be integrated (76 μs), $S_n(x_n, x, t)$ the compensated channel data for the n-th channel, $\alpha(d(x_n, x))$ the compensation term for the wave attenuation after transmission over the distance between x_n and x ($d(x_n, x)$), $c_n(t + d(x_n, x)/c)$ the received cavitation signal for the n-th channel after adjusting for the time delay based on the distance between x_n and x, and c the speed of sound. Integration was applied to improve the SNR of cavitation intensity.

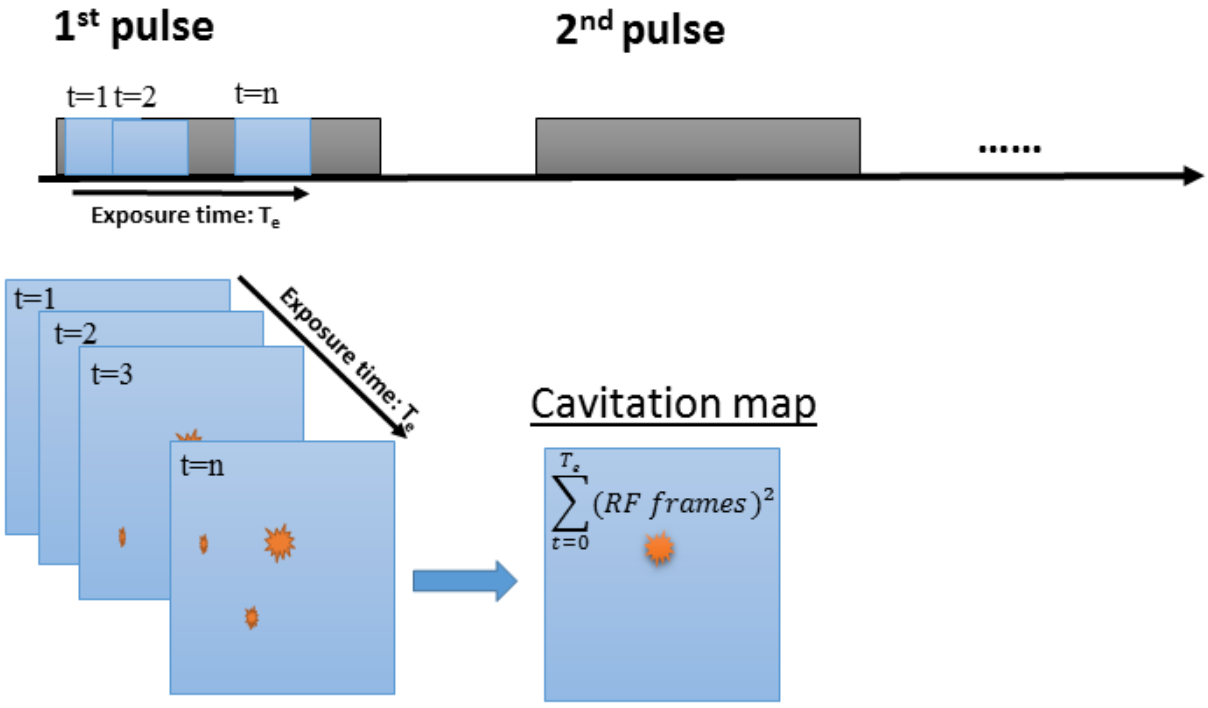

Figure 5.1 Schematic of passive cavitation mapping algorithm based on time exposure acoustics. The passive cavitation signal was acquired in a PCD array, stored as channel data for each sonicated pulse. Several passive frames were reconstructed in one single FUS pulse with different time windows representing the cavitation map in each time segment. They were summed together as integration over the exposure time (T_e) to enhance the cavitation signals in a spatial domain.

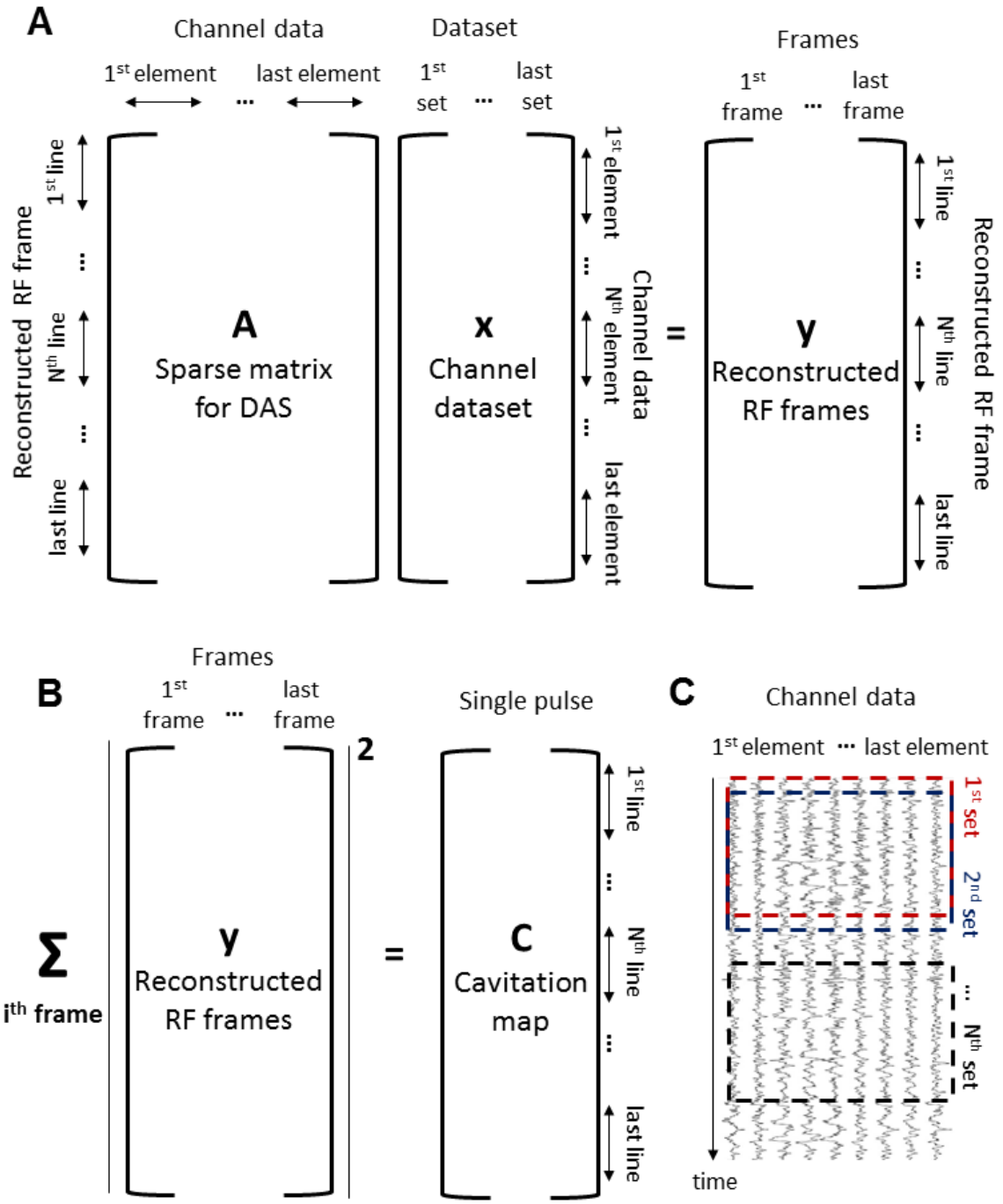

Figure 5.2. Matrix calculation for reconstructing a cavitation map. (A) Delay-and-sum (DAS) beamforming to reconstruct a series of radiofrequency (RF) frames using sparse matrix calculation. (B) The cavitation map of a single pulse is the sum of squared RF frames at each time window, i.e., the time integration of TEA. (C) The channel dataset in (A) is extracted from a series of time window in the channel data received from a single pulse during sonication.

5.2.3 Sparse-matrix beamforming

Beamforming has been widely used in ultrasound imaging both to transmit ultrasound beams and to reconstruct images after receiving scattered acoustic signals at the transducer. To reconstruct images efficiently, conventional delay-and-sum beamforming as a linear process can be programmed in a matrix format to perform fast sparse matrix computation in GPU [207]. It is a technique of software beamforming that could be implemented in Matlab with highly optimized sparse matrix multiplications. Briefly, the delay-and-sum calculation in receive beamforming could be transformed into a matrix multiplication $y = Ax$ (Fig. 5.2A) with a linear operator A based on the delay time (x and y are vectors for channel data and reconstructed image, respectively). A is a sparse matrix since only a small number of data points are taken from each channel for summation, and the rest of the matrix element in A are zeros. This concept could then be applied to the cavitation mapping in order to achieve fast reconstruction by replacing $\sum_{n=1}^{N} S_n(x_n, x, \tau)$ with a sparse matrix multiplication followed by summation of the squared RF frames (Fig. 5.2B) which were reconstructed frames based on channel data in a single pulse with a series of time window (Fig. 5.2C).

5.2.4 In vitro skull experiments

The experimental setup is shown in Fig. 5.3A. Similar to chapter 2, in-house, lipid-shell, monodisperse microbubbles (median diameter: 4-5 μm) were diluted to 2×10^5 bubbles/mL and injected to the 4-mm-in-diameter channel in the silicon phantom for sonication and cavitation detection. The PCD array and the diagnostic B-mode imaging system (Terason, MA, USA) were separately used to monitor the sonication (peak negative pressure (PNP): 100-600 kPa, pulse

length: 5000 cycles (10 ms), pulse repetition frequency (PRF): 10 Hz, duration: 2 s) in order not to interfere the PCD. B-mode images of bubble disruption were acquired to ensure the FUS focusing at the channel, which was performed through a linear array transducer (10L5, Terason, MA, USA; center frequency: 5.1 MHz) placed transversely to the FUS beam. Before each sonication, the microbubbles were injected and the old microbubbles were flushed out, which ensured the independence between each sonication and experiment. During the experiments for PCD only, the microbubbles were constantly replenished at around 0.25 mL/s in order to mimic the replenishment of the microbubbles in the brain. The PCD was performed either without or with the skull (NHP and human) in place between the channel phantom and the PCD array.

5.2.5 In vivo NHP experiments

The experimental setup is shown in Fig. 5.3B. Following the same animal procedure with the same FUS system in chapter 2 and 4, two male adult macaques (2 Macaca mulatta, weight: 9-11 kg, age: 18-20 yo) were sonicated at 0.45, and 0.6 MPa (excitation frequency = 0.5 MHz, pulse length = 10 ms, pulse repetition frequency = 2 Hz, duration = 2 min) with in-house microbubbles injected intravenously (lipid-shelled, 4-5 μm in diameter, 2.5×108 bubbles/kg), and targeted structures included the basal ganglia (caudate and putamen) and hippocampus. The PCD array was placed against temporal bone toward the FUS focus to acquire the cavitation signal for real-time monitoring of the cavitation maps during sonication. After the sonication, MRI was performed to assess the BBB opening and safety.

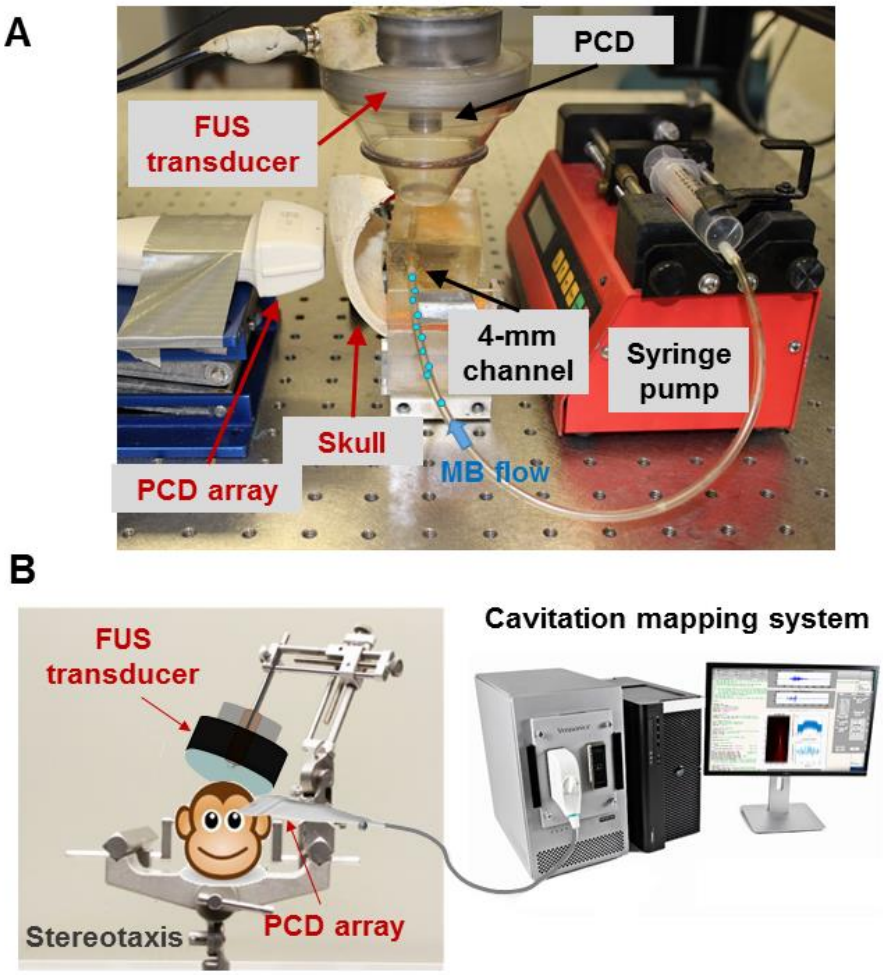

Figure 5.3. Experimental setups for (A) the in vitro skull and phantom and (B) the in vivo BBB opening in NHP. In the in vitro experiment, the FUS transducer was place on top of the channel phantom orthogonal to the PCD array, and the skull was placed in between the phantom and the PCD array for assessing the skull effects on the cavitation mapping. In the in vivo experiment, the FUS transducer was targeted to the region of interest based on the stereotaxis while the PCD array was placed against the temporal bone toward the FUS focus.

5.3 RESULTS

5.3.1 Mapping quality vs. computational time

The concept behind TEA is to enhance the continuously scattered signal and eliminate noise by summation over the exposure time (defined as the time difference between 1st time window and the last time window for extracting the channel data in a single pulse as shown in Fig. 5.1C), which also determines the computational load as the more RF frames need to be reconstructed for longer exposure time. This therefore emphasizes the importance of investigating the effect of exposure time on the computational time and the mapping quality in order to achieve real-time cavitation mapping with optimized mapping quality. The phantom experiments without the skull were performed to acquire cavitation signals in the channel data, with the cavitation maps processed off line to calculate the computational time and the mapping characteristics with respect to different exposure time or number of RF frames used for a single cavitation map.

Both the computational time and mapping characteristics are shown in Fig. 5.4. The computational time was linearly correlated the exposure time (Fig. 5.4A). In order to achieve real-time cavitation mapping, it requires a computational time lower than the pulse repetition time used in the FUS therapy, which is 0.5 s for BBB opening in NHP. Therefore, a maximum of 1.44 μs (30 RF frames reconstructed) is required to achieve real-time reconstruction and display of cavitation maps. For the mapping characteristics (Fig. 5.4B), the maximal intensity increased until reaching to a plateau at around 62.5 μs (1300 frames) due to the enhancement of the cavitation signal as more RF frames were included with a longer exposure time. The cavitation distribution started to form in the localized region even at a very short exposure time (1.44 μs for 30 frames). While the cavitation region (defined as -6 dB area from the maximal intensity) increased with exposure time at the beginning of 20 μs as more discrete spots were formed, it then started to decrease and reached a steady state at around 62.5 μs due to the enhancement of the cavitation signal in the focus.

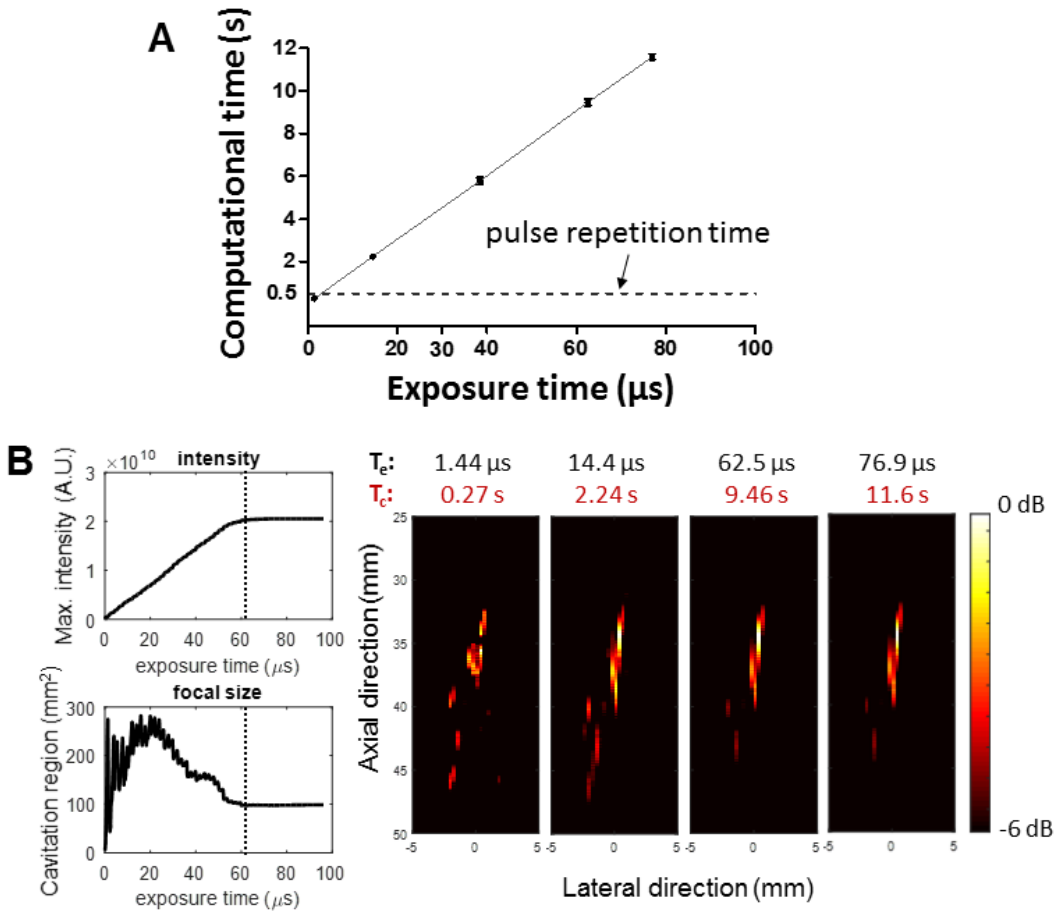

Figure 5.4. The impact of exposure time on computational time and mapping characteristics. **(A)** The exposure time (T_e) was linearly correlated with the computational time (T_c) since it determined the number of RF frames required to be reconstructed for one single cavitation map. (B) This exposure time also affected the mapping quality in terms of denoising and homogeneity of cavitation distribution. The maximal intensity of the map increased until reached to a plateau as more RF frames were added. This cavitation distribution also formed in a localized region at a very short exposure time (1.44 μs) as shown in the cavitation region (-6 dB area) until reaching a steady state at 62.5 μs. This representative case was performed at 450 kPa, while all other cases at various pressure showed the same trend.

5.3.2 Acoustic mapping through the primate skull

In the brain therapy such as BBB opening, the performance of transcranial detection is critical for clinical application. Therefore, detection threshold through the monkey and human skull were

investigated in the in vitro phantom experiments by placing the skull piece (parietal bone) in between the PCD array and the phantom from 150 to 600 kPa as shown in Fig. 5.5. Cavitation maps using 62.5-µs exposure time showed a localized cavitation distribution at all pressures applied (Fig. 5.5A), while successful transcranial detection was achieved at and above 300 kPa and 450 kPa for monkey skull (Fig. 5.5B) and human skull (Fig. 5.5C), respectively. This detection threshold lies in the range for successfully BBB opening, thus demonstrating its capability of monitoring the sonication transcranially.

Although through the skull the cavitation distribution was more disperse, it still presented as a single event. The displacement of the cavitation event through the skull was around 1 cm, which may be due to the skull causing distortion of the cavitation signal or the slight movement of the PCD array or the phantom in order to fit the skull piece in limited space (the PCD array was 2 cm away from the phantom where the channel was 1.5 cm deep).

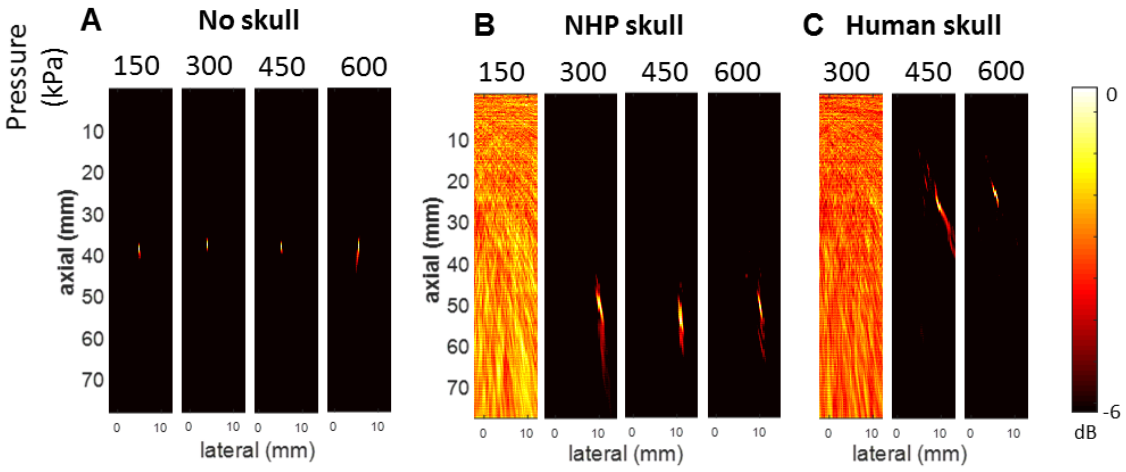

Figure 5.5. Detection threshold of cavitation mapping through the primate skulls. Cavitation maps at various pressures (A) without the skull in place, (B) with the NHP skull, (C) with the human skull in place were acquired. The cavitation distribution was successfully reconstructed at

all pressures from 150 kPa to 600 kPa. It can be detected at and above 300 kPa and 450 kPa through the monkey skull and human skull, respectively.

5.3.3 Acoustic mapping during BBB opening in NHP

After the in vitro assessment for the transcranial cavitation mapping, this technique was applied during BBB opening in NHP to show its in vivo feasibility of monitoring in large animals. The PCD array was placed against the temporal bone toward the FUS focus since it was the thinnest part of the skull close to the sonicated area, and the monitoring plane covered a lateral cross section of the ellipsoidal FUS focus (Fig. 5.3B). Two NHPs were sonicated at 450 kPa and 600 kPa to induce BBB opening, with the cavitation map, total intensity of the cavitation signal, and the spectrum monitored in real time (frame rate = PRF = 2 Hz).

A representative BBB opening and monitoring result at 450 kPa is shown in Fig. 5.6. Both a single-element PCD confocal to the FUS transducer and the PCD array were used to monitor the BBB opening (Fig. 5.6A). The single-element PCD showed a dramatic increase in both stable and inertial cavitation once microbubbles perfused the brain, which corresponded to the total intensity in the PCD array (summation of the squared channel data) over time (Fig. 5.6B). In the sequential cavitation maps, the cavitation distribution consistently demonstrated localized cavitation events in the same location (Fig. 5.6C). Cavitation mapping therefore provides both the spatial information and the intensity of cavitation.

Another representative BBB opening and monitoring result at 450 kPa is shown in Fig. 5.7 with only stable cavitation. Using a linearized intensity scale in the cavitation mapping allowed us to see both the spatial and the intensity of cavitation change over time (Fig. 5.7C). Interestingly, the cavitation events during the sonication seemed to occur at two locations. It may be due to the

cavitation occurred in the nearby vessel, sidelobe of the FUS transducer, or an artifact of the passive mapping. More information are required for investigation.

Moreover, in order to assess the treatment outcomes, the location of the PCD array relative to the brain is required to register the cavitation maps to the brain images. This can be achieved with a neuronavigation system, which will be described in Chapter 6.

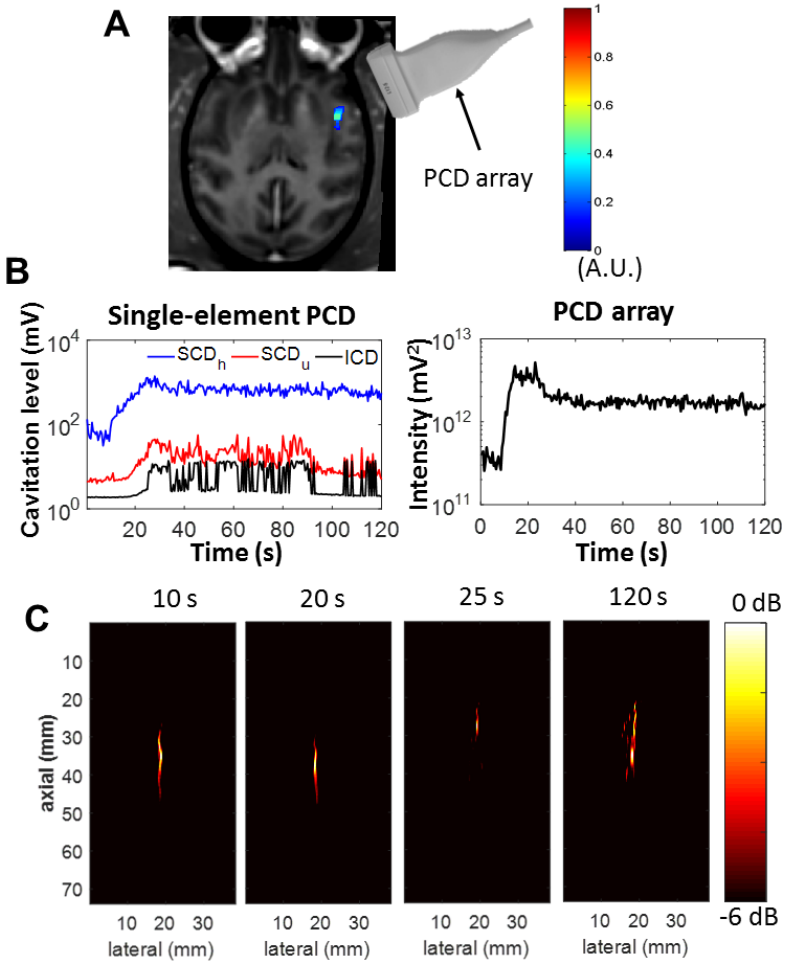

Figure 5.6. Cavitation mapping during BBB opening in NHP 1. (A) BBB opening (colored) revealed after post processing in the horizontal slice of the contrast-enhanced T1w MRI. BBB opening was induced at 450 kPa while the PCD array (placed against the temporal bone toward the FUS focus) acquired cavitation signals for reconstruction of cavitation maps. (B) Both the

single-element PCD and the PCD array acquired cavitation signal for real-time monitoring. The calculated cavitation doses from the single-element PCD is shown on the left, and the total intensity of cavitation signals (sum of the squared channel data) from the PCD array on the right. (C) The reconstructed cavitation maps at each time point revealed the location cavitation events in the brain (using the -6 dB scale relative to the maxima).

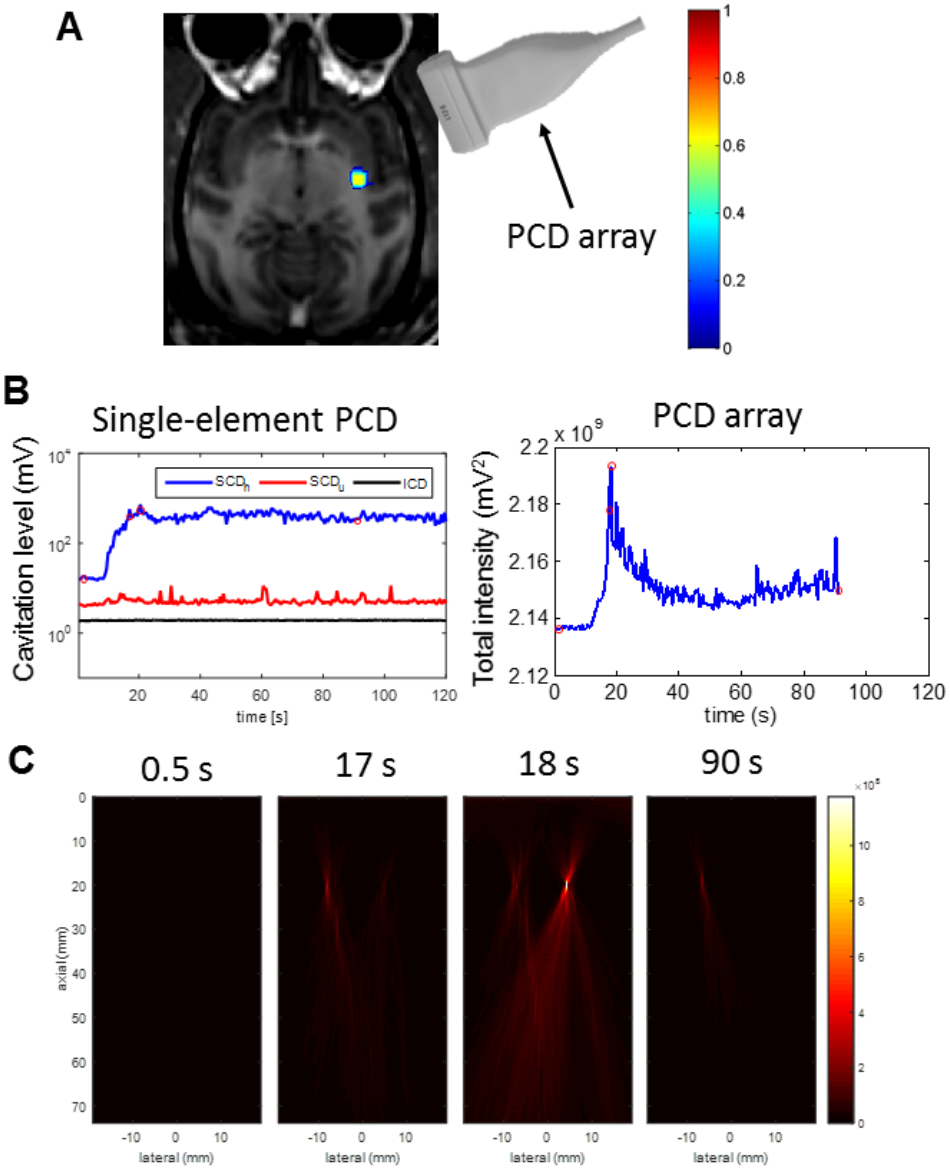

Figure 5.7. Stable cavitation mapping during BBB opening in NHP 2. (A) BBB opening (colored) revealed after post processing in the horizontal slice of the contrast-enhanced T1w MRI. BBB opening was induced at 450 kPa while the PCD array (placed against the temporal bone

toward the FUS focus) acquired cavitation signals for reconstruction of cavitation maps. (B) Both the single-element PCD and the PCD array acquired cavitation signal for real-time monitoring. The calculated cavitation doses from the single-element PCD is shown on the left, and the total intensity of cavitation signals from the PCD array on the right. (C) The reconstructed cavitation maps at each time point revealed the location and intensity increase of cavitation events in the brain (using the intensity as the color scale).

5.4 DISCUSSION

In this chapter, real-time transcranial cavitation mapping using sparse matrix beamforming with GPU computation was developed and assessed in vitro through the monkey and human skull, as well as in vivo during BBB opening in monkeys. This cavitation mapping provides both the intensity and spatial distribution of cavitation that potentially enables the assessment and control of FUS treatment associated with cavitation more precisely. The transcranial detection through the primate skull also allows translational capability to the clinics.

Passive cavitation mapping or passive acoustic imaging originally developed for seismic imaging to identify acoustic sources for military purposes [82] can monitor therapeutic ultrasound treatment associated with cavitation, since the cavitation events achieving the desired biological effects also serve as acoustic sources during sonication. It has been used in high-intensity focused ultrasound (HIFU) [83, 202, 203], drug delivery [205] as well as BBB opening [187, 204] owing to the use of long acoustic treatment pulses resulting in higher occurrence of cavitation emission relative to the background emission, while the reconstruction often takes hours.

Its application in BBB opening holds great promise to replace costly and time-consuming MRI. Besides, real-time cavitation mapping may allow feedback control of the safety and effectiveness of FUS treatment in different location as what has been developed with single-

element PCD [79]. Current challenges lie in the alignment of cavitation maps to the brain and the skull causing phase aberration and mapping distortion, and the use of neuronavigation and simulation could solve these problems.

5.5 CONCLUSION

Real-time transcranial cavitation mapping has been developed using sparse matrix beamforming with GPU computation in this study. It successfully demonstrated localized cavitation distribution at and above 150 kPa without the skull, 300 kPa through the monkey skull, and 450 kPa through the human skull, showing its capability of treatment monitoring. This real-time cavitation mapping was also applied in vivo during BBB opening in NHP, proving the monitoring feasibility in primates. Our technique is thus capable of translating to clinics.

5.6 SIGNIFICANCE & CONTRIBUTION

This chapter fulfilled the specific aim 2 to develop an online treatment monitoring tool together with Chapter 3 and 4. In the last two chapters, cavitation monitoring using single-element PCD was implemented in mice and NHP. It provided the measure of an overall cavitation dose without spatial information. In this chapter, passive cavitation mapping utilizing a PCD array and an imaging technique with GPU computing, the spatial distribution of cavitation could be constructed in real time for the first time, which shed lights on the location of BBB opening. The performance was assessed in monkeys in vitro and in vivo, and humans in vitro, which guaranteed the feasibility

of this technique in clinical use. Its use with BBB opening could potentially control the BBB opening in real time to ensure safety and effectiveness, and eventually replace the MRI as a post-treatment assessment tool.

The research contribution was shared with colleagues and interns in the lab. Julien Grondin (PhD, Biomedical Engineering, Columbia University) assisted in the development of sparse matrix reconstruction with GPU computing. Wenlan Zheng (B.S., Biomedical Engineering, Columbia University) and Marc Heidmann (M.S., Biomedical Engineering, Columbia University) assisted the in vitro experiments. Carlos Sierra Sanchez (PhD, Biomedical Engineering, Columbia University) and Amanda Buch (B.S., Biomedical Engineering, Columbia University) assisted the in vivo experiments. Yao-Sheng Tung (PhD, Verasonics Inc.) assisted the Verasonics system setting for data acquisition.

Chapter 6

Neuronavigation-Guided Focused Ultrasound and Acoustic Mapping for BBB Opening in Non-human Primates

6.1 INTRODUCTION

Both simulation (Chapter 2) and real-time cavitation monitoring during BBB opening (Chapter 3-5) have been developed to personalize the treatment planning and to ensure treatment safety and effectiveness. Since drug delivery often requires multiple applications, the treatment duration is especially critical in order to serve a large patient population. Currently, the bottleneck is the targeting procedure, which takes more than two hours using MRgFUS [12], while the process can be fairly efficient using frameless stereotaxic method, called neuronavigation. The objective of this chapter was to develop a seamless neuronavigation-guided transcranial ultrasound system with targeted sonication and acoustic mapping for clinical use, and the protocol demonstrated from in silico preplanning, online treatment and monitoring, to post-treatment assessment. The system and protocol were tested in both sedate and awake non-human primates (NHP) with BBB opening to evaluate the performance of simulation, targeting accuracy, and monitoring. The system for FUS sonication and acoustic mapping was assessed in both a sedate setting, where the animal was lying prone on the operating table under anesthesia, and an awake setting, while the animal was trained

to sit in a customized chair. The accuracy of targeting as well as the cavitation mapping was evaluated comparing to the BBB opening based on contrast enhanced MRI.

6.2 METHODS

6.2.1 Neuronavigation-guided ultrasound system

An armless neuronavigation system (Brainsight Vet System, Rogue Research Inc., Canada) designed for primates (both monkeys and humans) was customized to be used in conjunction with an ultrasound system. This neuronavigation system was based on paired-point registration with an optical tracking device and reflective spheres (Northern Digital Inc.), and the fiducial bite bar system (bite bars bearing six fiducials; Rogue Research Inc., Canada) were constructed for each individual with their unique tooth imprints in the sedate animal experiments (Fig. 6.1). For the awake animal experiments, in-house fiducial bearing pieces were designed attachable to the head post implantation of the animal. Two unique tool trackers with three reflective spheres were mounted separately on the therapy transducer and the monitoring transducer (Fig. 6.2A) and calibrated for the neuronavigation system in order to recognize them in the operating space.

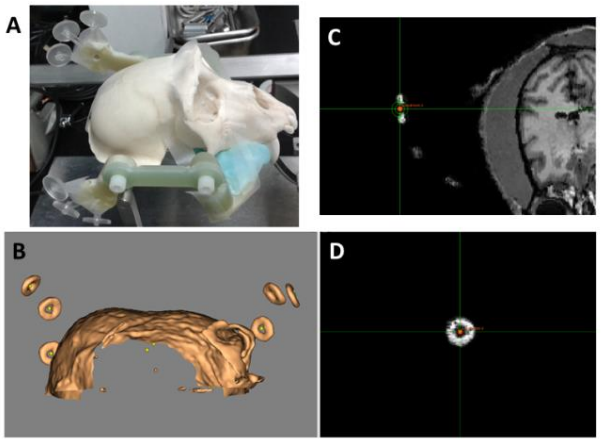

Figure 6.1. Acquiring preoperative anatomical images with fiducials for registration. (A) A NHP skull with a bite bar connecting unique teeth impression to the fiducial plates. (C) NHP brain images with donut-shape fiducials (D) in T1w MRI. The fiducial landmarks (center of the fiducials) were identified in the neuronavigation system for registration.

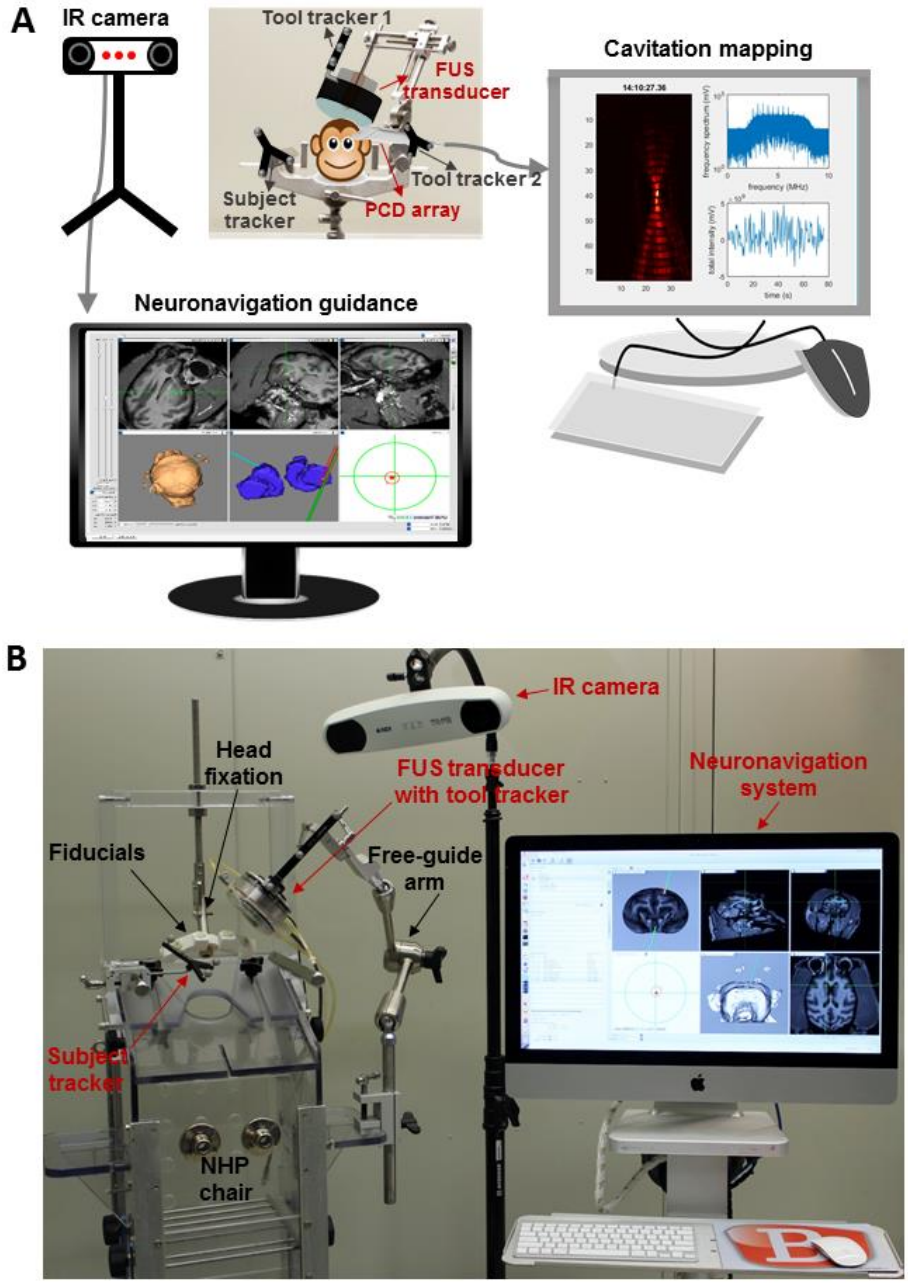

Figure 6.2. Experimental setup with neuronavigation for (A) the sedate and (B) the awake animal. Infrared (IR) camera was the position tracking device connected to the computer to process image registration in real time in the neuronavigation system. The trackers bared three reflective spheres for the IR camera to detect transducers (tool trackers) relative to the animal subject in the physical space (subject tracker). At the beginning of the treatment session, the fiducials were attached to the invariant traits (bite bars or head post) of the animal for registering the animal subject to the neuronavigation system. After the registration, the fiducials were removed and the FUS transducer was aligned to the preplanned targeting and secured with the free-guide arm or stereotactic arm for sonication.

The ultrasound system consisted of a focused ultrasound treatment unit controlled by a customized program in Matlab with a single-element, 0.5-MHz FUS transducer (diameter: 64 mm, focal depth: 62.6 mm; H-107, Sonic Concepts, WA, USA) triggered by a function generator (model 33220A, Agilent Technologies, CA, USA) after 50-dB amplification (A075, ENI, NY, USA), and an acoustic monitoring unit with a programmable acoustic signal acquisition system (Vantage 256, Verasonics, WA, USA) and an array of acoustic detectors (Philips ATL L7-4 linear array, bandwidth = 2 to 8 MHz, 38 mm wide with 128 elements) synchronized with the FUS system for real-time passive cavitation mapping and storage of the entire acoustic signals. Both the FUS and cavitation mapping were guided with the neuronavigation system during the FUS procedure.

6.2.2 Experimental design

All procedures were reviewed and approved by the Institutional Animal Care and Use Committees at Columbia University and the New York State Psychiatric Institute. Three male adult macaques (2 Macaca mulatta and 1 Macaca fascicularis, weight: 6-11 kg, age: 8-20 yo) sonicated at 0.3, 0.45, and 0.6 MPa (excitation frequency = 0.5 MHz, pulse length = 10 ms, pulse repetition frequency = 2 Hz, duration = 2 min) with in-house microbubbles injected intravenously (lipid-shelled, 4-5 μm in diameter, 2.5×108 bubbles/kg), and targeted structures included the basal ganglia (caudate and putamen) associated with neurodegenerative diseases such as Parkinson's and Huntington's disease as well as the primary motor cortex in the central sulcus and precentral gyrus. Three experimental groups (cohorts) were designed. First, neuronavigation + stereotaxic sonication (NHP 1, 2) to investigate the targeting and monitoring accuracy by locating the acoustic focus with neuronavigation intraoperatively with stereotaxic preplanning (Fig. 6.2A). Second, neuronavigation-guided sonication (NHP 1, 2) with preplanning on the neuronavigation system

was implemented with a free-guide surgical arm (Rogue Research Inc., Canada) coupling the FUS transducer to investigate the targeting and monitoring accuracy through neuronavigation guidance. The animals were under anesthesia in cohorts 1-2. Finally, neuronavigation-guided sonication was translated to an awake animal trained to sit on a customized chair (NHP 3) to mimic the clinical settings with its head fixated to the chair (Fig. 6.2B).

6.2.3 Preoperative image acquisition

Both CT and MRI were acquired preoperatively for personalized pre-planning and neuronavigation guidance. CT (helical scan, resolution = 0.2 × 0.2 × 0.6 mm; Siemens) was used to extract skull properties such as density and thickness in order to estimate the acoustic energy loss in simulation, and T1-weighted MRI (3D turbo field echo sequence, TR/TE = 11.1/5.1 ms, FA=8^0, resolution = 0.7 × 0.7 × 0.7 mm; Philips 3T) for the anatomical scan of the brain surrounded by 6 contrast-enhanced fiducials used for registration of the neuronavigation system.

6.2.4 Reconstruction of acoustic maps

Time-exposure acoustics [82] in combination of dynamic receive beamforming using sparse matrix calculation in the graphic processing unit [207] (GPU; Tesla K40, NVIDIA) were developed for the reconstruction of passive acoustic maps in real time during the sonication (frame rate = pulse repetition rate = 2 Hz). In a single pulse, 30 passive image frames (root-mean-square of the RF frame) were reconstructed and summed as an integration over an exposure time of 1.44 μs to enhance the cavitation signal and eliminate the background noise, and an exposure time of

62.5 μs (1300 passive image frames) was used for off-line processing in order to acquire the optimal acoustic mapping quality for post-comparison to the BBB opening.

6.2.5 Experimental procedure

The experimental setup is shown in Fig. 6.2. For animal anesthesia in experimental cohort 1-2, the animal was sedated with ketamine (10 mg/kg in conjunction with 0.04 mg/kg of atropine through intramuscular injection) for placement of an endotracheal tube and an intravenous catheter in the saphenous vein, and then transported to a dedicated suite for the anesthesia procedure (1-2% isoflurane-oxygen mixture) with vital signs monitored during the entire experiment9, 10. While for the awake animal experiments, the animal was lightly sedated with ketamine (5 mg/kg) for placement of an intravenous catheter in the saphenous vein prepared for injection of microbubbles, and then was placed into the chair with head fixed while awake30. During the treatment session, the animal subject in the physical space (represented by the subject tracker) was first registered to the virtual image space on the neuronavigation system. Specifically, the pointer tool recognized by the system was used to select the fiducials one-by-one, which were bared on the bite bar secured by the upper jaw of the animal after been fixed on the stereotaxic frame (sedate animals) or bared on the head post (awake animals). Once registered, the orientation of the tools (represented by the tool trackers) relative to the brain including the FUS transducer and the imaging probe could be displayed on the real-time reconstructed 2D and 3D images on the neuronavigation monitor. In cohort 1 (neuronavigation + stereotaxic sonication)(Fig. 6.2A), the stereotaxic targeting9 was visualized and recorded on the neuronavigation system. In cohort 2 (neuronavigation-guided sonication), the mechanical robotic arm was utilized to align the FUS transducer to the pre-planned targeting in terms of the focus and orientation. Lastly in cohort 3 for the awake animal setting (Fig.

6.2B), the animal was secured in the customized chair for neuronavigation-guided sonication. In all cohorts, the imaging probe for cavitation mapping was aligned to the FUS focus against the temporal bone, the thinnest part of the skull with less acoustic signal attenuation.

At the beginning of the sonication, the microbubbles were injected in a bolus intravenously (saphenous vein) followed by saline flush within 30 s, and the cavitation maps were displayed in real time during the entire sonication. In order to confirm the BBB opening and safety, MRI was performed 1 h after the sonication. T_1-weighted images (3D spoiled gradient echo sequence, TR/TE = 8.5/4.8 ms, FA = 8º, resolution = 1×1×1 mm) before and after gadolinium injection (Gd-DTPA-BMA, Omniscan®, GE Healthcare, NJ, USA; 0.2 mL/kg) for confirming BBB opening, T_2-weighted images (TR/TE = 3000/80 ms, flip angle or FA = 90º, resolution = 0.4×0.4×2 mm) for assessing potential edema, and susceptibility-weighted images (TR/TE = 19/27 ms, FA = 15º, resolution = 0.4×0.4×1 mm) for assessing potential hemorrhage.

6.2.6 Accuracy analysis of targeting and acoustic mapping

In analyzing the targeting accuracy for the BBB opening, the contrast enhancement from the sonicated region was first identified by taking a division of post to the pre-contrast T1w images and filtering the vessel signal with the control scan (pre- and post-contrast T1w images without sonication) as described previously [71]. The center and the trajectory of the BBB opening was defined as the center of mass in 3D and the linear fit of the center of mass in each 2D slices in the volume of interest (10 × 10 × 32.5 mm3), which was compared with the location and trajectory of the ultrasound focus recorded by the neuronavigation system in order to assess the target shift.

For analyzing the monitoring accuracy, the enhancement image corresponded to the imaging plane of the monitoring probe was interpolated based on the pixel position in the brain images, which was calculated based on the transformation matrix provided by the neuronavigation system. The center of the cavitation maps was then calculated and compared with the center of the BBB opening in the enhancement image in order to estimate the distance shift.

6.3 RESULTS

6.3.1 Feasibility with targeted BBB opening

6.3.1.1 Neuronavigation procedure

After acquiring the MRI and CT scan of the subject, three experimental groups were designed to compare the targeting accuracy with frame-based stereotaxis (Cohort 1), to implement neuronavigation-guided sonication in the sedate animal setting (Cohort 2), and to translate to an awake animal setting (Cohort 3) using the setup shown in Fig. 6.2B. Experimental cohort 1 (N=7) was planned with the stereotactic calculation while during the FUS session the location of the focus was visualized and recorded in the neuronavigation system. Experimental cohort 2 (N=6) was planned on the neuronavigation software before sonication, and the targeting was implemented with the free-guide mechanical arm through the guidance of the neuronavigation system during the sonication session. This cohort showed the feasibility of incorporating the neuronavigation system for sonication and BBB opening. Finally, experimental cohort 3 (N = 5) was to perform the sonication in the awake animal with planning and guidance through the neuronavigation system. The neuronavigation-guided cavitation mapping was performed in all

four cohorts. All the BBB opening results were used to quantify the targeting accuracy of neuronavigation-guided sonication as well as the cavitation mapping.

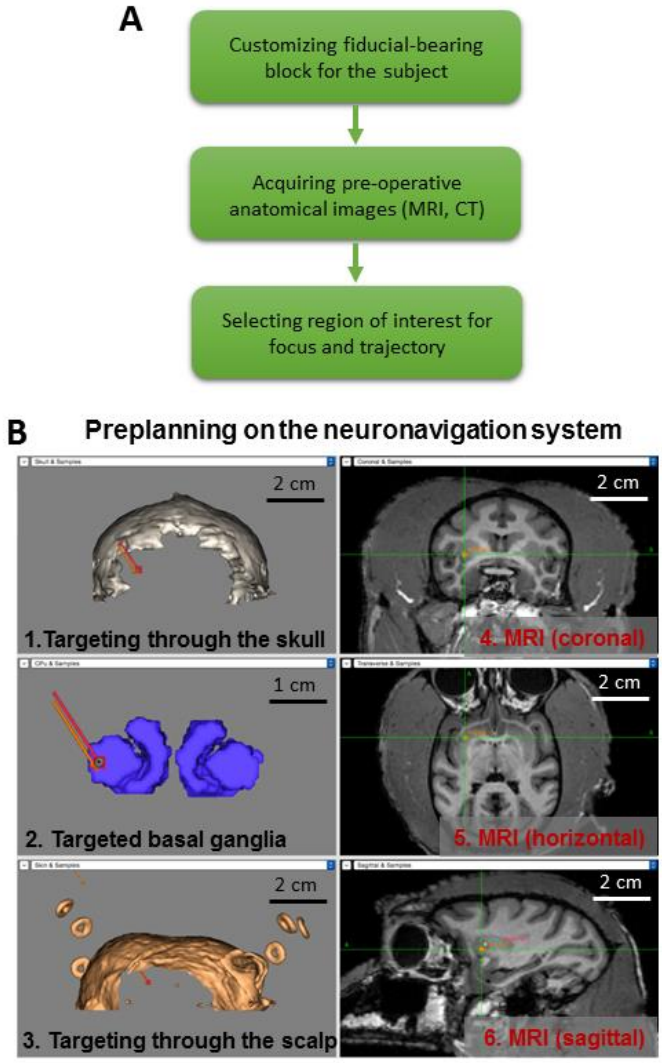

Figure 6.3. Preplanning procedure for FUS targeting. (A) Flowchart for preplanning and FUS treatment procedure of neuronavigation-guided ultrasound. (B) Screenshots of the preplanning on the neuronavigation system. Preplanning for the FUS target and trajectory through the 3D segmented and reconstructed skull (1), basal ganglia (2), and the scalp with the donut-shaped fiducials (3), and the focus was at the crosshair of the MRI slices (4-6) acquired preoperatively.

In the preplanning process on the neuronavigation system after acquiring the preoperative radiological images (Fig. 6.3), the 3D skull, subcortical structure, the scalp were segmented and visualized together with the MRI slices in order to assist the selection of the focal location and the trajectory by covering the region of interest and avoiding pre-existing lesions, large vessels, ventricles inside the brain, as well as physical hindrance such as implants, thicker part of the skull, or thick epicranial muscle in the beam path outside the brain.

During the sonication session, both the FUS beam and the monitoring probe were guided and aligned with neuronavigation system following the procedure described in Fig. 6.4A, and the screenshot of the neuronavigation system is shown in Fig. 6.4B. The subject was first registered to the pre-scanned anatomical images based on the donut-shaped fiducials in order to create a linkage between the operational space to the virtual image space shown on the screen, and the error for each fiducial was kept below 1.5 mm after registration. Followed by the installation of the transducer with the mechanical arm, the trajectory of the FUS beam and the focus were visualized in the virtual image space in real time with feedbacks of the targeting implementation accuracy as shown in the step 4 in Fig. 6.4B. Specifically, the distance and angle deviation was reflected by the distance of the red dot to the center of the green circle and to the red circle, respectively, which gave two concentric circles for a perfect implementation. This implementation accuracy, i.e., the deviation of the FUS beam to the pre-planned targeting in session was displayed and kept below 1 mm in distance and 5^0 in angle. After the FUS transducer was set to the preplanned targeting orientation, the monitoring probe was placed against the temporal bone toward the FUS focus with the imaging plane covering the focus through the neuronavigation guidance as shown in the step 5 in Fig. 6.4B. The entire procedure from registration of the subject (5 to 10 min), neuronavigation of the FUS beam and the monitoring probe (10 to 20 min), to the sonication (2 min) took around

30 min. Therefore, the room time was within 1 h including 2 min of the treatment time for single sonication.

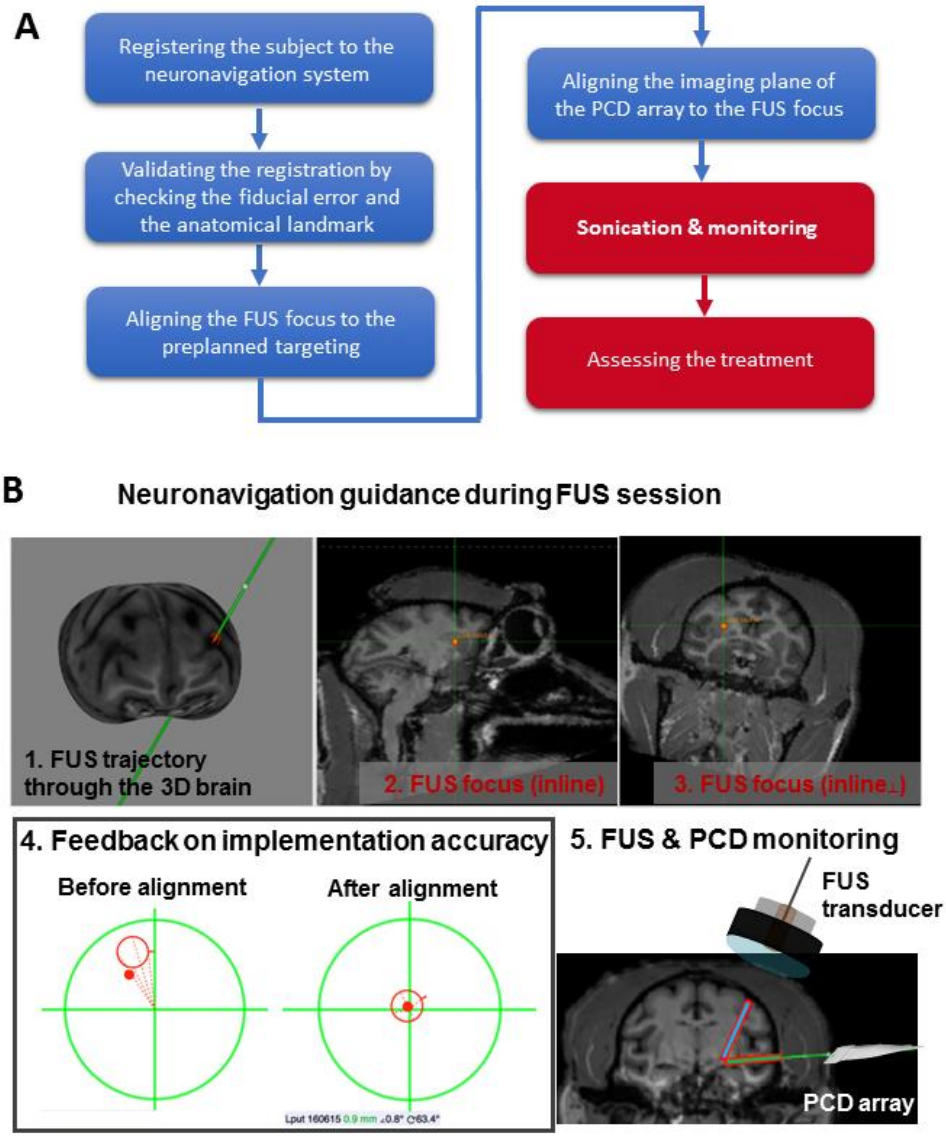

Figure 6.4. Neuronavigation-guided FUS treatment procedure. (A) Flowchart for implementing FUS targeting to the preplanning. (B) Screenshots of the online session showing the FUS trajectory in the reconstructed 3D brain (1) targeted the putamen in two orthogonal MRI slices, in which the vertical arrows represent the FUS trajectory pointing at the focus (2-3). (4) The implementation accuracy of the FUS transducer to the preplanning was displayed as a feedback for the distance (visualized as the distance between the red dot and the center of the larger circle) and the angle deviation (visualized as the distance between the red dot and the center of the smaller circle) during the guiding process. (5) The PCD array for cavitation mapping was aligned to the FUS focus before the sonication with neuronavigation guidance.

6.3.1.2 Sedate vs. awake animal setting

Both the basal ganglia and the cerebral cortex were targeted with successful BBB opening through neuronavigation guidance. The following shows the representative BBB opening results in both the sedate (Fig. 6.5) and the awake (Fig. 6.6) animal setup with the quantitative targeting accuracy summarized in Fig. 6.7. The average accuracy of neuronavigation was 3.1 mm, which was better than stereotaxis (4.3 mm) without statistical significance (Fig. 6.7A). Nevertheless, the lateral shift was found to be significantly improved from 3.2 mm to 1.8 mm after using neuronavigation while the axial shift and angle shift remained in the same range (2.6-3.2 mm and 8^0-9^0)(Fig. 6.7B). By comparing the targeting accuracy in the sedate and awake animal setting, the accuracy in the awake animal setting (3.0 mm) was comparable to the sedate animal setting (3.2 mm). Overall, the accuracy of the neuronavigation-guided FUS was consistent to what has been reported in neuronavigation-guided surgery (1.6-3.0 mm)[72].

In all the experiments performed, no acute damage such as hemorrhage (SWI) or edema (T2-weighted imaging) was detected in the radiologic examination in 2 h after sonication.

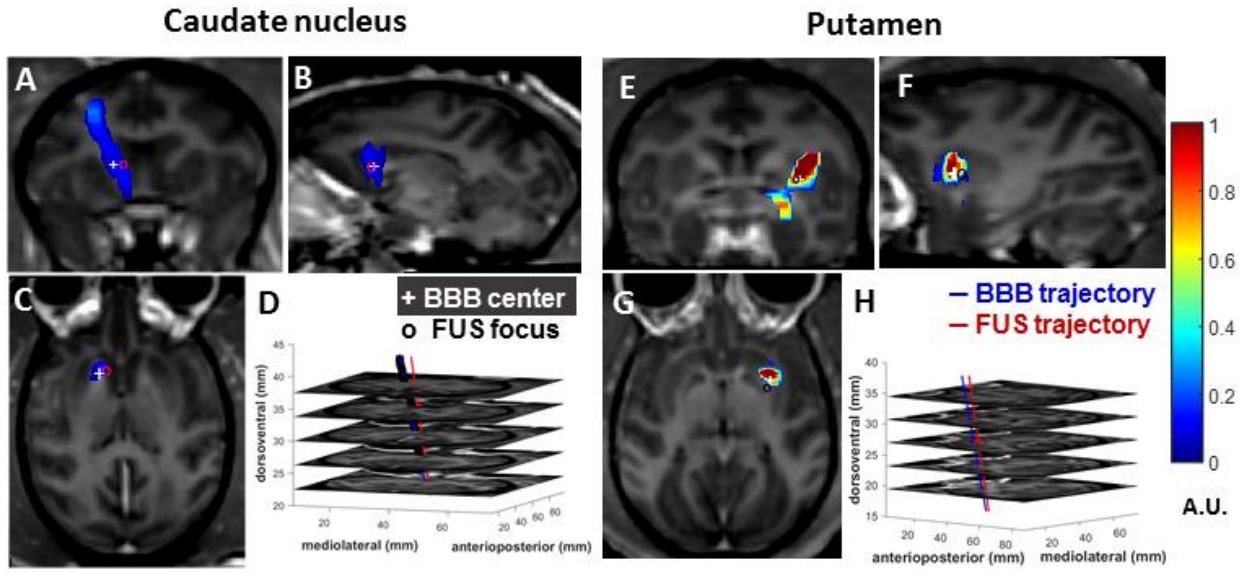

Figure 6.5. Neuronavigation-guided FUS for BBB opening in the sedate animal. Accurate BBB disruption were achieved with neuronavigation in the caudate nucleus (NHP 2 at 450 kPa) and in the putamen (NHP 3 at 600 kPa). The coronal slices in (A) and (E), the sagittal slices in (B) and (F), the horizontal slices in (C) and (G), and the stacked horizontal slices with the BBB opening trajectory (red line) and the planned trajectory (blue line) in (D) and (H). The cross represents the centroid of BBB opening and the circle the FUS focus in the neuronavigation system.

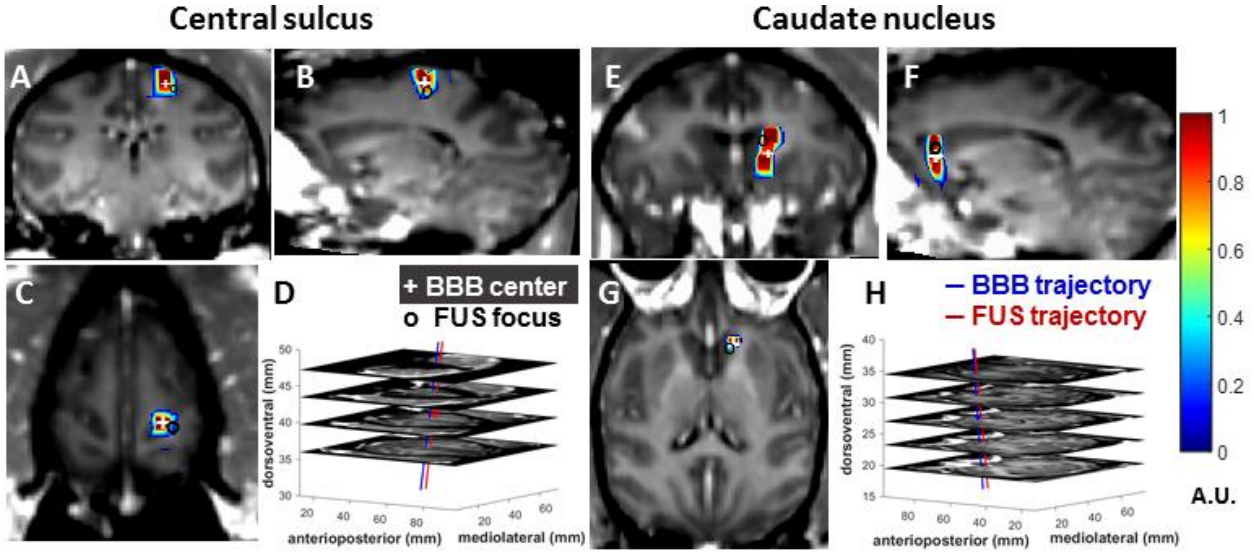

Figure 6.6. Neuronavigation-guided FUS for BBB opening in the awake animal trained to sit in the customized chair. Accurate BBB disruption were achieved with neuronavigation in the

central sulcus and in caudate nucleus (NHP 4 at 300 kPa). The coronal slices in (A) and (E), the sagittal slices in (B) and (F), the horizontal slices in (C) and (G), and the stacked horizontal slices with the BBB opening trajectory (red line) and the planned trajectory (blue line) in (D) and (H). The cross represents the centroid of BBB opening and the circle the FUS focus in the neuronavigation system.

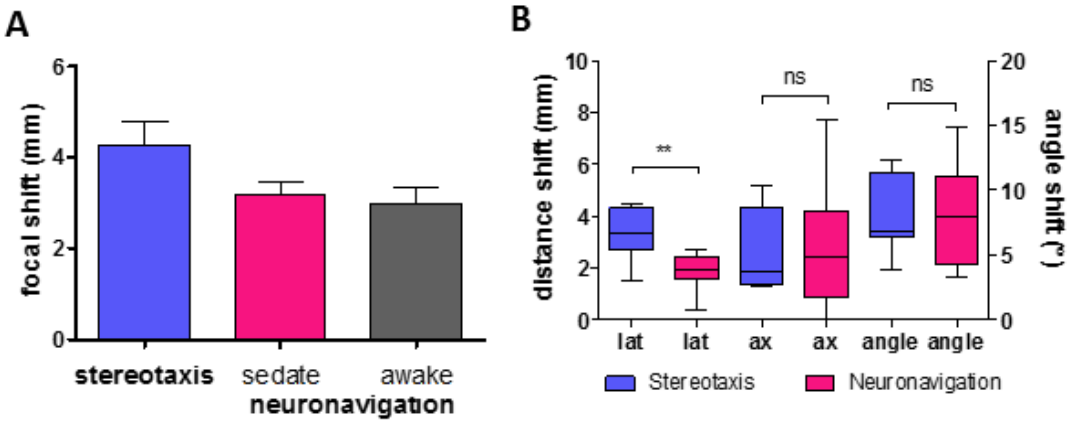

Figure 6.7. Accuracy for the neuronavigation-guided ultrasound system compared with frame-based method. (A) The total focal shift with the neuronavigation was slightly smaller than with the stereotaxis although it showed no statistical significance. (B) After breaking into the lateral (lat), the axial (ax) direction and the angle, the neuronavigation showed a significant improvement on the lateral direction.

6.3.2 Feasibility with acoustic mapping

Real-time cavitation mapping was performed with neuronavigation guidance during the sonication, and the monitoring results, the reconstructed maps with the corresponded BBB opening were shown in Fig. 6.8. The averaged frequency spectra in a single pulse of the acquired channel data showed a dramatic increase of cavitation signal (harmonics and ultraharmonics) after injecting microbubbles (Fig. 6.8A), and the total acoustic signal intensity (sum of the channel data in each single pulse) reflected the viability of microbubbles over the entire 2-min sonication duration in the brain (Fig. 6.8B). Both the post-reconstructed and the real-time cavitation maps revealed the

location of the cavitation event during sonication which overlapped with the BBB opening region in the caudate (Fig. 6.8C) and putamen (Fig. 6.8D). The overall quantitative results (Fig. 6.8E) showed an averaged distance between the centroids of BBB opening and the cavitation events of 2.5 mm (0.7 mm laterally and 2.2 mm axially), with no significant difference between animals or targeted regions.

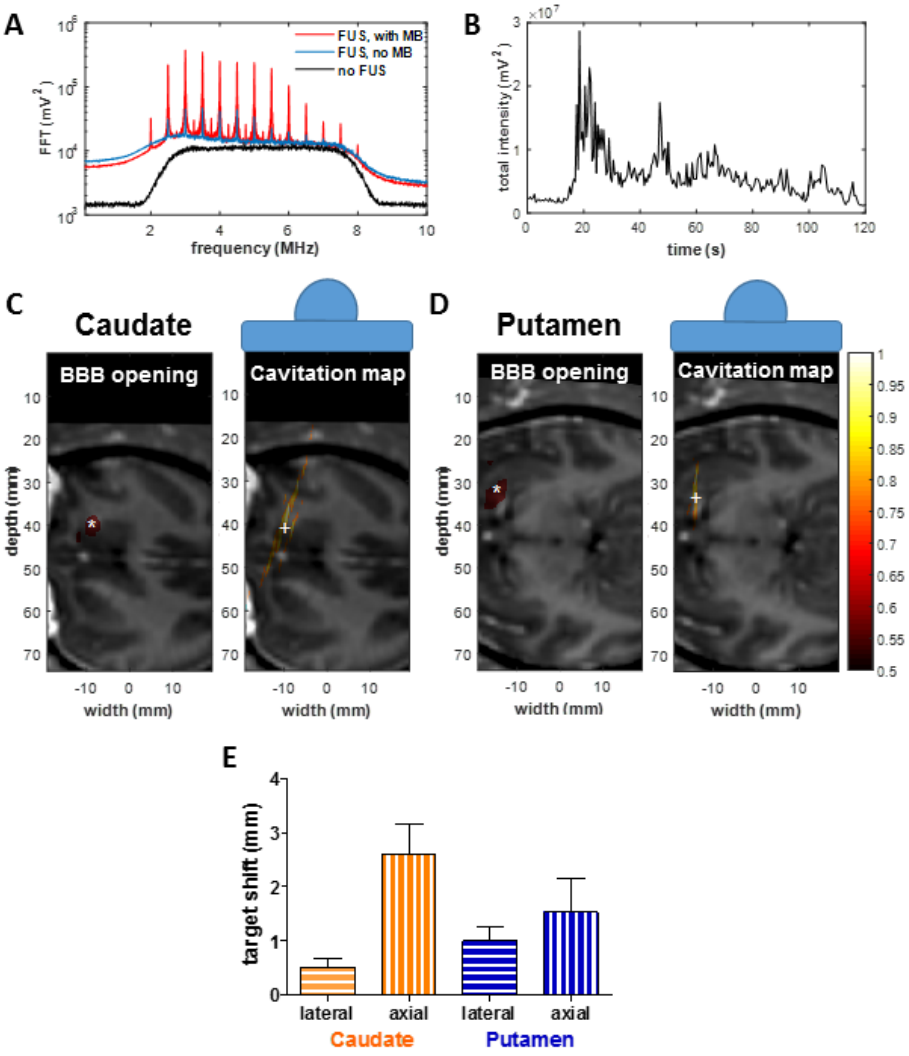

Figure 6.8. Neuronavigation-guided cavitation mapping during sonication for BBB opening. (A) The averaged frequency spectra in the channel data of the PCD array. (B) The total intensity of the channel data during the 2-min sonication showed significant cavitation response after microbubbles perfused the brain. The reconstructed cavitation maps showed the exact location of the BBB opening in the caudate at 450 kPa (C) and the putamen at 450 kPa (D). (E) The cavitation mapping showed an accurate monitoring at the location of BBB opening.

6.4 DISCUSSION

In this study, a novel protocol for the transcranial neuronavigation-guided ultrasound system has been demonstrated to disrupt the BBB in a precise location in both sedate and awake non-human primates from initial preplanning to on-line FUS procedure and acoustic monitoring. The fast procedure (30 min) with flexible targeting will benefit a broad patient population especially with diseases requiring repetitive treatment such as chemotherapy for brain tumors or neurodegenerative diseases. It will also facilitate the neuromodulation research using FUS in primates. Furthermore, real-time monitoring for the energy distribution of the acoustic cavitation in combination with the neuronavigation technology holds great potential to assess and control the treatment in the desired targeted regions.

The neuronavigation-guided ultrasound system tested in non-human primates both on the surgical table and in the chair maintains translational capability to a clinical setting. The proposed protocol covers from in silico preplanning, FUS treatment procedure, real-time monitoring, to post-treatment assessment. First, in the initial preplanning after acquiring the MRI with fiducials and CT, the region of interest and trajectory for the acoustic beam could be selected in the neuronavigation pre-planning panel assisted by the 3D reconstructed brain structure and scalp. Second, when an optimal targeting was decided, it is then implemented by the neuronavigation system for an online operation for sonication and cavitation mapping. Finally, the treatment outcome is evaluated. For BBB opening and drug delivery, the animal is currently evaluate with contrast-enhanced MRI using gadodiamide. This can potentially be replaced by acoustic monitoring technique as the cavitation mapping is now under development to control the safety and efficacy based on the distribution of cavitation occurred in situ.

Neuronavigation-guided ultrasound system holds several advantages compared with the currently available systems including MRgFUS[15] and the implantable ultrasound device[41] available for clinical trials. Different from MRgFUS, the mobility and fast treatment of our system could benefit a significantly larger crowd with seamless procedure, and cavitation associated with BBB opening could be monitored at ease without MRI interference. On the other hand, compared with the implantable ultrasound device our noninvasive technique with flexible targeting ensure adjustable treatment if different targeting or larger BBB opening region (e.g. tumor progression) is desired. Our system is thus suitable for applications based on mechanical effect such as BBB opening, drug delivery, and neuromodulation. However, it could potentially assists targeting for FUS surgery using MRgFUS system.

This technology also advanced upon our previous stereotactic method with single-element cavitation monitoring in several folds. First, the online visualization and guidance allowed an interactive adjustment for accurate targeting due to online visualization and feedback (Fig. 6.4). Whereas the stereotactic method is blinded during the sonication, and any slight misplacement of the animal or transducer in the stereotactic frame introduces error. Second, its flexibility in preplanning and implementation through the free-guide mechanical arm grants a higher degree of freedom to place the transducer, and enables the transducer orientation to align with the orientation of the brain structure[124] which is not application through the stereotaxic arm. Third, the cavitation mapping combined with neuronavigation technology envisions the spatial distribution of cavitation events associated with the treatment outcome. It could serve as an online tool to monitor and control the treatment like single-element passive cavitation monitoring, with a plus of the spatial information.

The targeting accuracy was determined by small errors in the neuronavigation system, the skull distorting the acoustic wave propagation, and the BBB opening results. While the monitoring accuracy was affected by both the neuronavigation system and the cavitation mapping acquired through the skull and its resolution. With the neuronavigation system, the targeting accuracy in the lateral direction was significantly improved compared with using stereotaxis. This improvement could be due to the variation in placing the animal to the stereotaxic frame with the ear bars. On the other hand, the axial shift and the angle shift remained in the same range and may be due to the skull based on the simulation results in Chapter 2 or the characteristics of BBB opening as the gray matter had higher probability of BBB opening than the white matter [71]. As shown in Chapter 2, an averaged focal shift of 1.8 mm was estimated in the acoustic pressure distribution in silico, which was close to the axial shift of 2.4 mm with neuronavigation (Fig. 6.7B). Although the skull could also affect cavitation mapping in terms of location and focal quality of the cavitation events due to phase aberration [208], the effect was minimal through the thin temporal bone in NHPs in this study. A more accurate monitoring assessment in the lateral direction in comparison to the axial direction could result from a better mapping resolution in the lateral direction.

There are, however, limitations of the proposed system, especially in targeting and monitoring technique. Sources of error in targeting are caused by registration errors with the neuronavigation system, the focal shift due to the skull, and the error in post-processing of the MRI, etc. To minimize the registration error, the location of the fiducials during the treatment session should be invariant to the pre-operative MRI with fiducials. In addition, since the neuronavigation system localized the tools relative to the subject tracker, maintaining a distance between the subject tracker and target as small as possible (< 10 cm) could improve the accuracy. To reduce the acoustic focal shift due to the skull, simulation of the acoustic pressure field and the

use of phased array focused ultrasound transducer with phase aberration correction could potentially compensate this type of error. On the other hand, in order to evaluate or control the treatment safety and efficacy, a robust acoustic monitoring technique such as cavitation mapping is required to minimize the need for an MRI.

6.5 CONCLUSION

This neuronavigation-guided transcranial ultrasound system and treatment protocol has successfully, efficiently, and accurately opened the BBB in non-human primates with both the animal lying on the surgical table and sitting on the customized chair. It holds great potential to facilitate both research and treatment for both drug delivery and neuromodulation in a clinical setting.

6.6 SIGNIFICANCE & CONTRIBUTION

This chapter fulfilled the specific aim 3 to develop a neuronavigation-guided ultrasound procedure in order to achieve an efficient and precise FUS treatment for future clinical applications. As current systems have several limitations such as lengthy procedure and limited targeting region (MRgFUS) or invasiveness (implantable ultrasound device), and the frame-based stereotactic method previously developed in our lab lacks of targeting flexibility and varying accuracy. Here, the neuronavigation was customized to guide both targeting and monitoring in primates for the first time. It time efficiency and targeting flexibility allows easy re-application and personalized

treatment that will not only benefit the brain research but also clinical trials for a broad patient population in the future.

The research contribution was shared with colleagues and collaborators. Christian Aurup (M.S., Biomedical Engineering, Columbia University) and Carlos Sierra Sanchez (PhD, Biomedical Engineering, Columbia University) assisted the study design and in vivo experiments. Vincent Ferrera (PhD, Neuroscience, Columbia University) facilitated the animal experiments.

Chapter 7

Conclusion & Future Works

7.1 CONCLUSION

The conclusion from each chapter is summarized as follows:

Acoustic wave simulation predicts BBB opening characteristics.

- **Chapter 2:** The developed simulation method for in situ acoustic pressure predicted the BBB opening characteristics such as the location and volume. It has been tested for pulse design to improve localization quality in mice by eliminating standing waves in mice. In the NHP study, it has been used to estimate the focal shift and the in situ pressure, both corresponded well with in vivo BBB opening results. The pressure after skull attenuation was found to be associated with the density and thickness of the skull in the acoustic beam path. The skull distortion of the acoustic focus also resulted in a 2 mm shift in monkeys. It is thus of vital importance to assess the pressure distribution of the acoustic focus through the skull before the FUS treatment to ensure a safe pressure distribution is applied in the brain. Lastly, the simulation method was used to evaluate the targeting effect through human skulls. Both the incidence angle and the focal depth below the skull affected the focal quality and the in situ pressure.

Cavitation monitoring reveals physical mechanism, and could assess and visualize BBB opening.

- **Chapter 3:** Passive cavitation detection (PCD) revealed the physical mechanisms with customized acoustic agents (microbubbles, nanodroplets) during BBB opening in mice in vivo. It demonstrated the usefulness of assessing the BBB opening with various agents. Furthermore, three acoustic agent design schemes were evaluated to improve drug delivery efficiency. First, lipid-shelled microbubble with long hydrophobic chain lengths could enhance the delivery of large molecules (> 40 kDa). Second, drug-loaded microbubbles required bubble disruption to enhance delivery. Third, acoustically-activated nanodroplets could achieve high amount of large molecule delivery (> 40 kDa) with a highly-volatile liquid core used.

- **Chapter 4:** PCD could be achieved through the monkey and human skull in vitro, and the monitored cavitation dose was positively correlated with BBB opening volume, amount of contrast agent delivered and the delivery efficiency in NHP in vivo. Results showed that through the macaque skull the pressure threshold for detecting the SCD_h remained the same as without the skull in place, while it increased for the SCD_u and ICD; through the human skull, it increased for all cavitation doses. In addition, using long pulses enabled reliable PCD monitoring and facilitate BBB opening at low pressures. The in vivo results showed that the SCD_h became detectable at pressures as low as 100 kPa; the ICD, at 250 kPa while it could occur at lower pressures; the SCD_u, at 700 kPa and was less reliable at lower pressures. Real-time monitoring of PCD was further implemented during BBB opening, with successful and safe opening achieved at 250-600 kPa in both the thalamus and the

putamen. Cavitation activity was correlated with the amount and concentration of gadolinium delivered through the BBB and its associated delivery efficiency as well as the BBB opening volume in non-human primates. Another important finding entails the effect of heterogeneous brain anatomy and vasculature of a primate brain, i.e., presence of large cerebral vessels, gray and white matter will also affect the cavitation activity associated with variation of BBB opening in different tissue types, which is not seen in small animals.

- **Chapter 5:** Passive cavitation mapping visualized the spatial distribution of cavitation at a pressure range feasible for BBB opening (150-600 kPa), and could be achieved through the monkey (at and above 300 kPa) and human skull (at and above 450 kPa) and during the in vivo BBB opening in NHPs. The computational time increased with the exposure time, while the mapping quality reach a plateau at the exposure time of 62.5 μs. To achieve real-time mapping, a short exposure time (1.44 μs) can be chosen for reconstruction with sparse matrix calculation in the GPU. This real-time mapping was successfully applied in vivo during BBB opening in two NHPs, demonstrating both the intensity and location of cavitation events during sonication.

Neuronavigation guidance provides streamlined targeting with real-time feedbacks.

- **Chapter 6:** Neuronavigation system was customized for FUS procedure, with protocol established from in silico planning, on-line navigation for sonication and acoustic mapping, to post-treatment assessment and offline analysis. This system and protocol was tested both in the sedate NHP in the surgical unit and in the awake NHP sitting on the customized chair. It provided fast (30 min) and precise (3 mm) FUS treatment. Its flexibility allowed

personalized targeting and monitoring independent of the MRI, and can be translated for human applications.

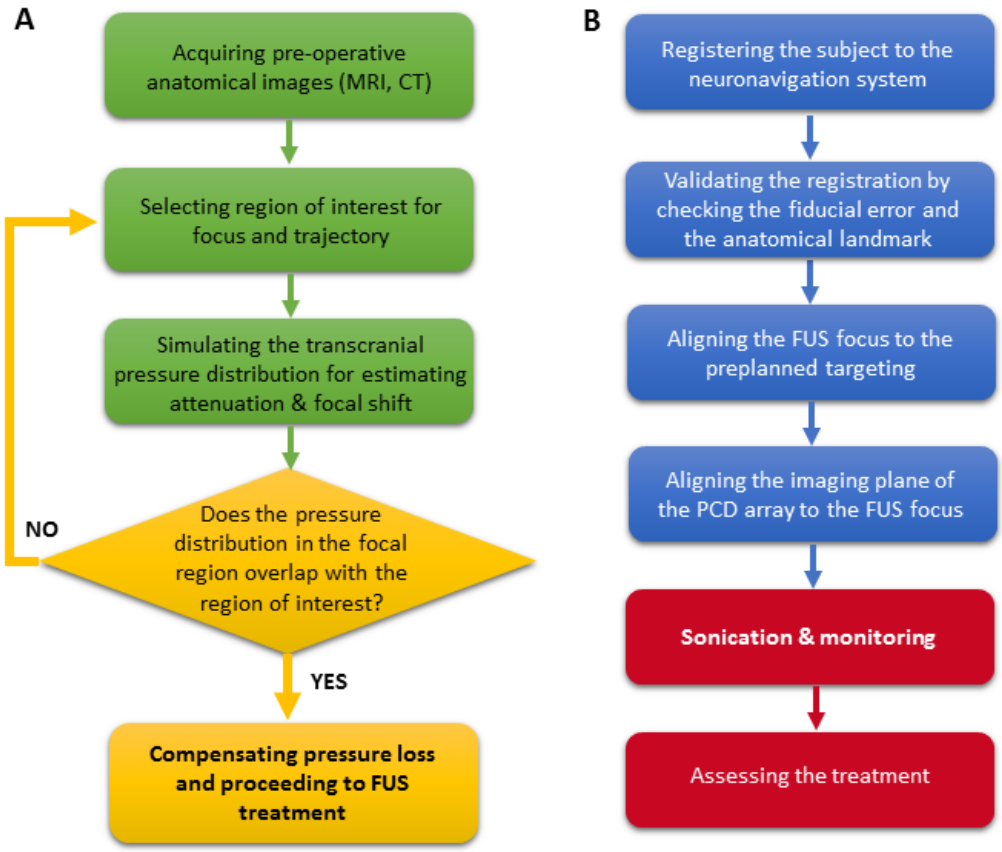

Figure 7.1. Flowcharts for the (A) in silico preplanning and (B) online FUS treatment procedure.

In a nutshell, a transcranial ultrasound system and protocol (Fig. 7.1) suitable for BBB opening in both clinical and preclinical studies was developed, covering from simulation of acoustic wave propagation for in silico preplanning, online targeting guidance with neuronavigation, real-time acoustic monitoring to uncover the physical mechanism and assess the treatment outcomes, to post-treatment assessment in sedate and awake non-human primates. To ensure a safe and effective BBB opening, the acoustic pressure distribution in the brain could be

simulated before the treatment to compensate for the skull distortion. After personalized preplanning of the FUS treatment, the targeting could be accurately and efficiently aligned with neuronavigation for sonication. During the sonication, the cavitation could be monitored in real time to assess the location and size of BBB opening. A clinical procedure for neuronavigation-guided FUS has been proposed in Fig. 7.1.

7.2 FUTURE WORKS

A novel FUS system and protocol from in silico planning and simulation to real-time targeting and monitoring has been developed and tested for BBB opening in primates. In order to facilitate its usage in clinical application, clinical trials in collaboration with medical doctors are required. There are thus several steps recommended to proceed. First, the system and protocol have been established and tested in monkeys in this thesis. It is required to get US Food and Drug Administration (FDA) approval of this system and microbubbles to be used in humans, and an Institutional Review Boards (IRB) approval for protocol of clinical trials for BBB opening. Second, simulation in this thesis has shown feasibility in predicting the characteristics of BBB opening in mice and monkeys. A simulation study should be continued in humans with various targeting for future treatment optimization. Third, several drug delivery studies have been performed in the lab previously such as neurotrophic factors (BDNF, Neurturin) and gene-carrying virus in wild-type or disease-model mice. In order to ease the transition to human applications, studies for delivery of pharmacological compounds should be performed in monkeys such as MPTP (1-methyl-4-phenyl-1,2,3,6-tetrahydropyridine) monkeys as a Parkinson's disease model to show FUS

treatment safety and efficacy. All these work will facilitate neuronavigation-guided FUS treatment in humans in the future.

On the other hand, there are also work to improve the system and protocol. First, the transducer through neuronavigation guidance is currently placed manually to the head. This procedure could be optimized with an implementation of a robotic arm as a way to reduce human error and streamline the navigating procedure. Second, MRI as it is currently used as a post-treatment assessment tool. In order to completely replace it to save time, the cavitation mapping in NHP should be continued to correlate with the size of BBB opening. Third, both CT and MRI are required for current preplanning. A new pulse sequence technique called ultrashort echo-time MRI may be developed for simulation instead of CT to improve the workflow. Lastly, nanodroplets have been shown feasible in mice and the cavitation monitoring correlated with the BBB opening outcomes. Its feasibility in large animals needs to be investigated in order to improve the quality of cavitation monitoring and facilitate its translation to future clinics.

References

1. Kahle, W. and M. Frotscher, *Color atlas and textbook of human anatomy*. 5th ed. 2002, Stuttgart ; New York: Thieme.
2. Netter, F.H., *Atlas of human anatomy*. 6th ed. 2014.
3. NIH. *National cancer institute: SEER training modules*. 2016; Available from: https://training.seer.cancer.gov/.
4. Abbott, N.J., L. Ronnback, and E. Hansson, *Astrocyte-endothelial interactions at the blood-brain barrier.* Nature Reviews Neuroscience, 2006. 7(1): p. 41-53.
5. World-Health-Organization, ed. *Neurological disorders: public health challenges*. 1st ed. 2006, WHO Press.
6. NINDS, *National institute of neurological disorders and stroke*. 2016, NIH.
7. Abbott, N.J., L. Ronnback, and E. Hansson, *Astrocyte-endothelial interactions at the blood-brain barrier.* Nat Rev Neurosci, 2006. 7(1): p. 41-53.
8. Leinenga, G., et al., *Ultrasound treatment of neurological diseases - current and emerging applications.* Nat Rev Neurol, 2016. 12(3): p. 161-74.
9. Elias, W.J., et al., *A pilot study of focused ultrasound thalamotomy for essential tremor.* N Engl J Med, 2013. 369(7): p. 640-8.
10. FUS-Foundation. *Essential Tremor: Focused ultrasound treatment for Essential Tremor has been approved by the Food and Drug Administration (FDA) in July 2016.* 2016.
11. National-Brain-Tumor-Society. *Tumor types: understanding brain tumors*. [cited 2016; Available from: http://braintumor.org/brain-tumor-information/understanding-brain-tumors/tumor-types/#glioblastoma-multiforme.
12. FUS-Foundation, ed. *Focused ultrasound for glioblastoma workshop summary*. 2015.
13. Hess, K.R., K.R. Broglio, and M.L. Bondy, *Adult glioma incidence trends in the United States, 1977-2000.* Cancer, 2004. 101(10): p. 2293-9.
14. Miller, D.L., et al., *Overview of therapeutic ultrasound applications and safety considerations.* J Ultrasound Med, 2012. 31(4): p. 623-34.
15. Jolesz, F.A., *MRI-guided focused ultrasound surgery.* Annu Rev Med, 2009. 60: p. 417-30.
16. FUS-Foundation, *An overview of the biological effects of focused ultrasound*. 2016.
17. Thanou, M. and W. Gedroyc, *MRI-Guided Focused Ultrasound as a New Method of Drug Delivery.* J Drug Deliv, 2013. 2013: p. 616197.
18. Leighton, T.G., *The Acoustic Bubble*. 1994.
19. Stride, E., *Physical principles of microbubbles for ultrasound imaging and therapy.* Cerebrovascular diseases (Basel, Switzerland), 2009. 27 Suppl 2: p. 1-13.
20. Hesley, G.K., K.R. Gorny, and D.A. Woodrum, *MR-guided focused ultrasound for the treatment of uterine fibroids.* Cardiovasc Intervent Radiol, 2013. 36(1): p. 5-13.
21. Blana, A., et al., *High-intensity focused ultrasound for the treatment of localized prostate cancer: 5-year experience.* Urology, 2004. 63(2): p. 297-300.
22. Roberts, W.W., et al., *Pulsed cavitational ultrasound: a noninvasive technology for controlled tissue ablation (histotripsy) in the rabbit kidney.* J Urol, 2006. 175(2): p. 734-8.
23. van Wamel, A., et al., *Vibrating microbubbles poking individual cells: drug transfer into cells via sonoporation.* J Control Release, 2006. 112(2): p. 149-55.
24. Hynynen, K., et al., *Noninvasive MR imaging-guided focal opening of the blood-brain barrier in rabbits.* Radiology, 2001. 220(3): p. 640-6.

25. Qin, S., C.F. Caskey, and K.W. Ferrara, *Ultrasound contrast microbubbles in imaging and therapy: physical principles and engineering.* Phys Med Biol, 2009. 54(6): p. R27-57.
26. Dayton, P., et al., *Acoustic radiation force in vivo: a mechanism to assist targeting of microbubbles.* Ultrasound Med Biol, 1999. 25(8): p. 1195-201.
27. Tyler, W.J., et al., *Remote excitation of neuronal circuits using low-intensity, low-frequency ultrasound.* PLoS ONE, 2008. 3(10): p. e3511.
28. Tufail, Y., et al., *Ultrasonic neuromodulation by brain stimulation with transcranial ultrasound.* Nat Protoc, 2011. 6(9): p. 1453-70.
29. Legon, W., et al., *Transcranial focused ultrasound modulates the activity of primary somatosensory cortex in humans.* Nat Neurosci, 2014. 17(2): p. 322-9.
30. FUS-Foundation, ed. *Focused Ultrasound State of the Field*. 1 ed. Vol. 1. 2016, Focused Ultrasound Foundation.
31. Gallay, M.N., et al., *Incisionless transcranial MR-guided focused ultrasound in essential tremor: cerebellothalamic tractotomy.* J Ther Ultrasound, 2016. 4: p. 5.
32. Leinenga, G. and J. Gotz, *Scanning ultrasound removes amyloid-beta and restores memory in an Alzheimer's disease mouse model.* Sci Transl Med, 2015. 7(278): p. 278ra33.
33. Burgess, A., et al., *Alzheimer disease in a mouse model: MR imaging-guided focused ultrasound targeted to the hippocampus opens the blood-brain barrier and improves pathologic abnormalities and behavior.* Radiology, 2014. 273(3): p. 736-45.
34. FUS-Foundation, ed. *Focused ultrasound for Alzheimer's disease workshop summary*. 2015.
35. Schlesinger, I., et al., *MRI Guided Focused Ultrasound Thalamotomy for Moderate-to-Severe Tremor in Parkinson's Disease.* Parkinsons Dis, 2015. 2015: p. 219149.
36. Guridi, J., et al., *[Neuroprotective subthalamotomy in Parkinson's disease. The role of magnetic resonance-guided focused ultrasound in early surgery].* Neurocirugia (Astur), 2016.
37. Lin, C.Y., et al., *Non-invasive, neuron-specific gene therapy by focused ultrasound-induced blood-brain barrier opening in Parkinson's disease mouse model.* J Control Release, 2016. 235: p. 72-81.
38. Samiotaki, G., et al., *Enhanced delivery and bioactivity of the neurturin neurotrophic factor through focused ultrasound-mediated blood-brain barrier opening in vivo.* J Cereb Blood Flow Metab, 2015.
39. McDannold, N., et al., *Transcranial magnetic resonance imaging- guided focused ultrasound surgery of brain tumors: initial findings in 3 patients.* Neurosurgery, 2010. 66(2): p. 323-32; discussion 332.
40. Coluccia, D., et al., *First noninvasive thermal ablation of a brain tumor with MR-guided focused ultrasound.* J Ther Ultrasound, 2014. 2: p. 17.
41. Carpentier, A., et al., *Clinical trial of blood-brain barrier disruption by pulsed ultrasound.* Sci Transl Med, 2016. 8(343): p. 343re2.
42. Pardridge, W.M., *The blood-brain barrier: bottleneck in brain drug development.* NeuroRx, 2005. 2(1): p. 3-14.
43. Nutt, J.G., et al., *Randomized, double-blind trial of glial cell line-derived neurotrophic factor (GDNF) in PD.* Neurology, 2003. 60(1): p. 69-73.
44. Doolittle, N.D., et al., *Safety and efficacy of a multicenter study using intraarterial chemotherapy in conjunction with osmotic opening of the blood-brain barrier for the treatment of patients with malignant brain tumors.* Cancer, 2000. 88(3): p. 637-47.
45. Prades, R., et al., *Applying the Retro-Enantio Approach to Obtain a Peptide Capable of Overcoming the Blood-Brain Barrier.* Angew Chem Int Ed Engl, 2015.

46. Vykhodtseva, N.I., K. Hynynen, and C. Damianou, *Histologic effects of high intensity pulsed ultrasound exposure with subharmonic emission in rabbit brain in vivo.* Ultrasound Med Biol, 1995. 21(7): p. 969-79.
47. Chen, H., et al., *Blood vessel deformations on microsecond time scales by ultrasonic cavitation.* Phys Rev Lett, 2011. 106(3): p. 034301.
48. McDannold, N., N. Vykhodtseva, and K. Hynynen, *Targeted disruption of the blood-brain barrier with focused ultrasound: association with cavitation activity.* Phys Med Biol, 2006. 51(4): p. 793-807.
49. Sheikov, N., et al., *Cellular mechanisms of the blood-brain barrier opening induced by ultrasound in presence of microbubbles.* Ultrasound Med Biol, 2004. 30(7): p. 979-89.
50. Sheikov, N., et al., *Effect of focused ultrasound applied with an ultrasound contrast agent on the tight junctional integrity of the brain microvascular endothelium.* Ultrasound in medicine & biology, 2008. 34(7): p. 1093-104.
51. Timbie, K.F., B.P. Mead, and R.J. Price, *Drug and gene delivery across the blood-brain barrier with focused ultrasound.* J Control Release, 2015.
52. Park, J., et al., *The kinetics of blood brain barrier permeability and targeted doxorubicin delivery into brain induced by focused ultrasound.* Journal of Controlled Release, 2012. 162(1): p. 134-142.
53. Baseri, B., et al., *Activation of signaling pathways following localized delivery of systemically administered neurotrophic factors across the blood-brain barrier using focused ultrasound and microbubbles.* Physics in Medicine and Biology, 2012. 57(7): p. N65-N81.
54. Jordao, J.F., et al., *Antibodies Targeted to the Brain with Image-Guided Focused Ultrasound Reduces Amyloid-beta Plaque Load in the TgCRND8 Mouse Model of Alzheimer's Disease.* Plos One, 2010. 5(5).
55. Burgess, A., et al., *Focused ultrasound for targeted delivery of siRNA and efficient knockdown of Htt expression.* Journal of Controlled Release, 2012. 163(2): p. 125-129.
56. Wang, S., et al., *Noninvasive, neuron-specific gene therapy can be facilitated by focused ultrasound and recombinant adeno-associated virus.* Gene therapy, 2015. 22(1): p. 104-10.
57. Nance, E., et al., *Non-invasive delivery of stealth, brain-penetrating nanoparticles across the blood-brain barrier using MRI-guided focused ultrasound.* J Control Release, 2014. 189: p. 123-32.
58. Mead, B.P., et al., *Targeted gene transfer to the brain via the delivery of brain-penetrating DNA nanoparticles with focused ultrasound.* J Control Release, 2016. 223: p. 109-17.
59. Burgess, A., et al., *Targeted delivery of neural stem cells to the brain using MRI-guided focused ultrasound to disrupt the blood-brain barrier.* Plos One, 2011. 6(11).
60. Chen, H. and E.E. Konofagou, *The size of blood-brain barrier opening induced by focused ultrasound is dictated by the acoustic pressure.* J Cereb Blood Flow Metab, 2014. 34(7): p. 1197-204.
61. Liu, H.L., et al., *Blood-brain barrier disruption with focused ultrasound enhances delivery of chemotherapeutic drugs for glioblastoma treatment.* Radiology, 2010. 255(2): p. 415-25.
62. Kovacs, Z., et al., *Prolonged survival upon ultrasound-enhanced doxorubicin delivery in two syngenic glioblastoma mouse models.* J Control Release, 2014. 187: p. 74-82.
63. Burgess, A., et al., *Focused ultrasound for targeted delivery of siRNA and efficient knockdown of Htt expression.* J Control Release, 2012. 163(2): p. 125-9.
64. Wu, S.K., et al., *Targeted delivery of erythropoietin by transcranial focused ultrasound for neuroprotection against ischemia/reperfusion-induced neuronal injury: a long-term and short-term study.* PLoS ONE, 2014. 9(2): p. e90107.

65. Marquet, F., et al., *Noninvasive, transient and selective blood-brain barrier opening in non-human primates in vivo.* PLoS ONE, 2011. 6(7): p. e22598.
66. Tung, Y.S., et al., *Feasibility of noninvasive cavitation-guided blood-brain barrier opening using focused ultrasound and microbubbles in nonhuman primates.* Applied Physics Letters, 2011. 98(16): p. 163704.
67. McDannold, N., et al., *Temporary disruption of the blood-brain barrier by use of ultrasound and microbubbles: safety and efficacy evaluation in rhesus macaques.* Cancer research, 2012. 72(14): p. 3652-63.
68. Downs, M.E., et al., *Long-Term Safety of Repeated Blood-Brain Barrier Opening via Focused Ultrasound with Microbubbles in Non-Human Primates Performing a Cognitive Task.* PLoS ONE, 2015. 10(5): p. e0125911.
69. Marquet, F., et al., *Real-time transcranial monitoring of safe blood-brain barrier opening in non-human primates.* PLoS ONE, 2014. 9(2): p. e84310.
70. Wu, S.Y., et al., *Transcranial cavitation detection in primates during blood-brain barrier opening--a performance assessment study.* IEEE Trans Ultrason Ferroelectr Freq Control, 2014. 61(6): p. 966-78.
71. Wu, S.-Y., et al., *Characterizing Focused-Ultrasound Mediated Drug Delivery to the Heterogeneous Primate Brain In Vivo with Acoustic Monitoring.* Sci Rep, 2016. 6.
72. Spetzger, U., G. Laborde, and J.M. Gilsbach, *Frameless neuronavigation in modern neurosurgery.* Minim Invasive Neurosurg, 1995. 38(4): p. 163-6.
73. Ganslandt, O., et al., *Neuronavigation: concept, techniques and applications.* Neurol India, 2002. 50(3): p. 244-55.
74. Wei, K.C., et al., *Neuronavigation-guided focused ultrasound-induced blood-brain barrier opening: a preliminary study in swine.* AJNR Am J Neuroradiol, 2013. 34(1): p. 115-20.
75. Krasovitski, B. and E. Kimmel, *Shear stress induced by a gas bubble pulsating in an ultrasonic field near a wall.* IEEE transactions on ultrasonics, ferroelectrics, and frequency control, 2004. 51(8): p. 973-9.
76. Tung, Y.S., et al., *The mechanism of interaction between focused ultrasound and microbubbles in blood-brain barrier opening in mice.* J Acoust Soc Am, 2011. 130(5): p. 3059-67.
77. Wu, S.Y., et al., *Effects of the microbubble shell physicochemical properties on ultrasound-mediated drug delivery to the brain.* J Control Release, 2015. 212: p. 30-40.
78. Chen, C.C., et al., *Targeted drug delivery with focused ultrasound-induced blood-brain barrier opening using acoustically-activated nanodroplets.* J Control Release, 2013. 172(3): p. 795-804.
79. O'Reilly, M.A. and K. Hynynen, *Blood-Brain Barrier: Real-time Feedback-controlled Focused Ultrasound Disruption by Using an Acoustic Emissions-based Controller.* Radiology, 2012. 263(1): p. 96-106.
80. Tsai, C.H., et al., *Real-time monitoring of focused ultrasound blood-brain barrier opening via subharmonic acoustic emission detection: implementation of confocal dual-frequency piezoelectric transducers.* Phys Med Biol, 2016. 61(7): p. 2926-2946.
81. Sun, T., et al., *Acoustic cavitation-based monitoring of the reversibility and permeability of ultrasound-induced blood-brain barrier opening.* Phys Med Biol, 2015. 60(23): p. 9079-94.
82. Norton, S.J. and I.J. Won, *Time exposure acoustics.* IEEE Transactions on Geoscience and Remote Sensing, 2000. 38(3): p. 1337-1343.
83. Gyongy, M. and C.C. Coussios, *Passive spatial mapping of inertial cavitation during HIFU exposure.* IEEE Trans Biomed Eng, 2010. 57(1): p. 48-56.
84. Molina, C.A., et al., *Transcranial ultrasound in clinical sonothrombolysis (TUCSON) trial.* Ann Neurol, 2009. 66(1): p. 28-38.

85. Culp, W.C., et al., *Successful microbubble sonothrombolysis without tissue-type plasminogen activator in a rabbit model of acute ischemic stroke.* Stroke, 2011. 42(8): p. 2280-2285.
86. Mehier-Humbert, S., et al., *Plasma membrane poration induced by ultrasound exposure: implication for drug delivery.* J Control Release, 2005. 104(1): p. 213-22.
87. Meijering, B.D.M., et al., *Ultrasound and Microbubble-Targeted Delivery of Macromolecules Is Regulated by Induction of Endocytosis and Pore Formation.* Circulation Research, 2009. 104(5): p. 679-U226.
88. De Cock, I., et al., *Ultrasound and microbubble mediated drug delivery: Acoustic pressure as determinant for uptake via membrane pores or endocytosis.* J Control Release, 2015. 197: p. 20-8.
89. Choi, J.J., et al., *Noninvasive, transcranial and localized opening of the blood-brain barrier using focused ultrasound in mice.* Ultrasound Med Biol, 2007. 33(1): p. 95-104.
90. Choi, J.J., et al., *Microbubble-size dependence of focused ultrasound-induced blood-brain barrier opening in mice in vivo.* IEEE Trans Biomed Eng, 2010. 57(1): p. 145-54.
91. Mehier-Humbert, S., et al., *Ultrasound-mediated gene delivery: influence of contrast agent on transfection.* Bioconjug Chem, 2007. 18(3): p. 652-62.
92. Borden, M.A. and M.L. Longo, *Dissolution behavior of lipid monolayer-coated, air-filled microbubbles: effect of lipid hydrophobic chain length.* Langmuir, 2002. 18(24): p. 9225-9233.
93. Borden, M.A., et al., *Influence of lipid shell physicochemical properties on ultrasound-induced microbubble destruction.* IEEE Trans Ultrason Ferroelectr Freq Control, 2005. 52(11): p. 1992-2002.
94. Kwan, J.J. and M.A. Borden, *Lipid monolayer dilatational mechanics during microbubble gas exchange.* Soft Matter, 2012. 8(17): p. 4756-4766.
95. Kwan, J.J. and M.A. Borden, *Lipid monolayer collapse and microbubble stability.* Adv Colloid Interface Sci, 2012. 183-184: p. 82-99.
96. Lewis, B.A. and D.M. Engelman, *Lipid bilayer thickness varies linearly with acyl chain length in fluid phosphatidylcholine vesicles.* J Mol Biol, 1983. 166(2): p. 211-7.
97. Kim, D.H., et al., *Mechanical properties and microstructure of polycrystalline phospholipid monolayer shells: Novel solid microparticles.* Langmuir, 2003. 19(20): p. 8455-8466.
98. Wu, J., *Theoretical study on shear stress generated by microstreaming surrounding contrast agents attached to living cells.* Ultrasound Med Biol, 2002. 28(1): p. 125-9.
99. Doinikov, A.A. and A. Bouakaz, *Theoretical investigation of shear stress generated by a contrast microbubble on the cell membrane as a mechanism for sonoporation.* J Acoust Soc Am, 2010. 128(1): p. 11-9.
100. Chen, C.C., et al., *An experimental study on the stiffness of size-isolated microbubbles using atomic force microscopy.* IEEE Trans Ultrason Ferroelectr Freq Control, 2013. 60(3): p. 524-534.
101. Kripfgans, O.D., et al., *Acoustic droplet vaporization for therapeutic and diagnostic applications.* Ultrasound Med Biol, 2000. 26(7): p. 1177-89.
102. Sheeran, P.S., et al., *Decafluorobutane as a phase-change contrast agent for low-energy extravascular ultrasonic imaging.* Ultrasound Med Biol, 2011. 37(9): p. 1518-30.
103. Mountford, P.A., A.N. Thomas, and M.A. Borden, *Thermal activation of superheated lipid-coated perfluorocarbon drops.* Langmuir, 2015. 31(16): p. 4627-34.
104. Dayton, P.A., et al., *Application of ultrasound to selectively localize nanodroplets for targeted imaging and therapy.* Mol Imaging, 2006. 5(3): p. 160-74.
105. Matsunaga, T.O., et al., *Phase-change nanoparticles using highly volatile perfluorocarbons: toward a platform for extravascular ultrasound imaging.* Theranostics, 2012. 2(12): p. 1185-98.
106. Zhou, Y., *Application of acoustic droplet vaporization in ultrasound therapy.* J Ther Ultrasound, 2015. 3: p. 20.

107. Sheeran, P.S., et al., *Contrast-enhanced ultrasound imaging and in vivo circulatory kinetics with low-boiling-point nanoscale phase-change perfluorocarbon agents.* Ultrasound Med Biol, 2015. 41(3): p. 814-31.
108. Sheeran, P.S., et al., *Formulation and acoustic studies of a new phase-shift agent for diagnostic and therapeutic ultrasound.* Langmuir, 2011. 27(17): p. 10412-20.
109. Wang, C.H., S.T. Kang, and C.K. Yeh, *Superparamagnetic iron oxide and drug complex-embedded acoustic droplets for ultrasound targeted theranosis.* Biomaterials, 2013. 34(7): p. 1852-61.
110. Liu, W.W., et al., *Nanodroplet-Vaporization-Assisted Sonoporation for Highly Effective Delivery of Photothermal Treatment.* Sci Rep, 2016. 6: p. 24753.
111. Rapoport, N., et al., *Ultrasound-mediated tumor imaging and nanotherapy using drug loaded, block copolymer stabilized perfluorocarbon nanoemulsions.* J Control Release, 2011. 153(1): p. 4-15.
112. Zhang, P. and T. Porter, *An in vitro study of a phase-shift nanoemulsion: a potential nucleation agent for bubble-enhanced HIFU tumor ablation.* Ultrasound Med Biol, 2010. 36(11): p. 1856-66.
113. Sheeran, P.S. and P.A. Dayton, *Phase-change contrast agents for imaging and therapy.* Curr Pharm Des, 2012. 18(15): p. 2152-65.
114. Choi, J.J., et al., *Molecules of various pharmacologically-relevant sizes can cross the ultrasound-induced blood-brain barrier opening in vivo.* Ultrasound Med Biol, 2010. 36(1): p. 58-67.
115. Emilio, Q., *Classification and safety of microbubble-based contrast agents*, in *Contrast media in ultrasonography - basic principles and clinical applications*. 2005.
116. Wilson, S.R. and P.N. Burns, *Microbubble-enhanced US in body imaging: what role?* Radiology, 2010. 257(1): p. 24-39.
117. Kitzman, D.W., et al., *Efficacy and safety of the novel ultrasound contrast agent perflutren (definity) in patients with suboptimal baseline left ventricular echocardiographic images.* Am J Cardiol, 2000. 86(6): p. 669-74.
118. Basilico, R., et al., *The first phase I study of a novel ultrasound contrast agent (BR14): assessment of safety and efficacy in liver and kidneys.* Acad Radiol, 2002. 9 Suppl 2: p. S380-1.
119. Piscaglia, F. and L. Bolondi, *The safety of Sonovue in abdominal applications: retrospective analysis of 23188 investigations.* Ultrasound Med Biol, 2006. 32(9): p. 1369-75.
120. *Risk of anaphylaxis in a hospital population in relation to the use of various drugs: an international study.* Pharmacoepidemiol Drug Saf, 2003. 12(3): p. 195-202.
121. Cochran, S.T., K. Bomyea, and J.W. Sayre, *Trends in adverse events after IV administration of contrast media.* AJR Am J Roentgenol, 2001. 176(6): p. 1385-8.
122. ScienceDaily. *Blood-brain barrier opened non-invasively with focused ultrasound for the first time*. 2015 [cited 2016; Available from: https://www.sciencedaily.com/releases/2015/11/151109085103.htm.
123. U.S.-National-Institutes-of-Health. *Sonothrombolysis Potentiated by Microbubbles for Acute Ischemic Stroke*. 2015 [cited 2016; Available from: https://clinicaltrials.gov/ct2/show/NCT01678495.
124. Deffieux, T. and E.E. Konofagou, *Numerical study of a simple transcranial focused ultrasound system applied to blood-brain barrier opening.* IEEE Trans Ultrason Ferroelectr Freq Control, 2010. 57(12): p. 2637-53.
125. Furuhata, H. and O. Saito, *Comparative Study of Standing Wave Reduction Methods Using Random Modulation for Transcranial Ultrasonication.* Ultrasound in Medicine and Biology, 2013. 39(8): p. 1440-1450.
126. *The Visible Human Project*. Available from: https://www.nlm.nih.gov/research/visible/applications.html.

127. Treeby, B.E., et al., *Modeling nonlinear ultrasound propagation in heterogeneous media with power law absorption using a k-space pseudospectral method.* J Acoust Soc Am, 2012. 131(6): p. 4324-36.
128. Treeby, B.E. and B.T. Cox, *k-Wave: MATLAB toolbox for the simulation and reconstruction of photoacoustic wave fields.* Journal of Biomedical Optics, 2010. 15(2).
129. Schneider, U., E. Pedroni, and A. Lomax, *The calibration of CT Hounsfield units for radiotherapy treatment planning.* Phys Med Biol, 1996. 41(1): p. 111-24.
130. Duck, F.A., *Physical properties of tissue at ultrasonic frequencies*, in *Physical properties of tissue: a comprehensive reference book*. 1990, Academic Press. p. 73-135.
131. Cobbold, R.S.C., *Foundations of biomedical ultrasound.* Oxford University Press, 2007.
132. Choi, J.J., et al., *Noninvasive and transient blood-brain barrier opening in the hippocampus of Alzheimer's double transgenic mice using focused ultrasound.* Ultrason Imaging, 2008. 30(3): p. 189-200.
133. Marquet, F., Y.S. Tung, and E.E. Konofagou, *Feasibility study of a clinical blood-brain barrier opening ultrasound system.* Nano Life, 2011. 1(3 & 4): p. 1-14.
134. Feshitan, J.A., et al., *Microbubble size isolation by differential centrifugation.* J Colloid Interface Sci, 2009. 329(2): p. 316-24.
135. Samiotaki, G., et al., *A quantitative pressure and microbubble-size dependence study of focused ultrasound-induced blood-brain barrier opening reversibility in vivo using MRI.* Magn Reson Med, 2012. 67(3): p. 769-77.
136. Smith, S.M., et al., *Advances in functional and structural MR image analysis and implementation as FSL.* Neuroimage, 2004. 23 Suppl 1: p. S208-19.
137. Smith, S.M., *Fast robust automated brain extraction.* Hum Brain Mapp, 2002. 17(3): p. 143-55.
138. Chapelon, J.Y., et al., *Reduction of cavitation using pseudorandom signals.* Ieee Transactions on Ultrasonics Ferroelectrics and Frequency Control, 1996. 43(4): p. 623-625.
139. White, P.J., G.T. Clement, and K. Hynynen, *Longitudinal and shear mode ultrasound propagation in human skull bone.* Ultrasound Med Biol, 2006. 32(7): p. 1085-96.
140. Miller, G.W., et al., *Ultrashort echo-time MRI versus CT for skull aberration correction in MR-guided transcranial focused ultrasound: In vitro comparison on human calvaria.* Med Phys, 2015. 42(5): p. 2223-33.
141. Klibanov, A.L., et al., *Targeted ultrasound contrast agent for molecular imaging of inflammation in high-shear flow.* Contrast Media Mol Imaging, 2006. 1(6): p. 259-66.
142. Kwekkeboom, R.F., et al., *Ultrasound and microbubble-induced local delivery of MicroRNA-based therapeutics.* Ultrasound Med Biol, 2015. 41(1): p. 163-76.
143. Phillips, L.C., et al., *Localized ultrasound enhances delivery of rapamycin from microbubbles to prevent smooth muscle proliferation.* J Control Release, 2011. 154(1): p. 42-9.
144. Sheeran, P.S., et al., *Design of ultrasonically-activatable nanoparticles using low boiling point perfluorocarbons.* Biomaterials, 2012. 33(11): p. 3262-3269.
145. Davies, E.R., *A Modified Hough Scheme for General Circle Location.* Pattern Recognition Letters, 1988. 7(1): p. 37-43.
146. Li, H.W., M.A. Lavin, and R.J. Lemaster, *Fast Hough Transform - a Hierarchical Approach.* Computer Vision Graphics and Image Processing, 1986. 36(2-3): p. 139-161.
147. Chen, H., et al., *A new brain drug delivery strategy: focused ultrasound-enhanced intranasal drug delivery.* PLoS ONE, 2014. 9(10): p. e108880.
148. Baseri, B., et al., *Multi-Modality Safety Assessment of Blood-Brain Barrier Opening Using Focused Ultrasound and Definity Microbubbles: A Short-Term Study.* Ultrasound Med Biol, 2010. 36(9): p. 1445-1459.

149. Hynynen, K., et al., *The threshold for brain damage in rabbits induced by bursts of ultrasound in the presence of an ultrasound contrast agent (Optison).* Ultrasound Med Biol, 2003. 29(3): p. 473-81.
150. Arvanitis, C.D., et al., *Controlled ultrasound-induced blood-brain barrier disruption using passive acoustic emissions monitoring.* Plos One, 2012. 7(9).
151. Jortner, B.S., *The return of the dark neuron. A histological artifact complicating contemporary neurotoxicologic evaluation.* Neurotoxicology, 2006. 27(4): p. 628-634.
152. Abou-Saleh, R.H., et al., *Poly(ethylene glycol) lipid-shelled microbubbles: abundance, stability, and mechanical properties.* Langmuir, 2014. 30(19): p. 5557-63.
153. Tinkov, S., et al., *New doxorubicin-loaded phospholipid microbubbles for targeted tumor therapy: in-vivo characterization.* J Control Release, 2010. 148(3): p. 368-72.
154. Sirsi, S.R., et al., *Polyplex-microbubble hybrids for ultrasound-guided plasmid DNA delivery to solid tumors.* J Control Release, 2012. 157(2): p. 224-34.
155. Fan, C.H., et al., *SPIO-conjugated, doxorubicin-loaded microbubbles for concurrent MRI and focused-ultrasound enhanced brain-tumor drug delivery.* Biomaterials, 2013. 34(14): p. 3706-15.
156. Huynh, E., et al., *In situ conversion of porphyrin microbubbles to nanoparticles for multimodality imaging.* Nature nanotechnology, 2015.
157. Wang, Y., et al., *Preparation of nanobubbles for ultrasound imaging and intracelluar drug delivery.* Int J Pharm, 2010. 384(1-2): p. 148-53.
158. Hwang, T.L., et al., *Development and evaluation of perfluorocarbon nanobubbles for apomorphine delivery.* J Pharm Sci, 2009. 98(10): p. 3735-47.
159. Garg, S., A.A. Thomas, and M.A. Borden, *The effect of lipid monolayer in-plane rigidity on in vivo microbubble circulation persistence.* Biomaterials, 2013. 34(28): p. 6862-70.
160. Choi, J.J., et al., *Noninvasive and localized blood-brain barrier disruption using focused ultrasound can be achieved at short pulse lengths and low pulse repetition frequencies.* J Cereb Blood Flow Metab, 2010.
161. Samiotaki, G. and E.E. Konofagou, *Dependence of the reversibility of focused- ultrasound-induced blood-brain barrier opening on pressure and pulse length in vivo.* IEEE Trans Ultrason Ferroelectr Freq Control, 2013. 60(11): p. 2257-65.
162. Sheeran, P.S., T.O. Matsunaga, and P.A. Dayton, *Phase-transition thresholds and vaporization phenomena for ultrasound phase change nanoemulsions assessed via high speed optical microscopy.* Physics in Medicine and Biology, 2013. In Review.
163. Moyer, L.C., et al., *High-intensity focused ultrasound ablation enhancement in vivo via phase-shift nanodroplets compared to microbubbles.* J Ther Ultrasound, 2015. 3: p. 7.
164. Chen, W.S., et al., *Inertial cavitation dose and hemolysis produced in vitro with or without Optison.* Ultrasound Med Biol, 2003. 29(5): p. 725-37.
165. Dollet, B., et al., *Nonspherical oscillations of ultrasound contrast agent microbubbles.* Ultrasound Med Biol, 2008. 34(9): p. 1465-73.
166. Tung, Y.S., et al., *Identifying the inertial cavitation threshold and skull effects in a vessel phantom using focused ultrasound and microbubbles.* Ultrasound Med Biol, 2010. 36(5): p. 840-52.
167. Marty, B., et al., *Dynamic study of blood-brain barrier closure after its disruption using ultrasound: a quantitative analysis.* J Cereb Blood Flow Metab, 2012. 32(10): p. 1948-58.
168. Samiotaki, G., et al., *Pharmacodynamic analysis and concentration mapping for efficient delivery through the FUS-induced BBB opening in non-human primates in vivo.* Journal of Therapeutic Ultrasound, 2015. 3(1).
169. Gilad Liberman, Y.L., Dafna Ben Bashat, *T1 mapping using variable flip angle SPGR data with flip angle correction.* Journal of Magnetic Resonance Imaging, 2014. 40: p. 171-180.

170. Sophie Laurent, L.V.E., Robert N. Muller, *Comparative study of the physicochemical properties of six clinical low molecular weight gadolinium contrast agents.* Contrast Media Mol Imaging, 2006. 1: p. 128-137.
171. Radhakrishnan, K., et al., *Relationship between cavitation and loss of echogenicity from ultrasound contrast agents.* Phys Med Biol, 2013. 58(18): p. 6541-63.
172. Chang, P.P., et al., *Thresholds for inertial cavitation in albunex suspensions under pulsed ultrasound conditions.* IEEE Trans Ultrason Ferroelectr Freq Control, 2001. 48(1): p. 161-70.
173. Chen, W.S., et al., *A comparison of the fragmentation thresholds and inertial cavitation doses of different ultrasound contrast agents.* J Acoust Soc Am, 2003. 113(1): p. 643-51.
174. Ammi, A.Y., et al., *Ultrasonic contrast agent shell rupture detected by inertial cavitation and rebound signals.* IEEE Trans Ultrason Ferroelectr Freq Control, 2006. 53(1): p. 126-36.
175. Bader, K.B. and C.K. Holland, *Gauging the likelihood of stable cavitation from ultrasound contrast agents.* Phys Med Biol, 2013. 58(1): p. 127-44.
176. Coussios, C.C., et al., *Role of acoustic cavitation in the delivery and monitoring of cancer treatment by high-intensity focused ultrasound (HIFU).* Int J Hyperthermia, 2007. 23(2): p. 105-20.
177. Datta, S., et al., *Correlation of cavitation with ultrasound enhancement of thrombolysis.* Ultrasound Med Biol, 2006. 32(8): p. 1257-67.
178. Coussios, C.C. and R.A. Roy, *Applications of acoustics and cavitation to noninvasive therapy and drug delivery.* Annual Review of Fluid Mechanics, 2008. 40: p. 395-420.
179. Sun, T., et al., *Ambient pressure dependence of the ultra-harmonic response from contrast microbubbles.* J Acoust Soc Am, 2012. 131(6): p. 4358-64.
180. Arvanitis, C.D., et al., *Controlled ultrasound-induced blood-brain barrier disruption using passive acoustic emissions monitoring.* PLoS ONE, 2012. 7(9): p. e45783.
181. Fry, F.J. and J.E. Barger, *Acoustical properties of the human skull.* J Acoust Soc Am, 1978. 63(5): p. 1576-90.
182. Pichardo, S., V.W. Sin, and K. Hynynen, *Multi-frequency characterization of the speed of sound and attenuation coefficient for longitudinal transmission of freshly excised human skulls.* Phys Med Biol, 2011. 56(1): p. 219-50.
183. Pinton, G., et al., *Effects of nonlinear ultrasound propagation on high intensity brain therapy.* Medical physics, 2011. 38(3): p. 1207-16.
184. Pinton, G., et al., *Attenuation, scattering, and absorption of ultrasound in the skull bone.* Med Phys, 2012. 39(1): p. 299-307.
185. Tung, Y.S., et al., *In vivo transcranial cavitation threshold detection during ultrasound-induced blood-brain barrier opening in mice.* Phys Med Biol, 2010. 55(20): p. 6141-55.
186. Arvanitis, C.D., M.S. Livingstone, and N. McDannold, *Combined ultrasound and MR imaging to guide focused ultrasound therapies in the brain.* Phys Med Biol, 2013. 58(14): p. 4749-61.
187. Jones, R.M., M.A. O'Reilly, and K. Hynynen, *Transcranial passive acoustic mapping with hemispherical sparse arrays using CT-based skull-specific aberration corrections: a simulation study.* Phys Med Biol, 2013. 58(14): p. 4981-5005.
188. Schambach, S.J., et al., *Ultrafast high-resolution in vivo volume-CTA of mice cerebral vessels.* Stroke, 2009. 40(4): p. 1444-50.
189. Kapoor, K., V.K. Kak, and B. Singh, *Morphology and comparative anatomy of circulus arteriosus cerebri in mammals.* Anat Histol Embryol, 2003. 32(6): p. 347-55.
190. Chamanahalli Appaji Ashwini, R.S., Kadaba Srinivasan Jayanthi, *Comparative anatomy of the circle of Willis in man, cow, sheep, goat, and pig.* Neuroanatomy, 2008. 7: p. 54-85.
191. Sassaroli, E. and K. Hynynen, *On the impact of vessel size on the threshold of bubble collapse.* Applied Physics Letters, 2006. 89(12): p. 123901.

192. Sassaroli, E. and K. Hynynen, *Cavitation threshold of microbubbles in gel tunnels by focused ultrasound.* Ultrasound Med Biol, 2007. 33(10): p. 1651-60.
193. Vlachos, F., Y.S. Tung, and E.E. Konofagou, *Permeability assessment of the focused ultrasound-induced blood-brain barrier opening using dynamic contrast-enhanced MRI.* Phys Med Biol, 2010. 55(18): p. 5451-66.
194. Bulte, D., et al., *Measurement of cerebral blood volume in humans using hyperoxic MRI contrast.* Journal of Magnetic Resonance Imaging, 2007. 26(4): p. 894-899.
195. Hamberg, L.M., et al., *Measurement of cerebral blood volume with subtraction three-dimensional functional CT.* AJNR Am J Neuroradiol, 1996. 17(10): p. 1861-9.
196. Ellenbogen, R.G., Sekhar, L.N., *Principles of neurological surgery*. 2012, Elsevier Inc.
197. Tang, M.X., R.J. Eckersley, and J.A. Noble, *Pressure-dependent attenuation with microbubbles at low mechanical index.* Ultrasound Med Biol, 2005. 31(3): p. 377-84.
198. Doinikov, A.A. and A. Bouakaz, *Review of shell models for contrast agent microbubbles.* IEEE Trans Ultrason Ferroelectr Freq Control, 2011. 58(5): p. 981-93.
199. Faez, T., et al., *20 years of ultrasound contrast agent modeling.* IEEE Trans Ultrason Ferroelectr Freq Control, 2013. 60(1): p. 7-20.
200. Qin, S. and K.W. Ferrara, *Acoustic response of compliable microvessels containing ultrasound contrast agents.* Phys Med Biol, 2006. 51(20): p. 5065-88.
201. Hosseinkhah, N. and K. Hynynen, *A three-dimensional model of an ultrasound contrast agent gas bubble and its mechanical effects on microvessels.* Phys Med Biol, 2012. 57(3): p. 785-808.
202. Jensen, C.R., et al., *Spatiotemporal monitoring of high-intensity focused ultrasound therapy with passive acoustic mapping.* Radiology, 2012. 262(1): p. 252-61.
203. Salgaonkar, V.A., et al., *Passive cavitation imaging with ultrasound arrays.* Journal of the Acoustical Society of America, 2009. 126(6): p. 3071-3083.
204. Arvanitis, C.D., M.S. Livingstone, and N. McDannold, *Combined ultrasound and MR imaging to guide focused ultrasound therapies in the brain.* Physics in Medicine and Biology, 2013. 58(14): p. 4749-4761.
205. Choi, J.J., et al., *Non-invasive and real-time passive acoustic mapping of ultrasound-mediated drug delivery.* Phys Med Biol, 2014. 59(17): p. 4861-77.
206. Hou, G.Y., et al., *Sparse Matrix Beamforming and Image Reconstruction for 2-D HIFU Monitoring Using Harmonic Motion Imaging for Focused Ultrasound (HMIFU) With In Vitro Validation.* Ieee Transactions on Medical Imaging, 2014. 33(11): p. 2107-2117.
207. Grondin, J., et al., *Real-time Monitoring of High Intensity Focused Ultrasound (HIFU) Ablation of In Vitro Canine Livers Using Harmonic Motion Imaging for Focused Ultrasound (HMIFU).* J Vis Exp, 2015(105): p. e53050.
208. Jones, R.M., M.A. O'Reilly, and K. Hynynen, *Experimental demonstration of passive acoustic imaging in the human skull cavity using CT-based aberration corrections.* Med Phys, 2015. 42(7): p. 4385-400.

List of Publications Related to the Thesis

1 JOURNAL PUBLICATIONS

1. C.C. Chen, **S.-Y. Wu**, J.D. Finan, B. Morrison III, E.E. Konofagou, "An experimental study on the stiffness of size-isolated microbubbles using atomic force microscopy", ***IEEE Transactions on Ultrasonics, Ferroelectronics, and Frequency Control****, vol. 60(3), 2013.*
2. C.C. Chen, P. Sheeran, **S.-Y. Wu**, O. Olumolade, P. Dayton, E.E. Konofagou, "Targeted drug delivery with focused ultrasound-induced blood-brain barrier opening using acoustically-activated nanodroplets," ***Journal of Controlled Release****, vol. 172(3), 2013.*
3. **S.-Y. Wu**, Y.-S. Tung, F. Marquet, M. Downs, C. Sierra Sanchez, C. Chen, V. Ferrera, E. Konofagou, "Transcranial cavitation detection in primates during blood-brain barrier opening – a performance assessment study," ***IEEE Transactions on Ultrasonics, Ferroelectronics, and Frequency Control****, vol. 61(6), 2014.* **(Highly Cited Article in 2016) (Editor's Selection in 2014 & 2015)**
4. F. Marquet, T. Teichert, **S.-Y. Wu**, Y.-S. Tung, M. Downs, S. Wang, C.C. Chen, V. Ferrera, E.E. Konofagou, "Real-time transcranial monitoring of safe blood-brain barrier opening in non-human primates," ***PloS One****, vol. 9(2), 2014.*
5. H. Chen, C.C. Chen, C. Acosta, **Shih-Ying Wu**, T. Sun, E.E. Konofagou, "A new brain drug delivery strategy: focused ultrasound-enhanced intranasal drug delivery," ***PloS One****, vol. 9(10), 2014.*
6. **S.-Y. Wu**, C.C. Chen, Y.-S. Tung, O. Olumolade, E.E. Konofagou, "Effects of the microbubble shell physicochemical properties on ultrasound-mediated drug delivery to the brain," ***Journal of Controlled Release****, vol. 212, 2015.* **(Cover Story)**
7. H.A.S. Kamimura, S. Wang, **S.-Y. Wu**, M. Karakatsani, C. Acosta, E. Konofagou, "Chirp- and random-based coded ultrasonic excitation for localized blood-brain barrier opening," ***Physics in Medicine and Biology****, vol. 60(19), 2015.*
8. G. Samiotaki, M.E. Karakatsani, **S.-Y. Wu**, A. Buch, E.E. Konofagou, "Pharmacodynamic analysis and concentration mapping for efficient delivery through the focused-ultrasound-induced blood-brain barrier opening in non-human primates," ***Journal of Therapeutic Ultrasound****, vol. 3, 2015.*
9. C. Sierra, C. Acosta, C. Chen, **S.-Y. Wu**, M.E. Karakatsani, M. Bernal, E.E. Konofagou, "Lipid microbubbles as a vehicle for targeted drug delivery using focused ultrasound-induced blood-brain barrier opening," ***Journal of Cerebral Blood Flow & Metabolism****, 2016.*
10. **S.-Y. Wu**, C. Sierra, G. Samiotaki, A. Buch, V. Ferrera, E.E. Konofagou, "Characterizing focused-ultrasound mediated drug delivery in the heterogeneous primate brain with acoustic monitoring," ***Scientific Reports****, vol. 6, 2016.*
11. **S.-Y. Wu**, C. Aurup, C. Sierra, J. Grondin, W. Zheng, V. Ferrera, E.E. Konofagou,

"Neuronavigation-guided ultrasound for blood-brain barrier opening," in review.

12. **S.-Y. Wu**, S. Fix, C. Arena, C. Chen, W. Zheng, O.O. Olumolade, V. Papadopoulou, A. Novell, P.A. Dayton, E.E. Konofagou, "Efficiency of acoustic droplet vaporization dictates drug delivery to the brain using focused ultrasound," in review.
13. **S.-Y. Wu**, J. Grondin, W. Zheng, M. Heidmann, E.E. Konofagou, "Real-time passive cavitation mapping through the primate skull during ultrasound-induced blood-brain barrier opening," in preparation.
14. S. Jimenez, N. Jimenez, **S.-Y. Wu**, E.E. Konofagou, F. Camarena, "Study of aberrations at the focus of an ultrasonic beam due to the propagation across different areas of the skull," in preparation.

2 MAJOR REFERENCES TO THE CHAPTERS

Chapter 2

H.A.S. Kamimura, S. Wang, **S.-Y. Wu**, M. Karakatsani, C. Acosta, E. Konofagou, "Chirp- and random-based coded ultrasonic excitation for localized blood-brain barrier opening," ***Physics in Medicine and Biology**, vol. 60(19), 2015.*

S.-Y. Wu, C. Aurup, C. Sierra, J. Grondin, W. Zheng, V. Ferrera, E.E. Konofagou, "Neuronavigation-guided ultrasound for blood-brain barrier opening," in review.

S. Jimenez, N. Jimenez, **S.-Y. Wu**, E.E. Konofagou, F. Camarena, "Study of aberrations at the focus of an ultrasonic beam due to the propagation across different areas of the skull," in preparation.

Chapter 3

S.-Y. Wu, C.C. Chen, Y.-S. Tung, O. Olumolade, E.E. Konofagou, "Effects of the microbubble shell physicochemical properties on ultrasound-mediated drug delivery to the brain," ***Journal of Controlled Release**, vol. 212, 2015.* **(Cover Story)**

C.C. Chen, P. Sheeran, **S.-Y. Wu**, O. Olumolade, P. Dayton, E.E. Konofagou, "Targeted drug delivery with focused ultrasound-induced blood-brain barrier opening using acoustically-activated nanodroplets," ***Journal of Controlled Release**, vol. 172(3), 2013.*

S.-Y. Wu, S. Fix, C. Arena, C. Chen, W. Zheng, O.O. Olumolade, V. Papadopoulou, A. Novell, P.A. Dayton, E.E. Konofagou, "Efficiency of acoustic droplet vaporization dictates drug delivery to the brain using focused ultrasound," in review.

C. Sierra, C. Acosta, C. Chen, **S.-Y. Wu**, M.E. Karakatsani, M. Bernal, E.E. Konofagou, "Lipid microbubbles as a vehicle for targeted drug delivery using focused ultrasound-induced blood-brain barrier opening," ***Journal of Cerebral Blood Flow & Metabolism****, 2016.*

Chapter 4

S.-Y. Wu, Y.-S. Tung, F. Marquet, M. Downs, C. Sierra Sanchez, C. Chen, V. Ferrera, E. Konofagou, "Transcranial cavitation detection in primates during blood-brain barrier opening – a performance assessment study," ***IEEE Transactions on Ultrasonics, Ferroelectronics, and Frequency Control****, vol. 61(6), 2014.* **(Highly Cited Article in 2016) (Editor's Selection in 2014 & 2015)**

S.-Y. Wu, C. Sierra, G. Samiotaki, A. Buch, V. Ferrera, E.E. Konofagou, "Characterizing focused-ultrasound mediated drug delivery in the heterogeneous primate brain with acoustic monitoring," ***Scientific Reports****, vol. 6, 2016.*

G. Samiotaki, M.E. Karakatsani, **S.-Y. Wu**, A. Buch, E.E. Konofagou, "Pharmacodynamic analysis and concentration mapping for efficient delivery through the focused-ultrasound-induced blood-brain barrier opening in non-human primates," ***Journal of Therapeutic Ultrasound****, vol. 3, 2015.*

Chapter 5

S.-Y. Wu, J. Grondin, W. Zheng, M. Heidmann, E.E. Konofagou, "Real-time passive cavitation mapping through the primate skull during ultrasound-induced blood-brain barrier opening," in preparation.

S.-Y. Wu, C. Aurup, C. Sierra, J. Grondin, W. Zheng, V. Ferrera, E.E. Konofagou, "Neuronavigation-guided ultrasound for blood-brain barrier opening," in review.

Chapter 6

S.-Y. Wu, C. Aurup, C. Sierra, J. Grondin, W. Zheng, V. Ferrera, E.E. Konofagou, "Neuronavigation-guided ultrasound for blood-brain barrier opening," in review.

3 CONFERENCE PRESENTATIONS & PROCEEDINGS

1. **S.-Y. Wu**, C. Aurup, C. S. Sanchez, M. E. Karakatsani, J. Grondin, W. Zheng, V. Ferrera, E. E. Konofagou, "Neuronavigation-guided focused ultrasound for blood-brain barrier

opening and cavitation mapping in non-human primates," IEEE International Ultrasonics Symposium (Tour, France), September 18 to 21, 2016.

2. C. Sierra, C. Acosta, C. Chen, **S.-Y. Wu**, M.E. Karakatsani, M. Bernal, E.E. Konofagou, "Lipid microbubbles as a vehicle for targeted drug delivery using focused ultrasound-induced blood-brain barrier opening," IEEE International Ultrasonics Symposium (Tour, France), September 18 to 21, 2016.

3. **S.-Y. Wu**, C. Aurup, C. S. Sanchez, M. E. Karakatsani, J. Grondin, W. Zheng, V. Ferrera, E. E. Konofagou, "Neuronavigation-guided focused ultrasound for blood-brain barrier opening and cavitation mapping in non-human primates," 5th International Symposium on Focused Ultrasound (North Bethesda, Maryland), August 28 to September 1, 2016.

4. C. Sierra, C. Acosta, C. Chen, **S.-Y. Wu**, M.E. Karakatsani, M. Bernal, E.E. Konofagou, "Lipid microbubbles as a vehicle for targeted drug delivery using focused ultrasound-induced blood-brain barrier opening," 5th International Symposium on Focused Ultrasound (North Bethesda, Maryland), August 28 to September 1, 2016.

5. **S.-Y. Wu**, J. Grondin, W. Zheng, M. Heidmann, M. E. Karakatsani, C. S. Sanchez, V. Ferrera, E. Konofagou, "Real-time, transcranial passive cavitation mapping for monitoring of the focused-ultrasound induced blood-brain barrier opening in primates," 16th International Symposium on Therapeutic Ultrasound (Tel Aviv, Israel), March 14 to 16, 2016.

6. **S.-Y. Wu**, C. C. Chen, Y.-S. Tung, O. O. Olumolade, E. E. Konofagou, "Effects of the microbubble shell physiochemical properties on ultrasound-mediated drug delivery to the brain," IEEE International Ultrasonics Symposium (Taipei, Taiwan), October 21 to 24, 2015.

7. H. A. S. Kamimura, S. Wang, **S.-Y. Wu**, M. E. Karakatsani, C. J. Acosta, A. A Carneiro, E. E. Konofagou, "Improving targeting of ultrasound-mediated blood-brain barrier opening using chirp and random-based modulations," IEEE International Ultrasonics Symposium (Taipei, Taiwan), October 21 to 24, 2015.

8. **S.-Y. Wu**, C. C. Chen, Y.-S. Tung, O. O. Olumolade, E. E. Konofagou, "The Effect of microbubble shell physicochemical properties on focused ultrasound-induced blood-brain barrier opening," 15th International Symposium on Therapeutic Ultrasound (Utrecht, Netherlands), April 15 to 18, 2015.

9. H. Chen, C. C. Chen, C. J. Acosta, **S.-Y. Wu**, T. Sun, E. E. Konofagou, "A new brain drug delivery strategy: Focused ultrasound-enhanced intranasal drug delivery," Neuroscience (Washington, DC, USA), November 15 to 19, 2014.

10. G. Samiotaki, M. E. Karakatsani, **S.-Y. Wu**, A. M. Buch, M. E. Downs, V. P. Ferrera, S. R. Jambawalikar, E. E. Konofagou, "Pharmacodynamic analysis for efficient drug delivery through the FUS-induced BBB opening in non-human primates in vivo," IEEE International Ultrasonics Symposium (Chicago, IL, USA), September 3 to 6, 2014.

11. **S.-Y. Wu**, C. S. Sánchez, M. E. Downs, A. M. Buch, G. Samiotaki, V. P. Ferrera, E. E. Konofagou, "Focused ultrasound-induced blood-brain barrier opening in non-human primates with transcranial cavitation detection in vivo," IEEE International Ultrasonics Symposium (Chicago, IL, USA), September 3 to 6, 2014.

12. **S.-Y. Wu**, C. S. Sánchez, M. E. Downs, A. M. Buch, G. Samiotaki, V. P. Ferrera, E. E. Konofagou, "Focused ultrasound-induced blood-brain barrier opening in non-human primates with transcranial cavitation detection in vivo," 14th International Symposium on Therapeutic Ultrasound (Las Vegas, NV, USA), April 2 to 5, 2014. (**Student's Travel Award**)

13. M. E. Downs, T. Teichert, V. P. Ferrera, **S.-Y. Wu**, E. E. Konofagou, "Minimally invasive ultrasound based drug delivery in the non-human primate," Neuroscience (San Diego, CA, USA), November 9 to 13, 2013.

14. C. C. Chen, P. S. Sheeran, **S.-Y. Wu**, O. O. Olumolade, P. S. Dayton, E. E. Konofagou, "Targeted drug delivery with focused ultrasound-induced blood-brain barrier opening ssing acoustically-activated nanodroplets," IEEE International Ultrasonics Symposium (Prague, Czech Republic), July 21 to 25, 2013.

15. **S.-Y. Wu**, F. Marquet, Y.-S. Tung, T. Teichert, M. E. Downs, C. C. Chen, V. P. Ferrera, E. E. Konofagou, "Monitoring of FUS-induced BBB opening in non-human primates using transcranial cavitation detection in vivo and the human skull effect," IEEE International Ultrasonics Symposium (Prague, Czech Republic), July 21 to 25, 2013.

16. C. C. Chen, P. S. Sheeran, **S.-Y. Wu**, O. O. Olumolade, P. S. Dayton, E. E. Konofagou, "Targeted Drug Delivery with Focused Ultrasound-Induced blood-brain barrier opening using acoustically-activated nanodroplets," 13th International Symposium on Therapeutic Ultrasound (Shanghai, China), May 12 to 15, 2013.

17. Y.-S. Tung, C. C. Chen, O. O. Olumolade, **S.-Y. Wu**, S. Wang, E. E. Konofagou, "The cavitation-dependent zonula-occludens-1 integrity after ultrasound-induced blood-brain barrier opening," Cold Spring Harbor Laboratory Meeting: The Blood-Brain Barrier (Cold Spring Harbor, NY, USA), December 5 to 8, 2012.

18. Y.-S. Tung, **S.-Y. Wu**, F. Marquet, E. E. Konofagou, "Quantification of stable cavitation dose during FUS-induced blood-brain barrier opening in mice and in non-human primates," IEEE International Ultrasonics Symposium (Dresden, Germany), October 7 to 10, 2012.

19. **S.-Y. Wu**, Y.-S. Tung, F. Marquet, C. C. Chen, E. E. Konofagou, "Non-human primate skull effects on the FUS-induced blood-brain barrier opening," IEEE International Ultrasonics Symposium (Dresden, Germany), October 7 to 10, 2012. (**Student's Travel Award**)

20. C. C. Chen, **S.-Y. Wu**, J. D. Finan, B. Morrison III, E. E. Konofagou, "An experimental study on the apparent stiffness of size-isolated microbubbles used for blood-brain barrier

opening applications," Proceedings of the IEEE International Ultrasonics Symposium (Dresden, Germany), October 7 to 10, 2012.

21. C. C. Chen, **S.-Y. Wu**, J. D. Finan, B. Morrison III, E. E. Konofagou, "An experimental study on the stiffness of size-isolated microbubbles with relevance to blood-brain barrier opening applications," Gordon Research Conference: Barriers of the Central Nervous System (New London, NH, USA), June 17 to 22, 2012.

22. Y.-S. Tung, O. O. Olumolade, S. Wang, **S.-Y. Wu**, E. E. Konofagou, "Physical mechanism of non-inertial cavitation induced blood-brain barrier opening using focused ultrasound and microbubbles," 12th International Symposium on Therapeutic Ultrasound (Heidelberg, Germany), June 10 to 13, 2012.

23. **S.-Y. Wu**, Y.-S. Tung, F. Marquet, E. E. Konofagou, "Non-human primate skull effects on the in vivo study of the mechanism of the FUS-induced blood-brain barrier opening," 12th International Symposium on Therapeutic Ultrasound (Heidelberg, Germany), June 10 to 13, 2012. (**Student's Travel Award**)

24. C. C. Chen, **S.-Y. Wu**, J. D. Finan, B. Morrison III, E. E. Konofagou, "An experimental study on the stiffness of size-isolated microbubbles used for blood-brain barrier opening," Proceedings of the 12th International Symposium on Therapeutic Ultrasound (Heidelberg, Germany), June 10 to 13, 2012.